3D vector flow imaging

Pihl, Michael Johannes; Nikolov, Svetoslav; Jensen, Jørgen Arendt

Publication date:
2012

Document Version
Publisher's PDF, also known as Version of record

Citation (APA):
Pihl, M. J., Nikolov, S., & Jensen, J. A. (2012). 3D vector flow imaging. Kgs. Lyngby: Technical University of Denmark (DTU).

Technical University of Denmark

Michael Johannes Pihl

3D vector flow imaging

PhD thesis, August 2012

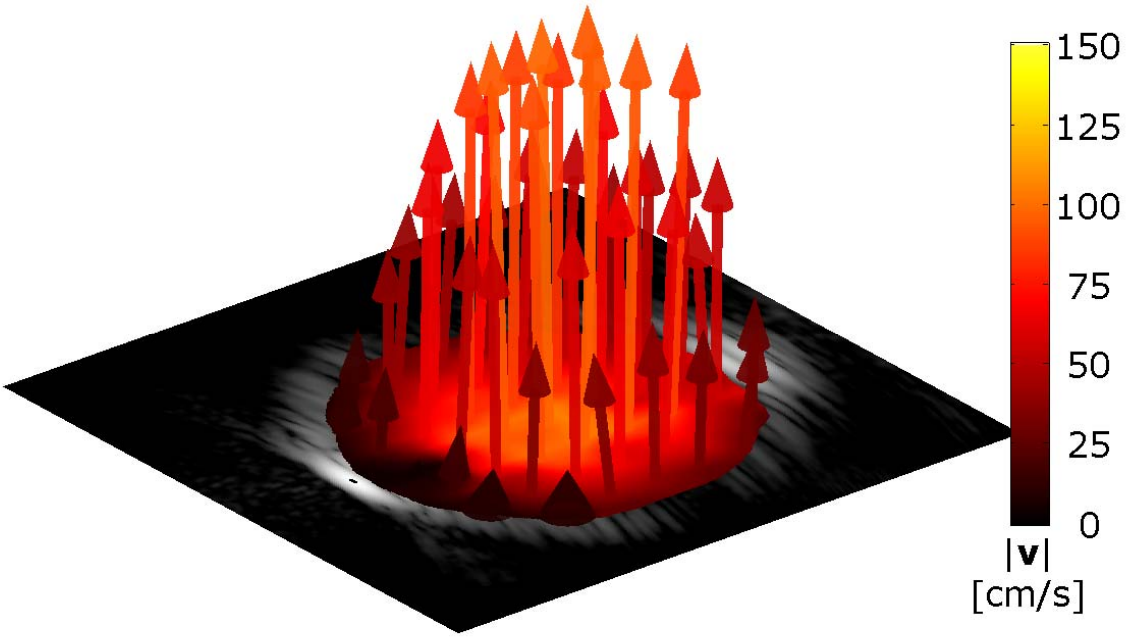

DTU Electrical Engineering
Department of Electrical Engineering

3D vector flow imaging

DTU Electrical Engineering
PhD Thesis

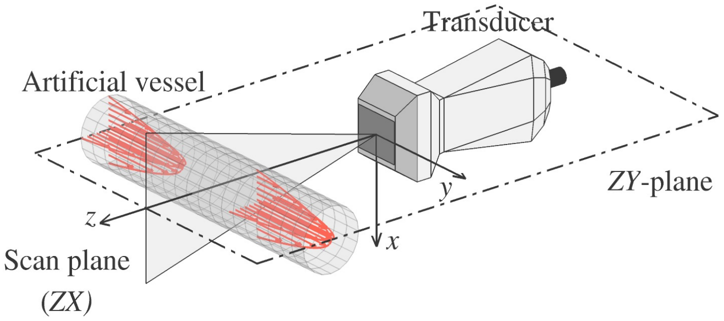

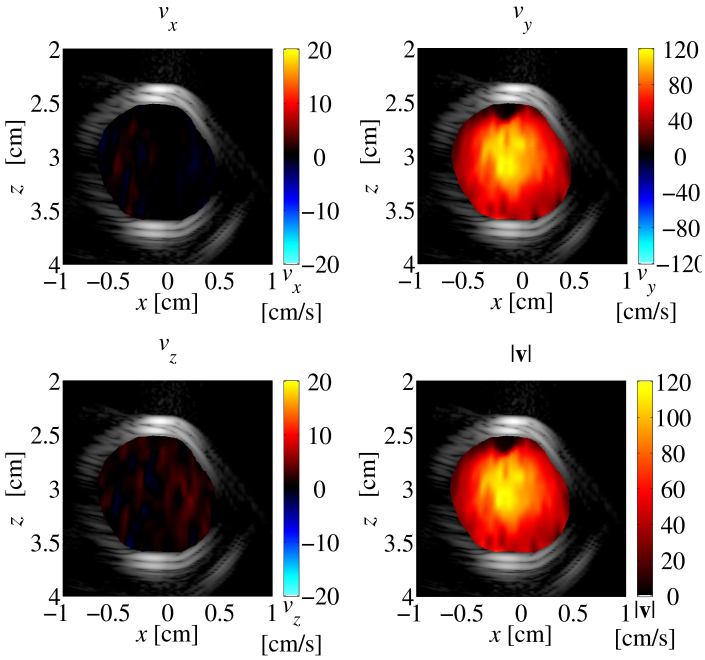

Author
Michael Johannes Pihl

August 2012

DTU Electrical Engineering
Department of Electrical Engineering

This thesis is submitted as partial fulfillment of the requirements for acquiring the PhD degree. The work had been carried out at the Center for Fast Ultrasound Imaging (CFU), Biomedical Engineering, Department of Electrical Engineering, Technical University of Denmark.

SUPERVISORS
Professor Jørgen Arendt Jensen, PhD, Dr. Techn.
Center for Fast Ultrasound Imaging, Department of Electrical Engineering, Technical University of Denmark

Svetoslav Ivanov Nikolov, PhD
BK Medical ApS, Herlev, Denmark

ASSESSMENT COMMITTEE
Chairman:
Professor Jens E. Wilhjelm, PhD
Department of Electrical Engineering
Technical University of Denmark

External examiners:
Professor Hans Nygaard, BME, DMSc
Biomedical Engineering, The Faculty of Health Sciences, University of Aarhus
Department of Cardiothoracic and Vascular Surgery
Aarhus University Hospital, Skejby

Assoc. Professor Tomas Jansson, PhD
Department of Electrical Measurements
Lund University

3D vector flow imaging
2nd edition, December 2012

Center for Fast Ultrasound Imaging
DTU Electrical Engineering
Biomedical Engineering
Technical University of Denmark
DK-2800 Kgs. Lyngby
Denmark

ISBN 978-87-92465-70-2

Cover illustration: Arrows representing the 3-D velocity vectors.
Title page illustration: Example of 3D vector flow imaging. See Section 7.7.

Preface

This PhD thesis has been submitted to the Department of Electrical Engineering at the Technical University of Denmark in partial fulfillment of the requirements for acquiring the PhD degree.

The research providing the foundation for the thesis has been conducted over a period of three years from August 17th, 2009 to August 15th, 2012 at the Center for Fast Ultrasound Imaging (CFU), Biomedical Engineering, Department of Electrical Engineering, Technical University of Denmark. The project was funded by grant 024-2008-3 from the Danish Advanced Technology Foundation and BK Medical Aps, Denmark. The thesis recapitulates the conducted research and included are three journal papers, three conference papers, and one extended abstract.

During my work I have had the opportunity to attend conferences in Rome, Copenhagen, San Diego, Cancún, Artimino, and Orlando to present my research, and it has let to many fruitful discussions. Traveling to these conferences has been a huge privilege, and the experiences have broadened my horizon of both the technical and the clinical side of medical ultrasound as well as within acoustics in general. Additionally, the conferences have given me the opportunity to nurture and expand my professional as well as social networks. I have also enjoyed and learned a lot from teaching and tutoring students in medical imaging systems through three semesters, and I especially value the experience of co-supervising a master's project. It has been a pleasure to share my knowledge within ultrasound imaging and velocity estimation with professors, colleagues, and students at the Biomedical Engineering Group.

Michael Johannes Pihl
Kgs. Lyngby, Denmark, August 2012

Abstract

The main purpose of this PhD project is to develop an ultrasonic method for 3D vector flow imaging. The motivation is to advance the field of velocity estimation in ultrasound, which plays an important role in the clinic. The velocity of blood has components in all three spatial dimensions, yet conventional methods can estimate only the axial component. Several approaches for 3D vector velocity estimation have been suggested, but none of these methods have so far produced convincing *in vivo* results nor have they been adopted by commercial manufacturers. The basis for this project is the *Transverse Oscillation* (TO) method, which estimates both the axial and the lateral velocity components.

The first part of the scientific contribution demonstrates that a commercial implementation of the TO method is feasible. Afterwards, the method is expanded to a phased array geometry, and performance metrics based on the TO fields are suggested. They can be used to optimize the TO method. In the third part, a TO method for 3D vector velocity estimation is proposed. It employs a 2D phased array transducer and decouples the velocity estimation into three velocity components, which are estimated simultaneously based on 5:1 parallel receive beamforming. Simulation results demonstrate the feasibility of the method.

In the final part, an experimental investigation of the 3D TO method is presented. Velocity measurements of steady flow were conducted in a flow-rig system, and the data were acquired using an experimental ultrasound scanner and a 2D transducer. The three velocity components along the center line are measured with relative (to the expected values) biases and standard deviations lower than 5 % and 12 %, respectively. At the center of the vessel, the mean and standard deviation of 100 estimated velocity vectors are (v_x, v_y, v_z) = (-0.03, 95, 1.0) ± (9, 6, 1) cm/s compared with the expected (0, 96, 0) cm/s. Afterwards, 3D vector flow images from a cross-sectional plane of the vessel are presented. The out of plane velocities exhibit the expected 2D circular-symmetric parabolic shape. The experimental results verify that the 3D TO method estimates the complete 3D velocity vectors, and that the method is suitable for 3D vector flow imaging.

Resumé

Hovedformålet med dette ph.d.-projekt er at udvikle en fremgangsmåde inden for ultralyd til 3D vektor strømningsbilleddannelse. Motivationen er at fremme feltet inden for hastighedsestimering i ultralyd, som spiller en vigtig rolle i klinikken. Blodets hastighedsvektor har komposanter i alle tre rumlige dimensioner, men konventionelle metoder estimerer alene den aksiale komposant. Adskillige fremgangsmåder til estimering af 3D hastighedsvektorer er blevet foreslået, men ingen af disse fremgangsmåder har hidtil produceret overbevisende *in vivo* resultater, og ingen er blevet implementeret af kommercielle producenter. Grundlaget for dette projekt er *Transverse Oscillation* (TO)-metoden, som estimerer både den aksielle og den tværgående hastighedskomposant.

Første del af det videnskabelige bidrag demonstrerer, at en kommerciel implementering af TO metoden er mulig. Dernæst udvides metoden til en *phased array* geometri, og performancemetrikker baseret på TO-felterne foreslås. De kan anvendes til at optimere metoden. I tredje del foreslås en fremgangsmåde til estimering af 3D hastighedsvektorer. Den anvender en 2D phased array transducer og afkobler hastighedsestimeringen i tre komposanter, som estimeres samtidigt baseret på 5:1 parallel *receive beamforming*. Simuleringsresultater demonstrerer gennemførligheden af metoden.

I den sidste del præsenteres en eksperimentel undersøgelse af 3D TO metoden. Hastighedsmålinger af stabilt flow blev udført i et flow-rig system, og data måltes med en eksperimentel ultralydsskanner og en 2D transducer. De tre hastighedskomposanter langs midterlinjen måles med en relativ (i forhold til den forventede værdi) bias og standardafvigelse mindre end henholdsvis 5 % og 12 %. I midten af karret er middelværdien og standardafvigelsen af 100 estimerede hastighedsvektorer $(v_x, v_y, v_z) =$ (-0,03; 95; 1,0) ± (9; 6; 1) cm/s i forhold til de forventede (0; 96; 0) cm/s. Efterfølgende præsenteres 3D vektor strømningsbilleder optaget i et tværsnitsplan af karret. Hastighederne ud af planet udviser den forventede 2D cirkulær-symmetriske og parabolske profil. De eksperimentelle resultater verificerer, at 3D TO-metoden måler den komplette 3D hastighedsvektor, og at fremgangsmåden er egnet til 3D vektor strømningsbilleddannelse.

Acknowledgments

First of all, I would like to thank my supervisors Professor Jørgen Arendt Jensen, PhD, Dr. Techn., from the Center for Fast Ultrasound Imaging (CFU) at the Technical University of Denmark and Svetoslav Ivanov Nikolovg, PhD, from BK Medical. I want to express my deepest appreciation of your positive and constructive cooperation in making this project successful. It has been an honor to benefit from your solid experience and knowledge.

I am grateful for all the help and supervision Jørgen has given me over the years, and I have enjoyed our many fruitful academic as well non-academic discussions. Thank you! Svetoslav, I especially want to thank you for your tremendous work on the research interface. Without your effort, many projects would never have made it as far as they have. Also, thanks to the remaining employees at BK Medical for having shown interest in the project.

To my office mate and fellow PhD student Jens Munk Hansen goes my warmest regards. We have spend many hours together engaged in concentrated silence, intriguing theoretical discussions, or sharing everyday life experiences. You have taught me a lot of things, and I admire your ability to always have a good story up your sleeve.

I would also like to thank my other fellow PhD students: Joachim Hee Rasmussen, you have been a good friend and colleague, and I especially treasure our breaks with home-brewed coffee and our common interest in single-speed biking for our daily commutes. Also thanks for always willingly proof-reading various manuscripts. Morten Fischer Rasmussen, thanks for help and productive discussions in regard to measurements using the 2D transducer and for taking the pictures of SARUS and the 2D transducer for me. Ye Li, thank you for our conversations on various velocity estimation techniques, but also Chinese culture. Additional thanks go to present and previous PhD students at CFU including Mette Funding La Cour, An Pahm, Yigang Du, PhD, David Bæk, PhD, and Klaus S. Andersen, PhD.

Many thanks go to Matthias Bo Stuart, PhD, and Borislav Gueorguiev Tomov, PhD for their hard work in making the SARUS system functional. My thanks are also extended to assistant professor Marie Sand Enevoldsen, PhD, for our many intriguing discussion regarding the crossover between ultrasonic velocity estimation and computational fluid dynamics modelling. Also thanks to assistant professor Martin Christian Hemmsen, PhD, for having provided assistance in regard to the research interface.

To the medical doctors Mads Møller Pedersen, PhD, and Peter Møller Hansen, I thank you both for always being ready to assist and for providing the clinical perspectives to the conducted research at CFU.

Without the help from the following people, my ability to concentrate on research would have been significantly hampered. Elna Sørensen, you have always been ready to provide help with administrative matters and issues in general, and I admire your energetic attitude towards biking in all kinds of weather—and that says a lot in Denmark. Nina Kjærsgaard, you have always had a positive attitude and been helpful especially with questions regarding communication. Furthermore, I appreciate all the technical help I have received from Henrik Laursen, who never hesitated to help. Also Jens Chr. Jensen has provided technical assistance and has helped constructing and repairing equipment when needed. Thanks to you all.

To Jønne Marcher, I extend my thanks for many fruitful hours in close collaboration—both during your master's thesis with me as your co-supervisor and afterwards. To Jacob Bjerring Olesen and Alejandro González González I would like to say: It has been a pleasure to spent time with you and to discuss various technical as well as non-technical issues. It has been a great experience to make friends whilst working. And to Jacob, thank you for having proof-read parts of several manuscripts.

To all I have been engaged with at CFU, thank you for many rewarding discussions and talks at our weekly Wednesday meetings and in general, and for many pleasant travels to conferences around the world. I would also like to thank everyone at the Biomedical Engineering Group for creating a pleasant work environment. Additionally, thanks to all the faculty members that have taking an interest in my project during the past three years.

I would also like to thankfully mention my former fellow MedTek students including Isa Conradsen, Anne Katrine Duun-Henriksen, Jonas Duun-Henriksen, Oline Vinter Olesen, Sune Kristian Buhl, and Christian Hollensen. We have had many good times together, and I appreciate all the moral support you have provided during the past three years. Thank you!

Special thanks are granted to Marie, Nina, Morten, and Jacob for proof-reading the thesis or selected parts hereof. I deeply appreciate your help!

Last, but definitely not least, I would like to express my sincerest thanks to my family and Saeid Khaleghi, who have lovingly supported me throughout the project and for understanding my high commitment and engagement to the project.

Papers and abstracts included in the thesis

Papers

I M. J. Pihl, S. I. Nikolov, M. C. Hemmsen, and J. A. Jensen. Performance of the Transverse Oscillation Method using Beamformed Data from a Commercial Scanner. In *Proc. IEEE Ultrason. Symp.*, pages 1-4, September 2009

II M. J. Pihl and J. A. Jensen Transverse Oscillations for Phased Array Vector Velocity Imaging. In *Proc. IEEE Ultrasons. Symp.*, pages 1323-1327, October 2010

III M. J. Pihl, J. Marcher and J. A. Jensen. Phased Array Vector Velocity Estimation using Transverse Oscillations. *IEEE Trans. Ultrasons., Ferroelec., Freq. Contr.*, In press, December 2012

IV M. J. Pihl and J. A. Jensen. 3D Vector Velocity Estimation using a 2D Phased Array. In *Proc. IEEE Ultrasons. Symp*, pages 430-433, October 2011

V M. J. Pihl and J. A. Jensen. A method for estimation of three-dimensional velocity vectors in ultrasound. *J. Acoust. Soc. Am.*, In review

VI M. J. Pihl and J. A. Jensen. Experimental investigation of three-dimensional velocity vector estimation. *J. Acoust. Soc. Am.*, In review

Abstracts

A M. J. Pihl and J. A. Jensen. Measuring 3D Velocity Vectors using the Transverse Oscillation Method. In *Proc. IEEE Ultrason. Symp. 2012*, Accepted and presented. Paper in press

B M. J. Pihl, M. B. Stuart, B. G. Tomov, J. M. Hansen, M. F. Rasmussen, and J. A. Jensen. Preliminary example of 3D vector flow imaging. In *SPIE Medical Imaging 2013*, Accepted

Contents

Abbreviations and acronyms

1D	One-dimensional
2D	Two-dimensional
3D	Three-dimensional
CFD	Computational fluid dynamics
CMUT	Capacitive micromachined ultrasound transducers
CW	Continuous wave
IQ	In-phase and quadrature
FDA	Food and Drug Administration
MRI	Magnetic resonance imaging
PEF	Pulse-echo field
PIV	Particle imaging velocimetry
PW	Pulsed wave
RASMUS	Remotely Accessible Software configurable Multi-channel Ultrasound Sampling (system)
RF	Radio frequency
RMS	Root-mean-square
SAD	Sum-absolute-difference
SARUS	Synthetic Aperture Real-time Ultrasound System
SNR	Signal-to-noise ratio
TO	Transverse oscillation

List of symbols and nomenclature

k_{prf}	Lag in pulse repetition frequency
$*$	Convolution operator
$\bar{\lambda}_x$	Mean transverse spatial wavelength
$\bar{\lambda}_y$	Mean elevation wavelength
$\bar{f}_x$	Mean transverse spatial frequency
$\bar{v}$	Mean velocity
$\hat{\phi}$	Estimated angle
$\Im\{\cdot\}$	Imaginary part
λ_x	Spatial wavelength in the transverse direction
λ_y	Spatial wavelength in the elevation direction
λ_z	Axial wavelength
$\mathcal{F}_{\mathrm{2D}}\{\cdot\}$	2D spatio-temporal Fourier transform
$\mathcal{F}\{\cdot\}$	Fourier transform
$\mathcal{H}\{\cdot\}$	Hilbert transform
μ	Viscosity
ϕ	Phase shift term
ϕ_1	Phase term of r_1

ϕ_2	Phase term of r_2
ϕ_{xy}	Flow angle in XY plane
ϕ_{zx}	Beam-to-flow angle in ZX plane
ϕ_{zy}	Beam-to-flow angle in ZY plane
$\Re\{\cdot\}$	Real part
ρ	Density
σ	Standard deviation (of the estimated velocities)
σ_{f_x}	Spread of the spatial frequencies
θ	Flow angle between the ultrasound beam and the direction of motion of the target—also known as the *beam-to-flow* angle
θ_0	Steering angle in the azimuth (ZX) plane
θ_{TO}	Angle between the two TO lines in the beamforming stage
θ_{zx}	Steering angle in the azimuth/transverse (ZX) plane
θ_{zy}	Steering angle in the elevation (ZY) plane
$\tilde{\sigma}$	Relative mean standard deviation of the velocity estimates
$\tilde{B}$	Relative mean bias of the velocity estimates
$\tilde{E}_{\mathrm{RMS}}$	Relative mean root-mean-square error of the velocity estimates
$\vec{v}$	Velocity vector
ξ	Position on the aperture (variable in integral)
a	Aperture function
$a_{\mathrm{rcv,xmt}}$	Combined transmit-receive aperture (also called the effective aperture)
a_{rcv}	Receive apodization
a_{xmt}	Transmit apodization
B	Bias (of the velocity estimates)
B_{λ_x}	Bias between the theoretical and the mean transverse wavelength

c	The speed of sound in the medium
c_1	Multiplicative phase factor
c_v	Coefficient of variation of the spread of the spatial frequencies σ_{f_x} over the mean spatial frequency $\bar{f}_x$
D	Depth
d	Distance between two apodization peaks (or center of masses)
d_e	Effective distance between the TO peaks on the receive aperture
E_r	Energy ratio of spatial frequencies in the left over the right half plane in the spatio-temporal frequency spectrum
E_{RMS}	Root-mean-square error of the velocity estimates
$F^{\#}$	F-number (z/d)
f_0	Center frequency of the emitted pulse
f_D	Doppler shift frequency
f_p	Frequency of the slow time signal
f_s	Temporal sampling frequency
f_t	Temporal frequency
f_x	Spatial frequency in x direction
f_{flops}	Floating point operations per second
f_{prf}	The pulse repetition frequency $(1/T_{\mathrm{prf}})$
f_{rcv}	Received ultrasound frequency
f_{xmt}	Transmitted ultrasound frequency
f_{ss}	Spatial sampling frequency
$f_{x'}$	Spatial frequency in the transverse x' direction
$f_{y'}$	Spatial frequency in the elevation y' direction
$g(-n)$	Time reversed emitted pulse at discrete samples n
$g(\cdot)$	Envelope of the emitted pulse

$h_{\mathrm{pe,comb}}$	Combined pulse-echo field from the TO lines
$h_{\mathrm{pe,left}}$	Pulse-echo field from the left TO line
$h_{\mathrm{pe,right}}$	Pulse-echo field from the right TO line
i	Emission number
j	$\sqrt{-1}$
k_w	Wave number ($2\pi f_0/c$)
L	Lateral width
n	Discrete sample
N_c	Number of calculations
N_i	The number of emissions
N_p	Number of profiles
N_s	Number of samples in one excitation pulse
$n_s(n)$	Noise signal
N_z	Number of discrete samples of a range of depth.
p	p-value (from statistics)
$P(x, z)$	Pressure field at spatial coordinates x and z
p_v	Fraction of time used for velocity estimation
$P_{\mathrm{rcv,xmt}}$	Combined transmit-receive pressure field
P_{rcv}	Received pressure field
P_{xmt}	Transmitted pressure field
Q	Volume flow
R	Radius
r	Radial position
$r(i)$	Received signal
$R(k)$	Complex autocorrelation at lag k

$R_1(k)$	Complex lag k autocorrelation value for $r_1(k)$
$R_2(k)$	Complex lag k autocorrelation value for $r_2(k)$
r_c	Center line beamformed in the direction of the steered beam
r_m	Match filtered signal
r_1	Generated signal based on samples from TO lines in the $Z'X'$ plane
r_2	Generated signal based on samples from TO lines in the $Z'X'$ plane
r_3	Generated signal based on samples from TO lines in the $Z'Y'$ plane
r_4	Generated signal based on samples from TO lines in the $Z'Y'$ plane
r_{left}	Signal from left TO line
r_{right}	Signal from right TO line
r_{sq}	Spatial quadrature sample pair
r_{tq}	Temporal quadrature sample pair
r_{bf}	Beamformed signal
r_{cf}	Clutter filtered signal
$r_{m,c}(n)$	Match filtered channel data
$r_{s,c}(n)$	Sampled signal from individual channels
$S(f_x, f_t)$	2D spatio-temporal frequency spectrum
$s(n)$	Signal
t	Time
T_{prf}	Time between consecutive pulse emissions ($1/f_{\text{prf}}$)
v	Velocity
v_0	Peak velocity
v_p	Estimated velocity profile
v_s	The velocity of the target or source

v_t	True or expected velocity profile
v_z	Axial velocity component
$v_{x'}$	Transverse velocity component in the transverse (x') direction relative to the steered beam
$v_{x_{\max}}$	Aliasing limit of the TO transverse velocity component
v_x	Transverse velocity component in the x direction
$v_{y'}$	Elevation velocity component in the elevation (y') direction relative to the steered beam
v_y	Elevation velocity component in the y direction
$v_{z'}$	Axial velocity component along the axis of the steered beam (in the z' direction)
$v_{z,\mathrm{TO}_{\max}}$	Aliasing limit of the TO axial velocity component
$v_{z_{\max}}$	Aliasing limit of the convetional axial velocity component
x	Spatial coordinate in the transverse direction of the transducer
x'	Spatial coordinate in the transverse direction relative to the steered beam
$X'Y'$	$X'Y'$ plane spanned by the vectors coinciding with the x' and the y' direction
$x(i)$	Real part of the complex signal
x_c	Position on aperture
XY	XY plane spanned by the vectors coinciding with the x and the y direction
y	Spatial coordinate in the elevation direction of the transducer
y'	Spatial coordinate in elevation direction relative to the steered beam
$y(i)$	Imaginary part of the complex signal
z	Spatial coordinate normal to the transducer surface (depth)
z'	Spatial coordinate along the axis of the steered beam

$Z'X'$	$Z'X'$ plane spanned by the vectors coinciding with the z' and the x' direction
$Z'Y'$	$Z'Y'$ plane spanned by the vectors coinciding with the z' and the y' direction
ZX	ZX plane spanned by the vectors coinciding with the z and the x direction
ZY	ZY plane spanned by the vectors coinciding with the z and the y direction

List of figures

List of tables

1

Introduction

The overall purpose of this PhD project is to develop an ultrasonic method for three-dimensional (3D) vector flow imaging. The motivation is to advance the field of velocity estimation in medical ultrasound—especially because velocity estimation over the last decades has been an important diagnostic tool in the clinic. As an example, velocity estimation in the carotid artery is a main diagnostic criteria in assessing the degree of stenosis [1, 2].

Current clinical practice relies on typically spectral (Doppler) techniques or color flow imaging. These methods are able to estimate only the axial velocity component. For the spectral estimator, the operator may compensate for the expected flow angle. However, this is not necessarily trivial, and is impossible in other cases [3, 4]. It also strongly limits the possibility of visualizing complicated flow patterns like disturbed or complex flow and vortices [4], which potentially carry pathological information about e.g. stenoses and malfunctioning valves [5].

Contrary to the estimation of one-dimensional (1D) velocities, hemodynamic studies have shown that the blood flow is far from unidirectional. It exhibits complex flow patterns, and the velocity vector has components in all three spatial dimensions as ultrasound measurements [4, 6, 7] as well as magnetic resonance imaging (MRI) [8–10] and computational fluid dynamics (CFD) modelling [11–14] have shown. In addition, hemodynamic shear stress has been linked to the development of atherosclerosis [15, 16], but disturbed flow itself has been suggested as an explanation for the focal nature of the disease [17]. How the geometry of the carotid bifurcation predicts its exposure to disturbed flow has also been investigated [18]. The topic of how atherosclerosis develops is still controversial and has received increased interest in recent years.

Moreover, it is important to bear in mind that blood flow directions in the human blood vessel rarely (if ever) are constant over time. On the contrary, the velocities vary as a function of time and space [4, 19]. Therefore, it is important to estimate the three velocity components simultaneously.

The above underlines the need for methods that can estimate the three-dimensional (3D) velocity vector. Several methods have been suggested for this. Yet, none have so far been adapted by commercial manufactures. The

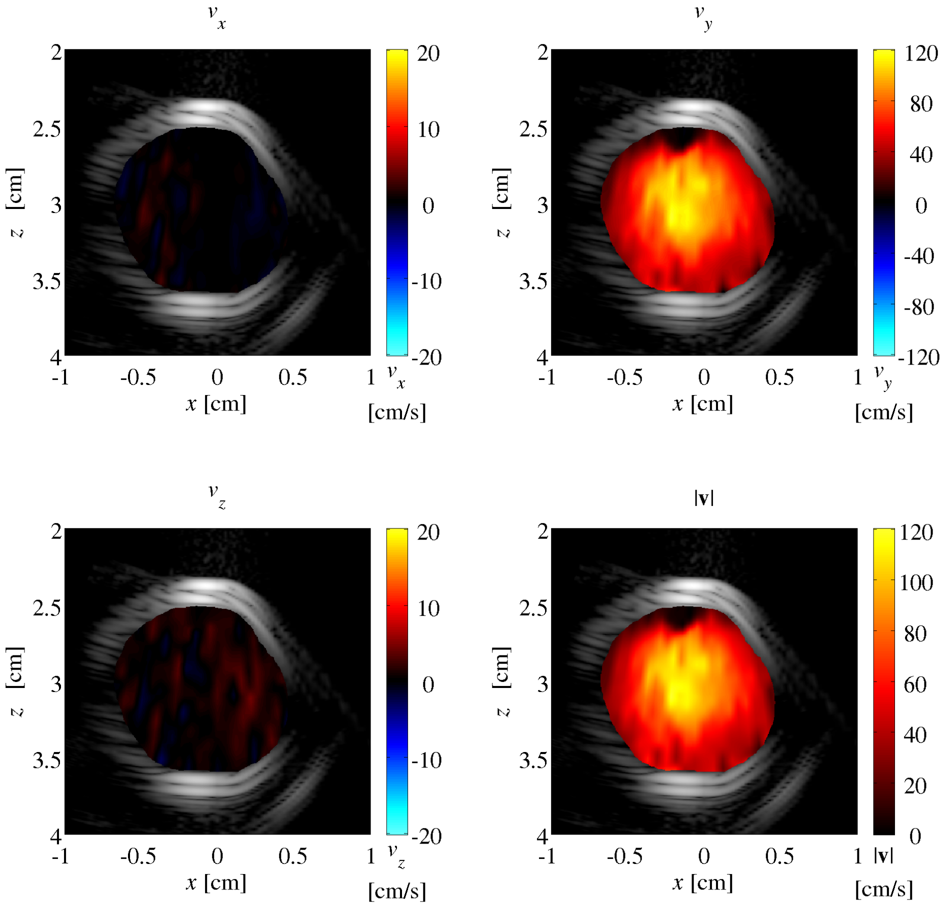

Figure 1.1 Measured 3D vector flow images in a scan plan for the three velocity components v_x, v_y, and v_z and the full velocity magnitude. The scan plan is orthogonal to the flow direction.

purpose of this research is to develop a method for simultaneous 3D velocity estimation suitable for real-time implementation.

The method developed during the PhD study is based on the Transverse Oscillation (TO) approach [20]. A crucial part of the method is to synthesize double-oscillating fields. The optimization of these fields and the beamforming strategy has been part of developing the 3D method. An example of the latest results showing 3D vector flow images is presented in Figure 1.1. This thesis goes through the background information and the theory required, as well as the research conducted for obtaining these 3D vector flow images.

1.1 Objectives

The objective of the conducted research is to develop a method for 3D vector velocity estimation based on the TO approach. Prior to this, optimizing approaches of the TO method and an expansion of the method to a phased array geometry are warranted. Afterwards, with simulations and subsequent experimental measurements, it is sought to demonstrate the feasibility and capability of the developed method for estimating all three components of the velocity vector. Finally, examples of 3D vector flow images are presented.

1.2 Structure of the thesis

The thesis is structured in two parts. The first two chapters introduce the technical background and the motivation for the present research. The subsequent chapters present the scientific contributions and are structured to demonstrate the progress of the conducted research. The thesis is presented as a whole, and the individual chapters are intended to be read in succession without the need for consulting or reading the individual papers. Hence, the content of the chapters presenting the scientific contributions include paragraphs that have direct correspondence to the respective papers.

Chapter 2 provides a review of the literature that leads up to the scientific contributions presented in this thesis. Included is a brief summary of the history of axial (1D) velocity estimation followed by brief reviews of suggested methods for two-dimensional (2D) and 3D velocity estimation. Additionally, examples of clinical use of velocity estimation are given.

Chapter 3 describes the theory of the Transverse Oscillation method for 2D velocity estimation using a linear array. The description is based on prior publications. The chapter also presents two clinical examples of 2D vector flow imaging from a commercial implementation.

Chapter 4 presents the results of a study investigating the feasibility of a commercial implementation of the TO method using a linear array. This work has been published in Paper I and in the paper by Hemmsen et al. [21].

Chapter 5 focuses on expanding the TO method from a linear array geometry to a phased array geometry. An alternative beamforming strategy as well as performance metrics to evaluate the performance of the TO method are presented. This chapter is composed upon Papers II and III.

Chapter 6 presents the proposed 3D Transverse Oscillation method. The method is capable of estimating all three components of the velocity vector simultaneously. The feasibility of the method is investigated through simulations. The chapter is composed upon Papers IV and V.

Chapter 7 presents the experimental investigations of the 3D TO method. The measurements are performed in a flow-rig using an experimental scanner and a 2D transducer, and 3D velocity profiles as well as 3D vector flow images are obtained. The work is presented in Paper VI as well as Abstract A and B.

Chapter 8 encompasses the final conclusion on the results of the conducted research, the perspectives, and ideas on future work.

1.3 Scientific contributions

The scientific contributions of this PhD project are mainly collected in the six papers and two abstracts. The author has also contributed to an additional journal paper by Hemmsen et al. The conducted research has also formed the basis for a patent application. Additional papers, abstracts, and dissemination are listed at the end.

1.3.1 Papers and abstracts included in the thesis

The the thesis is written upon the following six papers numbered I–VI and two abstracts designated A and B. The numbering corresponds to their order of appearance in the thesis and the appendix.

Journal papers

III M. J. Pihl, J. Marcher and J. A. Jensen. Phased Array Vector Velocity Estimation using Transverse Oscillations. *IEEE Trans. Ultrasons., Ferroelec., Freq. Contr.*, Accepted for publication

V M. J. Pihl and J. A. Jensen. A method for estimation of three-dimensional velocity vectors in ultrasound. *J. Acoust. Soc. Am.*, Submitted

VI M. J. Pihl and J. A. Jensen. Experimental investigation of three-dimensional velocity vector estimation. *J. Acoust. Soc. Am.*, Submitted

Conference papers

I M. J. Pihl, S. I. Nikolov, M. C. Hemmsen, and J. A. Jensen. Performance of the Transverse Oscillation Method using Beamformed Data from a Commercial Scanner. In *Proc. IEEE Ultrason. Symp.*, September 2009

II M. J. Pihl and J. A. Jensen Transverse Oscillations for Phased Array Vector Velocity Imaging. In *Proc. IEEE Ultrasons. Symp.*, pages 1323-1327, October 2010

IV M. J. Pihl and J. A. Jensen. 3D Vector Velocity Estimation using a 2D Phased Array. In *Proc. IEEE Ultrasons. Symp*, pages 430-433, October 2011

Abstracts

A M. J. Pihl and J. A. Jensen. Measuring 3D Velocity Vectors using the Transverse Oscillation Method. In *Proc. IEEE Ultrason. Symp. 2012*, Accepted

B M. J. Pihl, M. B. Stuart, B. G. Tomov, J. M. Hansen, M. F. Rasmussen, and J. A. Jensen. Preliminary example of 3D vector flow imaging. In *SPIE Medical Imaging 2013*, Submitted

1.3.2 Co-authored journal paper

The author has contributed to the following journal paper by writing the section titled *Transverse Oscillations for blood velocity estimation* (approximately two pages).

- M. C. Hemmsen, S. I. Nikolov, M. M. Pedersen, M. J. Pihl, M. S. Enevoldsen, J. M. Hansen, and J. A. Jensen. Implementation of a Versatile Research Interface Data Acquisition System Using a Commercially Available Medical Ultrasound Scanner. *IEEE Trans. Ultrason., Ferroelec., Freq. Contr.*, 59(7):1487-99, 2012

1.3.3 Patent application

On basis of the conducted research, a patent application on the 3D TO method has been filed by BK Medical.

- M.J. Pihl and J. A. Jensen. Three Dimensional (3D) Transverse Oscillation Vector Velocity Ultrasound Imaging, International Patent Application, Priority data: 2011.

1.3.4 Additional papers and abstracts

The following additional papers and abstracts are listed in chronological order.

2012

- M. M. Pedersen, M.J. Pihl, P. Haugaard, J. M. Hansen, K. L. Hansen, M. B. Nielsen, and J. A. Jensen. Comparison of Real-Time In Vivo Spectral and Vector Velocity Estimation. *Ultrasound Med. Biol.*, 38(1):145-151, 2012

- J. Marcher, M. J. Pihl and J. A. Jensen. The Transverse Oscillation Method using a Phased Array Transducer .In *Proc. IEEE Ultrason. Symp. 2012*, Accepted

2011

- M. M. Pedersen, M.J. Pihl, J. M. Hansen, P. M. Hansen, P. Haugaard, M. B. Nielsen, and J. A. Jensen. Arterial secondary blood flow patterns visualized with vector flow ultrasound. In *Proc. IEEE Ultrason. Symp.*, pages 1242-1245, 2011

- J. A. Jensen, S. Nikolov, J. Udesen, P. Munk, K. L. Hansen, M. M. Pedersen, P. M. Hansen, M. B. Nielsen, N. Oddershede, J. Kortbek, M. J. Pihl, and Y. Li. Recent advances in blood vector velocity imaging. In *Proc. IEEE Ultrason. Symp.*, pages 262-271, 2011

- M. M. Pedersen, M.J. Pihl, J. M. Hansen, P. M. Hansen, P. Haugaard, M. B. Nielsen, and J. A. Jensen. Preliminary comparison between real-time in-vivo spectral and transverse oscillation velocity estimates. In *Proc. SPIE – Medical Imaging – Ultrasound Imaging and Signal Processing*, vol 7968, 2011

2010

- J. A. Jensen, M. J. Pihl, J. Udesen, M. M. Pedersen, K. L. Hansen. Principle and performance of the transverse oscillation vector velocity technique in medical ultrasound. In *2nd Pan-American/Iberian Meeting on Acoustics*, 2010

- M. M. Pedersen, M.J. Pihl, P. Haugaard, M. B. Nielsen, and J. A. Jensen. Quantification of complex blood flow using real-time in vivo vector flow ultrasound. In *Proc. IEEE Ultrason. Symp.*, pages 1088-1091, 2011

- M.J. Pihl, P. Haugaard, and J. A. Jensen. Using Phased Array for Transverse Oscillation Vector Velocity Imaging. Presented at *10th EUROSON 2010*, Copenhagen, Denmark, 2010
- M. M. Pedersen, M.J. Pihl, P. Haugaard, M. B. Nielsen, and J. A. Jensen. Quantification of complex blood flow using real-time in vivo vector flow ultrasound. Presented at *10th EUROSON 2010*, Copenhagen, Denmark, 2010
- M. M. Pedersen, M.J. Pihl, P. Haugaard, J. M. Hansen, K. L. Hansen, M. B. Nielsen, and J. A. Jensen. Preliminary evaluation of vector flow and spectral velocity estimation. Presented at *10th EUROSON 2010*, Copenhagen, Denmark, 2010

1.3.5 Additional dissemination

Besides poster presentations or talks given at conferences listed above with the author of this thesis as first author, the following talks have been given.

Talks

- M. J. Pihl. Velocity Estimation in Human Blood Vessels using Ultrasound. Invited talk presented at *Dansis seminar – Human Fluid Dynamics*, March 28, 2012
- M. J. Pihl and J. A. Jensen. Phased Array TO in 2D. Presented at *Artimino Conference 2011*, Artimino, Italy, June 26-29, 2011
- J. A. Jensen, **M. J. Pihl**, J. Udesen, M. M. Pedersen, K. L. Hansen. Principle and performance of the transverse oscillation vector velocity technique in medical ultrasound. In *2nd Pan-American/Iberian Meeting on Acoustics*, 2010

2

Velocity estimation in medical ultrasound

Summary *Ultrasound imaging dates back to the 1950's. The first example of ultrasonic velocity estimation was presented by Satomura in 1957. It was a continuous-wave system based on the Doppler shift. Modern day scanners employ pulsed signals and combine the B-mode image with 2D images of the axial velocities. The axial velocities are (for the majority) estimated using an autocorrelation approach as suggested by Namekawa et al. and Kasai et al. The problem with the conventional estimators is the angle dependency, as only the axial velocity component can be estimated. Several 2D and 3D methods have been suggested to remedy this issue including cross-beam methods, speckle tracking, and, more recently, particle image velocimetry.*

2.1 Purpose and scope

The purpose of this chapter is to place the scientific contributions of this thesis in a historic and scientific context in terms of ultrasonic velocity estimation. The reader unfamiliar with ultrasound in general may acquire a brief introduction to ultrasound through e.g. Jensen [22].

Ultrasonic velocity estimation can been applied in two areas: Tissue motion estimation and blood velocity estimation. There are several differences, which affect the requirements for the two applications. For tissue motion estimation, the signals are often strong and the motion small. Conversely, for blood velocity estimation, the signals are often weak due to the weak scattering of blood and the motion is often—but not always—large. That poses different challenges. For tissue motion estimation, the signal-to-noise-ratio (SNR) is good and the estimator must be able estimate small displacements. Oppositely, for blood velocity estimation, the SNR is poor and the estimator must be able to estimate high (and sometimes) low velocities. The focus of this chapter is on blood velocity estimation.

The main developments leading up to the present research are highlighted. The chapter also describes the alternative methods to the Transverse Oscillation method, which forms the basis for the present work. It is outside the scope of this chapter to provide a technical review of the methods presented.

2.2 Background literature

The review of ultrasound velocity estimation is based on the papers by Jensen [22], Wells [23], Dunmire and Beach [24], and Evans et al. [25]. Further details are provided in the books by Evans et al. [26], Jensen [27], and Evans and McDicken [28].

2.3 A historic perspective

The focus in the following will be on the main path leading from the early days of ultrasound imaging over Doppler methods to real-time two-dimensional color flow imaging using an auto-correlation approach.

2.3.1 Background literature

The review of ultrasound velocity estimation in a historic perspective is based on the papers by Jensen [22], Wells [23], Dunmire and Beach [24], and Evans et al. [25]. Further details are provided in the books by Evans et al. [26], Jensen [27], and Evans and McDicken [28].

2.3.2 The early days of ultrasound imaging

According to Jensen [22] early experiments of ultrasound imaging were conducted by modified radar and sonar equipment in the early 1950's by Wild[1] and by Edler and Hertz[2]. Wells [23], on the other hand, refers to the pioneering work of Wild and Reid[3] and of Howry and Bliss[4].

---

[1] J.J. Wild. The use of ultrasonic pulses for the measurement of biological tissue and the detection of tissue density changes. *Surgery* 27:183-188, 1950

[2] I. Edler and C.H. Hertz. The use of ultrasonic reflectoscope for the continous recording of the movement of heart walls. Kungl. Fysiogr. Sällskap. i Lund Föhandl 24: 40-58, 1954

[3] J. J. Wild and J. M Reid. Further pilot echographic studies of the histologic structure of the living intact human breast. *Am. J. Pathol.* 28:839-61, 1952

[4] D. H. Howry and W. R. Bliss. Ultrasonic visualization of the soft tissue structures of the body. *J. Lab. Clin. Med* 40:579-92, 1952

Anatomic ultrasound imaging

Since the 1950's, ultrasound has evolved to be one of the major medical imaging modalities. A classic way to present the ultrasound data is the so-called *B-mode* image. It is a gray-scale image, which displays the reflectivity and the scattering strength—i.e. the brightness—of the tissue. Hence, the images give an indication of the anatomy, and medical ultrasound is used to image nearly all soft tissues in the body.

The images are produced in real-time, which is one of the strengths of ultrasound imaging. The technique does not use ionizing radiation, and is therefore safe for the patients. Additionally, the relatively small size of the ultrasound scanners themselves, makes ultrasound more accessible compared with other imaging modalities. For all of these reasons, ultrasound is widely used in the clinic within a broad range of medical disciplines and for a variety of diagnostic purposes.

In the field of medicine, not only the anatomy but also the physiology plays a key role in diagnosing various diseases. The hemodynamics in the human body plays a role in various diseases that are both directly or indirectly related to the cardiovascular system. Therefore, the estimation of blood velocity is a key diagnostic tool for many diseases. The foundation for the estimation of blood velocities using ultrasound dates back to the middle of the 19th century.

Doppler ultrasound

The so-called *Doppler effect* is named after the Austrian physicist Christian Andreas Doppler (1803-1853). The Doppler effect describes the change in frequency that occurs when the source or a target is in motion. In ultrasound, only the target moves and the difference in the transmitted and the received frequency yields the Doppler shift frequency, f_D, given by [28]

$$f_D = f_{\mathrm{xmt}} - f_{\mathrm{rcv}} = \frac{2 f_{\mathrm{xmt}} |v_s| \cos\theta}{c}, \tag{2.1}$$

where f_{xmt} and f_{rcv} are the transmitted (xmt) and received (rcv) ultrasound frequencies, respectively, v_s the velocity of the target or source, c the speed of sound in the medium, and θ the angle between the ultrasound beam and the direction of motion of the target—also known as the *beam-to-flow* angle. This angle accounts for the fact, that only the velocity component parallel to the direction of the ultrasound beam affects the Doppler shift.

The Doppler shift can be measured in continuous-wave (CW) systems, where the same frequency is emitted continuously from one transducer. A second transducer then receives the echoes, and the shift in frequency can be estimated. The earliest system was suggested by Satomura [29] using the shift to estimate motion—where the motion of the heart and heart valves was the original proposed application. The development of Doppler ultrasound has been efficiently described in brevity by Dunmire and Beach [24]:

> *The earliest Doppler ultrasound system was proposed by Satomura*[5] *in 1957. This was a continuous wave system that resolved the Doppler shift frequency, but lacked the ability to detect flow direction or tissue depth. In the late 1960's, McLeod*[6] *developed an analog solution to find the sign of the Doppler frequency shift, while Wells*[7] *and Baker*[8] *resolved the depth ambiguity by pulsing the transmit signal. The end result is the modern Doppler ultrasound machine.*

The pulsed wave (PW) mode consists of short ultrasound pulses followed by sampling of the received ultrasound echoes. Therefore, the same transducer can be used as both transmitter and receiver. Additionally, the time, t, can be related to depth, D, by

$$t = \frac{2D}{c}.$$

2.4 1D velocity estimation

The PW mode results in a broadband response, that contains several frequency components opposed to the monochromatic response in the CW mode. Due to frequency dependent attenuation in the tissue, it is difficult to detect the Doppler shift in PW mode. Yet, measuring repeatedly at the same depth, blood cells that pass the point of interest will give rise to a signal with a frequency proportional to the velocity as [27]

$$f_p = \frac{2v_z}{c} f_0, \tag{2.2}$$

---

[5] See Ref. [29]

[6] F. D. McLeod. A directional Doppler Flowmeter, In *Digest of the 7th International Conference on Medical and Biological Engineering*, p. 213, 1967

[7] P. N. T. Wells. A range gated ultrasonic Doppler system, *Med Biol Eng* 7:641-652, 1969

[8] D. W. Baker. Pulsed ultrasonic Doppler blood-flow sensing, *IEEE Trans Sonics Ultrason* SU-17:170-185, 1970

where f_0 is the center frequency of the emitted ultrasound pulse, and v_z is the axial velocity component. A simple model for the received radio frequency (RF) signal, $r(i)$, from a single moving scatterer as illustrated in Figure 2.1 is [27]

$$r(i) = g(i) \sin\left(2\pi \frac{2v_z}{c} f_0 i T_{\mathrm{prf}} - \phi\right), \tag{2.3}$$

where i is the number in the emitted pulse, $g(i)$ the envelope of the emitted signal, T_{prf} the time between consecutive pulse emissions, and ϕ a phase shift introduced by the propagation time of the ultrasound beam in the tissue. This signal is often denoted the *slow time* signal, as it is acquired over several ultrasound emissions. The frequency of this slow time signal is often still denoted the Doppler frequency [23, 28], probably because the right-hand-sides in (2.1) and (2.2) are identical as $v_z = v\cos\theta$. Yet, the frequency in (2.2) is not the Doppler shift frequency of the observed instantaneous CW signal as stated in (2.1).

The direction of the velocity, i.e. either towards or away from the transducer, can be obtained using in-phase and quadrature (IQ) data. The complex IQ data can be obtained either by applying the Hilbert transform ($y = \mathcal{H}\{x\}$) to the sampled data x or by sampling IQ data directly. The complex signal can be written as

$$r(i) = x(i) + jy(i), \tag{2.4}$$

where x is the real signal and y the imaginary signal.

2.4.1 Spectral estimator

With a collection of scatterers moving at different velocities, a superposition of the contribution of the individual scatterers is obtained. This gives rise to a spectral density of the signal which is equal to the density of the velocities. Applying the Fourier transform to the slow time signal (corresponding to the right graph in Figure 2.1) yields directly the velocity distribution of the scatterers for a given time. The power density spectra can be stacked together to yield the *spectrogram*, often referred to as the *Doppler spectrum*.

2.4.2 Autocorrelation estimator

An alternative approach to estimate the velocity of the scatterers is to use an autocorrelation approach. The autocorrelation approach estimates the mean velocity of the scatterers by estimating the mean phase shift from emission to emission (see Figure 2.1).

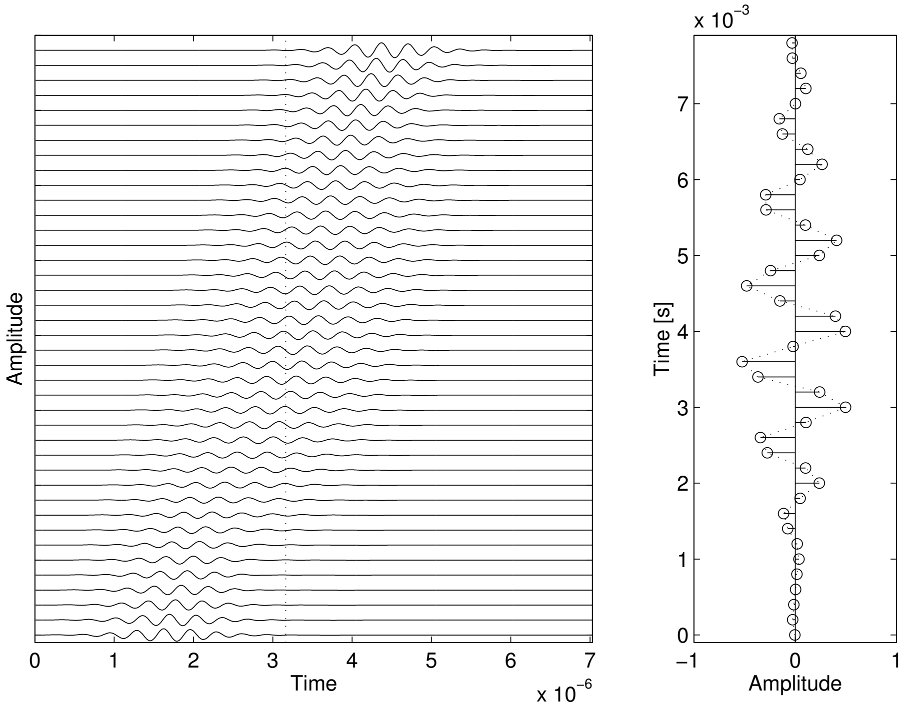

Figure 2.1 Sampling of a single scatterer moving away from the transducer. The left graph shows the different received RF lines, and the right graph is the sampled slow time signal. The dotted line indicates the time when the samples on the left are acquired. Courtesy of Jensen [27] – reprinted with permission.

The autocorrelation estimator suggested by Kasai et al. [30] is

$$v_z = -\frac{c}{4\pi f_0 k T_{\text{prf}}} \arctan\left(\frac{\sum_{i=1}^{N_i-k} y(i)x(i-k) - x(i)y(i-k)}{\sum_{i=1}^{N_i-k} x(i)x(i-k) + y(i)y(i-k)}\right), \tag{2.5}$$

where N_i is the number of emissions per estimate and k is the lag in the autocorrelation estimator which is usually 1. In short notation, this can be written as

$$v_z = -\frac{\lambda_z}{4\pi k T_{\text{prf}}} \arctan\left(\frac{\Im\{R(k)\}}{\Re\{R(k)\}}\right), \tag{2.6}$$

where $\Im\{\cdot\}$ denotes the imaginary part, $\Re\{\cdot\}$ the real part, and $R(k)$ the complex autocorrelation at lag k, and λ_z is the axial wavelength given by

$$\lambda_z = \frac{c}{f_0}. \tag{2.7}$$

2.4.3 Cross-correlation estimator

Another way to estimate the velocity is to use a cross-correlation approach. The method is based on temporal tracking of the spatial position of individual scatterers. In relation to Figure 2.1 this corresponds to tracking the change in position from emission to emission. Dotti et al. [31] were the first to suggest such an approach. Also Bonnefous and Pesqué [32] and Foster et al. [33] have contributed to the development of the time-based cross-correlation method. The cross-correlation method has not been used in this project, as the most commonly used axial velocity estimator is based on an autocorrelation approach [25]. For further details on the cross-correlation estimator, the reader is referred to the background literature stated in Section 2.3.1.

2.4.4 Color flow imaging

The advantage of the autocorrelation and the cross-correlation estimates are that only 8-16 emissions are required to obtain a velocity estimate. That makes these methods suitable for obtaining velocity estimates at several spatial positions. The velocity is then color coded and superimposed on to the gray-scale B-mode image. An example of this is illustrated in Figure 2.2.

The application of velocity estimation in ultrasound was drastically expanded after the introduction of real-time 2D images of axial velocities using the autocorrelation approach introduced by Namekawa et al. [34] and Kasai et al. [30]. The autocorrelation technique (with certain modifications) is the most widely used for color flow imaging [25].

Loupas et al. [35, 36] improved the autocorrelation approach in two distinct ways. Firstly, the estimate of the phase shift is formed by processing samples over a range of axial depths. This is also called RF averaging. Secondly, they suggested to use an approach that explicitly estimates not only the phase shift, but also the mean RF frequency. This estimated mean frequency can then be used instead of the center frequency, f_0, in (2.7). Especially in attenuating phantoms or tissue, where the center frequency of the ultrasound pulse in PW systems gets downshifted due to the frequency dependent attenuation, this approach reduces the bias that would otherwise arise.

Methods have also been suggested that provide the axial velocity component as color Doppler in a 3D volume [37, 38]. A review of the early history of 3D ultrasound imaging including 3D color flow imaging has been published by Nelson and Pretorius [39]. Berg et al. [40] suggested an approach to obtain volumetric blood flow measurements using a free-hand transducer, and generating the 3D volume by tracking the position of the transducer in 3D space. Pemberton et al. [41], on the other hand, have applied real-time 3D Doppler measurements for the assessment of stroke volume.

A major limitation for both 2D and 3D color flow imaging is the angle dependency between the ultrasound beam and the direction of the velocity. This is described in Section 2.5.

2.4.5 Clutter filtering

One major challenge with velocity estimation using ultrasound is the weak backscattering from blood. The normal scattering coefficient of blood is on the order of 10 to 100 times smaller than for the vessel boundaries and the surrounding tissue [27]. Therefore, the signals from the strong stationary echoes must be removed as they otherwise will dominate the signal. This can be achieved by applying high-pass filters. They can be very simple or very advanced. Only simple filters for clutter filtering or stationary echo cancelling have been applied in the work presented in this thesis. Examples of simple clutter filters are given by Jensen [27]. For more advanced filters, see for instance the work by Torp [42] and Bjærum et al. [43, 44].

2.4.6 Clinical applications

As stated by Evans et al. [25], the introduction of color flow imaging was a major breakthrough in medical ultrasound imaging. Conventional color flow imaging is used in many areas of vascular imaging and is highly utilized in cardiac imaging also know as echocardiography.

It is commonly used to evaluate and diagnose carotid artery stenosis. The formation of atherosclerotic plaque may cause stroke when small embolies detach from the vessel wall and travel with the blood stream to the brain. Early diagnosis and possibly treatment of carotid artery disease is therefore critical to reduce the number of mortalities. B-mode imaging combined with spectral Doppler and color flow imaging is the method of choice for the assessment of carotid artery disease [25]. An important diagnostic criteria in grading stenoses is the maximum peak velocity measured in the arteries [1, 2].

Other areas of application of color flow imaging are in diagnosing and assessment of renal artery stenosis, venous thrombosis, venous insufficiency, portal vein thrombosis and portal hypertension as well as assessment and follow-up of transplanted organs.

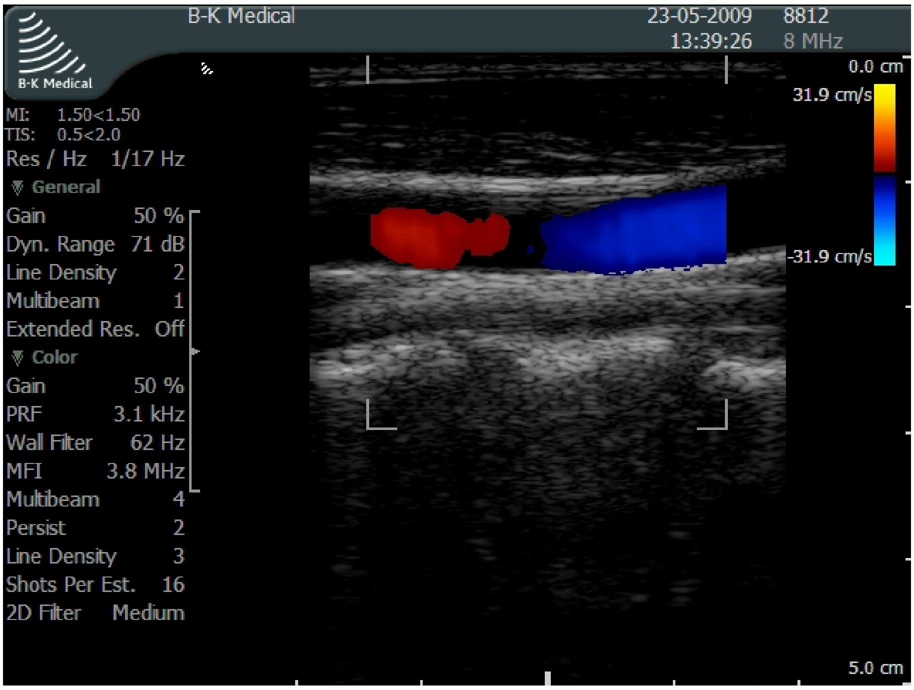
B-K Medical
23-05-2009 8812
13:39:26 8 MHz
MI: 1.50<1.50
TIS: 0.5<2.0
Res / Hz 1/17 Hz
General
Gain 50 %
Dyn. Range 71 dB
Line Density 2
Multibeam 1
Extended Res. Off
Color
Gain 50 %
PRF 3.1 kHz
Wall Filter 62 Hz
MFI 3.8 MHz
Multibeam 4
Persist 2
Line Density 3
Shots Per Est. 16
2D Filter Medium

Figure 2.2 Color flow image of estimated axial velocities on a B-mode image for a linear array transducer. The scan is of the carotid artery and the flow is from right to left towards the brain. Note the change from red to blue, and the apparent absence of velocities in the middle of the image.

2.5 The angle dependency problem

The conventional velocity estimators in ultrasound are only able to estimate the axial velocity component, v_z , which is parallel to the ultrasound beam. The axial velocity is

$$v_z = |\mathbf{v_{zx}}| \cos\theta$$

where $|\mathbf{v_{zx}}|$ is the velocity magnitude in the image plane—i.e. the ZX plane—. This means that only a part of the velocity magnitude can be estimated. If the beam-to-flow angle is close to 90° no velocity can be estimated as illustrated in Figure 2.2.

In some situations, the axial velocities can be angle corrected to obtain the velocity magnitude. This is done by

$$|\mathbf{v_{zx}}| = \frac{v_z}{\cos\theta}, \tag{2.8}$$

where the operator may set the expected flow angle, however, this is not necessarily trivial [3]. The common assumption is that the flow is parallel to the vessel. This assumption may be reasonable in long straight healthy vessels, but as soon as geometrical changes occur—such as curves, branches, bifurcations or narrowings—this assumption may be invalidated. Especially when complex flow is present, all bets are off [4]. Furthermore, this does not even consider the out of plane motion.

2.6 2D vector techniques

Several techniques have been proposed to remedy the angle dependency problem. The Transverse Oscillation method, which is the foundation for this project, is described in the next chapter. The suggested methods and the cited authors stated in the following are chosen primarily on the basis of their significance or because they serve as an example for a given approach.

2.6.1 Transverse Doppler

Newhouse et al. [45] proposed a method based on the transit-time spectral broadening effect of the Doppler bandwidth. The idea is that the spectral broadening is proportional to the transverse velocity component. This method works only if the Doppler bandwidth is largely or solely determined by the intrinsic spectral broadening. This requirement is compromised when the flow is non-stationary as under pulsatile flow conditions [28].

2.6.2 Cross-beam methods

Several authors have suggested cross-beam methods to estimate the velocity vector since the first introduction in 1970 [46]. Basically, these methods interrogate a sample volume from multiple independent directions. Based on the obtained axial velocity estimates and the known orientation of the beams, the two (or three) velocity components may be calculated using trigonometry. In 2D, measurements in two independent directions are enough. Dunmire et al. [46] and Dunmire and Beach [24] have published excellent reviews of the cross-beam vector methods. They describe the various permutations of single-element or array implementations of these methods. The following highlights the major developments in these systems.

The first simple systems were based on two single-element transducers. Fahrbach [47] suggested a method with two single transducers at 90°, whereas

Peronneau[9] suggested a more general approach. The issue with these methods is that they have beams that only intersect at one sample volume. Alternatively, in the areas where the beams do not intersect, they need to assume that the flow is constant and in the same direction.

Later, linear array transducers were employed taking advantage of beam steering. Thereby, the velocity in a plane could be obtained. Also, methods of electronically splitting the linear array into subapertures have been suggested and patented. Yet, the multibeam methods often struggle with small angle differences at larger depths, which increases the uncertainty of the estimates. A Doppler system for obtaining dynamic vector velocity maps from *in vivo* measurements have been presented by Capineri et al. [48].

More recently, Tortoli et al. [49] suggested a method for estimating the Doppler angle for angle compensation of the velocity estimates. The accuracy of the method has been investigated [50]. The method, however, assumes the same flow angle throughout the region of interest.

Arigovindan et al. [51] have developed a method to recover velocity vectors based on axial velocity estimates from different beam directions. The reconstruction problem is solved in continuous domain using regularization.

2.6.3 Decorrelation based techniques

In a different direction, it has also been demonstrated that the speckle decorrelation due to motion can be used to estimate the second velocity component [52].

2.6.4 Cross-correlation of beams

Bohs et al. [53] suggested an approach employing two parallel receive beams and 1D pattern matching and presented results from a laminar flow phantom.

The directional beamforming approach by Jensen [54] as well as Jensen and Bjerngaard [55] estimates the velocity by beamforming lines in the direction of the flow. The flow direction and the velocity is found by using cross-correlation estimators. The method has been combined with synthetic aperture imaging to yield *in vivo* measurements [56]. This method requires many calculations, especially if a 2D cross-correlation search has to be applied to find the flow angle [57].

Another method using a cross correlation approach was proposed by Henze *et al.* [58].

---

[9] P. Peronneau, J. P. Bournat, A. Bugnon, A. Barbet, M. Xhaard. Theoretical and practical aspects of pulsed Doppler flowmetry real-time application to the measure of instantaneous velocity profiles in vitro and in vivo. In: R. S. Reneman, ed. *Cardiovascular applications of ultrasound.* Amsterdam: North Holland Publishing, 1974:66-84

2.6.5 Speckle tracking

The speckle tracking technique suggested by Trahey et al. [59, 60] has been widely used for motion estimation. The suggested method is based on 2D cross-correlation searches. A small 2D kernel from one image is searched for in a larger area in a second image. Thereby, the motion can be determined

Bohs and Trahey [61] suggested using the sum-absolute-difference (SAD) algorithm for blood estimation in ultrasound. The SAD method is less computational demanding compared with the full 2D cross-correlation approach. A real-time system using the SAD method was constructed [62], and experimental and initial clinical results of 2D vector velocities were demonstrated by Bohs et al. [63, 64].

Sandrin et al. [65] suggested combining plane wave excitations and speckle tracking for ultrafast 2D velocity estimation. Udesen et al. [66] combined this with temporal coding (Barker codes) to increase the SNR to yield fast vector velocity images with a frame-rate of 100 Hz, and Hansen et al. [4] demonstrated *in vivo* examples of complex flow patterns.

The speckle tracking methods are in general computationally demanding, although, the SAD method reduces the required number of calculations. Additionally, these methods require a high frame rate to avoid speckle decorrelation between searches.

2.6.6 Particle image velocimetry

Speckle or particle tracking is also used in the more recent ultrasonic particle image velocimetry (PIV) approach [67–71]. The method is based on the optical digital particle image velocimetry technique [72]. The approach requires that a contrast agent is injected into the blood stream. The higher back-scattering from the particles yield better velocity estimates as the SNR is improved. However, this benefit comes with a trade-off. The injection of contrast agent results in the method no longer being a purely non-invasive technique.

2.6.7 B-flow

Another approach that has been proposed to visualize the flow motion is B-flow imaging, where the speckle signal from the blood scatterers is enhanced. The method was introduced for visualization of arterial blood flow in the late 1990's by GE Ultrasound [28]. The method has been investigated by several researchers including Chiao et al. [73], Bjærum et al. [44], and Løvstakken et al. [74, 75]. With this method the flow motion and direction may be followed qualitatively superimposed on the B-mode image. The drawback is that this method is not quantitative.

2.6.8 Frequency domain approaches

Oddershede et al. [76] suggested an approach that estimates the vector velocities by means of a multidimensional spectrum analysis. This method also creates transverse oscillations in the field, but estimates the velocities based on 3D spectrum analysis.

2.6.9 Spatio-temporal filtering

Marion and Vray [77] have suggested an approach using spatio-temporal filtering of ultrasound images to extract the direction of the motion.

2.7 3D vector techniques

Approaches to obtain the full 3D velocity vector have also been suggested. Some of these are expansions of 2D methods, whereas others were suggested as 3D methods from the beginning. A selection of suggested methods are presented below. The references are chosen either because of their significance or because they exemplify a family of techniques.

While reading about the following methods, it is important to bear in mind that all of the 3D methods mentioned below still have to demonstrate their clinical and commercial applicability for 3D vector flow imaging. Therefore, there is a need for a real-time implementable approach that is capable of estimating 3D velocities in a 3D volume.

2.7.1 Transverse Doppler

Newhouse et al. [78] expanded the transverse Doppler method to 3D velocity estimation by suggesting the use of two transducers. The 3D velocity were estimated based on a combination of the two Doppler mean frequencies and the Doppler spectral bandwidth. It was an improvement over the three transducers required by other methods at the time, but still required two transducers. The main disadvantages are the assumption of only one velocity in the region of interest and the dependence on the spectral broadening effect. The spectral broadening effect still suffers in non-stationary conditions as stated for the 2D method. Another disadvantage is that the two transducers are focused at one point, and hence, give the 3D velocities in a small sample volume only. McArdle et al. [79] demonstrated flow phantom measurements of the 3D velocity vector from a sample volume and compared the results to three and five transducer cross-beam methods.

2.7.2 Cross-beam methods

Three-dimensional single-element cross-beam methods were developed parallel to the 2D techniques. The first approach was the trans-esophageal instrument developed by Daigle et al. [80]. The elements in the esophageal probe had one point of beam convergence and had to be operated sequentially over several cardiac cycles because all the transducers operated at the same frequency. The flow angle was determined via triangulation, and the velocity estimates could therefore be angle corrected. This, however, assumed the flow had the same direction over the cross section of the vessel.

The system developed by Fox [81] and by Fox and Gardiner [82] for obtaining calibrated 3D Doppler velocimetry information employed continous-wave transmit/receivers sacrificing depth information, and the system had to be manually adjusted for a specific area of interest. The five-transducer and three-transducer system proposed by Overbeck et al. [83] and Dunmire et al. [46] also estimate the velocity in a single sample volume only. Therefore, they cannot be used for obtaining 3D velocity vector estimates over an entire volume.

Rickey et al. [84] modified a conventional color Doppler system to obtain images over a volume from three (known) directions. The volume and the resulting velocity vectors were reconstructed based on the three color flow images.

As 2D transducers become more available, several of these cross-beam methods may be expanded to 3D vector velocity estimation [46]. One approach would be to split the 2D aperture into subapertures and with beam-steering obtain independent estimates of the axial velocities and subsequently calculating the three velocity components using trigonometry.

2.7.3 Decorrelation based techniques

Rubin et al. [85] and Tuthill et al. [86] have suggested combining a cross-beam method for in-plane velocity estimation with a speckle decorrelation technique for estimating the out-of-plane velocity. Depiction of 3D velocities in a tube as well as measurements in a canine femoral artery were demonstrated [86].

2.7.4 Cross-correlation of beams

The method by Bonnefous [87] requires a 2D array transducer and five beamformers in parallel to obtain the velocity vector by means of five 1D cross-correlations. The method works for transverse motions, but breaks down if axial motion is present as it will dominate the signal change.

The approach by Hein [88, 89] employing a triple-beam lens transducer requires detailed consideration of beamwidth and beam separation, and suffers from low SNR.

The directional beamforming approach has also been applied to 3D velocity estimation [90]. The investigation was based on simulated data. The drawback of this approach is the larger number of calculations needed for 3D velocity estimation.

2.7.5 Speckle tracking

Bohs et al. [91] suggested the speckle tracking approach for multi-dimensional flow estimation. Yet, the formulation of the 3D volumetric approach was not stated, and the presented results were for 2D velocities. Speckle tracking has been been expanded to 3D tissue motion tracking [92, 93]. However, results from non-invasive speckle tracking for 3D flow estimation have yet to be presented. The issue with 3D speckle tracking is the very high number of calculations needed. Also, the high frame-rate required to avoid speckle decorrelation and—in consequence—the large amount of data generated pose a problem.

2.7.6 Particle imaging velocimetry

Reconstructed 3D flow using ultrasound PIV has been reported [94], but results from estimating the full 3D velocity vectors have yet to be reported. In general, the challenge with speckle tracking techniques, especially in 3D, is the fairly high number of calculations needed.

2.7.7 Feature tracking

Another approach is to apply feature tracking in 3D [95, 96], however, the approaches are limited by uncertainty in especially the transverse localization of the peak, false peak detection, and the duration of the tracked feature.

2.7.8 Frequency domain approaches

Ogura et al. [97] have suggested a method that they state derives the three velocity components by sampling signals with a 2D array. The data are first 2D Fourier transformed in the spatial domain parallel to the transducer and then a temporal 1D Fourier transform is applied.

2.8 Potential clinical application of vector flow imaging

First of all, 2D and 3D vector flow imaging of healthy volunteers will aid in obtaining a better understanding of the hemodynamics in the human body. With these methods it will be possible to visualize and quantize complex and secondary flow patterns including vortices.

In a longer perspective, it is very likely that vector flow imaging will be able to provide information about pathological flow patterns in e.g. early carotid artery stenosis or in cases of valve insufficiencies. Yet, the clinical impact of 2D and subsequently 3D vector flow imaging can be efficiently determined first when the methods are implemented on systems that are suitable for clinical investigations and trials.

To have clinical relevance, the methods should be able to measure the 2D or 3D velocities in planes or volumes in (at least close to) real-time. Commercial implementations of 2D vector flow imaging are available on the market, but currently, no implementation of 3D vector flow imaging exists. The most likely explanation is that none of the existing methods for 3D velocity estimation are suitable for real-time commercial implementation—at least not for the time being.

3

The Transverse Oscillation method

Summary *This chapter introduces the Transverse Oscillation method, which was proposed by Jensen and Munk [20] in 1998. The method synthesizes double-oscillating fields in receive. It uses a spatial quadrature approach and a special autocorrelation estimator to estimate the transverse velocity component. The theoretical derivation underlying the method is introduced, and the resulting pulse-echo field is described. Previous experimental* in vivo *results are mentioned, and clinical examples of 2D vector flow imaging obtained using the commercial implementation by BK Medical are presented. Finally, a discussion of the receive apodization and the clinical results as well as the perspectives of the method are given.*

3.1 Purpose

The purpose of this chapter is to give an introduction to the theory behind the Transverse Oscillation (TO) method in Section 3.3 to Section 3.6. Readers familiar with the TO method may choose to skip these first four sections and go to Section 3.7 and 3.8 that describe experimental and clinical applications of the TO method. Section 3.9 discusses the TO method described in this chapter and should not be skipped as it leads up to the scientific contributions presented in the following chapters.

3.2 Background and previous literature

The TO method is one of the techniques that solve the angle-dependency problem in traditional ultrasonic flow estimation. The method estimates both the axial and the transverse velocity components. The technique was suggested by Jensen and Munk [20, 98] in 1998. Initial work had been part of the M.Sc thesis by Munk [99]. A similar approach was suggested by Anderson [100, 101]. Yet, the *in vivo* results were not that convincing [102]. Sumi [103] has also described a lateral modulation approach.

The TO method has been further investigated and described in the PhD dissertations by Munk [104] and Udesen [105], and in papers by Munk and Jensen [106], Jensen [107], Udesen and Jensen [108], and Udesen et al. [109]. Furthermore, BK Medical has international patents on the method from 1996 [110] and on the velocity estimator from 2000 [111].

Liebgott et al. [112, 113] has applied the beamforming strategy from the TO method to tissue elasticity imaging, and the approach has also been expanded to a phased array [114, 115]. A combination of the TO approach and synthetic aperture imaging has also been proposed [116] along with an estimator suited for tissue motion estimation [117].

3.3 The basic idea

The basic mechanism that allows the traditional estimation of axial velocities, is the oscillations in the transmitted ultrasonic pulse. Using the same principle, an introduction of a transverse oscillation in the ultrasound field generates received signals that depend on the transverse oscillation. If the transverse oscillation is known, the velocity can be estimated.

3.3.1 The double oscillating field

A 2D field that oscillates in two dimensions can be illustrated with a simple example. If two rain drops hit still water, each drop will generate oscillations on the water surface. Where these oscillations interfere, a double oscillating field will be created as illustrated in Figure 3.1.

The analogy with the two rain drops in still water can be directly transferred to ultrasound. Both are based on the propagation of waves. The rain drops can be considered as point sources on a surface, and in ultrasound this can be seen as two single elements of a transducer array. An example of this is given in Figure 3.2, where the two half-circles represent two elements on a transducer array. If the elements are small compared to the distance to the point of observation, they can be seen as point sources or—in the area of signal processing—as two delta functions.

In ultrasound, where the axial wavelength is well-known based on (2.7), the transverse wavelength has to be estimated before the transverse oscillations can be used in estimating the transverse velocity component using autocorrelation based estimators. The generation of the double-oscillating field and the derivation of the corresponding transverse wavelength is the topic of the next section.

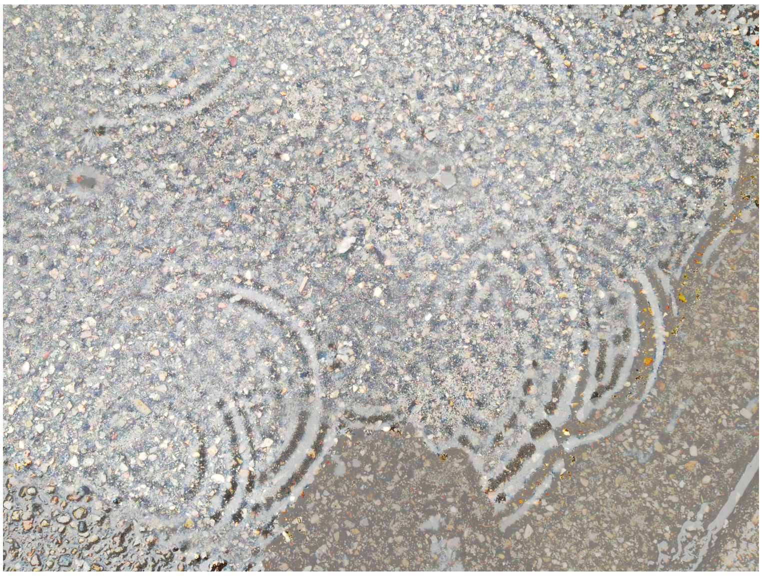

Figure 3.1 An example of the occurrences of double-oscillating fields in nature. The double-oscillating field appears where rings created by the raindrops interfere. The most distinct fields are in the lower right part of the image.

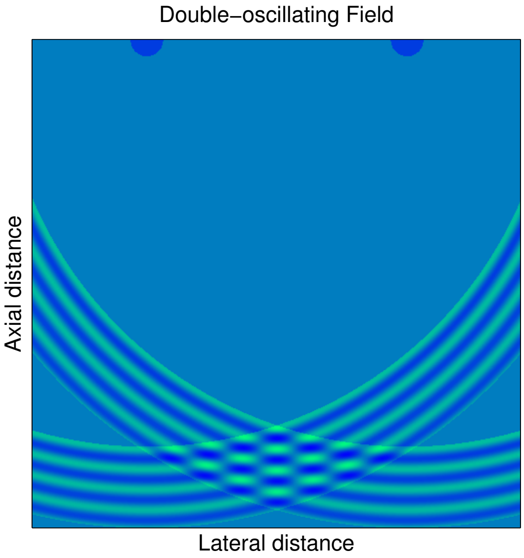

Figure 3.2 Simple illustration of a double-oscillating field created by two point sources. The point sources (half circles) represent the rain drops in Figure 3.1. Modified from [105].

3.4 Field generation and the transverse wavelength

The generation of the double-oscillating pulse-echo field (PEF) with both axial and transverse oscillations is described in the following. The derivation of the transverse wavelength is an integrated part of hereof. The transverse wavelength can be derived in two different ways; either by applying geometrical considerations [20, 105] or to use the Fourier relations between the aperture function and the field [20, 104, 108]. A review of latter is presented below.

3.4.1 Theoretical derivation

The following describes the theoretical derivation of the double-oscillating field and the associated transverse wavelength. This requires the introduction of the Fraunhofer approximation, which is followed by considerations of the transmitted field and the resulting transmit-receive field.

The Fraunhofer approximation

The shape of the transducer apodization is directly related to the transmitted CW field. In the far field and in the focus, the lateral dimension of the field has a Fourier relation to the apodization function. The far field is known as the *Fraunhofer diffraction* pattern. The relation can be expressed as [118]

$$\begin{aligned} P(x,z) &= \frac{e^{jk_w z} e^{jk_w \frac{x^2}{2z}}}{j\lambda_z z} \int_{-\infty}^{\infty} a(\xi) \exp\left[-j\frac{2\pi}{\lambda_z z} x\xi\right] \mathrm{d}\xi \\ &= c_1 \mathcal{F}\left\{a\left(\frac{x}{\lambda_z z}\right)\right\}. \end{aligned} \tag{3.1}$$

where x and z are spatial positions in the field, $k_w = 2\pi/\lambda_z$ is the wavenumber, ξ is the position on the 1D aperture, and c_1 is the multiplicative phase factor, which scales the field. The scaling factor is omitted in the following derivation. The Fourier transform $\mathcal{F}\{\cdot\}$ is evaluated at the spatial frequency

$$f_x = x/(\lambda_z z). \tag{3.2}$$

Disregarding the scaling factor, (3.1) demonstrates the Fourier relation between the aperture function and the lateral component of the field. The Fraunhofer approximation is valid when the distance to the observation plane is large compared to the width of the aperture, i.e. the following has to be satisfied

$$z \gg \frac{k_w \xi_{\max}^2}{2}.$$

Therefore, in conventional medical imaging using ultrasound, the depth of interest is never in the far field. However, due to the focusing, the Fourier relation still holds, albeit the scaling is different [118]. One may say that the focusing lenses or—in the field of ultrasound—electronic focusing brings the far field to the near field. The difference in the scaling factor does not influence the derivations, as the scaling of the Fourier transform in (3.1) has already been ignored.

Transmitted field

To derive the theoretical oscillation wavelength, a good place to begin is to consider the transmit aperture as two delta functions as in Section 3.3.1. If the transmit apodization $a_{\text{xmt}}(x)$ is two delta functions given by

$$a_{\text{xmt}} = \delta(x - x_c) + \delta(x + x_c), \tag{3.3}$$

then, if ignoring the multiplicative scaling factor, (3.1) yields a cosine in the field as

$$P_{\text{xmt}}(x, z) = \cos(2\pi f_x x), \tag{3.4}$$

where $P_{\text{xmt}}(x, z)$ is the lateral component of the field. If the distance between the two delta functions is $d = 2x_c$ and inserting the lateral spatial frequency from (3.2), the lateral wavelength $\lambda_x = 1/f_x$ of the cosine becomes

$$\lambda_x(z) = 2\lambda_z \frac{z}{d}. \tag{3.5}$$

This is the theoretically derived transverse oscillation wavelength for two point sources separated by the distance d, and where the focus point is positioned at depth z.

The transmit-receive field

The generation of ultrasound data relies on both transmitting acoustic energy and receiving acoustic energy. Hence, the resulting transmit-receive field depends on both the transmit and the receive aperture. Eq. (3.1) applies to both the transmitted ultrasound field P_{xmt} and the received[1] ultrasound field P_{rcv} in the far field and in the focal point. Denoting the transmit aperture function a_{rcv}, the receive aperture function a_{xmt}, and the lateral component

---

[1] The receive field corresponds to the ultrasound pressure field that would have been generated if the receive aperture had been used for transmitting ultrasound waves.

of the field at the focal point by $P_{\text{xmt,rcv}}$ yields [119, 120]

$$\begin{aligned} P_{\text{xmt,rcv}} &= P_{\text{xmt}} \cdot P_{\text{rcv}} \qquad (3.6) \\ &= \mathcal{F}\{a_{\text{xmt}}\}\,\mathcal{F}\{a_{\text{rcv}}\} \\ &= \mathcal{F}\{a_{\text{xmt}} * a_{\text{xmt}}\} \\ &= \mathcal{F}\{a_{\text{xmt,rcv}}\}\,, \qquad (3.7) \end{aligned}$$

where $*$ denotes the convolution operator and $a_{\text{xmt,rcv}} = a_{\text{xmt}} * a_{\text{rcv}}$ is called the *effective aperture*. Having the following apertures

$$\begin{aligned} a_{\text{xmt}} &= \delta(x) \\ a_{\text{rcv}} &= \delta(x - x_c) + \delta(x + x_c), \end{aligned}$$

it follows from (3.1) and (3.7) that the lateral component of the pulse-echo field also will be a cosine with the spatial transverse wavelength given by (3.5).

3.4.2 The resulting pulse-echo field

Although the above derivations were based under the assumption of a continuous-wave field, the generality has not been lost since the broadband response in a pulsed mode system can be obtained from a Fourier superposition of the monochromatic responses [120].

Furthermore, where the CW interference can be obtained at any point because the pulse length in theory is infinitely long, the pulsed mode length is finite. Therefore, the wave fronts must be aligned to create the double-oscillating interference patterns at the point of interest. Applying focusing also has the consequence of bringing the Fourier relation from the far field to the focus plane as mentioned in Section 3.4.1. Jensen and Munk [20] suggested using conical focusing—i.e. the delay curves have a triangular shape—to obtain the interference pattern at the desired point of interest. An alternative could be to use conventional dynamic receive beamforming with spherical delay profiles.

The double oscillating field in the TO method is synthesized artificially in receive. Hence, the transmitted field can be a conventional pulse as used for conventional axial velocity estimation using an autocorrelation approach. This is typically a pulse consisting of 6-8 cycles and with a transmit apodization function with the shape of e.g. a rectangular or a Hanning window. Yet, both the transmit apodization and the receive apodization can be varied yielding different PEFs.

The shape of the receive aperture can be derived. The derivation above considered the field based on the aperture function. The opposite approach is to consider the desired double-oscillating field, and then derive the desired aperture function. If the transverse oscillating field with wavelength λ_x and lateral width L is

$$P_{\text{xmt,rcv}} = \text{rect}(L)\cos\left(2\pi\frac{x}{\lambda_x}\right), \tag{3.8}$$

where the aperture function can be obtained by using the inverse Fourier transform. This yields two sinc functions, where the location of the maxima depend on the tranverse wavelength. The relation is the same as stated in (3.5). A derivation of this is presented in Refs. [20, 108].

In general, the PEF is the combined transmit-receive pressure field. It depends on the transducer geometry, the transducer impulse response, the excitation waveform, the transmit apodization, and the receive apodization. The consequence of this is discussed in Section 3.9.

3.5 Spatial quadrature beamforming

In conventional pulsed wave autocorrelation or spectral estimators, it is necessary to have a quadrature signal to estimate the direction of the axial velocity component. For the TO method, *spatial quadrature* data are required.

The spatial quadrature approach in the TO method differs from the method proposed by Anderson [101], who suggested that the spatial quadrature data be obtained by applying the Hilbert transform to some channels prior to the sum in the beamformer. The TO method beamforms two lines with the same modulations, but the fields are shifted 90°. In the TO method, it is possible to control the transverse oscillation period at which the double-oscillating field is sampled, whereas in the Anderson approach, the oscillation period is not directly controllable [104]. The differences are further discussed by Munk [104]. The similarities between the two methods as well as the vector Doppler approach have been discussed by Anderson [121], who states that despite the similarities in the pulse-echo fields, the differences in beamforming strategy will result in differences in performance—especially under non-ideal conditions.

The two TO beams are beamformed with a spatial separation in the transverse direction by $\lambda_x/4$. Thereby, the two fields are 90° phase-shifted and spatial IQ data can be obtained. Denoting the beamformed real samples from the two lines as r_{left} and r_{right} for the left and the right line, respectively, the spatial quadrature samples at a given depth are given by [107]

$$r_{\text{sq}}(i) = r_{\text{left}}(i) + j r_{\text{right}}(i),$$

where i is the pulse number of N_i emissions. To obtain the corresponding temporal quadrature signal, r_{tq}, the data can either be sampled as in-phase and quadrature components directly, or by using the temporal Hilbert transform $\mathcal{H}\{\cdot\}$ on r_{sq} as

$$r_{\text{tq}}(t) = \mathcal{H}\{r_{\text{sq}}\} = \mathcal{H}\{r_{\text{left}}(t)\} + j\mathcal{H}\{r_{\text{right}}(t)\},$$

where t denotes (discrete) time and the direction of the Hilbert transform is for the samples in $r_{\text{left}}(t)$ and $r_{\text{right}}(t)$, respectively, and not over the N_i emissions. The result is that the two sampled real signals have become two imaginary signals with both spatial and temporal IQ data. The next step is to estimate the phase changes for both the axial and the transverse motion.

3.6 Velocity estimation

The following gives a brief description of the TO velocity estimator suggested by Jensen [107]. Based on the spatial quadrature, r_{sq}, and temporal quadrature, r_{tq}, signals, two new signals, r_1 and r_2, can be generated

$$\begin{aligned} r_1(i) &= r_{\text{sq}}(i) + \mathrm{j}r_{\text{tq}}(i) = \exp(j2\pi i T_{\text{prf}}(f_{x'} + f_p)) \\ r_2(i) &= r_{\text{sq}}(i) - \mathrm{j}r_{\text{tq}}(i) = \exp(j2\pi i T_{\text{prf}}(f_{x'} - f_p)) \end{aligned}$$

where the frequency f_p is due to the axial pulse modulation and $f_{x'}$ is due to the spatial transverse modulation. To estimate the velocities, the phase change over the N_i emissions must be estimated. For the two signals the phase changes are

$$\begin{aligned} d\phi_1 &= 2\pi T_{\text{prf}}(f_{x'} + f_p) \\ d\phi_2 &= 2\pi T_{\text{prf}}(f_{x'} - f_p). \end{aligned}$$

The sum and difference between the two phase terms yields the transverse and axial velocities

$$\begin{aligned} v_x &= \frac{(d\phi_1 + d\phi_2)\lambda_x}{2\pi 2 T_{\text{prf}}} \\ v_z &= \frac{(d\phi_1 - d\phi_2)\lambda_z}{2\pi 4 T_{\text{prf}}}. \end{aligned}$$

Using the autocorrelation approach suggested by Jensen [107], the velocities can be estimated as

$$\begin{aligned} v_x =& \frac{\lambda_x}{2\pi 2kT_{\text{prf}}} \times \arctan\left(\frac{\Im\{R_1(k)\}\Re\{R_2(k)\} + \Im\{R_2(k)\}\Re\{R_1(k)\}}{\Re\{R_1(k)\}\Re\{R_2(k)\} - \Im\{R_1(k)\}\Im\{R_2(k)\}}\right) \\ v_z =& \frac{\lambda_z}{2\pi 4kT_{\text{prf}}} \times \arctan\left(\frac{\Im\{R_1(k)\}\Re\{R_2(k)\} - \Im\{R_2(k)\}\Re\{R_1(k)\}}{\Re\{R_1(k)\}\Re\{R_2(k)\} + \Im\{R_1(k)\}\Im\{R_2(k)\}}\right), \end{aligned}$$

where $R_1(k)$ is the complex lag k autocorrelation value for $r_1(k)$, and $R_2(k)$ is the complex lag autocorrelation k value for $r_2(k)$. The complex autocorrelation is estimated over N_i emissions. RF averaging is performed by averaging the autocorrelation estimate over the length of the excitation pulse [35, 107].

The aliasing limit of the TO transverse and axial velocity is

$$v_{x_{\max}} = \frac{1}{4}\frac{\lambda_x}{kT_{prf}} \tag{3.9}$$

$$v_{z,\text{TO}_{\max}} = \frac{1}{8}\frac{\lambda_z}{kT_{prf}}. \tag{3.10}$$

As an alternative, the axial velocity component can be calculated using an autocorrelation estimator as suggested by Loupas et al. [35] with RF averaging as

$$v_z = -\frac{\lambda_z}{2\pi 2kT_{\text{prf}}} \arctan\left(\frac{\Im\{R(k)\}}{\Re\{R(k)\}}\right), \tag{3.11}$$

where $R(k)$ is the autocorrelation of the center line at lag k. The aliasing limit of the conventional axial velocity is twice as large as the axial velocity estimated using the TO method. It is

$$v_{z_{\max}} = \frac{1}{4}\frac{\lambda_z}{kT_{prf}}.$$

3.7 Experimental *in vivo* results

The first *in vivo* results were presented by Udesen et al. [122, 123]. They demonstrated that the method could be used for *in vivo* measurements. The data were acquired using a linear array transducer and the experimental Remotely Accessible Software configurable Multi-channel Ultrasound Sampling (RASMUS) system [124]. Subsequently, the method was validated against MR angiograhpy by means of comparing stroke volume [125–127].

The correlation between the stroke volume estimated by TO to and magnetic resonance angiography was 0.91 ($p<0.01$), and the results indicated that vector velocity estimates obtained *in vivo* using the TO method were reliable. As with the previous data, these were also obtained using the experimental scanner RASMUS.

3.8 Commercial implementation and clinical examples

These *in vivo* measurements and the validation against MRI demonstrated that the method was ripe for a commercial implementation. The feasibility of implementing the method on a commercial scanner was investigated by the author [128]. The work was continued after commencement of the PhD study and the investigation is the subject of the next chapter.

Meanwhile, BK medical has implemented the technique on their Pro Focus UltraView scanner, demonstrating that a commercial implementation was indeed feasible. And early 2012, the technique has been approved by the Food and Drug Administration (FDA) in the United States. Examples of the method employed for clinical measurements are demonstrated in the following.

3.8.1 Clinical examples

Using the commercial implementation by BK Medical, Pedersen et al. [129] compared the real-time results obtained *in vivo* using the TO method and the spectral estimator. The results showed no difference in the TO estimated angle and the operator selected angle in the spectral estimation. However, there were differences in the peak systolic and end diastolic velocities. The difference in temporal resolution between the two methods may explain this difference. Furthermore, the paper highlighted the limitation in the potential use of the method, as it is (at the time of writing) limited to a linear array transducer and an imaging depth of 4–5 cm.

Pedersen et al. [131] and Pedersen [130] quantified the complex flow in the carotid artery. An example of the complex flow present in the carotid bulb is given in Figure 3.3. The 2D vector flow image illustrates the vortex present in the flow at some instances in the cardiac cycle. The figure also illustrates the problem of the angle-dependency of conventional axial velocity estimators. In the given frame, no single angle can be used to correct for the flow angle. Therefore the correct velocity magnitude in the plane cannot be determined for all positions using the 1D estimators. Hence, the strength

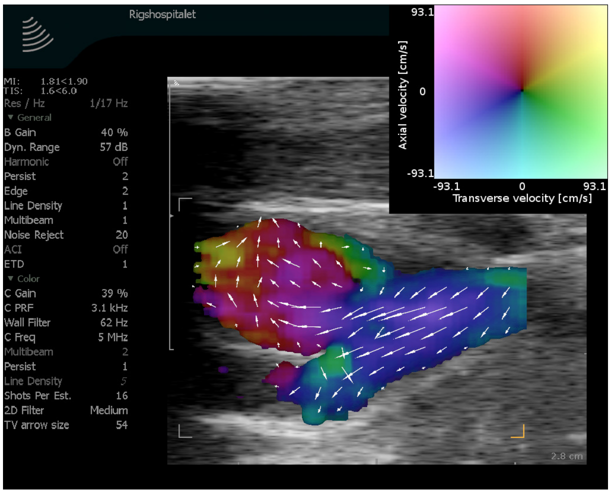

```
MI:      1.81<1.90
TIS:     1.6<6.0
Res / Hz          1/17 Hz
 ▾ General
B Gain               40 %
Dyn. Range          57 dB
Harmonic              Off
Persist                 2
Edge                    2
Line Density            1
Multibeam               1
Noise Reject           20
ACI                   Off
ETD                     1
 ▾ Color
C Gain               39 %
C PRF             3.1 kHz
Wall Filter         62 Hz
C Freq              5 MHz
Multibeam               2
Persist                 1
Line Density            5
Shots Per Est.         16
2D Filter          Medium
TV arrow size          54
```

Figure 3.3 2D vector flow *in vivo* scanning employing the commercial implementation of the TO method. The complex flow in the carotid bulb (top left of the vector flow image) is visible. The color coding for direction and magnitude is overlaid in the top right corner. Reprinted with permission and by courtesy of Mads Møller Pedersen [130].

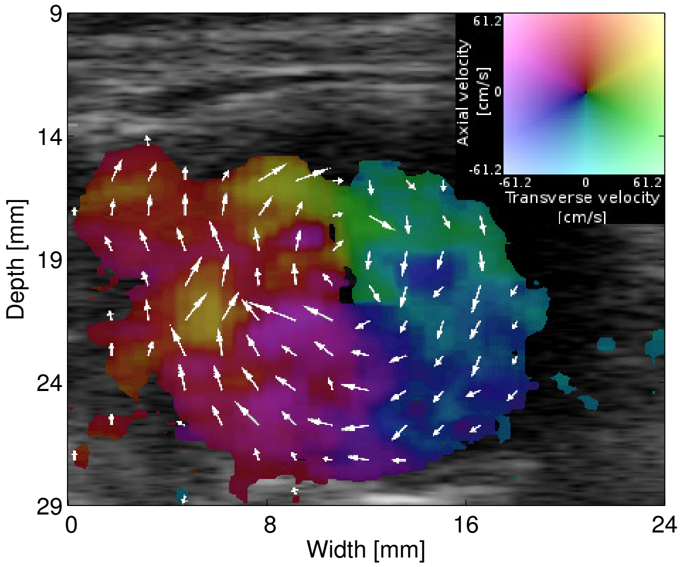

Figure 3.4 *In vivo* vector flow example of the abdominal aorta in the cross-sectional plane where secondary flow is present. Image courtesy of Mads Møller Pedersen [130] and reprinted with permission.

of 2D estimators is evident from this example. Additional examples of *in vivo* flow have been presented by Hansen et al. [19, 132].

Visualization of the secondary flow present in the abdominal aorta is presented by Pedersen [130] and Pedersen et al. [133]. An example of this is given in Figure 3.4. The scan is a cross-sectional plane of the abdominal aorta. The main part of the velocity vector is therefore expected to be out of the image plan. Yet, there are still considerable velocities in the scan plane. This illustrates the presence of secondary flow patterns. Thereby, Figure 3.4 demonstrates that the velocity vector has components in all three dimensions.

3.9 Discussion and perspectives

This section discusses the receive apodization and the resulting PEF as well as the clinical *in vivo* examples described above.

Regarding the receive apodization functions, the double oscillating field can be generated using various apodization functions. Using two single elements in receive would yield a very narrow band response, however, it would result in poor spatial resolution in the field and a poor SNR. The SNR would be poor because the SNR is proportional to the area under the apodization function. Convolving the two delta functions with a sinc function yields a rectangular window multiplied on the cosine field as demonstrated above. The sinc is in principle infinitely long, and would also result in a poorer SNR compared to other apodization types. Additionally, the spectrum of the TO field would in theory also have an infinite amount of frequency components yielding a poor definition of the transverse frequency. Using (3.1), rectangular apodizations yield a sinc modulation of the cosine in the field. The benefit is a high SNR, and the drawbacks are a poorer spatial resolution and a rectangular shape in the spatial frequency spectrum. Applying a Gaussian shape on the aperture would also yield a Gaussian windowing of the transverse oscillating field, and a Gaussian distribution around the theoretical transverse spatial frequency. A draw back here is the lower SNR compared to a rectangular apodization. Also, the Gaussian is in principle infinite, but may be truncated or substituted by a Hanning window. Other window functions can also be applied.

Perspectives

The above theoretical derivation is performed under the assumption of a monochromatic field and only applies in the far field or at the focal point. As the application is used in pulsed mode, and the resulting field depends on both the transmit and receive apodization, it can be difficult to predict the center or mean wavelength of the TO field correctly. Udesen [105] demonstrated a bias between the actual field and the theoretically predicted field and hence a difference in mean wavelengths. Yet, the theoretical approach yields a good starting point for predicting the transverse wavelength in the double-oscillating ultrasound field. As an alternative to the theoretical approach, an ultrasound simulation tool can be used to estimated the resulting PEF and based on this the mean transverse wavelength can be estimated. This is expected to yield improved results [20, 104]. To an increasing extend, this will be applied in the following chapters.

The clinical *in vivo* images exemplified the complex and secondary flow patterns that are present in the human blood vessel. The results illustrate the strength of 2D vector velocity methods over 1D methods. Additionally, the results demonstrate that the velocity vector has components in all three dimensions and varies both spatially and temporally. This also illustrates the need for methods that are capable of estimating the 3D velocity vector components simultaneously.

At the commencement of this PhD project, the commercial implementation was not yet available. Therefore, an investigation of the feasibility of a commercial implementation was warranted. This is the topic of the next chapter.

4

Feasibility study of a commercial implementation

Summary *Previously reported results of the obtained transverse velocity components using the TO method include interesting* in vivo *results. However, the results have been obtained using an experimental scanner. To obtain a clinical impact, the method must be implemented on commercial scanner. By using a research data acquisition system, beamformed data for the TO method were obtained using a commercial scanner. Based on these data, the transverse velocity component perpendicular to the ultrasound beam could be measured. The results demonstrate that the TO method is suitable for a commercial implementation. If the TO fields are poorly defined, it affects the performance of the estimator including the introduction of a bias. This bias can be compensated for, but the method should be optimized to improve both bias and standard deviation.*

4.1 Purpose

The purpose of this chapter is to demonstrate the feasibility of a commercial implementation of the TO method. The chapter also serves as a demonstration of the issues when the TO method or the TO fields are not optimized. The chapter is composed upon Paper I and parts of the paper by Hemmsen et al. [21] of which the author of this thesis wrote the section titled *Transverse Oscillation for blood velocity estimation* (approximately two pages).

4.2 Background and motivation

The previous section described the TO method. At the time the research presented in this chapter was conducted, the obtained transverse velocity estimates had been obtained using the experimental scanner RASMUS [134]. As mentioned in the previous chapter, both flow-rig and *in vivo* examples had been obtained using the experimental setup. However, to obtain a clinical impact, the method must be implemented on commercial scanner. Hence, the next step was to demonstrate the feasibility of such a commercial implementation.

In this chapter a small part of the work performed to demonstrate the feasibility of a commercial implementation of the TO method for clinical use is presented. The feasibility of a commercial implementation is investigated by modifying the settings in a commercial scanner, and subsequently acquire beamformed RF data through a research interface. The implementation is tested in a flow-rig system with a parabolic flow profile. The mean and standard deviation of the obtained velocity estimates are calculated and compared to the expected velocity profiles.

Additionally, this chapter demonstrates the consequence of using apodization functions which yield PEFs where the transverse oscillations are poorly defined. And, how this can be compensated for.

Structure of the chapter

In the following section the research hypotheses underlying the this chapter is presented. Section 4.4 presents the methods and materials used, and the results are presented and discussed in Section 4.5. Finally, the conclusion and the perspectives are stated in Section 4.6.

4.3 Research hypotheses

The main hypothesis underlying the scientific work presented in this chapter is:

- A commercial implementation of the TO method is feasible.

This is investigated by means of the following hypotheses:

1. The TO method can be used on beamformed data acquired using a commercial scanner.

2. A commercial scanner can be modified to create the TO fields.

3. Parabolic velocity profiles can be obtained in a flow-rig with steady flow.

4. Bias compensation can be employed to remove the bias.

Figure 4.1 The commercial BK Medical 2202 Pro Focus scanner and the BK8812 linear array transducer used to acquire beamformed RF data for velocity estimation. Photos courtesy of BK Medical – reprinted with permission.

4.4 Methods and materials

The velocity estimations presented in this chapter employ the TO method described in the previous chapter. The data are obtained using a commercial scanner equipped with a research interface, and the measurements are performed in a flow-rig system.

4.4.1 Commercial scanner

Beamformed data were acquired using a BK Medical (Herlev, Denmark) 2202 Pro Focus scanner, a BK8812 linear array transducer, and a BK UA2227 research interface connected to a standard PC through a DALSA (Waterloo, ON, Canada) X64-CL Express camera link [21]. The scanner and the linear array transducer are illustrated in Figure 4.1. The research interface allows beamformed RF data to be extracted from the scanner and stored offline for post processing.

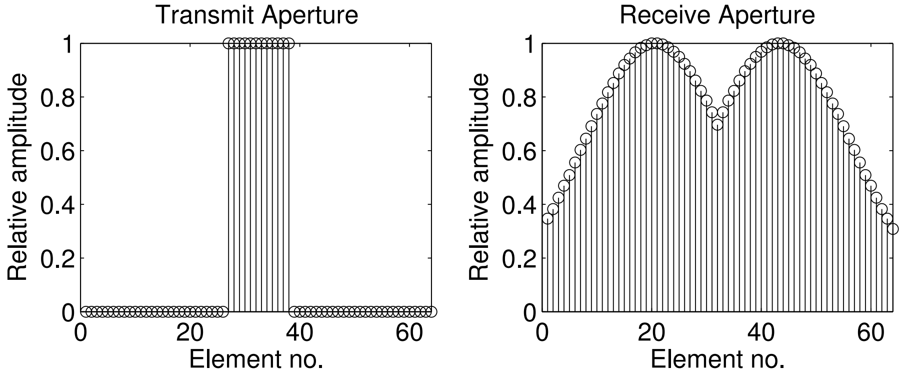

Figure 4.2 The transmit and receive aperture for the TO estimator with a transmit focal depth at 15 mm. The transmit aperture is rectangular, and the F-number is 4. The receive aperture is the TO apodization.

Implementation of the TO method

Only minor changes to the conventional color flow imaging setup are necessary to obtain the required data. The two most important ones are adjusting the apodization and delay profiles in receive.

The scanner was set up to beamform three lines in parallel in receive: Two TO lines and one center line for conventional axial velocity estimation. Subsequently, the color flow imaging receive delays and apodizations were downloaded from the scanner, modified according to the principles of the TO method, and then uploaded to the scanner again. The delay curves were based on dynamic receive focusing and were spherical. This was in opposition to the conical delays suggested by Jensen and Munk [20]. With a focal point at 15 mm, a line density of 1 line per element, and beamforming the two TO lines next to each other (i.e. $\lambda_x/4$ is equal to the pitch), the spacing between the two aperture peaks has to be 7.5 mm. The transmit and receive aperture functions are illustrated in Figure 4.2. However, at the time of data acquisition, this was not taken into consideration, and the spacing was 6.6 mm. The implications are discussed below.

Although data for whole color flow imaging frames were acquired, only the central color flow imaging line was extracted from each frame for further offline processing. 75 flow profiles were generated for the purpose of investigating the performance of the TO estimator.

The transmit and receive aperture functions used in the implementation presented in this chapter are illustrated in Figure 4.2. A narrow transmit

Table 4.1 Parameters for the experimental flow-rig measurements.

Parameter	**Value**
Transducer	
Name	BK8812
Type	Linear
System	
Sampling frequency [MHz]	20
Speed of sound [m/s]	1480
Active number of channels	64
Emitted pulse	
Center frequency [MHz]	5
No. of cycles	6
Window of emitted pulse	None
Focal depth [mm]	15
Steering angle [deg]	0
Apodizations	
Distance between TO peaks [mm]	6.6
Flow settings	
Center of vessel [mm]	16
Peak velocity of flow, v_0 [m/s]	0.215
Beam-to-flow angle [deg]	90
Data acquisition	
Pulse repetition frequency [kHz]	1.3
Velocity estimator	
Averaging length	1 pulse length (2.4 mm)
Transverse lag	1
Number of shots per estimate	16

aperture produces a broad transmit field. The relative high apodization values in the receive aperture increases the SNR.

Due to limitations in the current scanner setup, the TO apodization profile is kept constant over depth. This increases the spatial wavelength over depth. Therefore, the lateral velocity sensitivity changes over depth. This poses an optimization challenge, but does not affect the proof of concept.

The parameters for the measurements are shown in Table 4.1. The table includes information regarding the transducer, the system parameters,

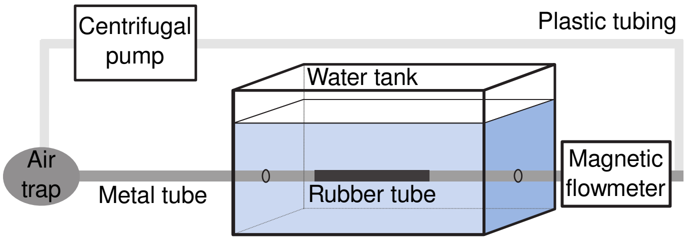

Figure 4.3 Illustration of the flow-rig system. It consists of a centrifugal pump, an air trap, a long rigid metal tube extending into a water tank followed by a magnetic flow meter. The tubing inside the water tank is replaced with rubber penetrable to ultrasound waves. A transducer fixation device can be lowered into the water tank at adjustable beam-to-flow angles. The radius of the metal tube and the rubber tube is 6 mm.

the emitted pulse and receive apodizations, the flow settings, the data acquisition, and the velocity estimator.

4.4.2 Flow-rig system

The measurements were performed on an in-house built flow-rig system as depicted in Figure 4.3. A Cole-Parmer (Vernon Hills, IL, US) centrifugal pump circulates a blood-mimicking fluid in a closed loop circuit. Part of the circuit is contained inside a tank filled with demineralized water, where part of the tubing is replaced with a heat-shrink tube, which is penetrable to ultrasound. The internal radius, R, is 6.0 mm, the thickness of heat-shrink tube is 0.5 mm, and the length of the metal tube prior to the rubber tube is 1.2 m to ensure fully developed laminar flow with a parabolic flow profile [27]. The fluid volume flow, Q, was measured with a MAG 1100 flow meter (Danfoss, Hasselager, Danmark). The transducer can be placed in a fixture and the beam-to-flow angle can be set to a known value. The fixture can then be placed in the water container prior to the measurements.

The tube is filled with a blood-mimicking fluid [135] consisting of water, glycerol, orgasol, Triton x-100, NaBenzoat, and K_2EDTA diluted 10 to 1 with demineralized water, resulting in a viscosity, μ, of $2.6 \cdot 10^{-3}$ Pa·s, and a density, ρ, of 10^3 kg/m^3 [108].

The centrifugal pump is only able to keep the flow constant at sufficiently low flow rates ($Q < 60$ L/h). The entrance length of the tube is more than 1.2 m, and under the given settings sufficient in length to ensure fully developed flow. Hence, the flow can modeled to be laminar with a parabolic flow profile as given by

$$v(r) = \left(1 - \frac{r^2}{R^2}\right) v_0, \tag{4.1}$$

where r denotes the radial position, R is the radius of the tube, and v_0 is the maximum (peak) velocity at the center of the tube.

Due to sediments in the tube the efficient radius was 5.7 mm in these measurements. After the results presented in this chapter and prior to the measurement results presented in the following chapters, the flow-rig system was cleaned, the rubber tube replaced, and a new blood-mimicking fluid mixed as described in Section 5.7.1. This does not influence the results in this or the following chapters. The only difference is that the vessel radius is 6 mm for the measurements presented in the following chapters.

4.4.3 Field II

Field II [136, 137] is used to perform simulations. Field II is a program for simulating ultrasound transducer fields and ultrasound imaging using linear acoustics. The underlying method used is the Tupholme-Stepanishen [138, 139] method for calculating pulsed ultrasound fields by means of the spatial impulse responses. The program can be used to simulate point targets, soft tissue, and flow. For flow, the scatterers are moved between emissions.

4.4.4 Statistics

To investigate the performance of the method, a statistical analysis is performed on the data collected from the flow rig setup. It is assumed that the velocity estimates are independent between depths and between velocity profiles, and that the volume flow is constant over a measurement sequence.

At each discrete depth in the vessel, the velocity is estimated from a number of emissions. The average, $\bar{v}(z)$, of N_p estimates and the estimated standard deviation, $\sigma(z)$, is calculated at each discrete depth as

$$\bar{v}(z) = \frac{1}{N_p} \sum_{p=1}^{N_p} v_p(z) \tag{4.2}$$

$$\sigma(z) = \sqrt{\frac{1}{N_p - 1} \sum_{p=1}^{N_p} \Big(v_p(z) - \bar{v}(z)\Big)^2}, \tag{4.3}$$

where $v_p(z)$ is the p'th velocity estimate at the discrete depth z.

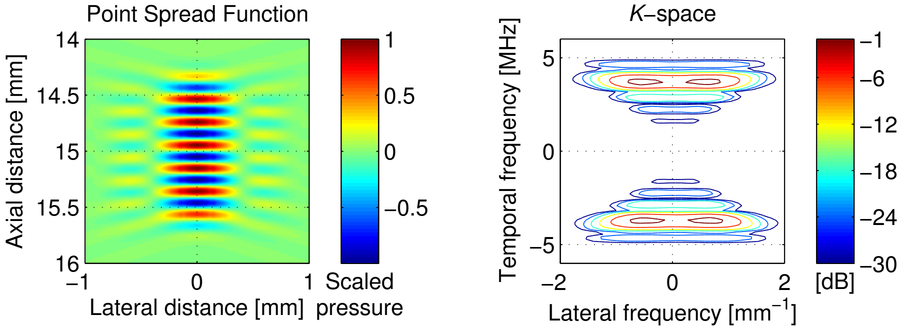

Figure 4.4 The pulse-echo field (or point spread function) at the focal depth calculated based on the used transmit and receive apertures (left). The 2D Fourier transform of the pulse-echo field, i.e. k-space representation (right)

4.5 Results and discussion

This section presents and discusses the pulse-echo fields and the measurement results of the transverse velocities obtained using beamformed RF data from a commercial scanner.

4.5.1 Pulse-echo fields

Based on the measurement settings and the apodizations, the pulse-echo fields are calculated using Field II. The result is illustrated in Figure 4.4, which also illustrates the 2D Fourier transform of the pulse-echo field (K-space). From Figure 4.4 it can be noted that the transverse oscillations are 14 dB lower compared with the main lobe. They are lower than the ones presented by Udesen and Jensen [108], where side lobes were around 2 dB down. This can also be observed from the spectrum where the distinction of the two lateral peaks is poorer. The differences in point spread functions affect the estimator.

Hence, the transverse oscillations are not very well defined, and this is expected to affect the velocity estimates. To optimize the method, the PEFs, i.e. the TO fields, should be improved.

4.5.2 Velocity estimates

Figure 4.5 shows the estimated lateral velocity component of the velocity profiles for 75 measurements at a beam-to-flow angle of 90°. The figure also indicates the mean estimate ± the range of one standard deviation as well as the expected, true velocity. The TO method is clearly able to estimate the lateral velocity component, which is not possible with conventional estimators. As expected, the estimated lateral velocity profile has a parabolic shape. However, the TO estimator underestimates the velocity. The bias is related to the poor definition of the transverse oscillations as described above.

The result is a mismatch between the theoretical λ_x from (3.5) and the simulated mean $\bar{\lambda}_x$ in the generated TO field, because the assumptions for the Fraunhofer approximation are not fully met. The consequence of this is underestimated velocities. Using Field II, the mean lateral wavelength can be estimated based on the 2D spatio-temporal frequency domain of the combined pulse-echo TO field. How to do this is further described in (5.4) in Section 5.4.3. At 15 mm, the theoretical λ_x is 1.35 mm and the simulated mean $\bar{\lambda}_x$ is 2.66 mm. Calculating the relative bias between the simulated mean value and the theoretical value one obtains (2.66-1.35)/2.66 = 0.494. The bias correction factor is therefore 1.494, and this value is multiplied to the estimated velocity. The mean $\bar{\lambda}_x$ is simulated for each 1/2 mm from 10 to 22 mm and interpolated before bias compensation is applied to the 75 velocity profiles. With this bias compensation, the mean of the estimated velocities follows the theoretical profile as apparent from Figure 4.6. The results demonstrate, that it is possible to perform bias compensation, that practically removes the bias.

The results have demonstrated the feasibility of a commercial implementation of the TO method. The commercial implementation should consider optimizing the TO fields, to reduce the mismatch between the expected theoretical wavelength and the actual mean wavelength in the field.

4.6 Conclusion and perspectives

The Transverse Oscillation method has been investigated using beamformed data from a commercial BK scanner. The estimated velocities exhibit the expected theoretical profile, and it is possible to compensate for the bias. Preferably, the TO fields should be optimized prior to velocity estimation. Nonetheless, the feasibility of a commercial implementation for real-time estimations of blood flow vector velocity has been demonstrated.

Perspectives

The results presented in this chapter demonstrated that a commercial implementation is feasible. As illustrated in the previous chapter, BK medical has implemented the technique on their Pro Focus UltraView scanner,

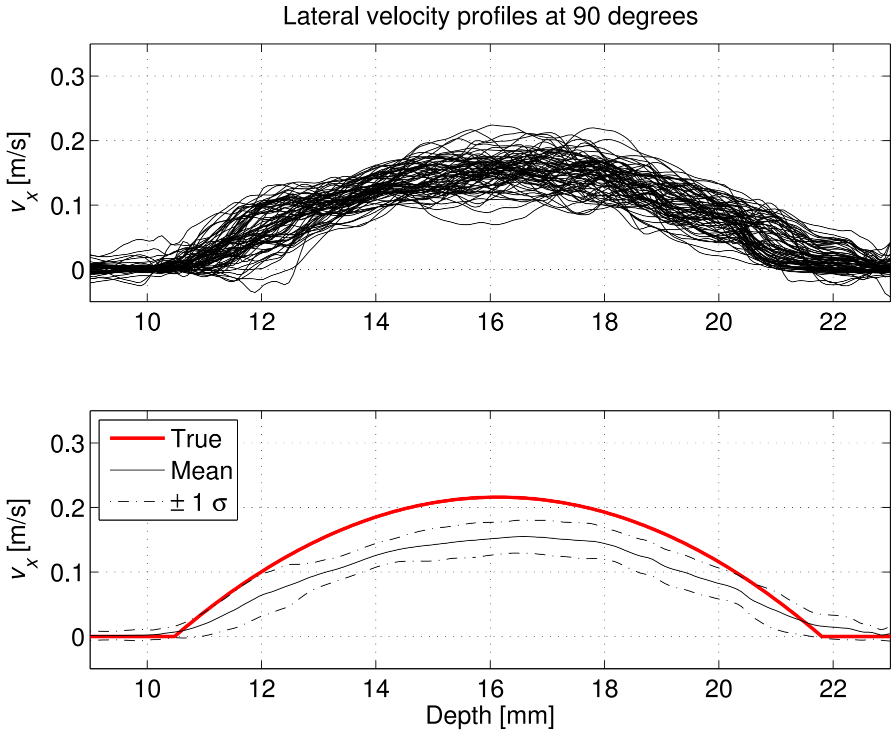

Figure 4.5 Transverse velocities for 75 flow profiles with a beam-to-flow angle of 90° *without* bias compensation (top). Mean estimate ± one standard deviation and expected theoretical velocity profile (bottom). No attempt has been made to suppress false velocity estimates at the vessel wall and in the surrounding water.

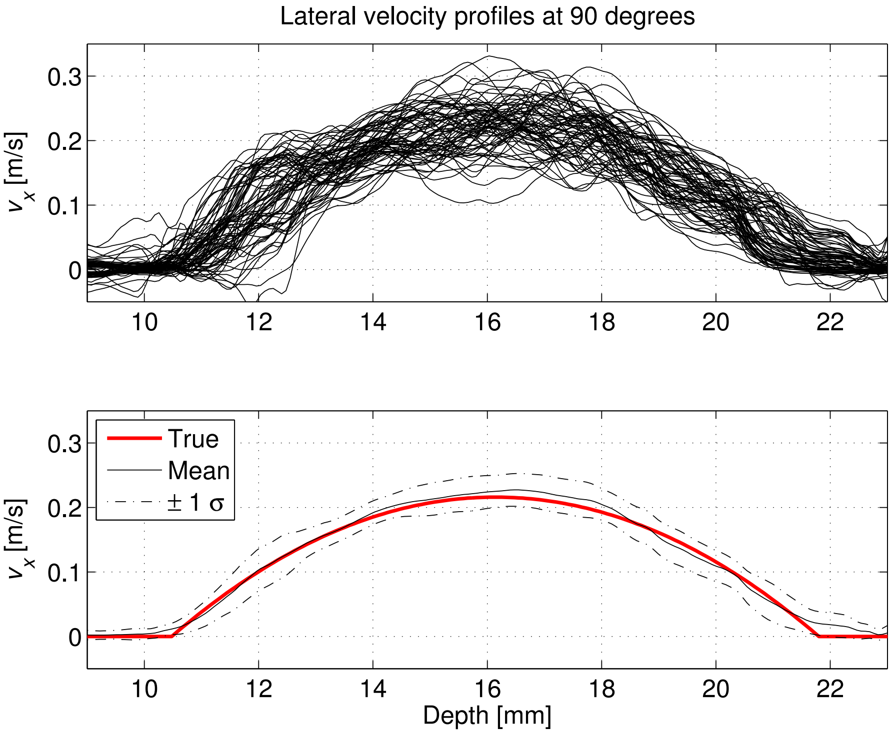

Figure 4.6 Transverse velocities for 75 flow profiles with a beam-to-flow angle of 90° *with* bias compensation (top). Mean estimate ± one standard deviation and expected theoretical velocity profile (bottom). No attempt has been made to suppress false velocity estimates at the vessel wall and in the surrounding water.

demonstrating that a commercial implementation was indeed feasible. And early 2012, the technique was FDA approved.

The implementation presented in this chapter, and the implementation by BK medical were both limited to a linear array transducer. Hence, it would be interesting to expand the method to other transducer geometries such as a phased array or a convex array.

The results also demonstrated, that even with poorly defined TO fields, the parabolic shape of the velocity profile can be estimated. Additionally, bias compensation was able to remove the bias. However, it is expected that the poor TO fields affect the standard deviation of the estimator, and hence, the TO fields should be optimized prior to performing velocity estimations.

5

Expanding the TO method to a phased array

Summary *The previously reported experimental results and the current implementation on the commercial scanner all use a linear array transducer. The TO method is therefore extended to be used in conjunction with a phased array transducer. Therefore, suitable TO fields must be created. To optimize that process, three performance measures are proposed that evaluate the created TO fields. It is demonstrated that these metrics based on the TO fields and the corresponding TO spectrum are correlated with the performance of the subsequently obtained velocity estimates. The performance measures of the TO spectrum can be readily obtained opposed to the velocity method. The beamforming approach is adjusted to the phased array by employing steered TO beams. Simulation results demonstrate, that a phased array implementation is feasible, and that velocities can be estimated down to a depth of 15 cm. A parameter study demonstrates the robustness of the method. Measurements also yield velocity estimates that behave as expected and are comparable with the simulation results. The results demonstrate that further optimizing is required to eliminate the velocity bias, e.g. by employing the mean transverse wavelength instead of the theoretical wavelength, which was used for these results.*

5.1 Purpose

The purpose of chapter is to expand the TO method to a phased array geometry, and to introduce performance measures that may help in optimizing the TO fields, and hence, the performance of the TO method. This chapter is composed upon Paper II and III.

5.2 Background and motivation

The TO method was introduced in Chapter 3 along with various experimental and *in vivo* results obtained using the method. The previous chapter presented flow-rig measurements obtained using a commercial scanner. However, all of the results have been obtained using a linear array transducer. Also, the commercial implementation of the method is currently limited to a linear array transducer where the scanning of the transverse velocities is limited to a depth of 4–5 cm. And from medical doctors there has been an interest in extending the method for use in other areas than currently possible.

The aim of this chapter is to expand the TO method to a phased array geometry using steered beams to broaden its potential clinical applicability because of the smaller footprint of the phased array transducer and its larger field of view compared to a linear array. The potential is especially within cardiac imaging. Additionally, this will be a first step in expanding the method to a 2D phased array transducer for 3D velocity estimation.

Expanding the TO method to a phased array geometry requires suitable PEFs with transverse oscillations. Variations in the TO fields affect the performance of the TO velocity estimator. However, the simulation of many scatterers for velocity estimation is very time consuming. Hence, if the performance of the method can be predicted based on the appearance of the TO fields and their corresponding TO spectrum, it will be very beneficial. A lot of computation time can be saved, and the TO fields and the method can be optimized much more easily. Therefore, three performance measures are suggested to evaluate the created double-oscillating TO fields and the corresponding TO spectrum. They are compared with performance measures of the velocity estimates to investigate if correlations between the two groups of performance measures exist. Additionally, it is sought to reduce the bias issues emphasized in the previous chapter.

Furthermore, velocity estimates are obtained both through simulations and measurements to demonstrate the feasibility of using the TO method in conjunction with a phased array transducer using steered beams.

Structure of the chapter

The following section highlights the research hypotheses underlying this chapter. Secondly, the TO method for a phased implementation is presented. Section 5.5 describes the measures used to describe the performance of the TO estimator, and the proposed measures used to evaluate the TO fields. Simulations are performed to demonstrate the feasibility of the implementation and are presented in Section 5.6, and Section 5.7 describes the measurement setup and the obtained results. All results are discussed in Section 5.8, and the conclusion and perspectives are given in Section 5.9.

5.3 Research hypotheses

The main hypothesis underlying the scientific contribution presented in this chapter is:

- The TO method is suitable for use in conjunction with a phased array transducer.

This is investigated by means of the following hypotheses:

1. Suitable TO fields can be created using a phased array transducer.
2. The developed performance measures based on the TO spectrum are correlated with the performance of the velocity estimates.
3. Velocities can be estimated down to a depth of 15 cm.
4. A parameter study will reveal what affects the method, and that the method is robust.
5. Measured velocities will follow the expected parabolic profiles.
6. Measurement and simulation results will reveal the same trends.

5.4 The TO method for a phased array

This section provides a brief description of the TO method for 2D velocity estimation using a phased array transducer.

5.4.1 Beamforming

For the phased array implementation, the transmitted beam is a standard focused beam with eight cycles in the excitation pulse as for the linear array implementation. Also, the transmit apodization is practically the same as the one used in conventional axial velocity estimation using a phase shift estimator, e.g. a rectangular or a Hanning apodization of the transmitting aperture.

Compared to (3.5), the transverse wavelength, is estimated only slightly differently as

$$\lambda_x(z) = 2\lambda_z \frac{z}{d\cos\theta_0}, \tag{5.1}$$

where θ_0 is the steering angle in the azimuth (ZX) plane. It should be noted, that when the steering angle is different from 0°, the effective aperture width and d decreases with the factor of $\cos\theta_0$. This is taken into consideration when evaluating (5.1), although the effect is small for small steering angles.

Two beams are beamformed in parallel in receive from one emission as depicted in Figure 5.1. To obtain a spatial quadrature signal for transverse velocity estimation, the two lines are separated by a distance of $\lambda_x/4$. Considering (5.1), it is clear that the theoretically derived λ_x increases with depth, unless d increases accordingly. While increasing d in the receive apodization function to maintain a constant λ_x is often possible for a linear transducer at shallower depths, the width of a phased array transducer is limited. In addition, the best performance at each depth is obtained by separating the TO peaks as much as possible, which yields the smallest transverse wavelength and best spatial resolution. In the case where the apodization function is kept constant (i.e. d is constant), the lateral wavelength increases with depth, however, at each depth, the best possible transverse wavelength is obtained. Keeping the apodization function fixed, the two TO lines can be beamformed with a fixed angle instead of a fixed lateral distance.

Using the tangent-relation (see Figure 5.1) and (5.1), the angle, θ_{TO}, between the two lines can be derived as

$$\theta_{TO} = 2\arctan\frac{\lambda_x/8}{z_0} = 2\arctan\frac{\lambda_z}{4d_e}, \tag{5.2}$$

where d_e is the effective distance between the TO peaks in the apodization function calculated as $d_e = d\cos\theta_0$. So for the phased array, instead of beamforming the TO lines with a fixed lateral distance, they diverge with a fixed angle.

The two TO lines are beamformed in parallel with dynamic focusing in receive, as opposed to the triangular focusing profiles originally presented in [104], where the focusing was obtained by steering plane waves so that they intersected at the point of interest by means of triangular delay curves.

Additionally, a center line is beamformed in parallel with the two TO lines for conventional axial velocity estimation.

5.4.2 PEFs and the combined TO field

The double oscillating PEFs at a given depth of interest for the left and the right TO beam are $h_{\text{pe,left}}(x,t)$ and $h_{\text{pe,right}}(x,t)$. They are obtained as the temporally sampled transmit-receive signal for a scatterer at a given distance. Several scatterers can be positioned next to each other to obtain the spatial change in e.g. the transverse direction of the transmit-receive pressure field. An example of the PEFs for the left and right beam for the phased array implementation is given in Figure 5.2. The PEFs from the left

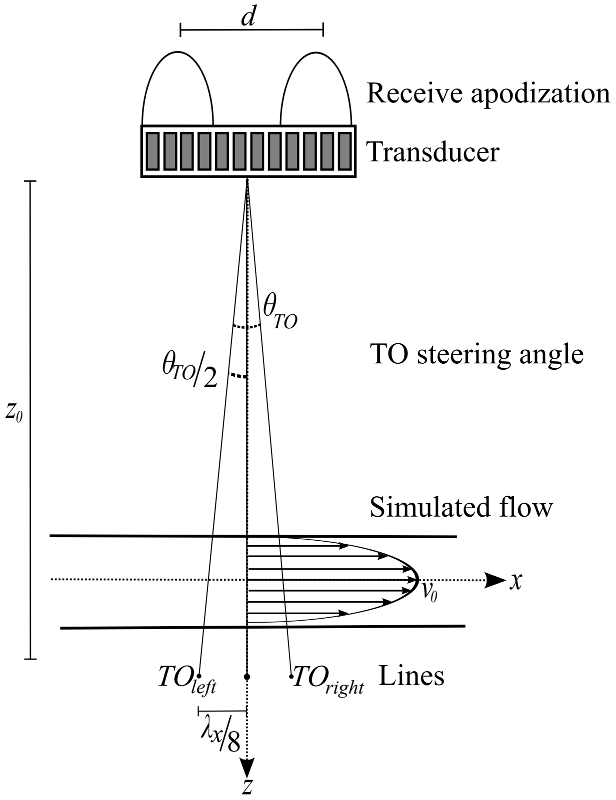

Figure 5.1 Beamforming approach based on a fixed receive apodization function with a fixed angle between beamformed lines. This angle corresponds to the increase of the spatial lateral wavelength with depth. The simulation phantom with a parabolic flow profile and peak velocity magnitude, v_0, is also indicated. For the simulations described in Section 5.6, the vessel direction is changed, so the flow direction by default is perpendicular to the steered beam, i.e. the vessel is parallel only to the transducer surface in the case above where the steered beam coincides with the z-axis. This means, that only the transverse velocity component contributes to the velocity magnitude as the axial velocity is 0 m/s. On the other hand, when investigating the effect of different beam-to-flow angles, the vessel was rotated around its center, so that an axial velocity component is present for beam-to-flow angles different than 90°. In the measurements presented in Section 5.7, however, the vessel is fixed and parallel to the transducer regardless of the direction of the steered beam (contrary to the simulations). Therefore, the axial velocity component contributes to the velocity magnitude, when the steering angle is different than 0°.

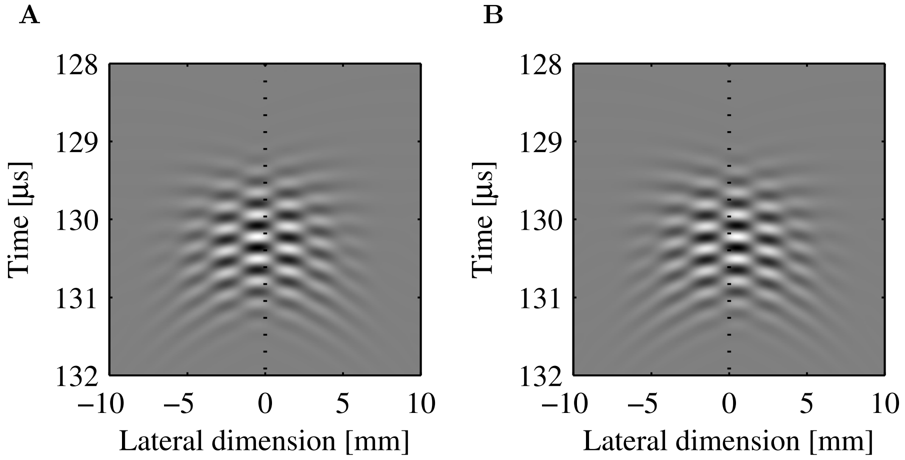

Figure 5.2 PEFs in normalized pressure at a fixed depth of 100 mm when the steering angle of the transmitted beam is 0° see Figure 5.1). **A** is for the left TO beam: $h_{\text{pe,left}}(x,t)$. **B** is for the right TO beam: $h_{\text{pe,right}}(x,t)$. Note that a conventional PEF for axial velocity estimation will not have oscillations in the lateral dimension. $h_{\text{pe,left}}(x,t)$ and $h_{\text{pe,right}}(x,t)$ are calculated using Field II with the standard parameter settings described in Section 5.6.1.

and the right beam can be combined to create the complex TO field by

$$\begin{aligned} h_{\text{pe,comb}}(x,t) = h_{\text{pe,left}}(x,t) + j\mathcal{H}\{h_{\text{pe,left}}(x,t)\} \\ + j\left(h_{\text{pe,right}}(x,t) + j\mathcal{H}\{h_{\text{pe,right}}(x,t)\}\right). \end{aligned} \quad (5.3)$$

5.4.3 TO spectrum

The corresponding 2D spatio-temporal frequency spectrum is then calculated as

$$S(f_x, f_t) = \mathcal{F}_{2D}\{h_{\text{pe,comb}}(x,t)\},$$

where f_x and f_t are the spatial (transverse) and temporal (axial) frequencies in the received signals, and $\mathcal{F}_{2D}\{\cdot\}$ denotes the 2D Fourier transform. The amplitude spectrum of $S(f_x, f_t)$ for the PEFs given in Figure 5.2 is illustrated in Figure 5.3.

Based on $S(f_x, f_t)$ an estimated value of the mean transverse wavelength, $\bar{\lambda}_x$, at the given depth of interest can be obtained as $1/\bar{f}_x$, where $\bar{f}_x$ can be

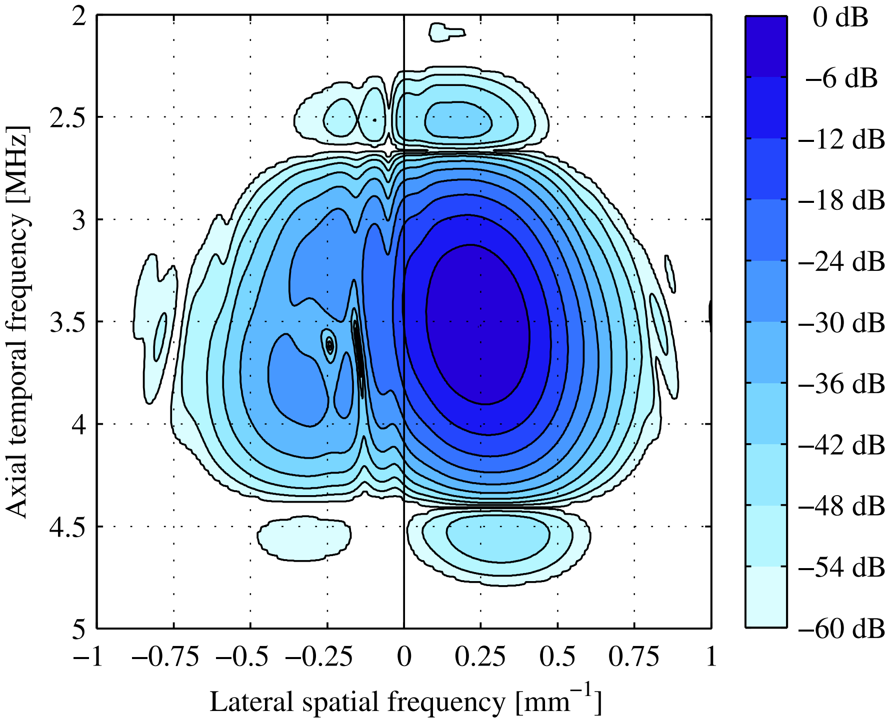

Figure 5.3 The amplitude spectrum of the 2D spatio-temporal frequency spectrum, $S(f_x, f_t)$, of the PEFs in Figure 5.2 when combined as described in (5.3). Note that the energy is mainly located in the fourth quadrant. The first and second quadrant are not shown, as the energy is zero for negative temporal frequencies due to the analytical signal by use of the Hilbert transform.

computed as

$$\bar{f}_x = \frac{\displaystyle\int_{-f_s/2}^{f_s/2} \int_{-f_{ss}/2}^{f_{ss}/2} f_x S(f_x, f_t)^2 \, \mathrm{d}f_x \mathrm{d}f_t}{\displaystyle\int_{-f_s/2}^{f_s/2} \int_{-f_{ss}/2}^{f_{ss}/2} S(f_x, f_0)^2 \, \mathrm{d}f_x \mathrm{d}f_t} \tag{5.4}$$

where f_s is the temporal sampling frequency and f_{ss} is the spatial sampling frequency.

Additionally, $\bar{\lambda}_x = 1/\bar{f}_x$ from (5.4) can be used instead of λ_x from (5.1) in (5.2), however, it requires that $\bar{\lambda}_x$ has been estimated prior to the beamforming stage.

5.4.4 Velocity estimation

The velocity estimation is performed in the same way as described in Section 3.6.

5.5 Performance measures

This section describes the performance measures used to evaluate the TO estimator based on the velocity estimates and the designed PEFs.

5.5.1 Velocity estimates

To investigate the performance of the TO method for velocity estimation, the average behaviour over a number of velocity estimates is investigated. It is assumed that the velocity estimates are independent.

Based on the mean and standard deviation of the velocity estimates, given by (4.2) and (4.3), respectively, the bias, $B(z)$, and the root-mean-square (RMS) error, $E_{\mathrm{RMS}}(z)$, are calculated as

$$B(z) = \bar{v}(z) - v_t(z), \tag{5.5}$$

$$E_{\mathrm{RMS}}(z) = \sqrt{\frac{1}{N_p}\sum_{p=1}^{N_p}(v_p(z) - v_t(z))^2}, \tag{5.6}$$

where v_t is the true (or expected) velocity profile.

For a better and more straightforward comparison of various parameter settings, three single measures for the bias, the standard deviation, and the RMS error are computed. Therefore, B, σ, and E_{RMS} are averaged over the entire vessel and divided by the peak velocity magnitude, v_0. The three non-dimensional quantities, the relative mean bias, $\tilde{B}$, the relative mean standard deviation, $\tilde{\sigma}$, and the relative mean RMS error, $\tilde{E}_{\mathrm{RMS}}$, of the velocity estimates are given by

$$\tilde{B} = \frac{1}{v_0 N_z}\sum_{z=1}^{N_z} B(z), \tag{5.7}$$

$$\tilde{\sigma} = \frac{1}{v_0}\sqrt{\frac{1}{N_z}\sum_{z=1}^{N_z}\sigma(z)^2}, \tag{5.8}$$

$$\tilde{E}_{\mathrm{RMS}} = \frac{1}{v_0}\sqrt{\frac{1}{N_z}\sum_{z=1}^{N_z}E_{\mathrm{RMS}}(z)^2}, \tag{5.9}$$

where N_z is the number of discrete samples within the vessel. These measures are used to describe the performance of the velocity estimates obtained using the TO estimator.

5.5.2 TO spectrum

If the performance of the velocity estimator can be predicted from the spatio-temporal frequency spectrum, the design of suitable PEFs will be made easier. Three metrics are suggested to characterize the combined TO fields based on the corresponding 2D spatio-temporal Fourier domain. These measures are correlated with the measures introduced in Section 5.5.1.

The advantage of the suggested performance metrics based on the TO fields and their corresponding TO spectrum is that they can be more readily obtained. They can be obtained based on the TO fields, which require much fewer calculations compared to a simulation study of moving scatterers. The TO fields can be estimated based on 100 points (scatterers) for each TO line, whereas a speckle phantom may require a factor of 100 or 1000 more scatterers for just one TO line for one emission. This number must then be multiplied with the number of emissions per estimate and the desired velocity profiles. Therefore, it is preferable to optimize the TO method based on these performance metrics compared to the obtained velocity estimates. For this to work, the performance metrics from the TO fields must be correlated to the performance of the velocity estimator.

Ideally, the lateral spatial frequencies of the 2D spatio-temporal frequency spectrum, $S(f_x, f_t)$, should yield a narrow one-sided spectrum (see Figure 5.3) in the lateral dimension of $S(f_x, f_t)$. Using temporal IQ sampled data or the Hilbert transform to generate analytical signals, the spectrum will already be one-sided in the axial dimension.

The mean spatial frequency depends on the aperture function, i.e. the spacing of the two apodization peaks as described in (5.1). The width of the apodization peaks determine the frequency spread in the spatio-temporal spectrum, $S(f_x, f_z)$.

One of the measures used to evaluate the designed PEFs is the coefficient of variation, c_v, of the spatial transverse frequencies, f_x, over the mean spatial frequency

$$c_v = \frac{\sigma_{f_x}}{\bar{f_x}} \tag{5.10}$$

where $\bar{f_x}$ is the mean transverse spatial frequency given in (5.4), and σ_{f_x} is the spread of the spatial frequencies given by

$$\sigma_{f_x} = \sqrt{\frac{\displaystyle\int_{-f_s/2}^{f_s/2}\int_{-f_{ss}/2}^{f_{ss}/2}(f_x - \bar{f}_x)^2 S(f_x, f_0)^2 \,\mathrm{d}f_x \mathrm{d}f_t}{\displaystyle\int_{-f_s/2}^{f_s/2}\int_{-f_{ss}/2}^{f_{ss}/2} S(f_x, f_0)^2 \,\mathrm{d}f_x \mathrm{d}f_t}}.$$

It is hypothesized that c_v is related to the standard deviation of the velocity estimates, where an increase in c_v should result in an increase in standard deviations.

Based on the simulated $\bar{\lambda}_x = 1/\bar{f}_x$ and the theoretically predicted lateral wavelength given in (5.1), the relative bias of λ_x can be estimated as

$$B_{\lambda_x} = \frac{\bar{\lambda}_x - \lambda_x}{\lambda_x}. \tag{5.11}$$

This bias arises due to the fact that the Fraunhofer approximation is not entirely valid, and because the spatial IQ approach does not work perfectly. The mean transverse wavelength, $\bar{\lambda}_x$, can be used in the estimator to yield a more unbiased estimate. Furthermore, $\bar{\lambda}_x$ instead of λ_x can be used in (5.2) to expectedly reduce the bias on the velocity estimates.

The third measure is the energy ratio, E_r, computed as

$$E_r = \frac{\displaystyle\int_{-f_s/2}^{f_s/2}\int_{-f_{ss}/2}^{0} S(f_x, f_t)^2 \,\mathrm{d}f_x \mathrm{d}f_t}{\displaystyle\int_{-f_s/2}^{f_s/2}\int_{-f_{ss}/2}^{f_{ss}/2} S(f_x, f_t)^2 \,\mathrm{d}f_x \mathrm{d}f_t}. \tag{5.12}$$

This provides information of the energy leak from the right half plane to the left half plane of the 2D frequency spectrum. Figure 5.3 serves as an illustration of the energy leak from positive spatial frequencies to negative spatial frequencies. It is hypothesized, that this gives an estimate of the overall performance of the TO velocity estimator. If the value of E_r approaches 50%, the amount of energy in both quadrants is increasingly the same, and velocity estimation is expected to be compromised, because the spatial quadrature approach has failed. Therefore, it is hypothesized that the relative mean standard deviation and $\tilde{E}_{\mathrm{RMS}}$ of the velocity estimates increase as E_r increases.

5.6 Simulations

Simulated data are used to evaluate the implementation of the TO method on a phased array. First, an initial example is constructed with a sensible

Table 5.1 Transducer parameters.

Parameter	**Value**
Transducer type	Phased array
Number of elements	128
Pitch [mm]	0.220
Kerf [mm]	0.022
Element height [mm]	15
Center frequency [MHz]	3.5
Impulse response	3 cycle sinusoid (Hanning windowed)
Elevation focus [mm]	85

choice of parameter settings. Afterwards, several parameter settings are varied around this initial operating point to investigate their effect on the performance of the estimator, which will provide an indication of the robustness of the method.

This section presents the simulation setup, the data generation and processing, and the results.

5.6.1 Simulation setup

The ultrasound simulation program Field II described in Section 4.4.3 was used for the simulation study. A phased array transducer with the characteristics shown in Table 5.1 was emulated. A blood vessel, as illustrated in Figure 5.1, was modeled as a circular cylindrical volume (radius = 6 mm, length = 20 mm) of moving scatterers surrounded by a block of stationary scatterers in a 20 mm × 20 mm × 20 mm volume. The flow was modeled to be laminar with a parabolic flow profile as given by (4.1).

The resolution cell size was conservatively calculated as $\lambda_z \cdot \mathrm{FWHM}_y \cdot \lambda_x / 4$, where the full-width-half-max (FWHM) in the elevation direction was calculated as $\mathrm{FWHM}_y = \lambda_z F^{\#}$, yielding approximately $1.2\,\mathrm{mm}^3$. Consequently, the number of scatterers was set to 80 000 to obtain at least 10 scatterers per resolution cell, which ensures fully developed speckle signals [140]. The flow angle was set to be perpendicular (90°) to the depth axis to obtain purely transverse flow at a steering angle of 0°. When scanning at steering angles different from 0°, the scatterer block was rotated around $(x, y, z) = (0, 0, 0)$ m according to the steering angle—i.e. even at steering angles different than 0° no axial velocity component was present. However, at beam-to-flow angles different from 90°, an axial velocity component was present. See also

Table 5.2 Fixed simulation parameters.

Parameter	**Value**
System	
Sampling frequency	100 MHz
Speed of sound	1540 m/s
Emitted pulse	
No. of transmit cycles in excitation pulse	8 cycles
Transmit excitation window	Hanning
Transmit focus (radial depth)	10 cm
Flow settings	
Maximum velocity of blood	1.0 m/s
Data acquisition	
Pulse repetition frequency	5 kHz

explanation in Figure 5.1.

The fixed simulation parameters are listed in Table 5.2. At a depth of 10 cm, the lateral wavelength was 4.1 mm, and the maximal detectable velocity with the given pulse repetition frequency was 5.15 m/s using (3.9). The peak velocity of 1 m/s was therefore only at about 20% of the aliasing limit.

Table 5.3 lists the parameters that were varied in the simulation study. A number of initial conditions were used to form a starting point in the parameter space as indicated with boldface in Table 5.3. During this study, the different parameters were kept fixed at their starting point (unless otherwise stated), and only the parameter under investigation was varied. Each simulation setup was repeated 100 times with random initial scatterer positions.

A few comments to some of the parameters in Table 5.3 are given here: For the different scan depths, the center of the vessel was placed at the given scan depths. In one case, the transmit focus depth was the same as the scan depth, and in the other, the transmit focus depth was fixed at 10 cm for all scan depths. For the apodization shapes, the Tukey window had a ratio of taper of 0.5. At a depth of 10 cm, the spacing of [33 49 65 81 97] elements corresponded to λ_x = [12.1 8.2 6.2 5.0 4.1] mm. For the TO apodization peak width investigation, the spacing was 65 elements (not 97), so that a TO peak width of 64 elements could be obtained. The lag in acquisition corresponded to effectively lowering the pulse repetition frequency by the given factor. According to the previous calculation of the aliasing limit, the

Table 5.3 Varied simulation parameters. The values in bold face are the default parameter values.

Parameter	**Value**
Emitted pulse	
Steering angle [deg]	[-45:5:45] (**0**)
F# in transmit	4 6 8 **10** 12
Apodization	
Transmit apodization shape	**Hanning**, Tukey, Rect.
Receive apodization shapes	**Hanning**, Tukey, Rect.
Spacing between TO apod. peaks [elements]	33 49 65 81 **97**
Width of TO apod. peaks [elements]	8 16 **32** 64
Flow phantom	
Scan depth with transmit focus at scan depth [cm]	2.5 5 7.5 **10** 12.5 15
Scan depth with fixed transmit focus at 10 cm [cm]	2.5 5 7.5 **10** 12.5 15
Beam-to-flow angle [deg]	[60:5:120] **(90)**
Velocity estimator	
Number of emissions per estimate	4 8 16 **32** 64
Lag in acquisition time	**1** 2 3 4 5
SNR [dB]	-3 0 3 6 9 12 ∞

peak velocity, v_0, with the given lag values, was at approximately [20 40 60 80 100] % of the aliasing limit of the transverse velocity estimator. As default, SNR $= \infty$, i.e. no noise was added. When changing the SNR, zero mean white Gaussian noise was added to the beamformed RF signals prior to the matched filtration. The matched filter improved the SNR by 18 dB, and the resulting SNR after matched filtration is listed in the table.

5.6.2 Data generation and processing

M-mode (motion mode) lines were simulated with Field II. In the post processing step, matched filtration was used by convolving the calculated RF signals with the time reversed emitted pulse, $g(-n)$, as

$$r_m(n) = r_{bf}(n) * g(-n), \tag{5.13}$$

where $r_{bf}(n)$ is the sampled and beamformed signal at discrete sample (time) n.

When stationary echo cancelling (clutter filtering) was applied, it was performed by subtracting the mean ensemble value of N_i emissions by

$$r_{cf}(n,i) = r_m(n,i) - \sum_{i=1}^{N_i} r_m(n,i). \tag{5.14}$$

Afterwards, the velocity estimation with RF averaging was employed. In addition, the PEF was simulated and the 2D spatio-temporal frequency spectrum was calculated. Subsequently, the performance measures listed in Section 5.5 were computed for both the velocity estimates and the 2D spatio-temporal Fourier domain. For the velocity estimates, the relative mean bias and standard deviations were averaged over the entire vessel–except for the outer 1 mm at either end of the vessel to reduce edge effects.

5.6.3 Simulation results

Initially, the simulated flow phantom was positioned at a (radial) depth of 10 cm at a steering angle of 0°. The transmit apodization of the transducer aperture was a Hanning function with a width corresponding to a F-number of 10. The two receive apodization shapes were two Hanning functions each 32 elements (7.0 mm) wide, and spaced 96 elements (21 mm) apart. These parameters affected the beamforming of the flow lines. The number of emissions per estimate, N_i, and the acquisition lag (i.e. the lag in the pulse repetition frequency), k_{prf}, are parameters that only affected the velocity estimator, and they were 32 and 1, respectively. Similarly, changing the flow angle only affected the estimated velocities.

The estimates of the transverse, v_x, and axial, v_z, velocity components from the 100 realizations are shown in Figure 5.4 and 5.5 without and with stationary echo cancelling, respectively. The velocity is fully transverse, hence, no axial velocity is present. This is reflected in the figure. The axial velocity component is estimated using a conventional axial velocity estimator, and is therefore not investigated further. With the standard settings, the relative mean bias, $\tilde{B}_{v_x}$, was -5.0% and the relative standard deviation, $\tilde{\sigma}_{v_x}$, was 7.9% without echo cancelling. With echo cancelling, $\tilde{B}_{v_x}$, was 3.8% and $\tilde{\sigma}_{v_x}$, was 7.8%. Although not considered further, for comparison it can be noted that no axial bias is present, and that the standard deviations for the axial velocity estimates are about an order of magnitude smaller than for the transverse velocity estimates.

The effect on the performance measures when changing the position of the simulated phantom in terms of (radial) scan depth is illustrated in Figures 5.6A and 5.6B. There is no large difference between the two types of focusing. The relative mean standard deviation increases with depth, and also the relative mean bias is depth dependent. With echo cancelling $\tilde{B}_{v_x}$ increases, whereas without echo cancelling $\tilde{B}_{v_x}$ is closest to 0% at around 75 mm for both transmit foci. As the depth increases, an increasing difference between $\tilde{B}_{v_x}$ with and without echo cancelling is visible.

At a depth of 15 cm, $\tilde{B}_{v_x}$ and $\tilde{\sigma}_{v_x}$ was 8.5% and 10%, with echo cancelling and transmit focus at 15 cm. For the fixed transmit focus at 10 cm and using echo cancelling, $\tilde{B}_{v_x}$ was 14% and $\tilde{\sigma}_{v_x}$ was 11%.

The effect of changing the steering angle (and also rotating the phantom), is visible in Figure 5.6C. The $\tilde{\sigma}_{v_x}$ is lowest at a steering angle of 0° with a value of 8.1% and increases with increasing steering angle. At ±45° $\tilde{\sigma}_{v_x}$ is 11%. Without echo cancelling $\tilde{B}_{v_x}$ ranges from -1% to -7% without a clear trend. However, with echo cancelling, $\tilde{B}_{v_x}$ is 3.3% at 0° and increases to 17% at ±45°. The difference between the relative mean bias with and without echo cancelling increases when steering away from 0°.

Regarding the beam-to-flow angle, the results are shown in Figure 5.6D. The relative mean standard deviation is lowest at 90° (8.3%) and highest at either 60° or 120° with an approximate value of 23%. The relative mean biases are more or less the same with and without echo cancelling except at values close to 90°. At 90° the difference is largest. Without echo cancelling there is no large variation in $\tilde{B}_{v_x}$, whereas with echo cancelling, a noticeable jump at a beam-to-flow angle of 90% can be observed.

On the transmit side, the F-number of the transmitting aperture was varied. The results can be seen in Figure 5.6E, which shows that the F-number has only a small effect on both $\tilde{B}_{v_x}$ and $\tilde{\sigma}_{v_x}$. The best performance is obtained at a transmit F-number of 6.

Combining the three different apodization shapes for the transmit aperture and receive aperture yields the results shown in Figure 5.6F. With the given (reference) spacing of the TO peaks, the apodization type does not affect $\tilde{\sigma}_{v_x}$ or $\tilde{B}_{v_x}$.

As mentioned, the receive TO apodization creates the transverse oscillations in the PEF. The result of changing the TO apodization peak spacing and width provides the results presented in Figure 5.6G and Figure 5.6H, respectively. Increasing the spacing between the two TO apodization peaks reduces $\tilde{\sigma}_{v_x}$ with and without echo cancelling, and $\tilde{B}_{v_x}$ with echo cancelling. The performance increase (reduction in $\tilde{\sigma}_{v_x}$) is larger when the spacing is lower than 64 elements. With a spacing of 32 elements, only 64 elements are used in receive with $\tilde{\sigma}_{v_x}$ being 25% and $\tilde{B}_{v_x}$ being 33%. These values are most likely not optimal for a 64-element transducer, where a smaller width of the TO apodization peak, and hence larger spacing of the TO apodization peak, is expected to be better.

As Figure 5.6I illustrates, increasing the number of emissions per esti-

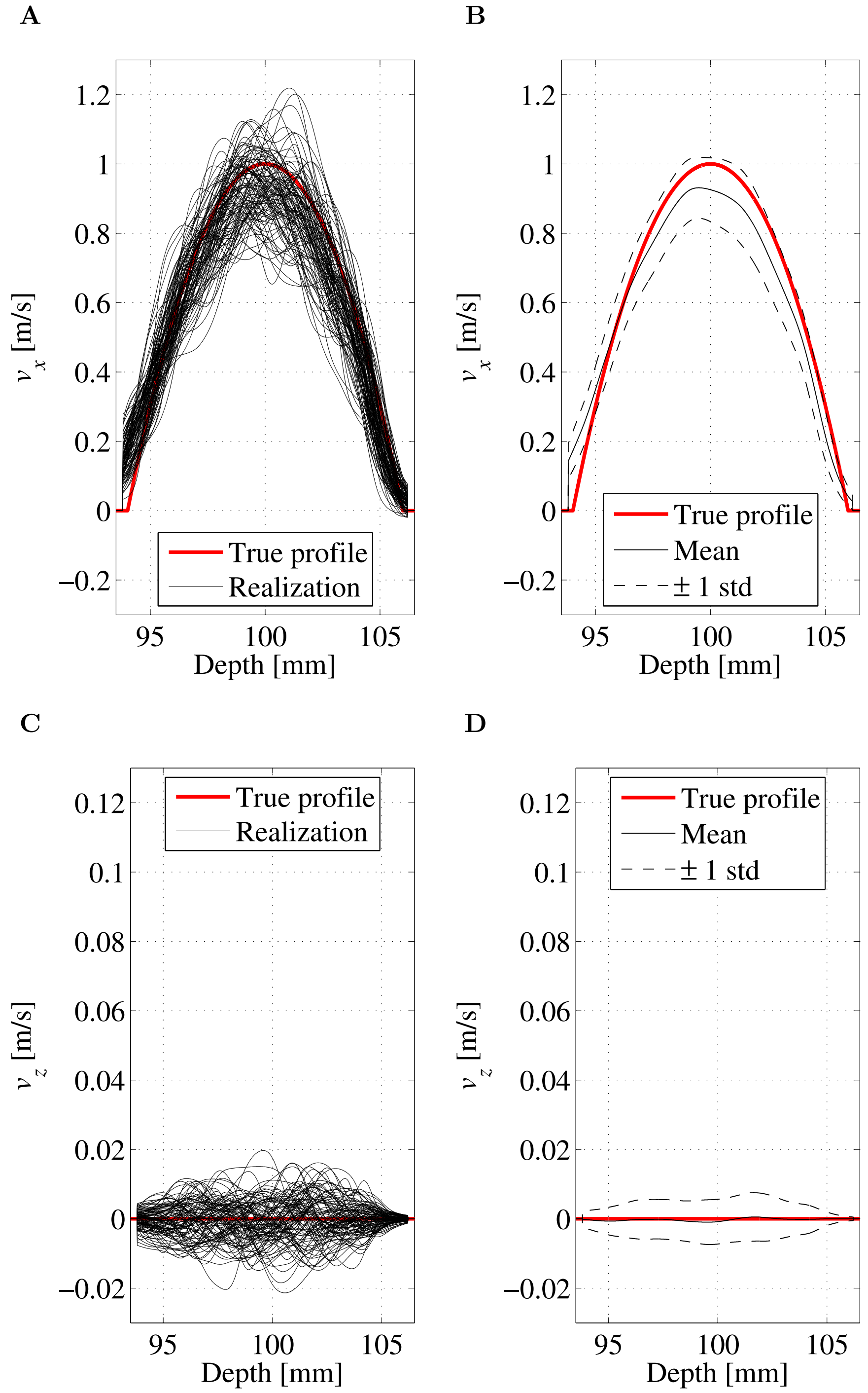

Figure 5.4 Transverse, v_x, and axial, v_z, velocity estimates *without* stationary echo cancelling from 100 simulated realizations (**A** and **C**) and the mean and the standard deviation (**B** and **D**). Note that the velocity range on the y-axis has been decreased with a factor 10 for the axial velocities compared with the transverse velocities.

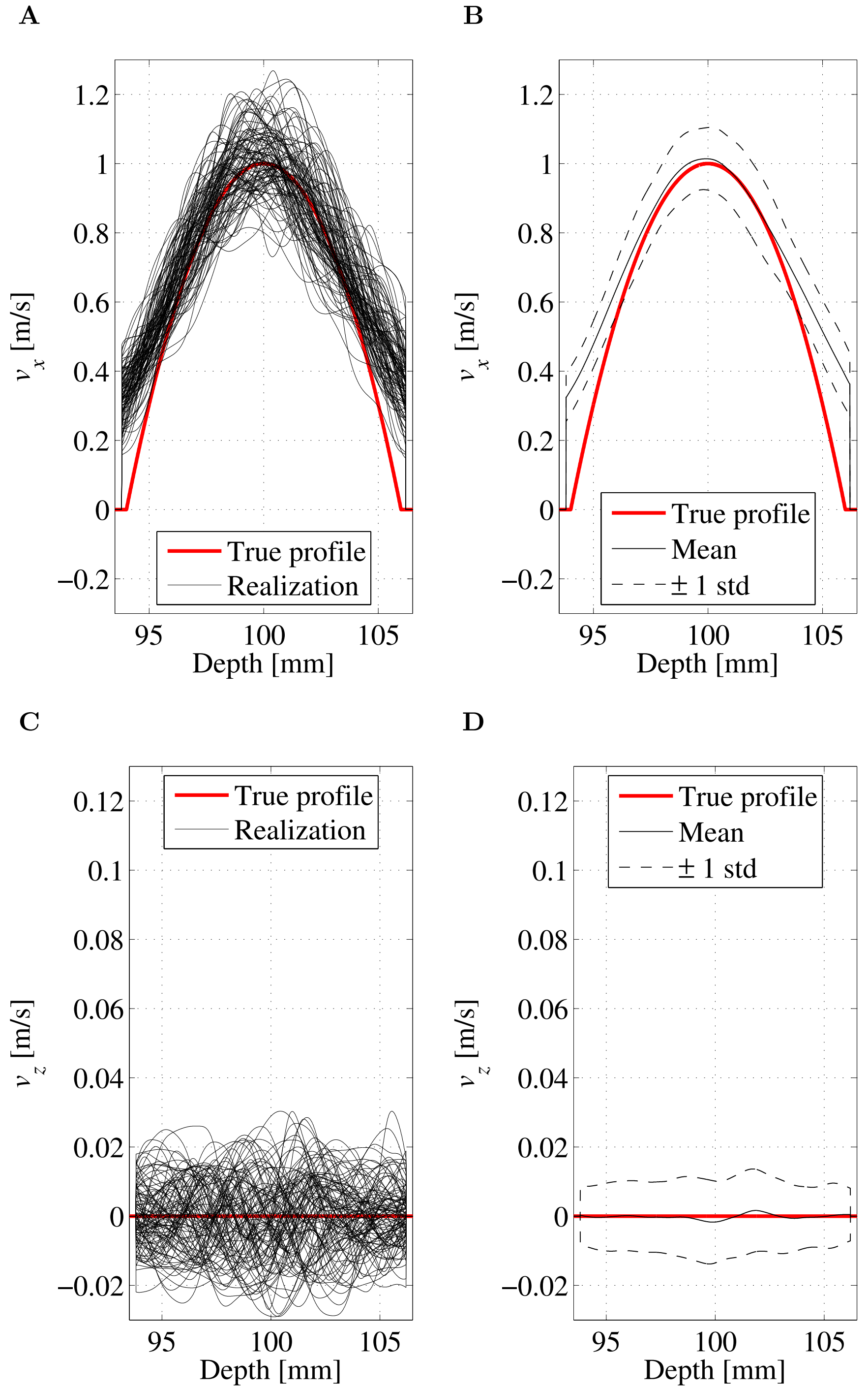

Figure 5.5 Transverse, v_x, and axial, v_z, velocity estimates *with* stationary echo cancelling from 100 simulated realizations (**A** and **C**) and the mean and the standard deviation (**B** and **D**). Note that the velocity range on the y-axis has been decreased with a factor 10 for the axial velocities compared with the transverse velocities.

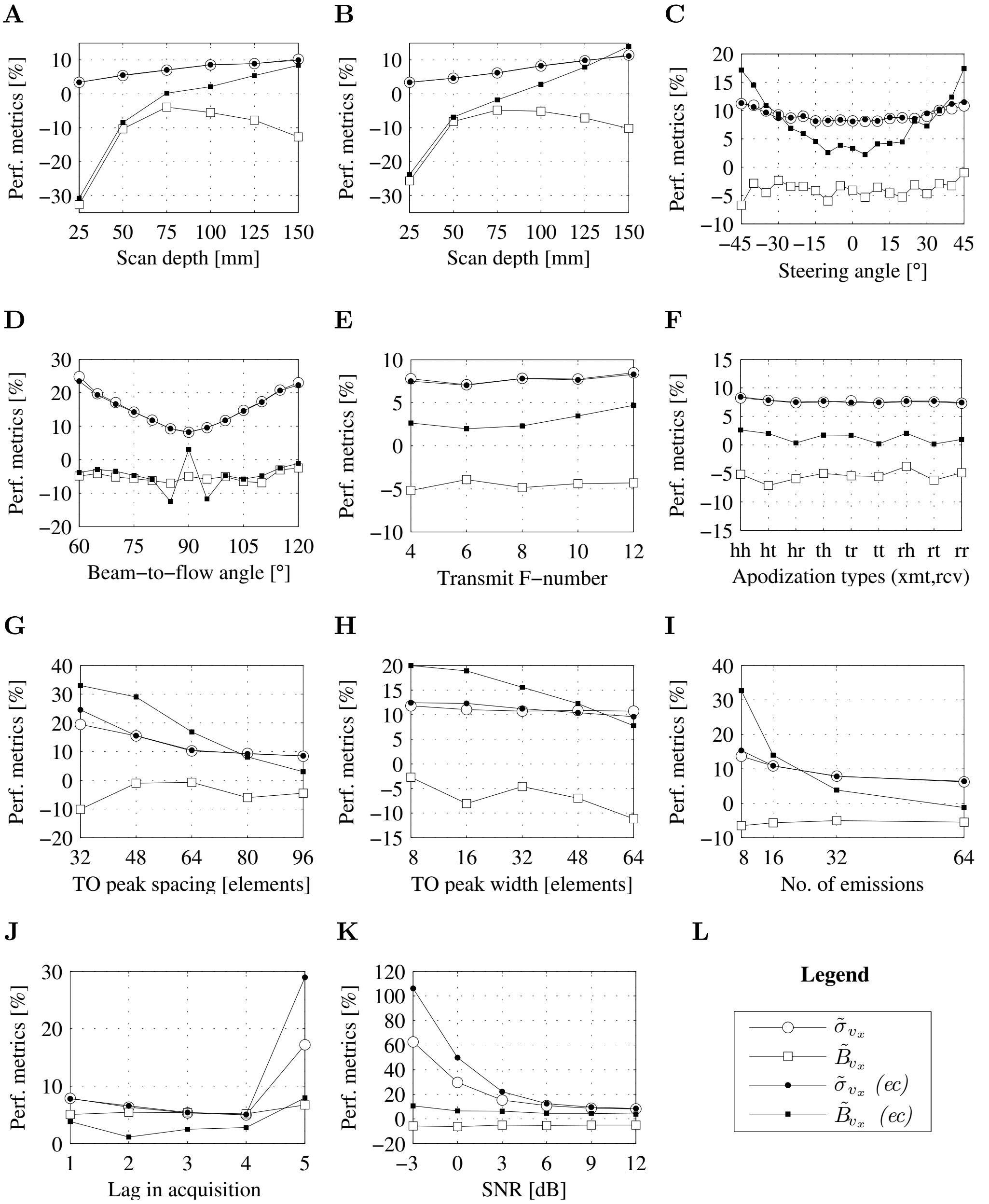

Figure 5.6 Performances measures ($\tilde{\sigma}_{v_x}$ and $\tilde{B}_{v_x}$) with and without echo cancelling (ec) for (see legend in **L**): **A** different scan depths with transmit focus at the given scan depth; **B** different scan depths with fixed transmit focus at 10 cm; **C** a number of steering angles; **D** a number of beam-to-flow angles; **E** various F-numbers in transmit; **F** the nine combinations of Hanning [h], Tukey [t], and rectangular [r] apodized aperture functions in transmit & receive; **G** different spacings between the two TO apodization peaks in receive; **H** different widths of the two TO apodization peaks in the receive; **I** varying the number of emissions per estimate; **J** five different lag values, k_{prf}, in the acquisition, so the pulse repetition frequency effectively is $5/k_{\text{prf}}$ kHz; and finally, **K** the performance depending on the SNR.

mate decreases $\tilde{\sigma}_{v_x}$ with approximately $1/\sqrt{N_i}$ as expected. Without echo cancelling, $\tilde{B}_{v_x}$ is not affected, however, with echo cancelling, $\tilde{B}_{v_x}$ drops from 33% to -1.2%.

Changing the acquisition lag (i.e. lowering the effective pulse repetition frequency) lowers the relative standard deviation, because the peak velocity gets closer to the aliasing limit. This can be observed from Figure 5.6J. When $k_{\text{prf}} = 4$, v_0 is at about 80% of the aliasing limit. For $k_{\text{prf}} = 5$, v_0 is at about 100% of the aliasing limit, and therefore, aliasing occurs, which affects both $\tilde{\sigma}_{v_x}$ and $\tilde{B}_{v_x}$ and results in a decreased performance.

Figure 5.6K displays the results of varying the SNR of the beamformed RF data. The matched filter improved the SNR by 18 dB. It can be observed that the echo cancelling (mean subtraction of ensemble values) improves the performance when the SNR is below 6 dB. The results also demonstrate, that when the SNR is below 3 dB, the performance degrades rapidly. Without echo cancelling the relative mean standard deviation is 22% and 50% at 3 dB and 0 dB, respectively, whereas with echo cancelling the values are 15% and 30%. The relative mean bias is unaffected with and without echo cancelling.

Overall it can be noted that echo cancelling does not affect $\tilde{\sigma}_{v_x}$. However, $\tilde{B}_{v_x}$ is affected, but primarily when the beam-to-flow angle is close to 90°.

To test the hypothesis that a correlation between the performance measures of the PEFs and the performance measures velocity estimates exist, pair-wise values are plotted in Figure 5.7. For these plots all the varied parameter values are included except the variation of the beam-to-flow angle, the number of emissions per estimate, and the acquisition lag, as these parameters do not affect the PEF. For the velocity estimates, only the values without echo cancelling are investigated, as the echo cancelling affects the performance of the estimator [27].

Figure 5.7A demonstrates the correlation between the coefficient of variation, c_v, of the transverse wavelength in the PEF and the relative mean standard deviation of the velocity estimates. The correlation value, R, of 0.96 (R^2=0.92) indicates a strong relation. Figure 5.7B presents the correlation between the bias of the mean transverse wavelength based on the simulated PEF compared to the relative mean bias of the velocity estimates. The correlation value is -0.91 (R^2=0.83) indicating that a positive bias of the mean wavelength leads to a negative bias on the velocity estimates. In Figure 5.7C the relation between the energy leak, E_r, and the relative mean RMS error shows a correlation of 0.43 (R^2=0.18). This indicates some relation between the two, however, the results tend to group into two trends, which lower the correlation value. A smaller group, where the same value of E_r results in different values for $\tilde{E}_{\text{RMS}}$, and a larger group where a

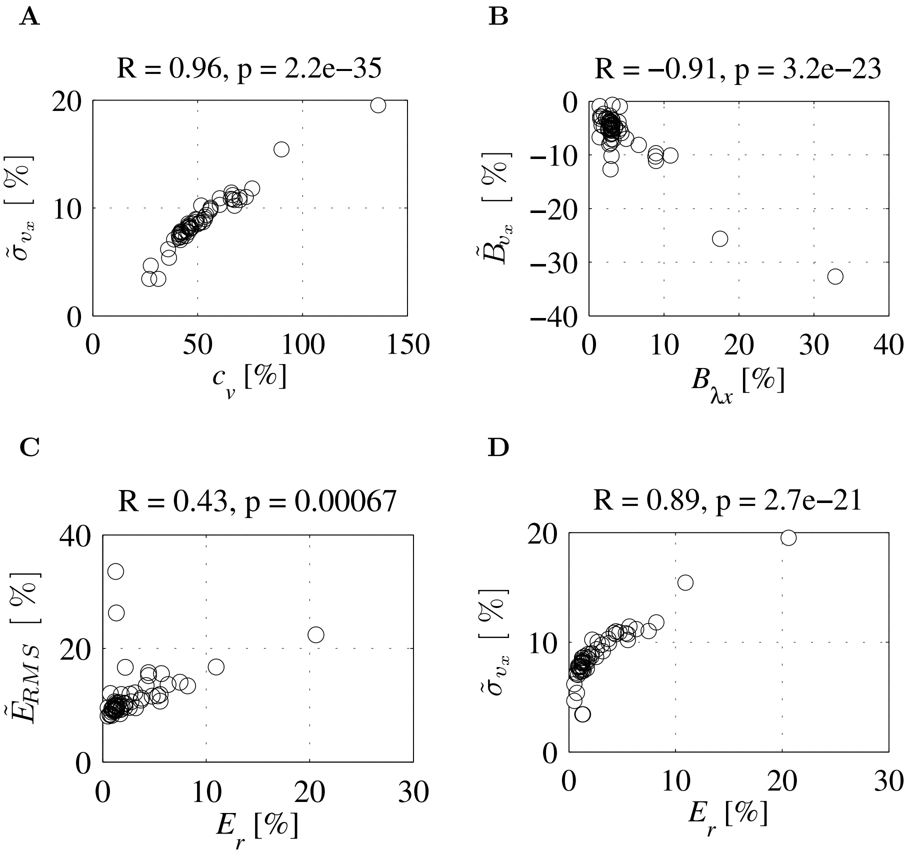

Figure 5.7 Correlation between the performance measures for the 2D spatio-temporal frequency spectrum and the performance measures for the velocity estimates. R indicates the correlation value, and p is the p-value for testing the hypothesis R=0. **A** is for the coefficient of variance, c_v, of the 2D spectrum compared to the relative mean standard deviation, $\tilde{\sigma}_{v_x}$. **B** Is the bias of the transverse wavelength, B_{λ_x}, in the 2D spectrum versus the bias of the velocity estimates, $\tilde{B}_{v_x}$. **C** is the energy ratio of energy leakage, E_r, in the 2D spectrum compared to the relative mean root-mean-square error, $\tilde{E}_{\text{RMS}}$, of the velocity estimates. **D** is E_r versus $\tilde{\sigma}_{v_x}$.

linear relation is observed. Therefore, E_r only to some extend can predict $\tilde{E}_{\mathrm{RMS}}$. Finally, Figure 5.7D indicates the correlation between the energy leak and the relative mean standard deviation. The correlation value is 0.89 (R^2=0.79) indicating a strong relation.

5.7 Measurements

To complement the findings from the simulations, measurements were conducted in a similar environment to the simulation study. First the measurement equipment, the experimental setup, and the data acquisition and processing are described. Afterwards, the experimental results are presented.

5.7.1 Measurements equipment

The following describes the Synthetic Aperture Real-time Ultrasound System (SARUS) and the flow-rig system.

SARUS

The experimental ultrasound scanner SARUS [141–143] was used to acquire data together with a transducer with the same parameters as the ones listed in Table 5.1. A photograph of SARUS can be found in Figure 5.8. It can sample RF data with a sampling frequency of 70 MHz with a precision of 12 bits. The full system has 1024 channels, whereas, only 128 channels were required for these measurements.

Flow-rig system

The measurements were performed on the in-house flow-rig system described in Section 4.4.2. Compared to the results in the previous chapter, the flow-rig system had been cleaned, and the rubber tube had been replaced. The internal radius was, hence, 6.0 mm.

Additionally, the fluid had been exchanged with a blood-mimicking fluid (Danish Phantom Design, Frederikssund, Denmark) containing 5 micron orgasol, glycerol, detergent, and demineralized water in its concentrated form. It was diluted 1:20 with demineralized water, and dextran was added to obtain a viscosity, μ, of 3.9 mPa·s, which is similar to that of blood. The density, ρ, was 1.0×10^3 kg/m^3.

5.7.2 Measurements setup

The peak velocity in the tube was set to 0.25 m/s in contrast to the 1 m/s in the simulations. This velocity was chosen to assure laminar and fully

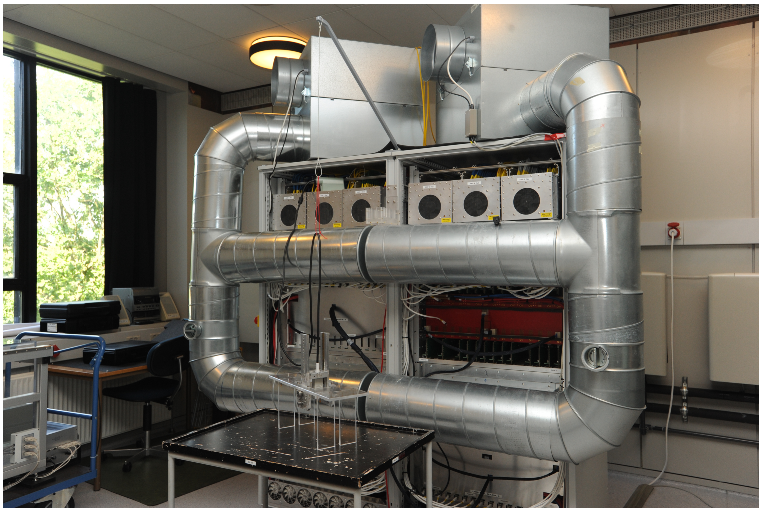

Figure 5.8 A photograph of SARUS, which has 1024 channels distributed over six transducer plugs. The phased array transducer used for the measurements in this chapter has only 128 elements. Therefore, it is plugged to one of the six sockets. The transducer is positioned in the transducer fixation device, which can be placed in the flow-rig water tank. Photo courtesy of Morten Fischer Rasmussen.

developed flow. The pulse repetition frequency was adjusted accordingly with a factor of four. With this setting, the peak velocity of 0.25 m/s was at approximately 20% of the aliasing limit.

The vessel was parallel to the transducer surface, and the center of the vessel was located 9.5 cm below the transducer. The parameters that were fixed for the measurements are listed in Table 5.4, and the varied parameters are listed in Table 5.5. The standard settings are typed in boldface. For the investigation of the TO apodization peak width, the spacing between the TO apodization peaks was 65 elements. For the optimal TO apodization peak spacing, the width of the TO apodization peaks are adjusted accordingly, so a spacing of [64 80 96 112 120] elements goes with TO apodization peak widths of [64 48 32 16 8] elements, respectively.

5.7.3 Data acquisition and processing

Using SARUS, data were sampled with 12 bits at 70 MHz from each transducer channel. The fixed measurement parameters are listed in Table 5.4. After data acquisition, the channel data were filtered with a matched filter

Table 5.4 Fixed parameters for measurements.

Parameter	**Value**
System	
Sampling frequency [MHz]	70
Speed of sound [m/s]	1480
Number of channels	128
Emitted pulse	
No. of transmit cycles in pulse [cycles]	8
Transmit focus (radial depth) [cm]	10
Transmit F-number	6
Flow settings	
Maximum velocity of blood mimicking fluid [m/s]	0.25
Center of vessel [cm]	9.5
Vessel orientation compared to transducer surface	Parallel
Data acquisition	
Pulse repetition frequency [kHz]	1.25

Table 5.5 Varied parameters for measurements.

Parameter	**Value**
Emitted pulse	
Steering angle [deg]	-30:5:30, **(0)**
Apodization	
Spacing between TO apodization peaks [elements]	33 49 65 81 **97**
Width of TO apodization peak [elements]	8 16 **32** 64
Optimal TO apodization peak spacing [elements] (not part of reference setup)	64 80 96 112 120
Velocity estimator	
Number of emissions per estimate	8 16 **32** 64

designed as the time-reversed excitation pulse as

$$r_{m,c}(n) = r_{s,c}(n) * g(-n), \tag{5.15}$$

where $r_{s,c}(n)$ is the sampled signal from individual channels.

Afterwards, the filtered RF data were beamformed using the Beamformation Toolbox 3 [144], which is a versatile MATLAB toolbox written in C++ for beamforming, and to quote Hansen et al. [144]: »It is a general 3D implementation capable of handling a multitude of focusing methods, interpolation schemes, and parametric and dynamic apodization.«

Stationary echo canceling was performed by subtracting the mean of an assemble of emissions as for the simulated data. As part of the velocity estimation, RF averaging was performed with a window length equal to the excitation pulse length.

5.7.4 Experimental results

Estimated transverse and axial velocities based on experimental flow-rig measurements are shown in Figure 5.9. Using the (default) parameters listed in Table 5.4 and 5.5, 45 velocity profiles are obtained for each velocity component. The expected profiles of the velocity components are illustrated as well. They are obtained based on the volume flow, the vessel radius, and an estimate of the beam-to-flow angle. The beam-to-flow angle was estimated to be approximately 89-90° based on B-mode images. For the transverse velocity components, it can be observed, that the mean profile follows the expected parabolic profile. For these data, the relative standard deviation and bias were 8.6 % and -9.2%, respectively. As Figure 5.9 illustrates, the axial velocity component is very small due to a beam-to-flow angle of almost 90°. As well known, it would not be possible to obtain the correct velocity magnitude based on the axial velocity alone as small changes in the estimated beam-to-flow angle would result in large changes of the estimated velocity magnitude due to the division by the $\cos\theta$-term in (2.8) on page 17.

Based on the estimated velocity components at the center of the vessel, the mean velocity magnitude over the 45 profiles is 0.247±0.023 m/s compared with an expected peak velocity magnitude of 0.252 m/s. The beam-to-flow angle is calculated to be 89.3°±0.77°. Excluding the almost zero velocities at the vessel boundaries, the mean angle off all estimates at all depths inside the vessel is 89.3°±0.85°.

Figure 5.10 illustrates the result of varying the different parameters listed in Table 5.5. Figure 5.10A demonstrates the results of increasing the number of emissions per estimate. Both $\tilde{\sigma}_{v_x}$ and $\tilde{B}_{v_x}$ decrease with

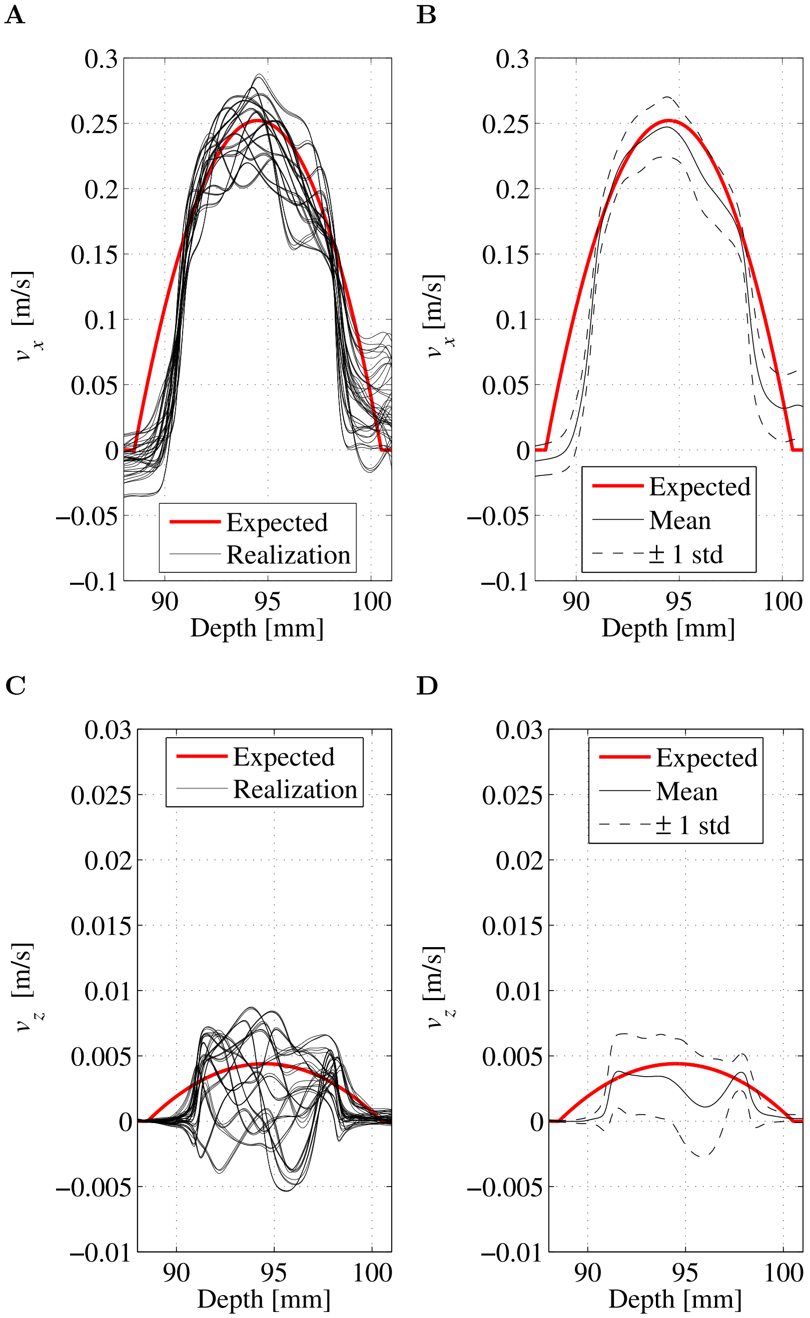

Figure 5.9 Measured transverse, v_x, and axial, v_z, velocity components at a beam-to-flow angle of approximately 89° in the experimental flow-rig system. **A** and **C** show the result of 45 estimated realizations of the velocity profiles using the standard settings and the expected parabolic profiles. **B** and **D** show the expected profiles, the mean of the estimated velocities plus/minus one standard deviation. The underestimation at the vessel boundaries is due to clipping in the sampled RF signals from the vessel walls. This was only a issues at beam-to-flow angle close to 90° (see Section 5.8 for more details). Note that the velocity range on the y-axis for the axial velocities (**C** and **D**) are reduced with a factor 10 compared to the transverse velocities (**A** and **B**).

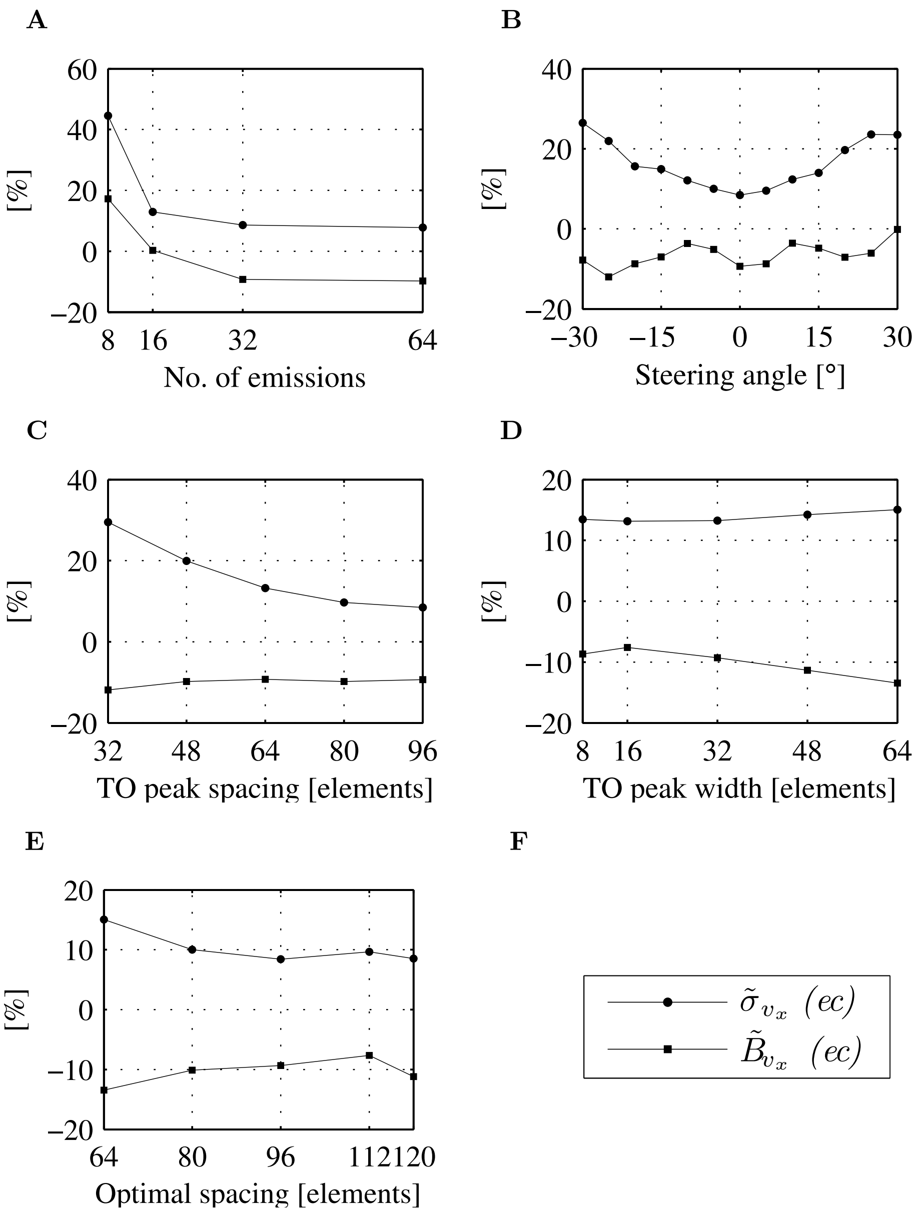

Figure 5.10 Illustration of the relative mean standard deviation and the relative mean bias with stationary echo cancelling for the measurements with (legend in **F**): **A** changing the number of emissions per estimate, **B** varying the steering angle, **C** changing the TO peak spacing, **D** changing the TO peak width, and **E** optimizing the TO peak spacing.

increasing numbers. The negative $\tilde{B}_{v_x}$ is due to clipping in the RF signals from the vessel walls.

Figure 5.10B illustrates the effect of changing the steering angle. However, it must be noted that this differs from the simulations in the regard that the vessel was parallel to the transducer surface for all steering angles, and not rotated as the simulation phantom was. In the simulations, a beam-to-flow angle of 90° was maintained for all steering angles, yielding full transverse flow and no axial velocity component. For the measurements, the vessel was perpendicular to the transducer surface for all steering angles. Therefore, the beam-to-flow angle was $90° + \theta_0$. Hence, for a steering angle different than 0°, the beam-to-flow was no longer 90° resulting in a reduced transverse velocity component and an increase in the the axial velocity component. Additionally, the vessel location (radially) was farther away from the transducer as the steering angle is moved away from 0°. With that in mind, the results still demonstrate that larger steering angles result in larger standard deviations, however, if the angle is below ±20°, the relative standard deviation remains below 20%.

The effect of changing the TO peak spacing in the receive beamforming is illustrated in Figure 5.10C. As the spacing increases, $\tilde{\sigma}_{v_x}$ decreases, whereas $\tilde{B}_{v_x}$ is practically unaffected.

Figure 5.10D shows the effect of changing the peak width. The effect on $\tilde{\sigma}_{v_x}$ is small, but there is an effect on $\tilde{B}_{v_x}$.

Finally, Figure 5.10E demonstrates the effect of using an optimal TO peak spacing based on the different TO peak widths. Both $\tilde{\sigma}_{v_x}$ and $\tilde{B}_{v_x}$ are affected by this.

5.8 Discussion

This section covers the discussion of the results from the simulations and the results obtained from flow-rig measurements.

From (5.1) the transverse spatial wavelength, λ_x, increases as a function of depth, and therefore, the velocity range of the TO estimator increases in accordance with (3.9). The simulations show that the relative mean standard deviation, $\tilde{\sigma}_{v_x}$, increased with depth (Figures 5.6A and 5.6B). Two factors can explain this. First, c_v was observed to increase with depth. Secondly, the simulated peak velocity was kept constant, and as λ_x increases, the velocities get further and further away from the aliasing limit, and therefore, the standard deviation on the velocity estimates increases. Both factors are suspected to contribute to the observed increase in relative standard deviation as the depth increases. The latter reason is supported by Figure 5.6J. This demonstrates, that it is important to adjust the pulse repetition frequency to match the expected peak velocity. In the reference setup, the peak velocity was at approximately 20% of the aliasing limit of the TO estimator at a depth of 10 cm. When the velocity was at 80% of the aliasing limit, $\tilde{\sigma}_{v_x}$ was 5.1% (see Figure 5.6J).

The bias in the velocity estimates arises from the discrepancy between the mean transverse wavelength in the PEF, and the theoretically derived wavelength. As the simulations results have demonstrated a difference in the relative mean bias depending on whether echo cancelling was used or not exists. This demonstrates that the echo cancelling filter biases the velocity estimates towards an overestimation. However, as Figure 5.6D demonstrates, this happens only in simulations where the beam-to-flow-angle is close to 90°, and is expected to be a consequence of the lack of axial motion when employing the echo cancelling filter. It is expected that better echo cancelling filters can remedy or improve this.

Both simulations and measurements (Figures 5.6C and 5.10B) show that the performance degrades as the steering angle increases. Several factors come into play: 1) The effective aperture decreases, hence, the lateral wavelength increases with the same effect as described above. 2) In the measurements, the angle sensitivity of the elements influence the SNR and therefore the performance of the TO estimator. 3) The radial depth for the measurements increases with the steering angle due the fixed positions of the vessel and the transducer.

The bias for the measurements depending on the steering angle. It was expected to have a minimum at a steering angle of 0° where the beam-to-flow angle is 90° (Figure 5.10B). Yet, this is not the case. As mentioned previously, this is a consequence of clipping in the RF signals originating from the vessel wall. A large part of the signal energy was reflected at the incident angle of 90°. At the same time, the gain was set too high, so that the sampled signals were saturating the analog-to-digital converter. This was the case for the signals originating from the vessel wall, but due to the 8 cycles in the transmitted pulse, the clipping also occurred inside the vessel wall drowning the additional small signal amplitudes from the scatterers in the fluid. Therefore, the sampled and beamformed signals at those depths were constant over time, leading to an estimated velocity of 0 m/s. On that account, the minimum around 0° is expected to be an artifact. Also, the different values for $\tilde{B}_{v_x}$ arise due to different PEFs and radial vessel location when steering the beam. Therefore, the results in Figure 5.6C cannot be directly compared with the results in Figure 5.10B.

The results demonstrate that it is important to estimate the true wavelength for a given setup, so the TO angle in the beamforming step can be adjusted. Alternatively, the velocity estimates can be bias compensated based on the difference in wavelengths. As Figure 5.7B indicates, a 10% bias in wavelength, corresponds to approximately a -10% relative mean bias in the velocity estimates from the simulations. This relation is an approximation. Yet, if the actual transverse wavelength is 10% larger than expected, then an underestimation of 10% is not surprising if using a transverse wavelength in (6.3a) that is 10% too small.

The results also indicate, that the bias is a function of depth depending on the parameter settings. For optimal bias compensation, this function has to be derived for a given setup. The true transverse wavelength can be estimated based on simulations or hydrophone measurements, yet, the process of optimizing the actual (mean) transverse wavelength in the PEF and the TO angle is a recursive process, because the estimated $\hat{\lambda}_x$ influences the TO angle, θ_{TO}, which again affects PEFs, and therefore, the estimation of $\hat{\lambda}_x$.

The transmit F-number should be optimized for the given field of view for the velocity estimates. The transmitted field must be broad enough to cover the diverging TO beams. The optimal F-number is 6 for the standard simulation setup. This value was used in the measurements.

Varying the apodization types (either in transmit or in receive) did not affect performance (Figure 5.6F). The larger the area under the apodization functions, the better SNR can be obtained in a noisy environment, and therefore, rectangular or Tukey-windowed apodizations may be advantageous at low SNRs.

Performance decreases when peak separation in receive decreases (see Figs. 5.6G and 5.10C), due to a lower spatial frequency. Additionally, a poorer spatial resolution is obtained. If the larger standard deviation is accepted, an implementation on a 64 element transducer is possible. Figure 5.6H indicates that increasing the TO apodization peak widths decreases $\tilde{\sigma}_{v_x}$, although the effect is small. Broader TO peaks increase the SNR. The results in Figure 5.10D show a slight increases in $\tilde{\sigma}_{v_x}$ when increasing the width. The SNR in the flow-rig measurement is large due to practically no attenuation in water, so the effect may be different in tissue. The results from the TO apodization peak width and peak distance in Figure 5.10E show the optimal (for these two parameters only) combination of width and spacing. Again, these results may be different when the SNR is low. As the results in Figure 5.6K demonstrate, the performance of the estimator degrades rapidly when the SNR decreases below 3 dB. So, in cases where the SNR is low, an increase in the amount of receive energy is expected to be beneficial and outweigh the drawback of increasing the apodization peaks. This reduces the TO spacing, which under ideal conditions increases the standard and therefore increases and thereby also reduce the TO spacing.

The correlation coefficient between the PEF metrics and the performance measure indicate that correlations between the PEF metrics and the performance measures exist. The PEF metric c_v is related to $\tilde{\sigma}_{v_x}$. There is also a relation between the bias, B_{λ_x}, of the mean transverse wavelength compared with the theoretical wavelength and the relative mean bias, $\tilde{B}_{v_x}$, of the velocity estimates. A relation between the energy leak, E_r, and the $\tilde{\sigma}_{v_x}$ exists, but the relation between E_r and $\tilde{E}_{\mathrm{RMS}_{v_x}}$ is not as clear.

5.9 Conclusion and perspectives

The simulation and measurement results demonstrate that the TO method is suitable for use in conjunction with a phased array transducer, and that 2D vector velocity estimation is possible down to a depth of 15 cm.

Suitable TO fields can be obtained using a phased array transducer. And in general, a lot can be learned by investigating and optimizing the TO fields prior to performing velocity simulations. The squared correlation value for three pairs of measures relating the performance of TO fields with the performance of the velocity estimates ranged from 0.79 to 0.92. In other words, the PEF metrics can be used as an initial assessment of the expected estimator performance. The benefit is, that PEF metrics can be readily computed opposed to the simulated velocity data and the derived performance measures.

Various parameters have been investigated in a simulation study around a reference point at 10 cm's depth, where the relative mean bias, $\tilde{B}_{v_x}$, was estimated to 7.8% and the relative mean standard deviation, $\tilde{\sigma}_{v_x}$, was estimated to 3.8% with echo cancelling. At a depth of 15 cm, it was possible to estimate the lateral velocity in the simulations using echo cancelling with $\tilde{B}_{v_x}$ and $\tilde{\sigma}_{v_x}$ being 8.5% and 10%, respectively.

The flow-rig measurements resulted in $\tilde{\sigma}_{v_x}$ equal to 8.3% and $\tilde{B}_{v_x}$ equal to 11% at a depth of 9.5 cm with 32 shots per estimate. At the center of the vessel, the velocity magnitude was estimated to be $0.247 \pm 0.023\,\mathrm{m/s}$ compared with an expected peak velocity magnitude of 0.252 m/s and the beam-to-flow angle was calculated to be $89.3° \pm 0.77°$ compared with an expected value between 89° and 90°. For steering angles up to ± 20°, $\tilde{\sigma}_{v_x}$ was below 20%. Hence, the measurement and the simulation results are comparable. The results also showed, that a 64 element transducer implementation is feasible, but with a poorer performance compared with a 128 element transducer.

Overall, the estimator is robust with values of $\tilde{\sigma}_{v_x}$ less than 10% for most parameter settings.

Perspectives

This chapter has demonstrated that a phased array implementation of the TO method is feasible. This was demonstrated through simulations and experimental measurements using the experimental scanner SARUS. The results warrant further investigation, and a test implementation on a commercial platform. This has been the aim of the Master's thesis *"Vector Velocity Imaging using a Commercial Scanner - Implementation of the Transverse Oscillation Method using a Phased Array Transducer"* by Marcher [145], where the author of this thesis was co-supervisor. Furthermore, an abstract based on that work has been accepted for the IEEE 2012 International Ultrasonics Symposium [146]. The prospective clinical application is for cardiac imaging, and vector flow imaging of the heart has the potential to markedly improve diagnosis based on the hemodynamic investigations.

This chapter also introduced three performance measures based on the TO spectrum that are correlated with the performance of the velocity estimates has been proposed. This will speed up the future optimizing of the method as one or more of these measures can be used to optimize the method. Furthermore, it was proposed that the mean transverse wavelength, $\bar{\lambda}_x$, should be used instead of the theoretical value to reduce the bias. This should be investigated as a first step to reduce the bias.

Additionally, the implementation of the TO method on a phased array transducer is a first step to developed a method that estimates 3D velocities based on a transverse oscillation approach and employing a 2D phased array transducer.

6

A TO method for 3D vector velocity estimation

Summary *The blood flow in the human body moves in complex patterns, and the velocities are essentially three-dimensional. None of the existing 3D velocity estimation techniques have been adopted by commercial manufactures, nor have they demonstrated convincing clinical results. Therefore, there is still a need for a real-time implementable method that estimates the 3D velocity components simultaneously. A 3D method based on the Transverse Oscillating approach is suggested. The method decouples the three velocity components and estimates them simultaneously. Based on simulations, a proof of concept is provided. The results obtained in that study are biased, and therefore, an approach to reduce the bias is presented. The effect of this is demonstrated. Additionally, a range of parameters and their effect on the 3D TO velocity estimator are investigated. In conclusion, the simulated results demonstrate that the 3D TO method estimates the full 3D velocity vectors.*

6.1 Purpose

The purpose of this chapter is to present a method for estimating 3D velocities using a Transverse Oscillation approach and to demonstrate the feasibility of the method. The method should be implementable in real-time. The chapter is composed upon Paper IV and V. Additionally, the methodology and the proof of concept study presented in this chapter were part of a confidential document written by the author. That document founded the basis for the patent application mentioned in Section 1.3.3.

6.2 Background and motivation

As pointed out in Chapter 2, the velocity vector is three-dimensional and the blood flow exhibits complex flow patterns. Additionally, the difficulty to determine the flow angle [3, 4] and compensate for it underlines the need for methods that can estimate the three-dimensional (3D) velocity vector and provide 3D vector flow images. The 3D Transverse Oscillation (TO) method estimates the two transverse velocity components based on two double-oscillating fields and spatial quadrature sampling. With the 3D TO method, the velocity estimation is decoupled into the three velocity components obtained simultaneously. The feasibility of the method is demonstrated in a simulation study. Further results are presented including an approach to optimize the method and results from a parameter study. It is also illustrated that the method is implementable on modern scanners. The physical requirements are limited to a 2D matrix array transducer, and the number of calculations needed are within the capability of modern scanners making a real-time implementation possible.

The presented method is based on the same principle as the Transverse Oscillation (TO) method suggested by Jensen and Munk [20], which was described in Chapter 3. The method also draws on the work presented in the previous chapter regarding a phased array implementation of the TO method. Furthermore, the relation between the performance of the TO fields and the performance of the velocity estimation also presented in the previous chapter is used to optimize the 3D TO method.

Other approaches have been suggested to estimate the 3D velocity vector. They were described in Chapter 2. All of those methods still have to demonstrate their clinical and commercial applicability for 3D vector flow imaging. Hence, there is still a need for a method implementable for real-time 3D velocity estimating including 3D vector flow imaging. Furthermore, it is important to develop a method that is able to estimate the 3D velocity components independently and simultaneously, as the blood velocities vary spatially and temporally on short time scales.

Structure of the chapter

The objectives highlighted in the following section are achieved by, firstly, introducing the 3D Transverse Oscillation method in Section 6.4. Secondly, a proof of concept is demonstrated in Section 6.5, and an approach to optimize the method is employed in Section 6.6. The simulation results and the discussion of the parameter study can be found in Section 6.7, and the conclusions are stated in Section 6.8.

6.3 Research hypotheses

The main hypothesis underlying the scientific contribution presented in this chapter is:

- The 3D TO method is able to simultaneously estimate the full 3D velocity vectors.

This is investigated by means of simulations. The obtained results are investigated by means of the following hypotheses:

1. The velocity estimation can be decoupled into v_x, v_y, and v_z.
2. The three velocity components can be obtained simultaneously.
3. The 3D TO method can be implemented in real-time on a commercial scanner.
4. A simple plug-flow example can demonstrate the proof of concept.
5. The 3D TO method can be optimized to reduce the bias
6. A parameter study will reveal what parameters affect the method.

6.4 The 3D Transverse Oscillation method

The following describes the concept, the beamforming approach, and the velocity estimation of 3D velocity vectors using a Transverse Oscillation approach.

6.4.1 The concept

In the 3D case, the concept is to create two double oscillating fields perpendicular to each other. By employing special receive apodizations, the synthesized fields should oscillate only in one direction. This is illustrated in Figure 6.1, where transverse oscillations are present only in the transverse (x-direction) when beamforming the two TO lines in transverse ZX plane, whereas there are no oscillations in the elevation direction. The opposite (not shown) holds for the two TO lines beamformed in the elevation ZY plane.

Furthermore, it is assumed that the velocity estimation can be decoupled into estimating three independent velocity components: The axial, $v_{z'}$, the transverse, $v_{x'}$, and the elevation, $v_{y'}$, velocity component. The three

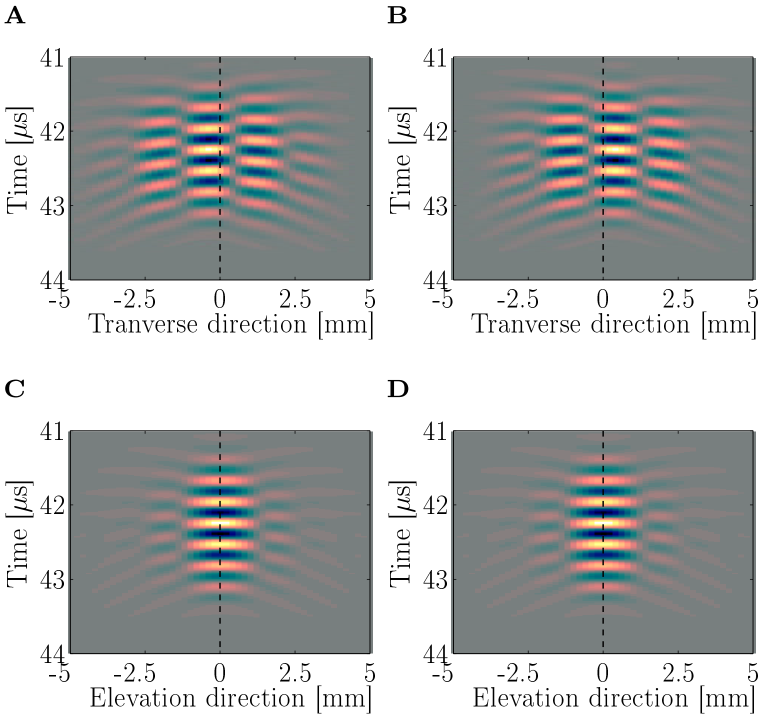

Figure 6.1 Transverse oscillating PEFs simulated at a depth of 30 mm across 10 mm in either the transverse direction (**A** and **B**) or the elevation direction (**C** and **D**). **A** and **C** are for the left beam in the transverse (ZX) plane and **B** and **D** are for right beam in the transverse (ZX) plane. Transverse oscillations are present only in the transverse direction, and the oscillations for the left and right beams in the transverse direction are shifted by 1/4 of a spatial transverse wavelength. In the elevation direction, there are no oscillations for the left and the right beams in the ZX plane. This example illustrates that the transverse fields in the ZX plane oscillate only in the transverse direction and not in the elevation direction. There is a 90° spatial phase shift between the TO fields in the transverse directions, and none in the elevation direction. The opposite is the case for the two TO beams in the ZY plane, where the TO fields oscillate only in the elevation direction and not in the transverse direction (not shown).

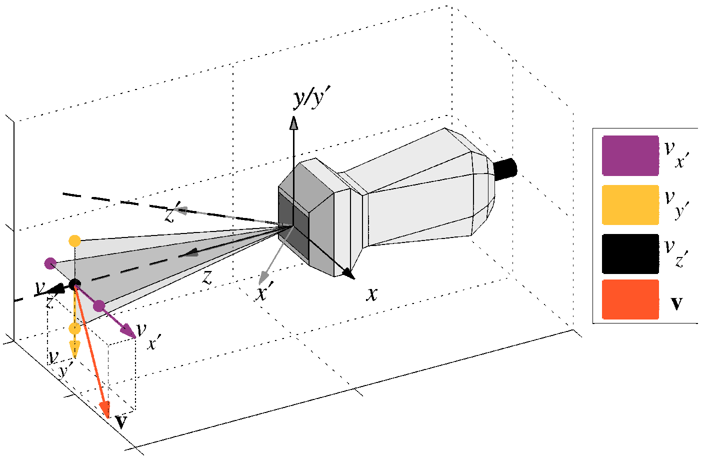

Figure 6.2 Beamforming approach for 3D velocity estimation using a 2D matrix phased array transducer. The estimation of the 3D velocity vector is decoupled into three components orthogonal to each other. The coordinate system of the transducer is (x,y,z), and the sampling coordinate system along the direction of the steered beam is (x',y',z'). The dashed lines indicate two different steered beam lines: One coinciding with the z-axis and the other is steered in the ZX plane with an angle θ_{zx}. Spheres indicate beamformed samples at a given depth: A center line is beamformed for conventional axial velocity $v_{z'}$ estimation, and two pairwise TO lines are beamformed for estimation of the transverse and elevation velocities $v_{x'}$ and $v_{y'}$. They are pairwise steered at specific fixed angles, $\theta_{TO_{zx}}$ and $\theta_{TO_{zy}}$, such that the spacing is a quarter spatial wavelength at every sample depth. For illustration purposes, $\theta_{TO_{zx}}$ and $\theta_{TO_{zy}}$ have been exaggerated. For a 64x64 transducer, they are 0.6° with respect to the z-axis. The gray shaded areas illustrate the $Z'X'$- and $Z'Y'$ planes here coinciding with the ZX-, and the ZY planes.

estimated velocity components can be obtained, so that they are orthogonal in a primed coordinate system (x',y',z'), which depends on the direction of the steered beam. If the steered beam z'-axis coincides with the z-axis, $v_{x'}$, $v_{y'}$, and $v_{z'}$ are equal to v_x, v_y, and v_z, respectively. This is illustrated in Figure 6.2 where the sampled signals for the estimation of v_x, v_y and v_z are orthogonal, and where the axial velocity, v_z, is along the beam axis.

The estimation of the transverse velocity, v_x, was described in the previous chapter along with the transverse wavelength, yet, the latter is stated again below for the sake of completeness. With the 3D TO method, the velocity component in the elevation direction, v_y, is obtained by creating an oscillation in the elevation direction perpendicular to the ultrasound beam. The transverse and elevation wavelengths are given by

$$\lambda_x(z) = 2\lambda_z \frac{z}{d_x \cos\theta_{zx}} \tag{6.1a}$$

$$\lambda_y(z) = 2\lambda_z \frac{z}{d_y \cos\theta_{zy}}, \tag{6.1b}$$

where z is the axial depth, d_x and d_y are the distances between the apodization peaks in the x- and the y-direction of the transducer, and the $\cos\theta_{zx}$- and $\cos\theta_{zy}$-terms account for the steering angles in the transverse and the elevation plane, respectively. This can be obtained using a 2D phased array. Essentially, the process of estimating v_y is the same as for v_x, except for a rotation of the steered beams and the receiving aperture of 90° in the transducers XY plane.

6.4.2 Beamforming in 3D

The beamforming approach is illustrated in Figure 6.2. For each sample depth, five samples are beamformed. One along the center axis for conventional axial estimation r_c, and two pairs of the left and right TO samples for spatial IQ in both transverse, r_{left_x} and r_{right_x}, and elevation, r_{left_y} and r_{right_y}, direction. These signals can be combined to

$$\begin{aligned} r_{\text{sq}_x}(i) &= r_{\text{left}_x}(i) + j r_{\text{right}_x}(i) \\ r_{\text{sq}_y}(i) &= r_{\text{left}_y}(i) + j r_{\text{right}_y}(i), \end{aligned}$$

where i is the pulse number of N_i emissions. Taking the temporal Hilbert transform or sampling temporal IQ data directly, one obtains

$$\begin{aligned} r_{\text{sqh}_x}(i) &= \mathcal{H}\{r_{\text{sq}_x}(i)\} \\ r_{\text{sqh}_y}(i) &= \mathcal{H}\{r_{\text{sq}_y}(i)\}. \end{aligned}$$

To create one flow line with the 3D velocity vectors along it, five lines are beamformed per emission as illustrated in Figure 6.2. A center line along the beam axis is beamformed for use in estimating the axial velocity, $v_{z'}$, and two TO lines are beamformed in the $Z'X'$ plane for estimation of the transverse velocity, $v_{x'}$. These are the same as for the 2D case using a 1D transducer. In the 3D case, two additional TO lines are beamformed. They are steered in the $Z'Y'$ plane for the estimation of the elevation velocity $v_{y'}$. The velocity vector estimation is, thus, decoupled into these three components, as illustrated in Figures 6.1 and 6.2.

In transmit, the emitted ultrasound pulse may be focused, a plane wave, or unfocused, but it is crucial that the beam is broad enough to cover all lines and the two transverse oscillating fields. On the receive side, the five lines are beamformed dynamically in parallel. The center line is in the direction of the transmitted beam axis. The pairwise TO beams are beamformed, so that they are spaced a quarter of the respective lateral spatial wavelength apart. Thereby, spatial IQ pairs can be obtained in both the transverse and the elevation directions. In the transverse (azimuth) plane, this distance is determined by (6.1a), and in the elevation plane by (6.1b).

The width of the 2D transducer limits the use of an expanding aperture to keep λ_x and λ_y constant. This was addressed in the previous chapter in the 2D case by beamforming the TO lines radially, so that at each depth, the distance between the pair of TO lines is equal to a quarter spatial wavelength at each depth. The same approach is employed in the 3D case. The angle, θ_{TO}, between the two TO lines in the transverse direction was stated in the previous chapter. For the 3D case, the two pairs of TO lines have the following TO angles

$$\theta_{TO_{zx}} = 2\arctan\frac{\lambda_x/8}{z_0} = 2\arctan\frac{\lambda_z}{4d_x\cos\theta_{zx}} \tag{6.2a}$$

$$\theta_{TO_{zx}} = 2\arctan\frac{\lambda_y/8}{z_0} = 2\arctan\frac{\lambda_z}{4d_y\cos\theta_{zy}}. \tag{6.2b}$$

Thus, instead of beamforming the TO lines with a fixed lateral distance over depth, they diverge with a fixed angle.

The receive apodization for the TO lines will typically be two peaks with a given width, and a given spacing, d_x or d_y. The two pairs of TO lines are beamformed orthogonal to each other, and therefore, the required apodization functions are merely the same except for a rotation of 90°.

All five lines are beamformed in parallel in receive based on the same transmission, so only five beamformers in receive are required. However, the method may be expanded to beamform several flow lines in parallel.

As the lines are beamformed in parallel, the three velocity components are estimated simultaneously.

6.4.3 Velocity estimation

The estimation of the transverse and elevation velocity components, $v_{x'}$ and $v_{y'}$, follows the one presented by Jensen [107] which was described in Section 3.6. The velocity estimation is the same for $v_{x'}$ and $v_{y'}$, each based on one pair of the four TO lines. Based on the spatial quadrature, $r_{\mathrm{sq}}(i)$, and temporal quadrature, $r_{\mathrm{sqh}}(i)$, signals in the ZX plane obtained at a specific depth, two new signals, $r_1(i)$ and $r_2(i)$, can be generated. Similarly, two new signals in the ZY plane $r_3(i)$ and $r_4(i)$ are generated. The four new signals are given by

$$\begin{aligned}
r_1(i) &= r_{\mathrm{sq_x}}(i) + j r_{\mathrm{sqh_x}}(i) = \exp(j2\pi i T_{\mathrm{prf}}(f_{x'} + f_p)) \\
r_2(i) &= r_{\mathrm{sq_x}}(i) - j r_{\mathrm{sqh_x}}(i) = \exp(j2\pi i T_{\mathrm{prf}}(f_{x'} - f_p)) \\
r_3(i) &= r_{\mathrm{sq_y}}(i) + j r_{\mathrm{sqh_y}}(i) = \exp(j2\pi i T_{\mathrm{prf}}(f_{y'} + f_p)) \\
r_4(i) &= r_{\mathrm{sq_y}}(i) - j r_{\mathrm{sqh_y}}(i) = \exp(j2\pi i T_{\mathrm{prf}}(f_{y'} - f_p)),
\end{aligned}$$

where $f_{y'}$ is due to the spatial elevation modulation. The transverse, $v_{x'}$, and the elevation velocity, $v_{y'}$, are then calculated by

$$\begin{aligned}
v_{x'} =& \frac{\lambda_x}{2\pi 2k T_{\mathrm{prf}}} \times \\
& \arctan\left(\frac{\Im\{R_1(k)\}\Re\{R_2(k)\} + \Im\{R_2(k)\}\Re\{R_1(k)\}}{\Re\{R_1(k)\}\Re\{R_2(k)\} - \Im\{R_1(k)\}\Im\{R_2(k)\}}\right) \qquad (6.3a) \\
v_{y'} =& \frac{\lambda_y}{2\pi 2k T_{\mathrm{prf}}} \times \\
& \arctan\left(\frac{\Im\{R_3(k)\}\Re\{R_4(k)\} + \Im\{R_4(k)\}\Re\{R_3(k)\}}{\Re\{R_3(k)\}\Re\{R_4(k)\} - \Im\{R_3(k)\}\Im\{R_4(k)\}}\right), \qquad (6.3b)
\end{aligned}$$

where $R_l(k)$ is the complex lag k autocorrelation value of $r_l(k)$ for $l = 1, \ldots, 4$. The complex autocorrelation is estimated over N_i emissions. RF averaging is performed by averaging the autocorrelation estimate over the length of the excitation pulse [35, 107]. Both λ_x and λ_y can be calculated theoretically using (6.1a) and (6.1b) based on the given sampling depth, z. Bias compensation may be performed by substituting λ_x and λ_y with for instance the mean lateral wavelengths, $\bar{\lambda}_x$ and $\bar{\lambda}_y$, which can be estimated based on simulations or measurements as described in the previous chapter.

As an alternative to the method described above, a heterodyning demodulation approach as suggested by Anderson [147] can be applied. In that case, the following signals are formed

$$
\begin{aligned}
r_{12}(i) &= r_1(i) \times r_2(i) = \exp(j2\pi i T_{\text{prf}} 2 f_{x'}) \\
r_{12^*}(i) &= r_1(i) \times r_2^*(i) = \exp(j2\pi i T_{\text{prf}} 2 f_p) \\
r_{34}(i) &= r_3(i) \times r_4(i) = \exp(j2\pi i T_{\text{prf}} 2 f_{y'}) \\
r_{34^*}(i) &= r_3(i) \times r_4^*(i) = \exp(j2\pi i T_{\text{prf}} 2 f_p).
\end{aligned}
$$

In stead of calculating the phase change in the complex signals over time directly [147], an autocorrelation approach [30] with RF averaging [35] is applied to estimate the phase change. The estimation of the transverse and elevation velocity components then become

$$v_{x',\text{het}} = \frac{\lambda_x}{2\pi 2 k T_{\text{prf}}} \arctan\left(\frac{\Im\{R_{12}(k)\}}{\Re\{R_{12}(k)\}}\right) \tag{6.4a}$$

$$v_{y',\text{het}} = \frac{\lambda_x}{2\pi 2 k T_{\text{prf}}} \arctan\left(\frac{\Im\{R_{34}(k)\}}{\Re\{R_{34}(k)\}}\right), \tag{6.4b}$$

where $R_{12}(k)$ and $R_{34}(k)$ are the complex lag k autocorrelation values of $r_{12}(k)$ and $r_{34}(k)$, respectively. Because this approach multiplies the generated signals $r_1(k)$ and $r_2(k)$ directly prior to the autocorrelation, it is suspected that this approach will be more susceptible to noise compared to the TO approach, which estimates the autocorrelations first, prior to the pairwise multiplication of the autocorrelation values.

The axial velocity component is calculated using an autocorrelation estimator [30] with RF averaging [35] as

$$v_{z'} = -\frac{\lambda_z}{2\pi 2 k T_{\text{prf}}} \arctan\left(\frac{\Im\{R_c(k)\}}{\Re\{R_c(k)\}}\right),$$

where $R_c(k)$ is the autocorrelation of the center line at lag k.

Because the velocity estimations are based on autocorrelation approaches, the aliasing limits of the axial, transverse, and elevation velocity components are

$$
\begin{aligned}
v_{z',\max} &= \frac{1}{4} \frac{\lambda_z}{k T_{\text{prf}}} \\
v_{x',\max} &= \frac{1}{4} \frac{\lambda_x}{k T_{\text{prf}}} \\
v_{y',\max} &= \frac{1}{4} \frac{\lambda_y}{k T_{\text{prf}}}.
\end{aligned}
$$

6.4.4 Number of operations

The number of operations needed (both additions and multiplications) for the 3D velocity estimation is calculated in the following. The calculation assumes that the temporal quadrature data have already been obtained either by IQ sampling or by means of the Hilbert transform.

Per set of four samples used for estimating $v_{x'}$ and $v_{y'}$, the following number of operations are required

$$N_{c,\mathrm{TO}} = 2 \cdot \left(2 \cdot (10 + 1 + 2) + \frac{7}{N_i}\right),$$

where the first 2 is for v_x and v_y, the second 2 is for two autocorrelation functions per velocity component, 10 is the number of operations to calculate one autocorrelation value in $R_i(1)$, the +1 for summing the autocorrelation values, and the +2 is for the adding the latest value and subtracting the oldest in the RF averaging. For every N_i emissions, the final velocity calculation as described in (6.3a) is performed. This requires additional five multiplications, two additions and one arctan look-up.

The required floating point operations per second (flops) can be calculated as

$$f_{\mathrm{flops,TO}} = N_{c,\mathrm{TO}} \cdot f_s \cdot p_v,$$

where p_v is fraction of time used for velocity estimation. Assuming N_i is 16, the sampling frequency is 15 MHz, and 80 % of the time is used for flow estimation, the required flops for estimating v_x and v_y are

$$f_{\mathrm{flops,TO}} \approx 53 \cdot 15\,\mathrm{MHz} \cdot 0.8 = 0.64\,\mathrm{Gflops}.$$

The amount of floating point operations per seconds is within the capabilities of standard CPUs, whose capabilities are at least 1 Gflops.

For comparison, the number of calculations needed by the conventional axial velocity estimator is

$$N_{c,\mathrm{conv}} = (6 + 1 + 2) + \frac{1}{N_i}.$$

Consequently, the flops for the autocorrelation estimator in the given examples are

$$f_{\mathrm{flops,conv}} \approx 9 \cdot 15\,\mathrm{MHz} \cdot 0.8 = 0.11\,\mathrm{Gflops}.$$

As it can be observed, the number of calculations required for the two transverse velocities is approximately a factor of 6 larger than for the conventional estimator. For a realistic example, the combined flops required for estimating v_x, v_y, and v_z are 0.75 Gflops. This is less than 1 Gflops, which is a lower limit of the capabilities of standard CPUs today. Based on the above, it is concluded that the 3D TO method is suitable for a real-time implementation on a modern scanner.

6.5 Proof of concept study

This section presents results from the initial proof of concept simulations. First the simulation setup is presented, followed by the results and the discussion.

6.5.1 Simulation setup

The simulations were performed using Field II. The simulation setup is outlined in Table 6.1. To obtain temporal IQ data, the Hilbert transform was used to create the analytical signal. The velocities were estimated based on 32 emissions, and for each flow angle the simulations were repeated 10 times. No bias compensation was performed in the velocity estimations.

A 64x64 elements 2D phased array is emulated, however, only 1024 active channels are used. A second transducer is emulated with 32x32 elements, but otherwise with the same characteristics.

In transmit, only the center 32x32 elements of the 64x64 transducer is used, i.e. 1024 active channels. The focal point is set to 25 mm, whereas the point of interest is at 15 mm. For the 32x32 transducer, the transmit apodization is identical to the center 32x32 elements of the 64x64 transducer, whereas the focus point is moved to 100 mm to increase the beam width at 15 mm. The transmit apodizations are illustrated in Figure 6.3A and C. For receive, also only 1024 active channels are used. To increase the spatial transverse wavelength, the apodization peaks are placed as far as part as possible. This gives the transducer apodizations as demonstrated in Figure 6.3B and D. The receive apodizations are for the two lines in the ZX plane used for estimating v_x. The apodizations for the ZY plane are merely a 90° rotation as described above.

6.5.2 Results and discussion

The center of the plug flow phantom was placed at $(x, y, z) = (0{,}0{,}15)$ mm. Only velocities in the XY plane were simulated, hence, the results from the estimation of the axial velocity are not shown. The estimated velocities for flow in the x-direction (ϕ_{xy} equal to 0°) and y-direction (ϕ_{xy} equal 90°) for the 64x64 transducer are shown in Figure 6.5. The true velocities are $(v_x,v_y) = (1{,}0)$ m/s and $(v_x,v_y) = (0{,}1)$ m/s for the two flow directions, respectively. The figure demonstrates the agreement between the theoretical profiles and the obtained velocity estimates, v_x and v_y, from the simulations at both flow angles. At 15 mm, v_x was 0.97 ± 0.026 m/s and v_y was 0.011 ± 0.061 m/s for flow in the x-direction ($\phi_{xy} = 0°$). For flow in the y-direction where ϕ_{xy} is 90°, v_x was 0.029 ± 0.065 m/s and v_y was 0.98 ± 0.038 m/s.

Table 6.1 Simulation setup for proof of concept study.

Parameter	**Value**
Transducer	
Transducer type	2D phased array
Layout [elements]	64x64 or 32x32
Center frequency [Mhz]	3
Impulse response	3 cycle sinusoid (Hanning windowed)
Pitch	$\lambda/2$
Kerf	$\lambda/100$
System	
Sampling frequency [MHz]	120
Speed of sound [m/s]	1480
No. of active channels	1024
Emitted pulse	
Center frequency [MHz]	3
No. of cycles	8
Windowing of emitted pulse	Tukey
Ratio of taper for window	0.75
Focal depth [mm]	25 or 100
Flow settings	
Flow phantom [mm x mm x mm]	10x10x10
Flow type	Plug flow
Flow speed [m/s]	1
Flow position (center) [mm]	$(x, y, z) = (0, 0, 15)$
Flow angle ϕ_{xy} [deg]	0 15 30 45 60 75 90
Beam-to-flow angle ϕ_{zx} [deg]	90
Beam-to-flow angle ϕ_{zy} [deg]	90
Post processing	
Stationary echo cancelling (clutter filtering)	None
Matched filter	Time-reversed excitation pulse
SNR	∞
Velocity estimator	
Shots per estimate	32

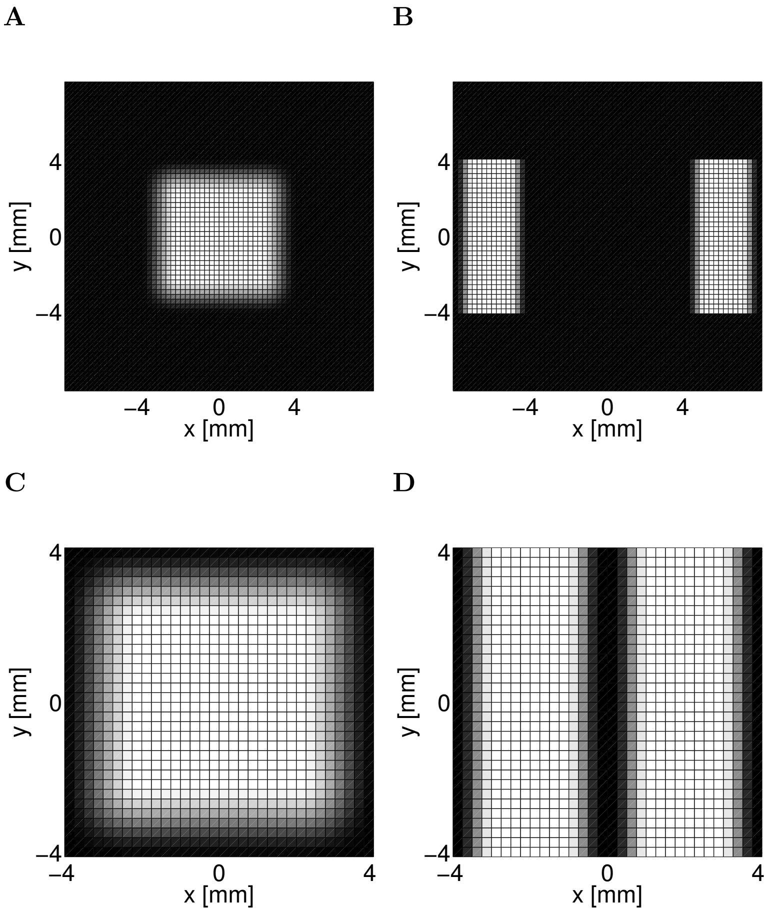

Figure 6.3 Apodization functions in transmit (**A** and **C**) and receive (**B** and **C**) for the 64x64 (**A** and **B**) and 32x32 (**C** and **D**) apertures (beams in ZX plane). Colorbar: Black→white = 0→1. Each small square represents an element. For all four apertures, 1024 active channels are used. The transmit apodizations are the same for each receive line, whereas the depicted receive apertures are for the estimation of v_x. The apodization functions are Tukey windows with a ratio of taper of 0.5.

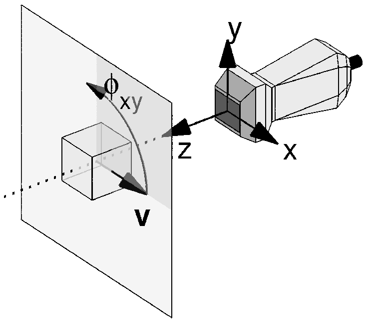

Figure 6.4 Illustration of the simulation setup for the 2D transducer. The dotted line is the scan line (here coinciding with the z-axis). The light gray shaded plane is orthogonal to the scan line. The cube represents the flow phantom and the black arrow the velocity vector $\mathbf{v}$. In the simulations, the cube is rotated around the z-axis at different angles, $\phi_{xy} = \theta_{xy}$, within the darker shaded quadrant.

Table 6.2 Overall performance of the estimator at the center of the vessel for the proof of concept study.

Metric	64x64	32x32
Mean $\lvert\mathbf{v}\rvert$ [m/s]	0.97± 0.047	0.94± 0.11
Mean $B_{\hat{\phi}}$ [deg]	-0.73±3.3	-0.48±7.7

The flow angle in the XY plane, ϕ_{xy}, was varied from 0° to 90° in steps of 15°. The velocity components v_x and v_y at depth 15 mm were estimated for each angle, and the mean and the standard deviation of the transverse velocity components were calculated. The results for the seven different angles are shown in Figure 6.6 for the 64x64 and the 32x32 transducer, respectively.

The average performance for all 70 estimates at 15 mm depth is shown in Table 6.2 for the two transducers. Listed are the mean speed, $|\mathbf{v}|$, and the standard deviation of all speeds as well as the mean estimated angle bias, $B_{\hat{\phi}}$, between the true angles and the estimated flow angles, which are estimated by

$$\hat{\phi}_{xy} = \arctan \frac{v_y}{v_x}. \tag{6.5}$$

From the results it can be observed, that the bias and the standard deviation is higher when using the 32x32 compared with the 64x64 transducer.

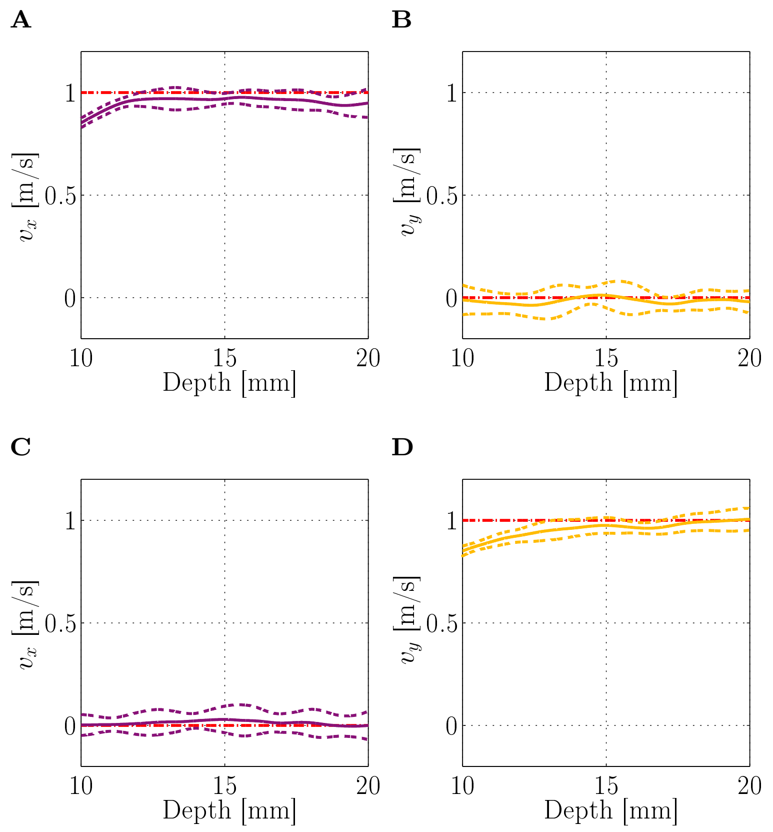

Figure 6.5 Velocity estimates of v_x and v_y for flow in the XY plane orthogonal to the ultrasound beam. The results are for the 64x64 transducer. Dot-dashed lines indicate true velocity, solid lines the mean of 10 profiles, and dashed lines one standard deviation. In **A** and **B** ϕ_{xy} is 0°, and ϕ_{xy} is 90° for **C** and **D**.

This is expected, because d is smaller for the 32x32 transducer compared with the 64x64 transducer, and hence, the transverse wavelength is larger for the 32x32 transducer than for the 64x64 transducer. Consequently, the velocity range is larger for the 32x32 transducer compared with the 64x64 transducer. And as the velocity and the pulse repetition frequency, $f_{\text{prf}} = 1/T_{\text{prf}}$, are the same in the two cases, the velocity estimates for the 32x32 transducer will have higher standard deviations compared with the 64x64 transducer. In addition, the separation between the peaks is smaller for the 32x32 transducer compared with the 64x64 transducer, which results in a poorer defined TO field which affects both bias and standard deviation. This also indicates that the TO field should be optimized for a given setup.

The 2D temporal and spatial Fourier domain is calculated based on the

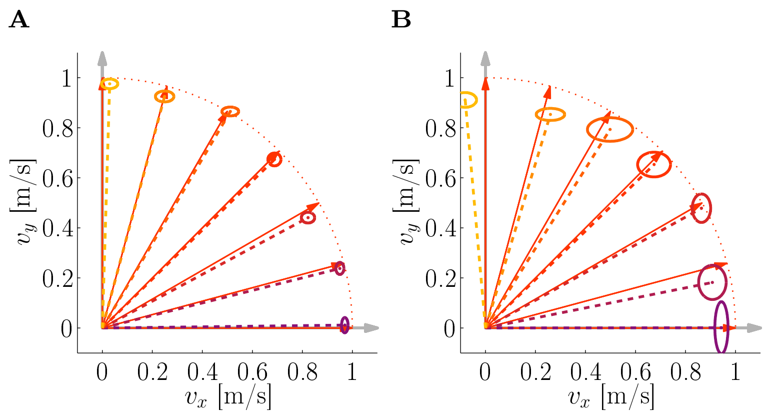

Figure 6.6 Velocity estimates for flow in the XY plane orthogonal to the ultrasound beam as a function of flow angle ϕ_{xy}. **A** is for the 64x64 transducer and **B** for the 32x32 transducer. Thin solid arrows indicate the true simulated velocities, dashed lines the estimated velocity vectors, and the ellipses (solid) the standard deviations for v_x and v_y, respectively.

complex combined TO field obtained when the left beam is the real part, and the right is the imaginary part. The theoretical lateral spatial frequency is 0.85 mm^{-1}, whereas the mean frequency is 0.80 mm^{-1}. This gives a bias of -6 % between the theoretical and the mean of the simulated spatial frequencies. For the 32x32 transducer, the values are 3.4 and 4.2 mm^{-1} for the mean and theoretical spatial frequencies, respectively. The bias is -20%. This demonstrates, that to reduce the bias, it is necessary to optimize the TO fields and the velocity estimation.

The results shown in Figures 6.5 and 6.6 demonstrate that the 3D TO method can estimate v_x and v_y, and that the estimation is decoupled. The relative bias is -3 % and -6 %, respectively, and the relative standard deviation is 5 % and 11 % for the 64x64 and the 32x32 transducer, respectively. The estimated angle is practically unbiased, and the relative standard deviation of the angle is 1 % and 2 %, respectively. However, the bias of the velocity estimates should be reduced. Nonetheless, the results serve as proof of concept.

6.6 Optimizing the method

A part of optimizing the TO method is to ensure a good agreement between the transverse wavelength, λ_x, used when beamforming the TO lines and the resulting $\bar{\lambda}_x$ in the combined TO field. This section presents and discusses results that illustrate how the bias arising from the mismatch between λ_x and $\bar{\lambda}_x$ can be eliminated.

6.6.1 Investigation of the TO spectrum

Based on the 32x32 transducer and the default parameters given in the Section 6.7.1, the PEFs are simulated with a range of λ_x. Based on the combined TO spectrum, the resulting $\bar{\lambda}_x$ and the corresponding bias between the theoretical and the estimated mean wavelength is calculated using (5.4) and (5.11), respectively. Furthermore, the coefficient of variation, c_v, is calculated based on (5.10), and the energy ratio, E_r, is computed using (5.12).

The effect of varying λ_x in the beamforming stage on $\bar{\lambda}_x$ is displayed in Figure 6.7A. The transverse wavelength is used when calculating $\theta_{TO_{zx}}$ with (5.2). The theoretically calculated λ_x is 3.38 mm for the given parameters. The optimal point where the input λ_x equals the output $\bar{\lambda}_x$ occurs at a transverse wavelength of 3.71 mm. It can also be noted that the shape of the mean transverse wavelength as a function of the transverse wavelength in the beamforming is a flat parabola. The minimum value of $\bar{\lambda}_x$ based on the TO spectrum is 3.69 mm. This value is obtained when a value of λ_x of 3.38 mm is used in the beamforming stage.

Figure 6.7B shows B_{λ_x} corresponding to the wavelengths shown in Figure 6.7A. Consequently, the optimal point where the bias is 0 is at λ_x=3.71 mm. B_{λ_x} is -8.35 % at the theoretical value of λ_x.

The energy ratio of the energy in the left versus the right of the TO spectrum is shown in part Figure 6.7C. The lower the value the better. At the theoretical λ_x, E_r is -16.1 dB, and at the optimal point E_r is -16.4 dB for λ_x equal to 3.56 mm.

In Figure 6.7D c_v is shown. The optimal point is at 3.47 mm with a value of 52.4 %. For the theoretical value of λ_x, c_v is 52.7 %.

The above results demonstrate that the optimal value for λ_x in the beamforming in terms of bias is 3.71 mm, whereas when considering c_v and E_r the value is a little lower. The results also demonstrate, that there is little difference when operating around the optimal point. So it is not crucial that λ_x in the beamforming stage is exactly the same as $\bar{\lambda}_x$. However, the estimated $\bar{\lambda}_x$ should be used in the velocity estimation instead of the theoretical λ_x to reduce the bias. In this case this value is approximately 3.7 mm. The flat parabolic shape of $\bar{\lambda}_x$ in Figure 6.7A indicates that it is not crucial to optimize the λ_x-$\bar{\lambda}_x$-relation in this case, but it suffices to estimate

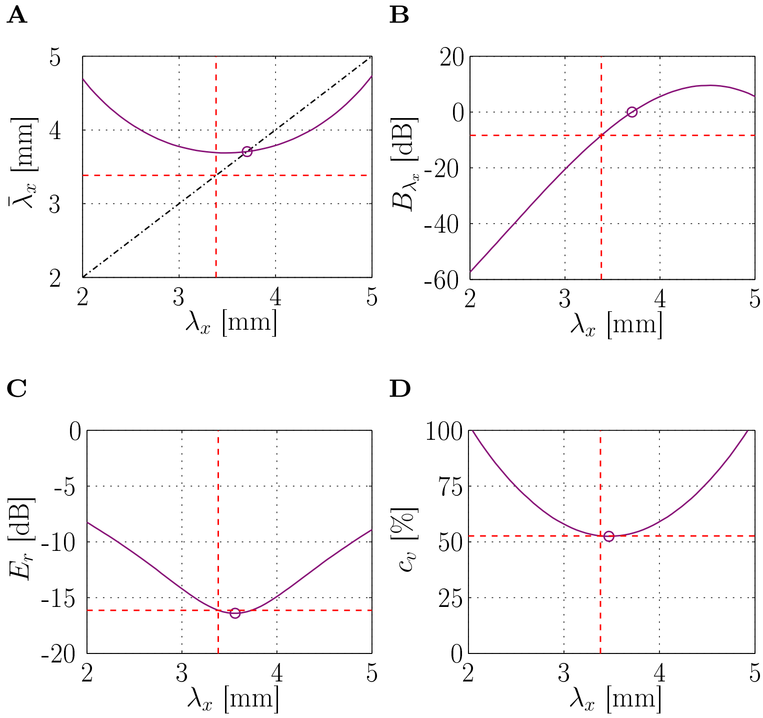

Figure 6.7 Illustration of the effect of varying the transverse wavelength in the beamforming stage on the TO spectrum. Solid lines indicate the input/output relation, dashed lines the values for the theoretical wavelength, circles the optimal point, and the dot-dashed line indicates the output=input curve. **A** Shows the mean estimated transverse wavelength as a function of input λ_x in the beamforming of the TO lines, **B** depicts the corresponding bias between the theoretical and the mean wavelength, **C** displays E_r as a function of λ_x, and **D** shows c_v a function of λ_x.

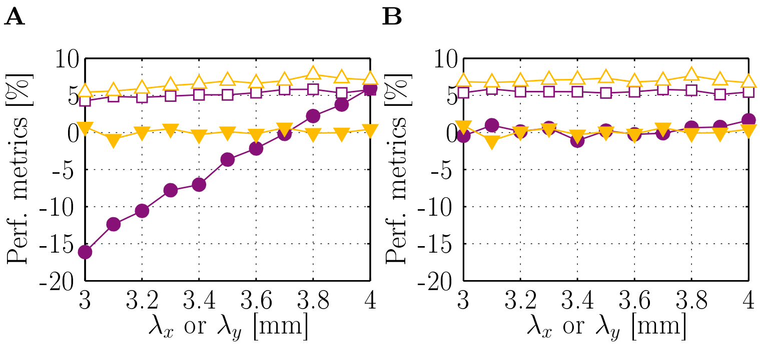

Figure 6.8 Performance metrics of the velocity estimates as a function of λ_x: The relative mean standard deviations $\tilde{\sigma}_{v_x}$ (□) and $\tilde{\sigma}_{v_y}$ (△), and the relative mean biases $\tilde{B}_{v_x}$ (●) and $\tilde{B}_{v_y}$ (▼). **A** The relative mean and standard deviation of the velocity estimates, when the transverse wavelength used in the beamforming (x-axis) is used in the velocity estimation as well. **B** The mean TO wavelengths are used in the velocity estimation. They are calculated based on the TO fields, which are simulated for the different wavelengths (x-axis) used in the beamforming stage.

$\bar{\lambda}_x$ based on TO spectrum obtained when using the theoretical λ_x in the beamforming.

6.6.2 Bias compensation of velocity estimates

The predictions based on the performance metrics are tested in a simulation of velocities using the standard parameters previously described, where the velocity is in the x-direction. In these simulations the transverse and elevation wavelengths, λ_x and λ_y, used in the beamforming are varied from 3.0 mm to 4.0 mm in steps of 0.1 mm. Afterwards, the velocity estimation is performed in two different ways. To quantify the effect of varying the velocity estimation, the relative mean bias, $\tilde{B}_{v_x}$, and the relative mean standard deviation, $\tilde{\sigma}_{v_x}$, are calculated for each set of 100 velocity profiles. No echo cancelling is used in this case.

Figure 6.8A shows the relative mean biases and standard deviations when the transverse and elevation wavelengths used in the velocity estimation are the same as the ones used for beamforming. In Figure 6.8B the mean transverse and elevation wavelengths calculated based on the TO spectrum are used in the velocity estimation. In both cases, the relative mean standard deviations, $\tilde{\sigma}_{v_x}$ and $\tilde{\sigma}_{v_y}$, are practically unaffected by varying the wavelengths, and they are approximately 5–7 % and 4–6 %, respectively. In addition, the relative mean bias $\tilde{B}_{v_y}$ is practically constant at approximately 0 % for the range of the elevation wavelengths, λ_y. Considering the relative mean bias $\tilde{B}_{v_x}$, it increases from -16 % to 6 % and is 0.001 % at 3.7 mm in Figure 6.8A. In Figure 6.8B the metric is more or less constant at values of approximately 0 %.

These results illustrate that the bias is not an offset, but rather reflects a wrong scaling factor of the velocity estimates, and that this wrong scaling factor is determined by the mismatch between the theoretically derived spatial wavelengths and the actual mean spatial wavelengths in the TO fields.

If mean stationary echo cancelling is applied prior to the velocity estimation, the trends of the results are the same as for the results presented in Figure 6.8, and therefore, the results are not shown. The differences are stated here. The relative mean standard deviation $\tilde{\sigma}_{v_x}$ is unaffected and the relative mean standard deviation $\tilde{\sigma}_{v_y}$ is 1–2 percentage points larger. In terms of the relative mean biases, $\tilde{B}_{v_y}$ is unaffected, whereas $\tilde{B}_{v_x}$ is offset with approximately 2 percentage points in all cases. However, it should be noted that simulation results presented in the previous chapter indicated that this offset was present only at beam-to-flow angles close to 90°. A main contribution to the increase in $\tilde{B}_{v_x}$ comes from the clutter filter that gives rise to edge effects, where the velocity is overestimated at the vessel boundaries.

In conclusion, it is beneficial to optimize the TO field based on one of the optimization criteria. Additionally, bias compensation should be addressed. In this case, neither E_r nor c_v were far from their optimal points when using the theoretical wavelength. This illustrates that the method is robust in terms of TO wavelengths. The velocity estimations were improved by compensating for the bias. This was achieved by substituting the theoretical TO wavelengths, λ_x and λ_y, with the mean TO wavelength, $\bar{\lambda}_x$ and $\bar{\lambda}_y$, in (6.3a) and (6.3b), respectively.

6.7 Parameter study

This section presents the simulation setup and the results from the parameter study and discusses them.

Table 6.3 Simulation setup for parameter study.

Parameter	**Value**
Transducer	
Transducer type	2D phased array
Layout [elements]	32x32
Center frequency [Mhz]	3.5
Impulse response	2 cycle sinusoid (Hanning windowed)
Pitch [mm]	0.3
Kerf	$\lambda/100$
System	
Sampling frequency [MHz]	100
Speed of sound [m/s]	1480
No. of active channels	1024
Emitted pulse	
Center frequency [MHz]	3
No. of cycles	8
Windowing of emitted pulse	Hanning
Focal depth [mm]	-
Emitted beam	Plane wave
Post processing	
Stationary echo cancelling (clutter filtering)	Mean subtraction
Matched filter	Time-reversed excitation pulse
SNR	∞
Velocity estimator	
Shots per estimate	32

6.7.1 Simulation setup

The simulation and post processing environments consist of a number of parameters. Some of these parameters are different than the ones used in the proof of concept study. The parameters are listed in Table 6.3. The variables in the parameter study are mentioned, and their respective values are listed in Table 6.4. Bold face values correspond to the reference setup. For each parameter value, 100 realizations, N_p, were performed with random scatterer initialization in terms of position and amplitude.

As default, the transmit beam was steered in the direction of the z-axis, but the steering angles, θ_{zx} and θ_{zy}, were varied in the parameter study. All 1024 channels were used for transmitting the pulse. The default was

Table 6.4 Variables in the parameter study.

Parameter	**Values**
Steering angle θ_{ZX} [deg]	**0**,5,. . . ,45
Steering angle θ_{zy} [deg]	**0**,5,. . . ,45
Transmit apodization (in 2D)	Hanning, Tukey, **Rect**
TO peak apod. (osc. direction)	Hanning, Tukey, **Rect**
TO peak apod. (non-osc. direction)	Hanning, Tukey, **Rect**
No. of elements in TO peak spacing	8,12,16,20,**24**
No. of elements in TO peak width	2,4,**8**,12,16
Flow direction ϕ_{xy} [deg]	**0**,15,. . . ,90
Flow direction ϕ_{zy} [deg]	0,15,. . . ,**90**
Flow direction ϕ_{zx} [deg]	0,15,. . . ,**90**
No. of emissions per estimate	8,16,**32**,64
SNR [dB]	-6,-3,. . . ,12,∞ (default is ∞)

an apodization of 1 for all elements (rectangular). The receive aperture for the conventional axial velocity estimation was apodized with a circular symmetrical Hamming window. The receive apodization for both pairs of TO lines were two peaks with widths of w and spaced a given distance d apart. The apodization of the TO peaks was varied in both dimensions, i.e. in the direction with oscillations (osc.) and in the direction without oscillations (non-osc.). The difference between the pair of TO lines in the x direction and the y direction was merely a 90° rotation.

As part of the parameter study, the number of emissions per estimate, and the SNR was varied. As default, an ensemble length of 32 emissions was used, and no noise was added to the simulated RF signals. When testing the effect of varying the SNR, zero mean white Gaussian noise was added to the beamformed RF data prior to the match filtration. The amplitude of the noise was varied to obtain different SNR values. The matched filtration improved the SNR by 18 dB. The SNR values after the matched filtration

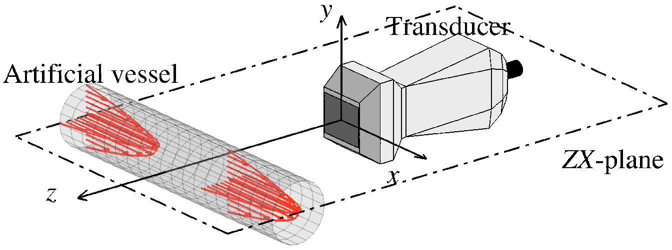

Figure 6.9 Illustration of the flow phantom emulated in the parameter study with the default parameter settings.

are listed in Table 6.4. The default value used in the simulations unless otherwise stated is ∞, i.e. no noise was added.

A 20 mm x 20 mm x 20 mm cube with a cylinder with a length l of 20 mm and a radius r of 6 mm centered inside the block—mimicking e.g. the carotid artery. The scatterers inside the cylinder were moving with a circular symmetric parabolic velocity profile as illustrated in Figure 6.9, and the scatterers outside the cylinder were stationary. The simulations were performed with a fixed peak speed $|\vec{v}_0|$ of 1 m/s, whereas the direction of the flow $\vec{v}_0/|\vec{v}_0|$ was varied by rotating the block of scatterers. The artificial vessel was located at $(x, y, z) = (0{,}0{,}30)$ mm. The steering direction and the radial depth were varied. Depending on this, the block of scatterers was rotated and translated accordingly to obtain velocity vectors orthogonal to the ultrasound beam. The plug flow phantom was used for a simple proof of concept, whereas the parabolic flow phantom was used in the parameter study.

6.7.2 Results and discussion

Firstly, examples of estimated 3D velocities at the reference point are presented. Secondly, the mean and standard devations of 3D velocity vectors obtained by varying the flow angle are visualized. Subsequently, the results of varying the parameters are investigated in terms of the relative mean bias and the relative mean standard deviation of the velocity profiles.

3D velocities at reference point

With the reference parameter values, 3200 emissions were simulated where the motion followed a circular symmetric parabolic profile. The flow direction was in the x direction with a peak velocity of 1 m/s. The steering angles were both 0°.

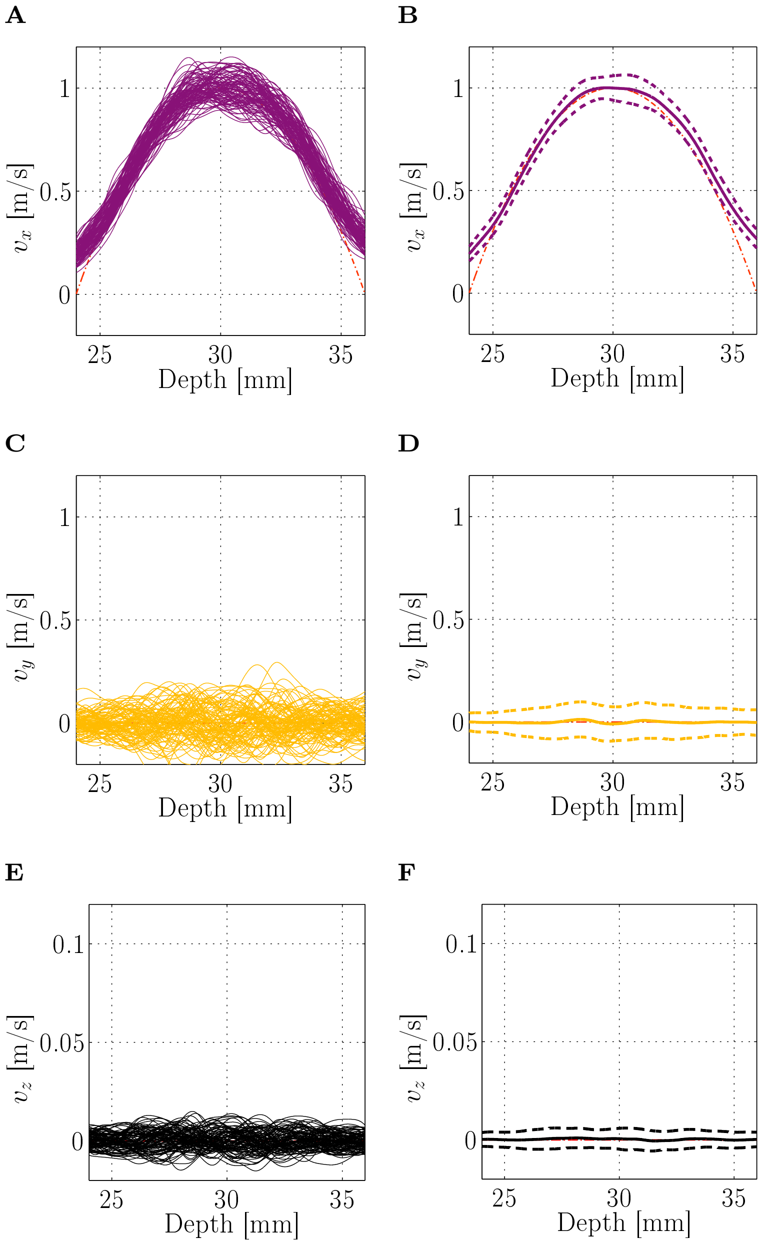

Figure 6.10 Velocity estimates of v_x, v_y, and v_z where ϕ_{xy} is 0°. Thin dot-dashed lines indicate the true velocity, thin solid lines individual estimates, thick solid lines the mean of the 100 profiles, and dashed lines one standard deviation. **A**, **C**, and **E** show 100 estimated velocity profiles. **B**, **D**, and **F** show the mean and standard deviations of the profiles. Note, that the velocity range for v_z has been reduced with a factor of 10 compared with v_x and v_y.

Table 6.5 Overall performance of the estimator at the center of the vessel for the parameter study.

Metric / Plane	ZX	ZY	XY
Mean $\|\mathbf{v}\|$ [m/s]	1.01 ± 0.093	1.00 ± 0.098	1.03 ± 0.083
Mean $B_{\hat{\phi}}$ [deg]	0.92±8.9	1.4±9.2	-0.14±4.2

One hundred estimates of the velocity components were estimated based on 32 emissions per estimate. Clutter filtering was applied. The results for v_x, v_y, and v_z are displayed in Figure 6.10. The left panels show the 100 estimated velocity profiles, and the right panels the mean and standard deviation. Both the transverse and elevation velocities were bias compensated as discussed in Section 6.6, e.g. λ_x equal to 3.4 mm was substituted with $\bar{\lambda}_x$ equal to 3.7 mm in (6.3a).

At the center of the vessel at 30 mm, the average velocity was

$$\bar{\mathbf{v}} = \begin{pmatrix} \bar{v}_x \\ \bar{v}_y \\ \bar{v}_z \end{pmatrix} = \begin{pmatrix} 1.00 \\ -0.0091 \\ 0.00059 \end{pmatrix} \pm \begin{pmatrix} 0.059 \\ 0.083 \\ 0.0053 \end{pmatrix} \text{m/s},$$

where the true velocity was $(v_x, v_y, v_z) = (1{,}0{,}0)$ m/s. At this position and normalized with the speed, the relative biases were smaller than 1 %, and the relative standard deviations were 6 %, 8 %, and 0.5 %, respectively.

Visualization of estimated flow directions

The flow directions contained in either the ZX, the ZY, or the XY plane were investigated. The flow angle in the individual planes were varied from 0° to 90° in steps of 15°. As in the above case, the mean velocity vector at the center of the vessel was calculated for each variation, and the results are presented in 3D in Figure 6.11. For clarity, the pair-wise velocity components in the ZX, the ZY, and the XY plane are presented in Figure 6.12. The overall performance of the mean speed, $|\mathbf{v}|$, and the mean estimated angle bias, $B_{\hat{\phi}}$, at the center of the vessel for all angles in the three respective planes are summarized in Table 6.5.

The results show that in the XY plane the velocity in either the x direction or the y direction is determined without bias, whereas at angles

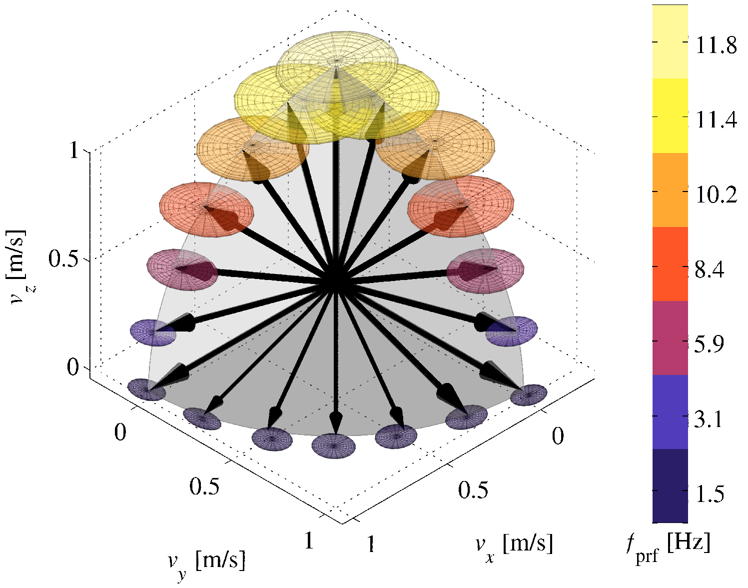

Figure 6.11 The average of the estimated 3D velocity vectors at the center of the vessel for different flow angles in the ZX, ZY, and XY plane. Black arrows indicate the true flow direction. Ellipsoids represent estimated velocities. The center of the ellipsoids is the mean of the 100 estimates, and the three radii of the ellipsoids are one standard deviation for v_x, v_y, and v_z, respectively. Note, that the pulse repetition frequency, f_{prf}, had to be increased with an increasing axial velocity component (see color coding of the colorbar). This resulted in higher standard deviations on the transverse and elevation velocity estimates. The ellipsoids appear to be discs because the standard deviation of the axial velocities are about an order of magnitude smaller compared to the transverse and elevation velocities. The results are shown in 2D in Figure 6.12.

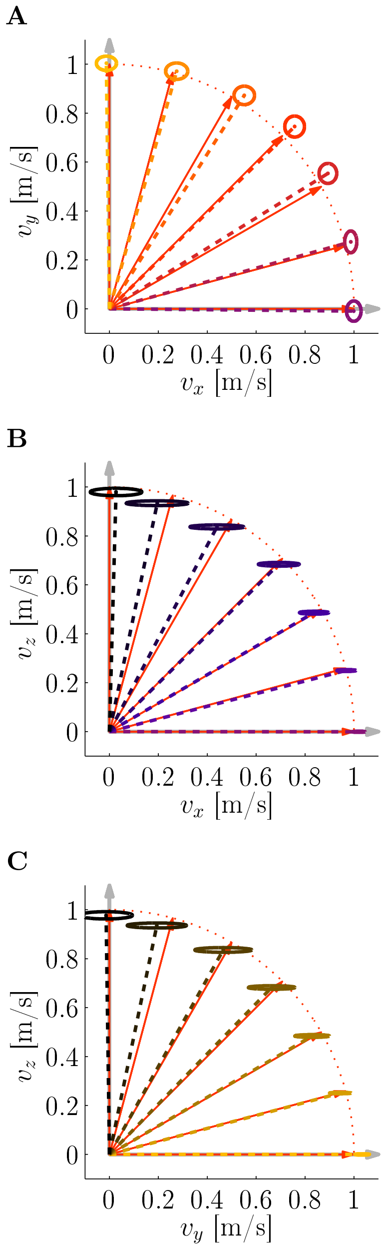

Figure 6.12 3D velocity estimates as shown in Figure 6.11 displayed here as the velocity components in **A** the ZX plane, **B** the ZY plane, and **C** the XY plane. Thin solid arrows indicate the true simulated velocity vectors at the center of the vessel, dashed lines the estimated mean velocity vectors, and ellipses (solid) the standard deviations for pairs of v_x, v_y, or v_z, respectively.

around 45°, there is a positive bias of 6 %. Overall, for all seven angles, the relative bias of the speed at the center of the vessel is 3 %. The corresponding relative standard deviation is 8 %. For comparison, the relative bias of the average speed is 1 % and 0 % for the ZX and the ZY plane. The mean angle bias is -0.14°±4.2° in the XY plane, and in the ZX and the ZY plane the bias is less than 1.4° with standard deviations less than 10°.

It should be noted, that with an increasing axial velocity component, it is necessary to increase the pulse repetition frequency, f_{prf}, to avoid aliasing. It is increased, so that the axial velocity component is maintained at 80 % of the aliasing limit. As a consequence, the aliasing limit for the transverse and elevation velocity components increases, and the poorer use of the velocity range results in the increased standard deviations observed for v_x and v_y. However, this drawback is to some degree alleviated by the fact that most vessels run more or less parallel to the skin surface, and hence, the transducer surface. Additionally, it can be observed that the standard deviations for the conventionally estimated axial velocity are about an order of magnitude smaller than for the transverse and elevation velocity components.

Based on the results shown in Figure 6.11, Figure 6.12, and Table 6.5, it can be concluded that the speed and the angle of the peak velocity in the XY plane on average are determined practically without bias, and that 95 % of the estimates are within 8.4°, which is 2.3 % of 360°. For the ZX and the ZY plane the performance is comparable, but slightly inferior because of the increasing mismatch between the magnitude of the transverse and elevation velocity components and the corresponding aliasing limits.

Varying the parameters

The previous paragraphs demonstrated the ability of the 3D TO method to estimate 3D velocity vectors. The following presents the results of varying the previously outlined parameters. In the parameter study, the relative mean bias and relative mean standard deviations are computed according to (5.7) and (5.8) for each set of mean velocity profiles for the various parameter settings. This allows for a more straight-forward comparison of the performance over the different parameters and their values. To reduce the effect of the vessel boundaries, the performance metrics are calculated over the entire vessel except for the outermost 1 mm at either end. As default, the flow in is the x direction, unless the flow angle is changed.

To recapitulate the results from Section 6.7.2 in the framework of the parameter study, the relative mean bias and standard deviations for v_x and v_y are shown in Figures 6.13A–6.13C for the velocities with flow angles ϕ_{zx}, ϕ_{zy}, and ϕ_{xy}, respectively. From Figures 6.13A and 6.13B it is obvious

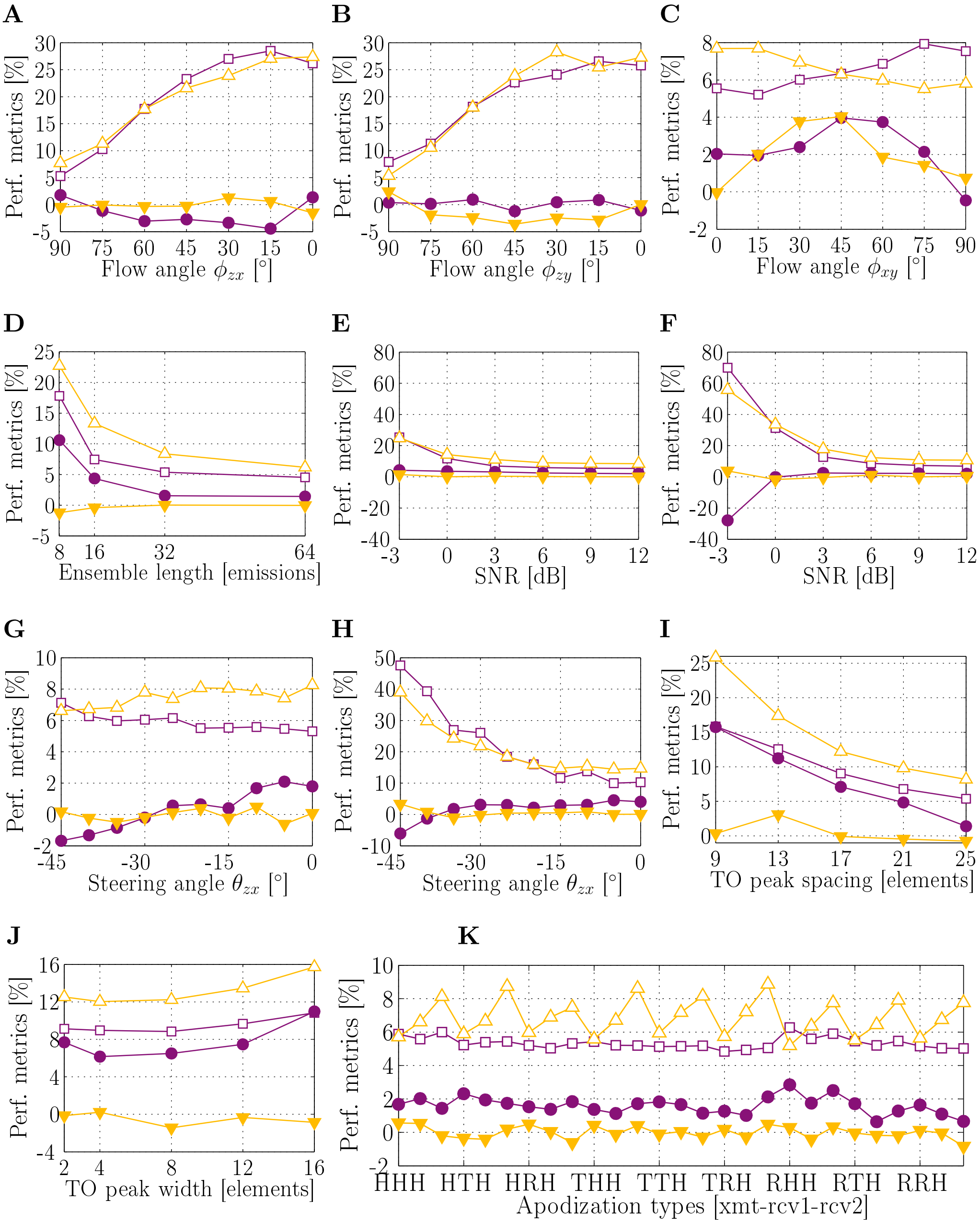

Figure 6.13 Performance metrics as a function of various parameter settings and their values: The relative mean standard deviations $\tilde{\sigma}_{v_x}$ (□) and $\tilde{\sigma}_{v_y}$ (△), and the relative mean biases $\tilde{B}_{v_x}$ (●) and $\tilde{B}_{v_y}$ (▼). The reader is referred to the text for details.

that the relative mean biases, $\tilde{B}_{v_x}$ and $\tilde{B}_{v_y}$, are more or less unaffected, whereas the relative standard deviations, $\tilde{\sigma}_{v_x}$ and $\tilde{\sigma}_{v_y}$, increase as the flow angle decreases and the axial velocity components increases. As previously mentioned, this is due to the increase in the pulse repetition frequency. The shape of the curves is similar to the increase in f_{prf} (see values in Figure 6.11). The relative increase in the relative mean standard deviations is largest at large flow angles, which reflects that the largest relative increase in f_{prf} occurs when going from a flow angle of 90° to 80°.

The results in Figure 6.13C show that the relative mean standard deviation for v_x increases from about 6 % to about 8 % as the flow angle, ϕ_{xy}, is increased from 0° to 90°. As the angle increases, the transverse velocity component decreases from 1 m/s to 0 m/s. The opposite is the case for the elevation velocity component. The results show that the relative mean standard deviation increases as the magnitude of the velocity component decreases. The relative mean biases for v_x and v_y have a parabolic shape. The values are between 0% and 2% at 0° and 90°, and 4% at 45°. This was also apparent from Figure 6.12C.

The number of emissions per velocity estimate affects the performance. The results are shown in Figure 6.13D. As the number of emissions increases, the relative mean standard deviation decreases, e.g. when the ensemble length is increased from 16 to 64, $\tilde{\sigma}_{v_x}$ and $\tilde{\sigma}_{v_y}$ decrease from 7.4 % and 13 % to 4.5 % and 6.2 %, respectively. The decrease in standard deviation is expected, because the standard deviation should decrease with a factor of $1/\sqrt{N_i}$, if the N_i signals are uncorrelated. The relative mean bias for v_x decreases from 10 % to 1.5 %, whereas the relative mean bias for v_y is unaffected.

The effect of varying the SNR is demonstrated in Figure 6.13E and 6.13F. Figure 6.13E shows the result of using the TO estimator — Eqs. (6.3a) and (6.3b) — compared with the heterodyning approach — Eqs. (6.4a) and (6.4b) — in Figure 6.13F. For the TO approach with a SNR of ∞ and 0 dB, the relative mean biases for v_x and v_y are increased from 5 % to 12 % and from 8 % to 14 %, respectively. For the heterodyning approach [147], the relative mean standard deviations increase from 7 % to 31 % for v_x and from 10 % to 34 % for v_y when the SNR is changed from ∞ to 0 dB. The difference is more than a factor of 2. In addition, the heterodyning approach breaks down with a SNR between 0 dB and -3 dB, whereas the TO approach first breaks down with a SNR between -6 dB and -3 dB. The results confirm the suspicion raised in Section 6.4.3 that the heterodyning approach is more susceptible to noise compared with the TO approach. This observation is in agreement with the results reported by Udesen and Jensen [108].

Figure 6.13G show the result of changing the steering angle θ_{zx}. The results for θ_{zy} are similar and are therefore not shown. As the results indicate, the relative standard deviation is almost unaffected with values between 5 % and 7 %. The relative mean biases vary from -2 % to 2 %. These values are obtained by using the theoretically calculated transverse and elevation wavelengths based on (6.1a) and (6.1b) in the beamforming. The values for λ_x and λ_y increase as a function of steering angle because of the $\cos\theta$-term. However, the most accurate velocity estimates (with the smallest bias) were obtained using $\bar{\lambda}_x$ and $\bar{\lambda}_y$ calculated at steering angles of 0° in the velocity estimation. That observation and the low values for especially the relative mean standard deviations were surprising. It was expected that steering the beam would degrade the performance of the velocity estimator. An explanation may reside in the ideal conditions of the Field II simulation environment, and the fact that no noise is added. Hence the drop in SNR due to the angular sensitivity has not been captured. To test this hypothesis, the velocity estimation was repeated with white Gaussian noise added, so that the SNR was changed to 0 dB at a steering angle of 0°. The noise amplitude is kept constant for all steering angles. The result can be observed in Figure 6.13H. When the steering angle increases, the received energy is lower, and hence the SNR decreases if the noise is constant. The decrease in SNR degrades the performance and the relative mean standard deviations increase. The relative mean bias is affected only at large steering angles. The results confirm the hypothesis, that the performance degrades when steering the beam.

The result of changing the spacing of the TO peaks is illustrated in Figure 6.13I. As the spacing increases, the relative mean standard deviations decrease. The relative mean bias for v_y is 0 % for almost all settings, but decreases for v_x. Figure 6.13J shows the effect of changing the TO peak width. Increasing the TO peak width slightly increases the relative mean standard deviations. The relative mean bias for v_x has a flat parabolic shape. For v_y, the relative mean bias is unaffected.

Figure 6.13K presents the results of combining various apodization shapes. Three different apodization shapes are used: A Hanning window, a Tukey window with a ratio of taper of 0.5, and a rectangular window. These windows are applied to the transmitting aperture, the receive aperture with the TO peaks in the transverse oscillating direction, and with apodizations across the TO peaks in the non-oscillating direction. All 27 combinations are investigated. The first data point in Figure 6.13K is denoted HHH. It is an abbreviation for applying Hanning, Hanning, and Hanning windowing in transmit, receive (oscillation direction), and receive (non-oscillation direction), respectively. The next point is HHT denoting Hanning, Hanning, and Tukey, and the third data point is HHR, denoting Hanning, Hanning, and Rect. The fourth data point is HTH, and the pattern is repeated. The results indicate that the relative mean biases are practically unaffected as well as the relative mean standard deviation for v_x. For v_y, however, the relative mean standard deviation has a serrated appearance. The relative standard deviation is around 7 % when the apodization in the non-oscillating direction is a rectangular window, and it is about 5 % when it is Hanning apodized.

When deciding on which apodization to use, it is important to remember that the SNR is proportional with the area under the apodization functions. The consideration of SNR and the area under the apodization functions is also important when considering the peak width. The results indicate, that in a noisy environment, there will be a trade-off between the TO spacing, the TO peak width, and the apodization functions where the SNR affects the optimal setting.

Overall, the parameter study demonstrates that the TO method is robust in terms of creating the TO fields and the appertaining transverse and elevation wavelengths. The theoretical values of the TO wavelengths can be used, but for bias optimization, the mean TO wavelengths based on the TO fields should be computed. Additionally, the TO fields themselves should be optimized by means of the performance metrics to reduce the bias and standard deviations of the velocity estimates. Furthermore, the TO method is less susceptible to noise compared with the heterodyning approach.

6.8 Conclusion and perspectives

A method for estimation of 3D velocity vectors using the Transverse Oscillation approach is presented in Section 6.4.3. Initial results from the plug flow simulation presented in Section 6.5 serve as a proof of concept, and demonstrate that the estimation of the velocity vector is decoupled into v_x, v_y, and v_z. It is further demonstrated that it is beneficial to optimize the TO method and to perform bias compensation by estimating the mean TO wavelengths based on the TO fields as described in Section 6.6.

As demonstrated in Section 6.7, velocity estimates are obtained with relative mean biases around 0 % and relative mean standard deviations less than 5% when optimized. The mean speed at the center of the vessel is estimated with a relative bias less than 3 % and a relative standard deviation less than 10 %. In the XY plane, the flow angle is estimated without bias, and with 95 % of the estimates within $\pm 8.4^\circ$. For the given reference setup with a SNR of 0 dB, the parameter study presented in Section 6.7.2 shows that the relative mean standard deviation is increased from 5 % to 12 %. In the presence of noise, the performance degrades as the steering angles are increased, and at high levels of noise, the method breaks down. Overall, the results demonstrate that 3D TO method is able to estimate the three velocity components under various parameter settings, and that the method is robust in terms of the transverse and elevation wavelengths.

Perspectives

The simulation results presented are promising and warrant further investigation and experimental verification. Besides requiring a 2D phased array matrix transducer, the complexity of the 3D TO method is within the capabilities of modern scanners. With measurements of 3D velocity vectors, it will be possible to measure the full 3D vortices and rotational flow as found for instance in the carotid artery.

Where simulations may be a great development tool, the real interesting application of the 3D TO method will be in measurements of velocities in clinical settings. First, however, the conclusion drawn in this chapter that the suggested 3D TO method is capable of estimating the 3D velocity vectors should be experimentally verified.

7

Experimental investigation of the 3D TO method

Summary *Experimental verification of the 3D TO method is warranted. This is obtained by use of a custom-manufactured 2D matrix array and the experimental ultrasound scanner SARUS. Measurements of the TO field are performed in a scanning tank system, and the first experimentally obtained estimates of 3D velocities are measured along the diameter of an artificial vessel in a flow-rig system with steady flow. The measurements are compared with simulation results obtained using the same parameter settings and under similar conditions, and the results are comparable. The experimental results validate the results obtained through simulations and verify that the 3D TO method estimates the full 3D velocity vectors and the correct velocity magnitude. In a cross-section of a vessel 3D vector flow images are acquired. As expected, only the out-of-plane component is present. Conventional and 2D methods would have failed to measure any velocity, whereas the 3D TO method estimates all three velocity components and the correct velocity magnitude. The results demonstrate, that the 3D TO method is suitable for 3D vector flow imaging.*

7.1 Purpose

The purpose of this chapter is to provide the background for the results obtained from experimental measurements of 3D velocity vectors, to present the obtained results, and to reflect on these. There are two goals. The first is to experimentally verify the ability of the 3D TO method to estimate the 3D velocity vectors and compare the results with simulation results. The second is to demonstrate the feasibility of employing the 3D TO method for 3D vector flow imaging. This goals are met by presenting experimentally obtained 3D velocity profiles and preliminary 3D vector flow images in a cross section of an artificial vessel. The work presented in this chapter is also presented in Paper VI and Abstract A and B.

7.2 Background and motivation

In the previous chapter, a method for estimating 3D velocity vectors using the transverse oscillating approach was introduced. The feasibility of the method was demonstrated by use of simulations.

This chapter presents the first experimental measurements of 3D vector velocities in a steady flow-rig system using the 3D TO method to validate the simulation results and the method described in the previous chapter. This is attained in two steps. Firstly, measurements of the TO fields are compared with simulated TO fields. Secondly, the measured 3D velocity profiles from an artificial vessel obtained using an experimental scanner and a 2D matrix array are compared with simulated results.

Several other approaches have provided experimental measurements of the 3D velocity vector as described in Chapter 2. Yet, convincing *in vivo* results still have to be demonstrated, and none of the methods have been adopted by commercial manufacturers. This is probably due to their individual limitations such as restricted field of view, high computational demands, or the need for contrast agents. The 3D TO method, on the other hand, enables simultaneous measurements of the three velocity vector components, and the velocities can be estimated over a range of depths, in an image plane, or even in an image volume.

Hence, the motivations for performing the experimental investigation are multiple. First of all, the measurements serve as the first example of 3D velocity vectors obtained using the 3D TO method. The velocities are estimated along the diameter of an artificial vessel. Secondly, the results are an experimental proof of concept, which validates the method empirically. The results also validate the previously presented simulation results. Additionally, the effect of using the simulated mean spatial wavelengths in the beamforming and the velocity estimation is investigated in terms of bias reduction.

Finally, these measurements are the first step in the process of obtaining volumetric 3D vector velocity images from phantoms and *in vivo* measurements.

Structure of the chapter

The hypotheses stated in the following section are investigated by measuring and simulating the TO fields and flow velocities. Therefore, the methods and the materials used are presented followed by a description of the data acquisition and processing. Subsequently, the results are presented in three parts: The measured and simulated TO fields and their corresponding spectra; the estimates of the 3D velocity vectors; and thirdly, the preliminary examples of 3D vector flow imaging. The chapter is concluded by stating the conclusion and the perspectives.

7.3 Research hypotheses

The main hypothesis underlying the scientific contribution presented in this chapter is:

- The 3D TO method is able to simultaneously estimate the full 3D velocity vectors in an experimental setup.

The obtained results are investigated by means of the following hypotheses:

1. The 3D TO approach generates independent spatial IQ pairs in the transverse and elevation direction.
2. Experimental and simulation results will yield comparable results in terms of TO fields and velocity estimates.
3. The measured velocity profiles will follow the expected profiles.
4. Employing the simulated mean spatial wavelengths in the beamforming and the velocity estimation eliminates the bias.

7.4 Methods and materials

This section describes the methods and materials used to obtain the experimental data. Two types of measurements were conducted. First, measurements of the TO fields using a scanning tank system were performed. Second, velocity measurements in an in-house built flow-rig system were carried out.

Simulations were performed in order to compare the measurement results with the simulated results. New simulations were performed because the transducer geometry for the physical 2D transducer is different than the one used in the previous chapter. Another difference compared with the results presented in the previous chapter is that the flow data was simulated as individual channel data for subsequent beamforming using the same approach as used for the measurements. The data processing is further described below.

The 3D TO method described in the previous chapter was employed in the experimental measurements and for the simulated results. For both the measurements and the simulations, the mean spatial transverse, $\bar{\lambda}_x$, and elevation, $\bar{\lambda}_y$, wavelengths were used in the beamforming stage and in the subsequent velocity estimation.

7.4.1 Measurement equipment

The main requirement for experimentally measuring the TO fields and the 3D vector velocities is a 2D array transducer and a system that can sample the element data from the corresponding number of channels. Both are introduced below followed by a description of the scanning tank system used for measuring the TO fields.

2D transducer and SARUS

The transducer used was a 2D matrix array transducer fabricated by Vermont S.A., Tours, France. It is depicted in Figure 7.1. The transducer has 32x32 active elements. These 1024 elements on the transducer are connected to the 1024 channels on SARUS, which was described in Section 5.7.1 on page 71. The difference here compared with the use in Chapter 5 is that the full system, i.e. all 1024 channels, is used for the 3D measurements. The data from all 1024 channels were sampled at a frequency of 70 MHz.

The center frequency of the transducer is 3.5 MHz, and the pitch of the transducer is 0.3 mm, hence it is not entirely a $\lambda/2$-pitch phased array transducer. The element layout consists of four blocks each consisting of 8x32 elements. The four blocks are stacked together and are separated by an inactive row of elements. Hence, the transducer layout is not identical in the in the x and y direction. Furthermore, the layout differs from the dense matrix layout used in the simulations in the previous chapter. The effect is that λ_x and λ_y may be slightly different depending on how the TO apodizations are applied to the receiving 2D aperture.

The TO apodizations used for the left and the right beam are illustrated in Figure 7.2 for the x and the y direction, respectively. Due to the three inactive rows, the distance between the centers of the TO peaks are different for the x and the y direction (25 and 28 elements, respectively). This results in a difference in the theoretical spatial wavelengths, where λ_x will be slightly larger than λ_y. Additionally, the TO fields will differ in the two dimensions due to the inactive rows.

Another difference can be noticed. The TO apodization for the x-direction is only half the size of the one in the y-direction. The explanations follow here. Prototype transducers often come with a higher degree of fabrication errors compared with a product line transducer. For the transducer in question, several elements are short-circuited in pairs or more, some

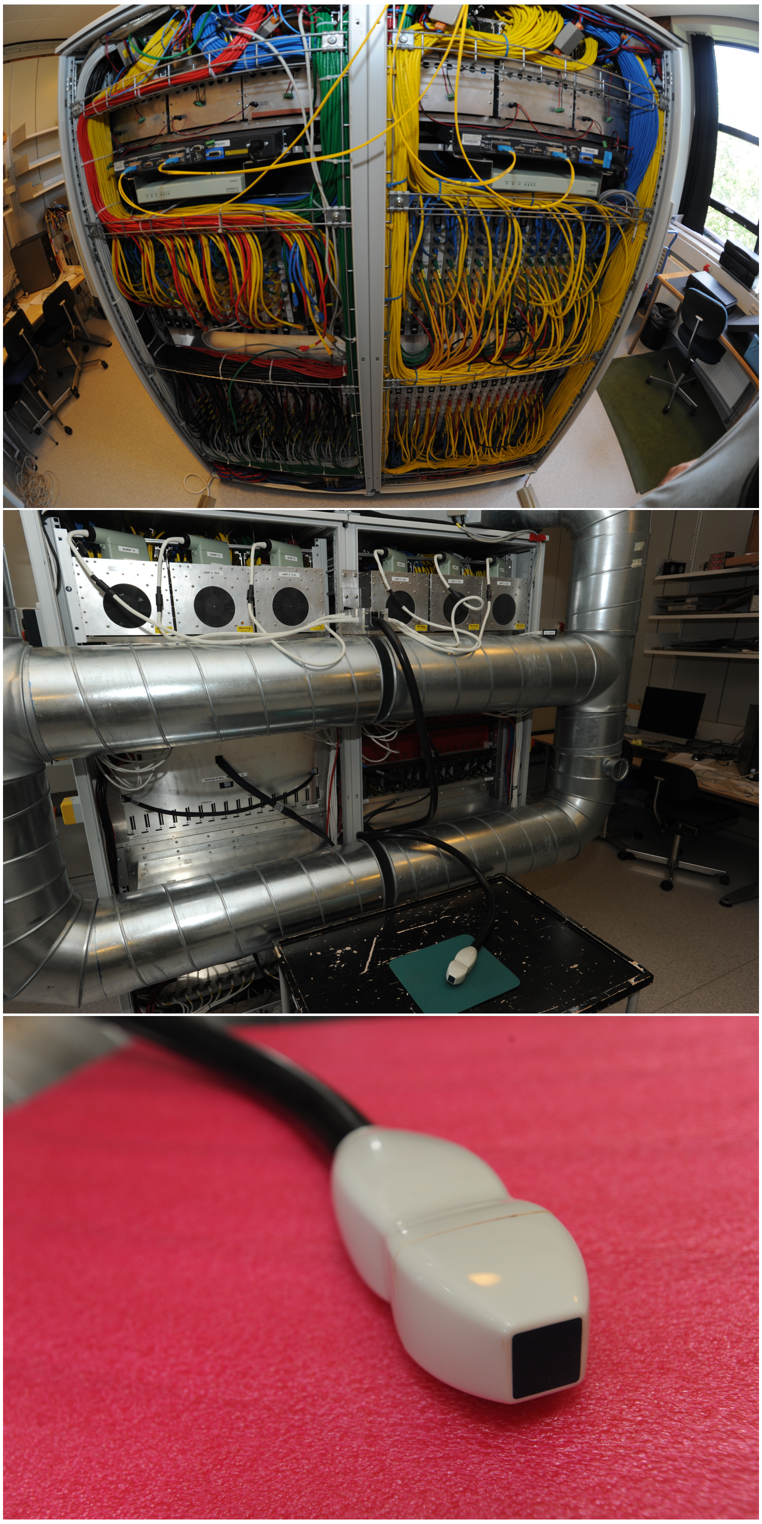

Figure 7.1 Photographs of (from top to bottom) the back of SARUS and the many cables needed for sampling from the 1024 channels, the front of SARUS with the six transducer plugs required for the 2D transducer connected, and a close-up of the 2D transducer. Photos courtesy of Morten Fischer Rasmussen.

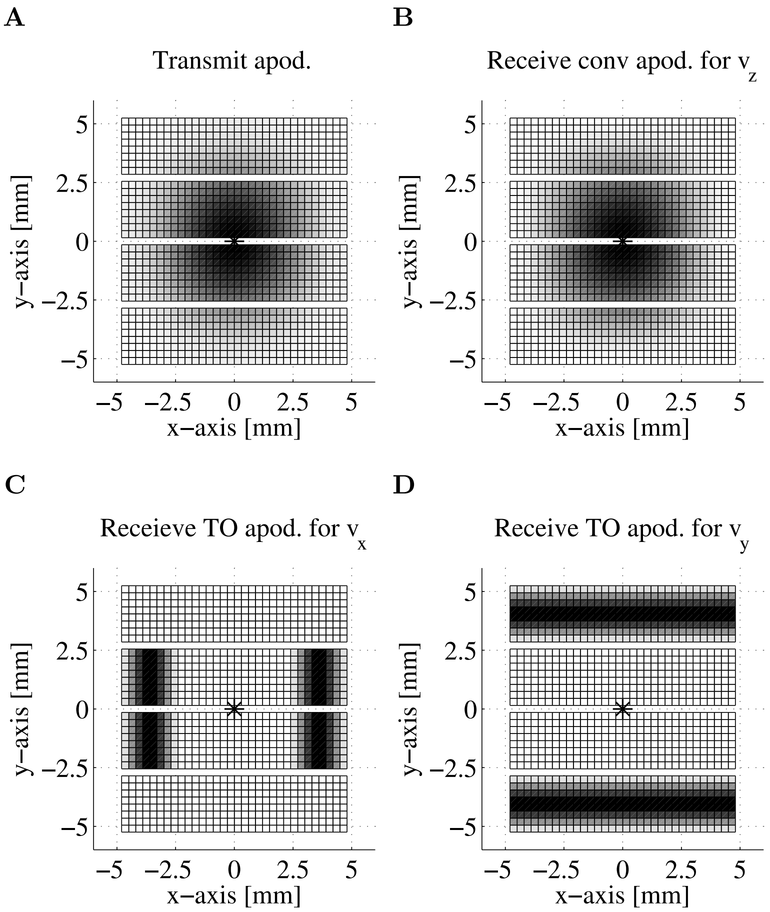

Figure 7.2 Apodization functions for **A** the transmit aperture, **B** the receive apodization for beamforming the center line used for the conventional estimation of v_z, **C** the receive TO apodization for beamforming the TO lines used for estimating v_x, and **D** the receive TO apodization for the estimation of v_y. The stars indicate the origin of the beamformed lines. For illustrative purposes, the rectangular apodizations of the TO receive apertures used in this chapter have been replaced with Hanning apodizations.

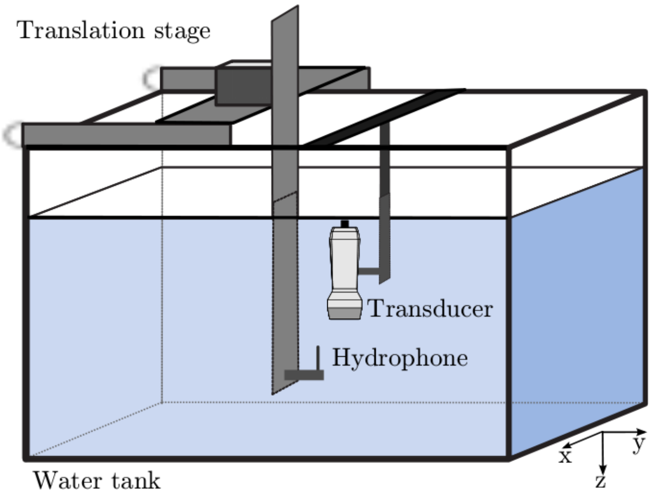

Figure 7.3 Illustration of the scanning tank system with mounted hydrophone and 2D transducer.

elements suffer from phase errors, the sensitivity varies, and some elements are practically dead. Besides the inaccuracies in the transducer, SARUS introduces noise to the measurements, however, the noise levels vary on the individual channels. Some channels have very high noise amplitudes. Two measures were taken to reduce these issues. First, the receive apodization was changed for the x-direction as illustrated in Figure 7.2. Secondly, the channels with the most noise was removed. This is further explained in Section 7.4.2.

Scanning tank system

Besides sampling the data from transducers, SARUS can sample data from a hydrophone. A HGL-0400 capsule hydrophone (Onda, Sunnyvale, CA) was mounted in an AIMS III Scanning Tank (Onda, Sunnyvale, CA), which can control the position of the hydrophone in all three dimensions. The setup is illustrated in Figure 7.3. The hydrophone is connected through a preamplifier to either an oscilloscope or to SARUS. SARUS and the scanning tank system can be controlled from the same MATLAB program to ensure synchronized data acquisition.

Flow-rig system

The flow-rig system used for the experimental velocity measurements was described in Section 4.4.2 on page 44. The flow in the flow-rig is steady

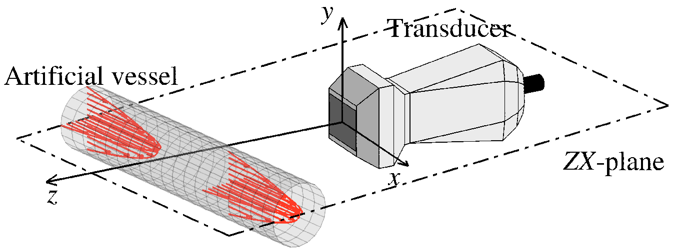

Figure 7.4 Illustration of the flow phantom used for measurements and simulations. Here, the beam-to-flow angle in the ZX-plane is 80°.

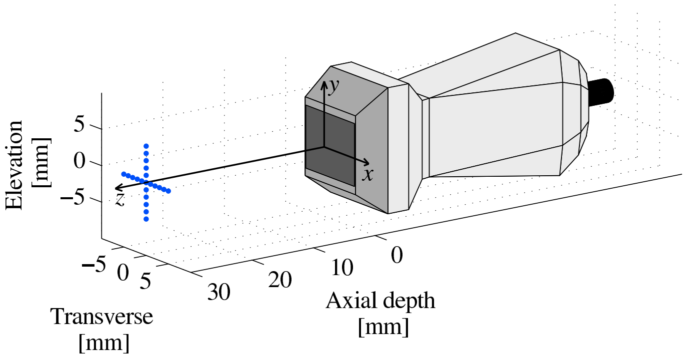

Figure 7.5 Illustration of the positions where the TO field is sampled. A dot denotes a position of the point target. For the data acquisition, 81 points were sampled both in the x and y direction with a spacing of 0.25 mm.

and has a parabolic profile as illustrated in Figure 7.4. Using the read-out volume flow rate and considering transducer and vessel orientations, the expected velocity profiles can be determined.

The peak velocity was calculated based on the volume flow rate from the flow-meter and the radius of the vessel. The velocity was set to be approximately 0.25 m/s, because the pump cannot deliver a steady flow at high velocities. The same velocity was used in the simulations. The pulse repetition frequency, f_{prf}, was set low accordingly (see Table 7.1). If the velocity was approximately 1 m/s as e.g. in the carotid artery, the pulse repetition frequency should just be increased to 2.4 kHz.

7.4.2 Data acquisition and processing

The TO fields were investigated through pulse-echo measurements in the scanning tank system where the hydrophone was used as a point target.

Table 7.1 Default parameter settings for the measurements and the simulations.

Parameter	**Value**
Transducer	
Geometry [elements]	35x32
Active elements	32x32
Rows of inactive elements (by design)	$3{\times}32$
Pitch [mm]	0.3
Center frequency [MHz]	3.5
Bandwidth (two-way) [%]	67
System	
Sampling freq. (simulations) [MHz]	100
Sampling freq. (measurements) [MHz]	70
Speed of sound [m/s]	1480
Number of receive channels (on SARUS)	1024
Emitted pulse	
Center frequency [MHz]	3.5
No. of cycles	8
Windowing of emitted pulse	Hanning
Focal depth [mm]	30
Steering angle in azimuth plane, θ_{zx} [deg]	0
Steering angle in elevation plane, θ_{zy} [deg]	0
Apodizations	
Transmit apodization	Hamming(32x32)
Receive for center line	Hanning(32x32)
Receive TO peak apodization (osc. direction)	Rectangular
Receive TO peak apod. (non-osc. direction)	Rectangular
Receive TO distance d_x [elements]	25
Receive TO distance d_y [elements]	28
Receive TO window width [elements]	8
Flow settings	
Flow angle ϕ_{xy} [deg]	0 or 90
Beam-to-flow angle ϕ_{zx} [deg]	80 or 90
Beam-to-flow angle ϕ_{zy} [deg]	90 or 80
Peak speed [m/s]	0.253
Flow profile	Parabolic
Data acquisition	
No. of emissions	1600
Pulse repetition frequency [Hz]	600
Post processing	
Matched filter	Time-reversed excitation pulse
Stationary echo cancelling (clutter filtering)	Subtraction of ensemble average
Velocity estimator	
Ensemble length [emissions]	32
SNR [dB]	7-10

The TO fields were sampled at points forming a cross with the center at $[x, y, z]$=[0,0,30] mm and points along the the x-axis and the y-axis as illustrated in Figure 7.5. The transducer was centered at $[x, y, z]$=[0,0,0] mm. For each position of the point target an excitation waveform was emitted and the signals from all 1024 channels were sampled. Subsequently, the same four TO lines were beamformed for each position simultaneously. Simulations with the same parameters were performed for comparison. Obtaining these TO lines across the transverse and the elevation direction yields the TO fields.

To obtain the corresponding TO spectra, the temporal IQ data of the TO fields are obtained by use of the Hilbert transform on the time-sampled signals. Then the signals from the left and right beams are combined to create the complex TO fields and the corresponding TO spectrum is obtained by applying a Fourier transform on the complex TO fields as described in Section 5.4.3 on page 56. Ideally, if the spatial IQ process worked for all spatial frequencies, the TO spectra should be one-sided in the oscillating direction and symmetrical around $0\,\mathrm{mm}^{-1}$ in the non-oscillating direction. A performance metric to evaluate how well the spatial IQ process has worked is the ratio of energy at negative spatial frequencies over the ratio of energy at positive spatial frequencies denoted E_r introduced in Section 5.5.2.

Velocity measurements were performed in the flow-rig system. The transducer was positioned, so that the center of the vessel was located at an axial depth of 30 mm. Two different flow directions were employed with flow either in the x direction or in the y direction. These two directions were obtained by rotating the transducer 90°. To add an axial velocity component, the transducer was rotated setting the beam-to-flow angle in the ZX plane to 80°. Hence, the flow direction was expectantly confined in the ZX plane as illustrated in Figure 7.4. Similarly, for the second case, the flow direction was confined to the ZY plane with an beam-to-flow angle in the ZY plane of 80°. The two setups were mimicked in the simulations. Before the velocity estimation was performed, clutter filtering was applied by subtracting the mean ensemble value of N_i emissions as described in Section 5.6.2. To improve the performance of the velocity estimates, the mean transverse wavelength, $\bar{\lambda}_x$, and the mean elevation wavelength, $\bar{\lambda}_y$, were used in both the beamforming stage and in the velocity estimation. This lowers the standard deviation and reduces the bias as mentioned in the previous chapters. The estimated mean values are determined from simulations. To obtain the TO spectra, however, the theoretical values were used in the beamforming stage for both the measured and the simulated data.

The parameters used for both types of measurements with their respective values are listed in Table 7.1. These values were used unless stated otherwise for obtaining both the measurement and the simulation data. The data processing was performed offline. The raw channel data from measurements or simulations were match filtered and beamformed using the Beamformation Toolbox 3. The subsequent processing of the TO fields and the velocity estimation followed the approaches described in the previous chapter.

The measurement system inherently introduces noise to the measurements. In SARUS, the noise level varies over various channels. Therefore, channels with high noise levels were removed in the beamforming. The standard deviation over 100 emissions are calculated for each sample covering the vessel wall (300 samples in total). For each channel, the mean of the standard deviations is calculated. Now, the mean and standard deviations across the channels are computed. Channels, where the mean standard deviation is higher than the mean of all channels plus 2 standard deviations (i.e. above the 95% interval), are removed. In all, 33 channels were removed.

The amount of noise in the system affects the SNR, which in turn affects the performance of the velocity estimator. The SNR of the beamformed RF data inside the vessel was calculated based on 100 emissions where the flow had been turned off. The SNR was calculated as

$$\mathrm{SNR_{dB}}(n) = 10\log_{10}\frac{\sum\limits_{n=-N_s/2}^{N_s/2} s^2(n)}{\sum\limits_{n=-N_s/2}^{N_s/2} n_s^2(n)},$$

where n denotes discrete time samples, $s(n)$ is the received sampled signals, $n_s(n)$ is calculated as the residuals after subtracting the average of $s(n)$ over the 100 emissions from $s(n)$, and N_s is the number of samples in one excitation pulse. The final value of the SNR is averaged over the 100 emissions, and over the vessel lumen. For the simulation of velocities, zero mean Gaussian white noise was added to the individual channels prior to matched filtration and beamforming. The noise amplitude was adjusted to obtain the desired SNR.

7.5 The TO fields and their corresponding spectra

The results from measuring the TO fields with the scanning tank system and the corresponding TO spectra are presented and compared with results obtained through simulations.

The TO method depends on creating the two double-oscillating fields where the oscillations are in the axial and the transverse direction, but not in the elevation direction, and conversely, where the oscillations are in the axial and the elevation direction, but not in the transverse direction.

Figure 7.6 shows the pulse-echo measurements of the TO fields for a specific time instance in the sampled signals. The point target was positioned at a depth of 30 mm. Figure 7.6A is for the left and the right beam in the ZX plane when sampling along the x direction. Ideally, the right beam should overlap with the Hilbert transform of the left beam for the spatial IQ modulation to work perfectly. The same should be the case in Figure 7.6D, where the samples from the two TO beams in the ZY plane were obtained sampling along the y direction. Oppositely, in Figure 7.6B and C, the left and right beam should be in phase, because in those two cases, the TO fields were sampled in the non-oscillating direction.

The measured fields exhibit the expected trends, and they can be compared with the simulated results shown in Figure 7.8. The behaviour of the simulated results is more ideal, and reflects the fact, that the simulation environment is free of the system noise and the phase errors present in the measurements. Yet, the simulated as well as the measured TO fields demonstrate, that the spatial IQ approach has worked, and that the TO fields oscillate only in either the transverse or the elevation direction.

The results shown in Figures 7.6 and 7.8 were obtained at one specific time instance in the pulse-echo responses. The TO spectra presented in Figures 7.7 and 7.9 are obtained by taking the 2D spatio-temporal Fourier transform of the combined complex 2D TO fields as described in Section 5.4.3. The section also described how to calculate $\bar{\lambda}_x$ and $\bar{\lambda}_y$.

Calculating the mean transverse and elevation wavelengths based on the measured TO spectra (Figures 7.6A and C) yield 8.0 mm and 5.4 mm, respectively. In terms of frequency, this corresponds to $0.124\,\text{mm}^{-1}$ and $0.186\,\text{mm}^{-1}$. The simulated results are 3.7 mm and 3.3 mm for $\bar{\lambda}_x$ and $\bar{\lambda}_y$, respectively, which corresponds to $0.270\,\text{mm}^{-1}$ and $0.302\,\text{mm}^{-1}$. The theoretically calculated values, λ_x and λ_y, based on (6.1a) and (6.1b) are 3.4 mm and 3.0 mm. The differences in λ_x and λ_y are a result of the geometrical differences in the x- and the y-direction as described above.

An explanation for the differences between the measured and the simulated mean spatial wavelength comes from the phase errors and the noise in the measurement system, which are not present in the simulations. Additionally, the energy for the higher spatial frequencies is present both at negative and positive frequencies in the otherwise one-sided spectra. That effectively lowers the mean frequency, and thereby increases the mean wavelength.

In addition, the signals in Figures 7.6A and B are slightly off axis, which means, that the signals in Figure 7.6C and D were not obtained at the center. Furthermore, the scan plan may not have been completely aligned to the transmitted beam, meaning that the transmitted beam may not have been normal to the scan plane, which affects the appearance of the TO fields, and hence, the calculated TO spectra. Again, these issues are not present in the simulations.

The differences between the simulations and the measurements also affected the performance metric E_r, which was described in Section 5.5.2 on page 59. The energy ratio is -14 dB for Figure 7.6A and -8.5 dB for Figure 7.6D. The equivalent values from the simulations are -16 dB and -18 dB for Figures 7.8A and D, respectively. This indicates, that the spatial IQ approach has worked better in the simulations compared with the measurements because the TO spectra are more one-sided for the simulations as the values of E_r indicate.

The results mentioned above are for the transverse oscillating directions. In the non-oscillating directions, the measurements yield mean spatial frequencies of -0.031 mm^{-1} and -0.0021 mm^{-1} and energy ratios of 4.5 dB and -3.2 dB for Figures 7.6B and C, respectively. Ideally, the spectra should be one-sided with a mean frequency of 0 mm^{-1} and correspondingly an energy ratio of 0 dB. The simulations yielded mean frequencies of 0 mm^{-1} with the values of E_r being -0.021 dB and -0.027 dB for Figures 7.8B and C, respectively. Anew, the results from the simulations behave more ideal than the measured results due to the reasons discussed above. Nonetheless, both the measured and the simulated TO fields confirm the presence of the two double-oscillating fields, where the left and the right beam are approximately 90° phase-shifted in the oscillation direction and approximately in-phase in the non-oscillating direction.

As potential misalignment, phase errors in the transducer, and system noise affect the measured TO fields, it is recommended to use the simulated data to calculate the “mean” spatial wavelengths. Improved results for the measured data may be obtained by deriving another approach to calculate the actual spatial wavelengths. Perhaps, the median spatial frequency may yield a better estimate for the measured data. Meanwhile, the simulated $\bar{\lambda}_x$ and $\bar{\lambda}_y$ are used in the beamforming and the velocity estimation of the flow data.

In conclusion, the presented results of the TO fields demonstrate that the essential assumption of the 3D TO approach generating spatial IQ pairs is fulfilled. The next step is to perform measurements of 3D velocities.

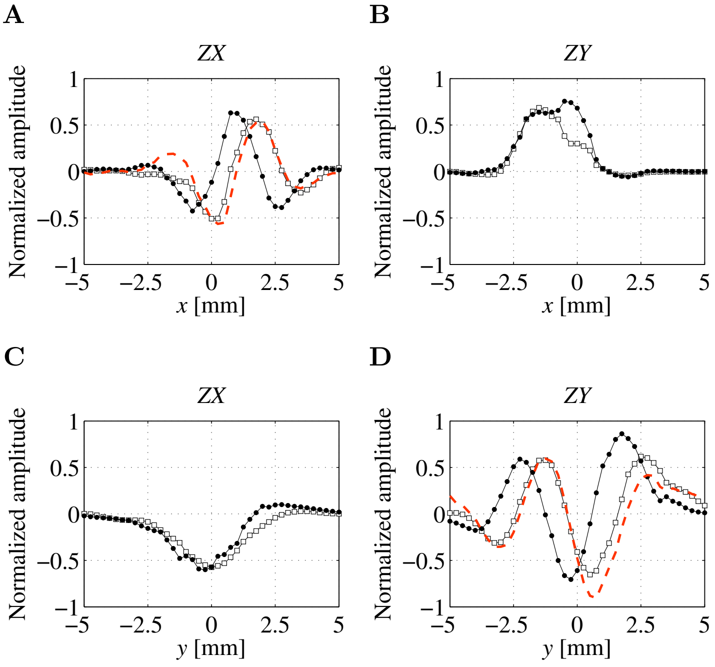

Figure 7.6 Measured TO fields at a depth of 30 mm for a fixed time across either the transverse (**A** and **B**) or the elevation (**C** and **D**). Dots (·) and squares (□) denote samples for the left and right beam, respectively. **A** and **C** are for the two beams in the ZX plane. **B** and **D** are for the beams in the ZY plane. The dashed line is the Hilbert transform of the left beam (in **A** and **D**).

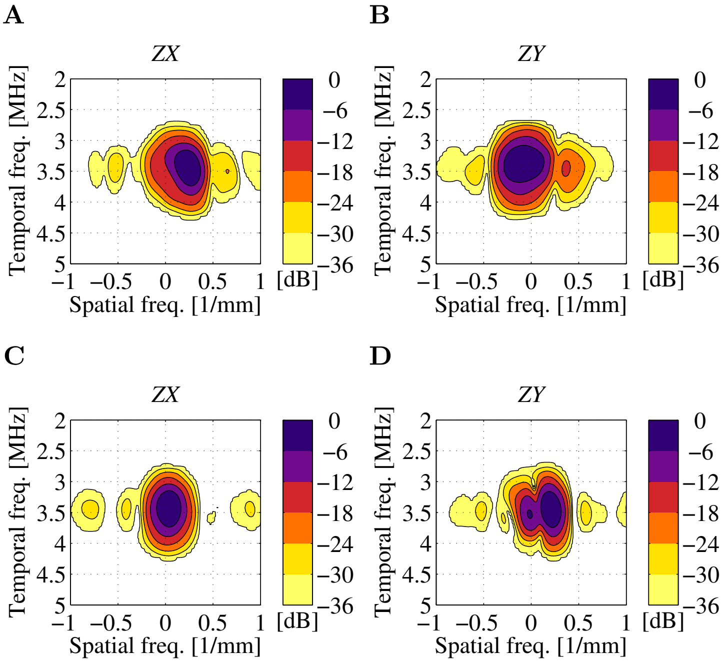

Figure 7.7 The TO spectra corresponding to the TO fields in Figure 7.6.

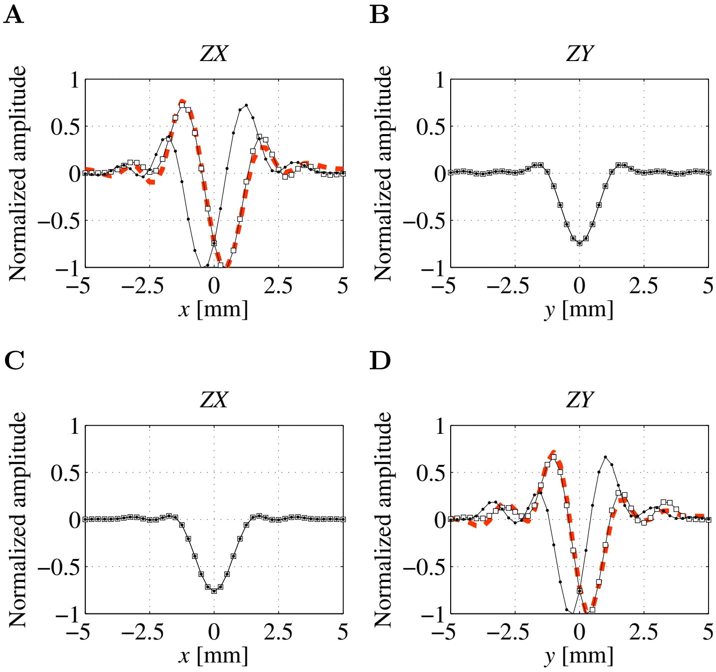

Figure 7.8 Simulated TO fields at a depth of 30 mm for a fixed time across either the transverse (**A** and **B**) or the elevation (**C** and **D**). Dots (·) and squares (□) denote samples for the left and right beam, respectively. **A** and **C** are for the two beams in the ZX plane. **B** and **D** are for the beams in the ZY plane. The dashed line is the Hilbert transform of the left beam (in **A** and **D**).

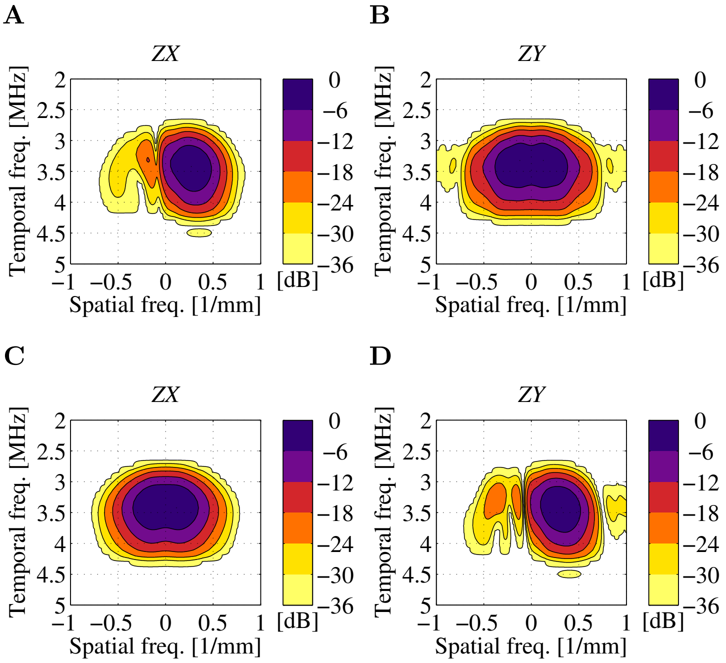

Figure 7.9 The TO spectra corresponding to the TO fields in Figure 7.8.

7.6 3D vector velocity estimation

The results from the velocity estimation based on the experimental flow-rig measurements and flow phantom simulations are introduced and discussed in the following.

Measurements were performed in the flow-rig with steady flow to evaluate the performance of the 3D TO estimator. The velocity components v_x, v_y, and v_z where estimated using the 3D TO method and 50 velocity profiles were obtained. They are demonstrated in Figure 7.10.

The left panels in Figure 7.10 are for the flow direction expectedly confined to the ZX plane, and the right panels for the flow direction in the ZY plane. The actual beam-to-flow angle was determined to be 78° and 79° in the two cases, respectively. For the case of the flow direction being confined to the ZX plane, v_y was expected to be $0\,\mathrm{m/s}$. The actual value of ϕ_{zx} and is within the expected uncertainty of the transducer fixation devices.

Comparing the velocity profiles for v_x and v_y, it can be observed, that several of the flow lines for v_x have higher fluctuations than for v_y. This is a consequences of the issues concerning the 2D transducer and SARUS described in Section 7.4.1. The standard deviations of the estimated v_x and v_y are 5–8 times higher than for v_z. This is in agreement with the findings in the previous chapters. To further investigate the estimated velocities, the average velocity profile and the range of ± one standard deviation is calculated. The estimated mean and standard deviation for v_x, v_y, and v_z for the two cases are displayed in Figure 7.11. In all the six subplots, the mean of the estimated velocity components follows the expected profiles. Simulations were performed for comparison with the same parameter settings. To ensure similar conditions, noise was added to the simulated RF signals to obtain SNRs comparable to the measurements. The result is shown in Figure 7.12 for both cases. The standard deviations for v_x and v_y are comparable, although slightly lower for v_y than for v_x. The standard deviation is considerably lower for v_z than for v_x and v_y. For all six velocity profiles, almost no bias is present except close to the vessel boundaries.

By visual comparison of the measured and the simulated velocities, the results are comparable, with slightly lower standard deviations for v_y compared with v_x. For both types of data, almost no bias is present except close to the vessel walls. A more quantitative comparison is performed by investigating the mean velocities at the center of the vessel. The mean velocities ± the range of one standard deviation, the expected velocity, and the corresponding bias are listed in Table 7.2 and Table 7.3 for the measured

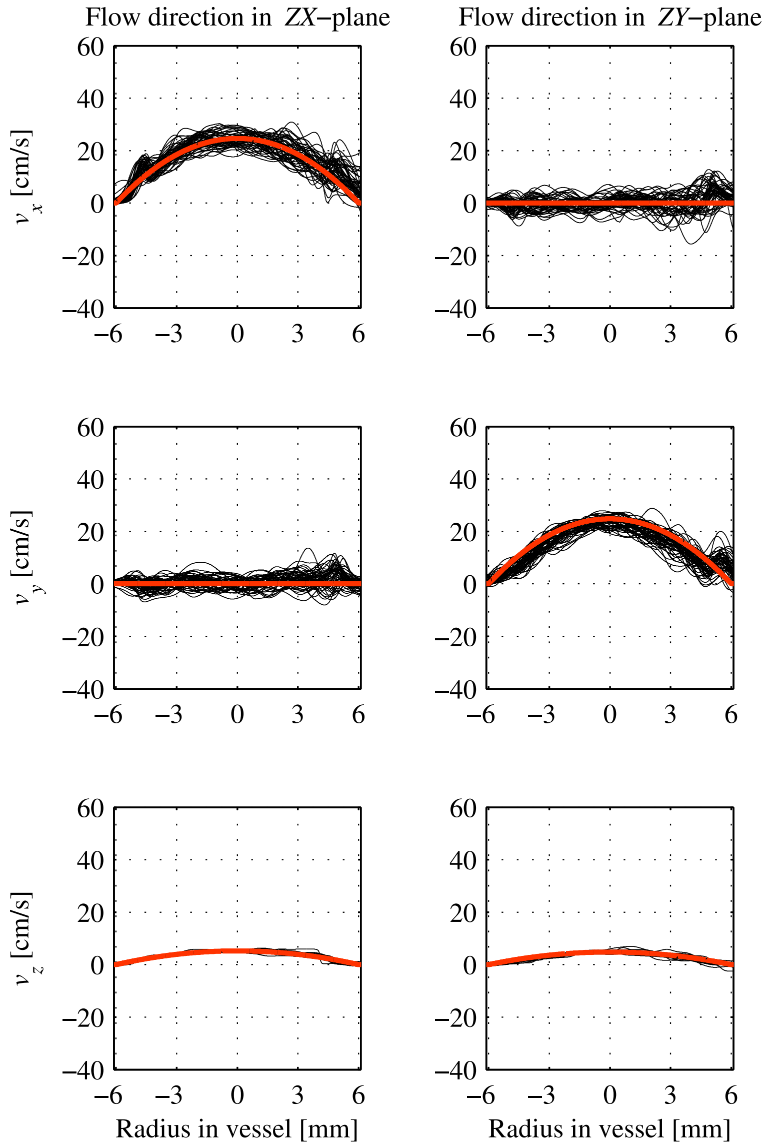

Figure 7.10 Estimated velocity profiles of the three components v_x, v_y, and v_z based on experimental measurements in a flow-rig. The center of the vessel was located at an axial depth of 30 mm. Left panels are for a flow direction primarily in the ZX-plane. Right panels are for a flow direction in the ZY-plane. Thin lines represent individual estimated profiles, and thick lines represent the expected flow profiles.

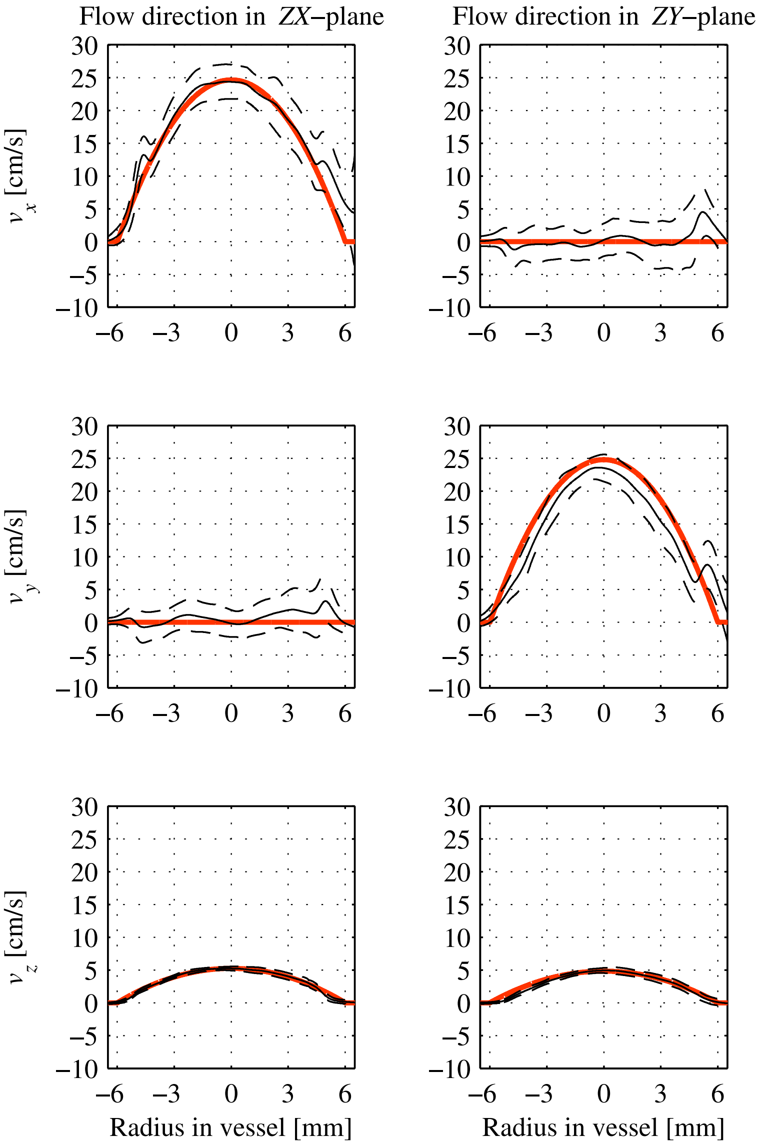

Figure 7.11 Mean and standard deviation of the 50 measured velocity profiles for the three estimated velocity components. Thick lines indicate the expected velocity profile, thin lines indicate the mean of the profiles, and dashed red lines one standard deviation. Compare with the simulated results in Figure 7.12.

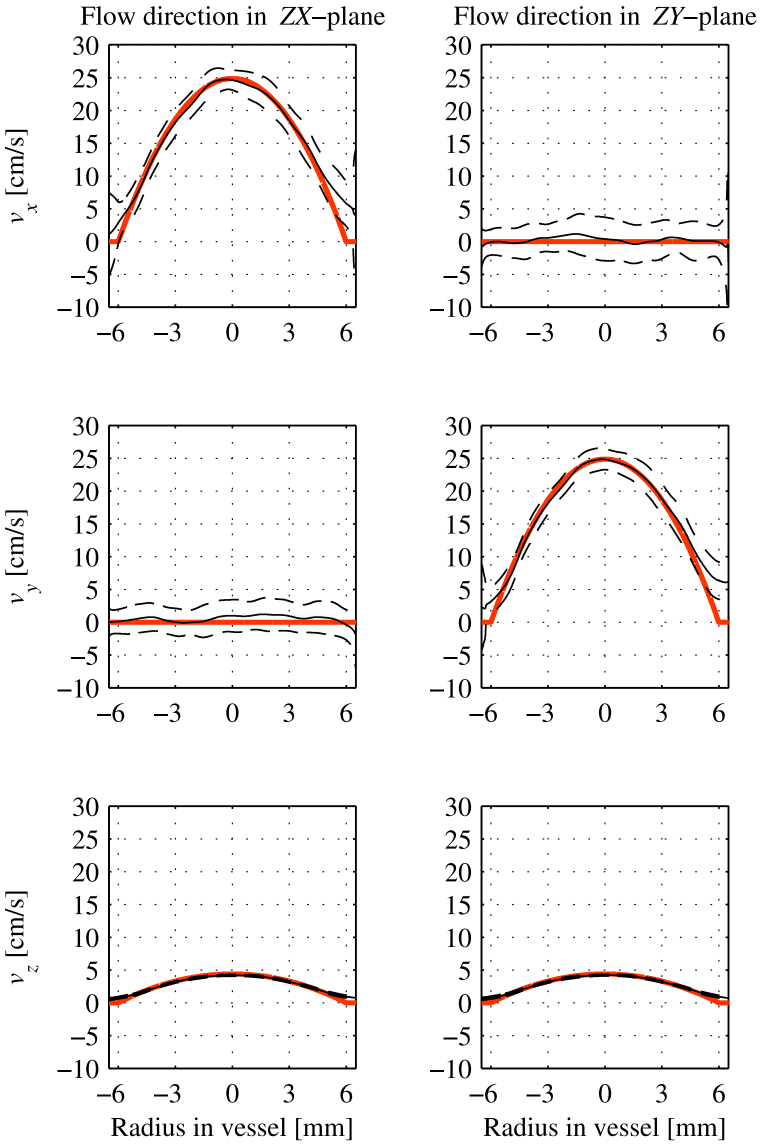

Figure 7.12 Mean and standard deviation of the 50 simulated velocity profiles for the three estimated velocity components. Thick lines indicate the expected velocity profile, thin lines indicate the mean of the profiles, and dashed red lines one standard deviation. Compare with the measured results in Figure 7.11.

Table 7.2 Experimental measurements: The mean—$\bar{\mathbf{v}}$—of the 3D velocity vector at the center of the vessel at 30 mm, the expected velocity vector—$\mathbf{v}_{\mathrm{exp}}$—, and the resulting bias—$\mathbf{B}_{\mathbf{v}}$—for the two cases with the flow direction confined in the ZX plane or the ZY plane, respectively.

$$\bar{\mathbf{v}}_{\mathbf{zx}} = \begin{pmatrix} \bar{v}_x \\ \bar{v}_y \\ \bar{v}_z \end{pmatrix} = \begin{pmatrix} 24.4 \\ -0.21 \\ 5.22 \end{pmatrix} \pm \begin{pmatrix} 2.6 \\ 2.3 \\ 0.31 \end{pmatrix} \mathrm{cm/s}$$

$$\bar{\mathbf{v}}_{\mathbf{zy}} = \begin{pmatrix} \bar{v}_x \\ \bar{v}_y \\ \bar{v}_z \end{pmatrix} = \begin{pmatrix} 0.25 \\ 23.5 \\ 4.92 \end{pmatrix} \pm \begin{pmatrix} 2.5 \\ 2.1 \\ 0.39 \end{pmatrix} \mathrm{cm/s}$$

$$\mathbf{v}_{\mathrm{exp,zx}} = \begin{pmatrix} 24.6 \\ 0.00 \\ 5.24 \end{pmatrix} \mathrm{cm/s}$$

$$\mathbf{v}_{\mathrm{exp,zy}} = \begin{pmatrix} 0.00 \\ 24.8 \\ 4.82 \end{pmatrix} \mathrm{cm/s}$$

$$\mathbf{B}_{\mathbf{v}_{\mathbf{zx}}} = \begin{pmatrix} -0.30 \\ -0.21 \\ -0.023 \end{pmatrix} \mathrm{cm/s}$$

$$\mathbf{B}_{\mathbf{v}_{\mathbf{zy}}} = \begin{pmatrix} 0.25 \\ -1.28 \\ 0.10 \end{pmatrix} \mathrm{cm/s}$$

Table 7.3 Simulation results: The mean—$\bar{\mathbf{v}}$—of the 3D velocity vector at the center of the vessel at 30 mm, the expected velocity vector—$\mathbf{v}_{\text{exp}}$—, and the resulting bias—$\mathbf{B}_{\mathbf{v}}$—for the two cases with the flow direction confined in the ZX plane or the ZY plane, respectively.

$$\bar{\mathbf{v}}_{\mathbf{zx}} = \begin{pmatrix} \bar{v}_x \\ \bar{v}_y \\ \bar{v}_z \end{pmatrix} = \begin{pmatrix} 24.6 \\ 0.97 \\ 4.18 \end{pmatrix} \pm \begin{pmatrix} 1.5 \\ 2.5 \\ 0.14 \end{pmatrix} \text{cm/s}$$

$$\bar{\mathbf{v}}_{\mathbf{zy}} = \begin{pmatrix} \bar{v}_x \\ \bar{v}_y \\ \bar{v}_z \end{pmatrix} = \begin{pmatrix} 0.38 \\ 24.8 \\ 4.21 \end{pmatrix} \pm \begin{pmatrix} 3.3 \\ 1.6 \\ 0.14 \end{pmatrix} \text{cm/s.}$$

$$\mathbf{v}_{\text{exp,zx}} = \begin{pmatrix} 24.9 \\ 0.00 \\ 4.38 \end{pmatrix} \text{cm/s}$$

$$\mathbf{v}_{\text{exp,zy}} = \begin{pmatrix} 0.00 \\ 24.9 \\ 4.38 \end{pmatrix} \text{cm/s,}$$

$$\mathbf{B}_{\mathbf{v_{zx}}} = \begin{pmatrix} -0.24 \\ 0.97 \\ -0.21 \end{pmatrix} \text{cm/s}$$

$$\mathbf{B}_{\mathbf{v_{zy}}} = \begin{pmatrix} 0.38 \\ -0.024 \\ -0.17 \end{pmatrix} \text{cm/s.}$$

and the simulated data, respectively. Comparing the mean of the three estimated velocity components from measurements and simulations at the center of the vessel shows that the standard deviations are comparable ranging from 1.5 cm/s to 3.3 cm/s. In the measurements, the relative standard deviation normalized to the peak velocity magnitude ranges from 8 % to 12 %. In the simulations, it ranges from 6 to 13 %.

One of the reasons for the higher variation and variance of the profiles for v_x compared with v_y is due to differences in the electronics. For estimation of v_x, other transducer elements and system channels are used compared with the ones used for estimating v_y as previously described. The elements used for estimating v_x have more errors (in phase and cross-talk) than the ones used for v_y. Additionally, there is more electronic noise present on the channels used to estimated v_x. The noise amplitude fluctuates, and hence, affects the different estimated velocity profiles differently. Additionally, some of the sampling boards are unstable, yielding increases in noise over time. This affects v_x, where the large fluctuations for v_x especially for the flow direction in the ZY plane arose at the end of the measurements and progressively got worse. Channels involved in estimating v_y were not affected by this. These issues where addressed and to some extend alleviated by removing channels with large fluctuations from the beamforming. This is also reflected in the SNR, which was about 3 dB lower for v_x compared with v_y. Additionally, the SNR dropped considerably inside the vessel down to approximately 3 dB at the distal vessel wall. As the SNR begins to drop below 6 dB and then 3 dB, the performance of the estimator begins to degrade markedly as demonstrated in the previous chapter. This is the reason for the poor performance at the distal vessel for v_x in the measurements. The simulations where not affected by this as there was no structure to the noise added and no phase error or short-circuits or temporal fluctuations. Hence, for the measurements, it is expected that the difference in standard deviations for v_x compared with v_y are higher compared with the simulations. This is in general the case when comparing Figures 7.11 and 7.12.

Similarly, the biases from measurements and simulations are of the same size and fluctuates around 0. The largest bias is less than 5 %. This demonstrates that using the mean spatial wavelengths obtained from simulations in the beamforming and the velocity estimation instead of the theoretically derived wavelengths eliminates the bias otherwise present.

The results also demonstrate, that under the same conditions, measurements and simulations provide comparable results. Thereby, the validity of the simulation results presented here and previously reported has been verified.

With estimates of all three velocity components, it is possible to obtain

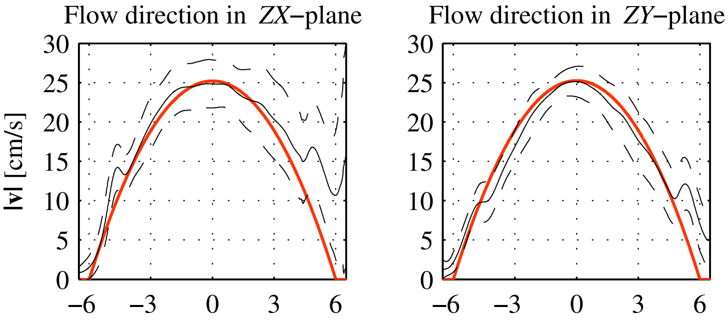

Figure 7.13 Mean and standard deviation of the 50 measured velocity magnitude profiles with an ensemble length in the velocity estimation of 32. The x-axis is radius of the vessel in mm. Thick lines indicate the expected velocity profile, thin lines indicates the mean of the profiles, and dashed lines the range of one standard deviation.

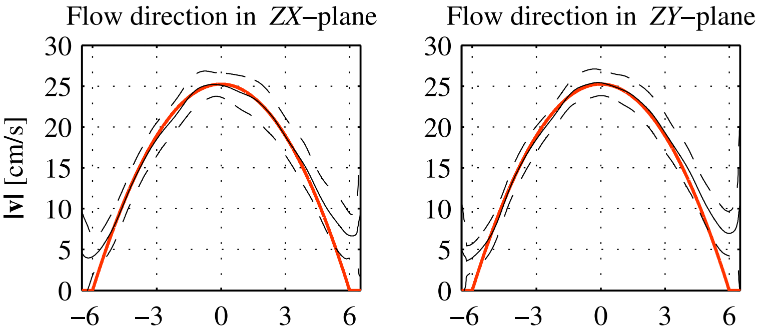

Figure 7.14 Mean and standard deviation of the 50 simulated velocity magnitude profiles with an ensemble length in the velocity estimation of 32. The x-axis is radius of the vessel in mm. Thick lines indicate the expected velocity profile, thin lines indicate the mean of the profiles, and dashed lines the range of one standard deviation.

Table 7.4 Estimated velocity magnitude at the center of the vessel in terms of mean ± one standard deviation and bias compared with the expected values for measurements and simulations. The results are divided into groups, where the flow direction is confined in either the ZX or the ZY plane.

Metric	Measurements		Simulations		Unit
	ZX	ZY	ZX	ZY	
Expected $\|\mathbf{v}\|$	25.2	25.2	25.2	25.2	[cm/s]
Mean ± std. of $\|\mathbf{v}\|$	24.8±3.1	25.1±1.9	25.1±1.5	25.4±1.6	[cm/s]
Bias	-0.36	-0.12	-0.13	0.17	[cm/s]

the true velocity magnitude. The velocity magnitude for the measurements and the simulations can be found in Figure 7.13 and Figure 7.14, respectively. The results for the center of the vessel are listed in Table 7.4. The performance is comparable for simulations and measurements, and the relative standard deviation is less than 13 %, whereas almost no bias is present. The performance in the simulations is slightly better due to the reasons discussed above.

Besides noise, another parameter that affects the performance of the 3D TO estimator is the ensemble length, i.e. the number of pulses used in the calculation of the autocorrelation values. The velocity estimation was repeated for ensemble lengths of 8, 16, 32, 64, and 128 emissions per estimate. The resulting velocity magnitude profiles can be found in Figure 7.15. For an ensemble length of 8, the standard deviations are high, especially at the far end of the lumen. As the ensemble length increases, the standard deviations decrease, yielding a better performance. The drawback of increasing the ensemble length, is of course the drop in frame-rate, and often, a compromise between frame-rate and precision has to be made. The performance increase is visualized in Figure 7.16, which shows the relative standard deviation and relative bias at the center of the vessel lumen. As expected, the standard deviations are halved when the ensemble length is increased by a factor of 4. This is due to the noise being uncorrelated, and therefore, the standard deviation drops with $1/\sqrt{N_i}$. The relative bias only changes slightly.

Overall, the results demonstrate, that the 3D TO method is robust, and that it is able to estimate the full 3D velocity vectors. Even with system noise, phase errors, and other transducer inaccuracies, the standard deviation of the velocity estimates is not much higher compared with the

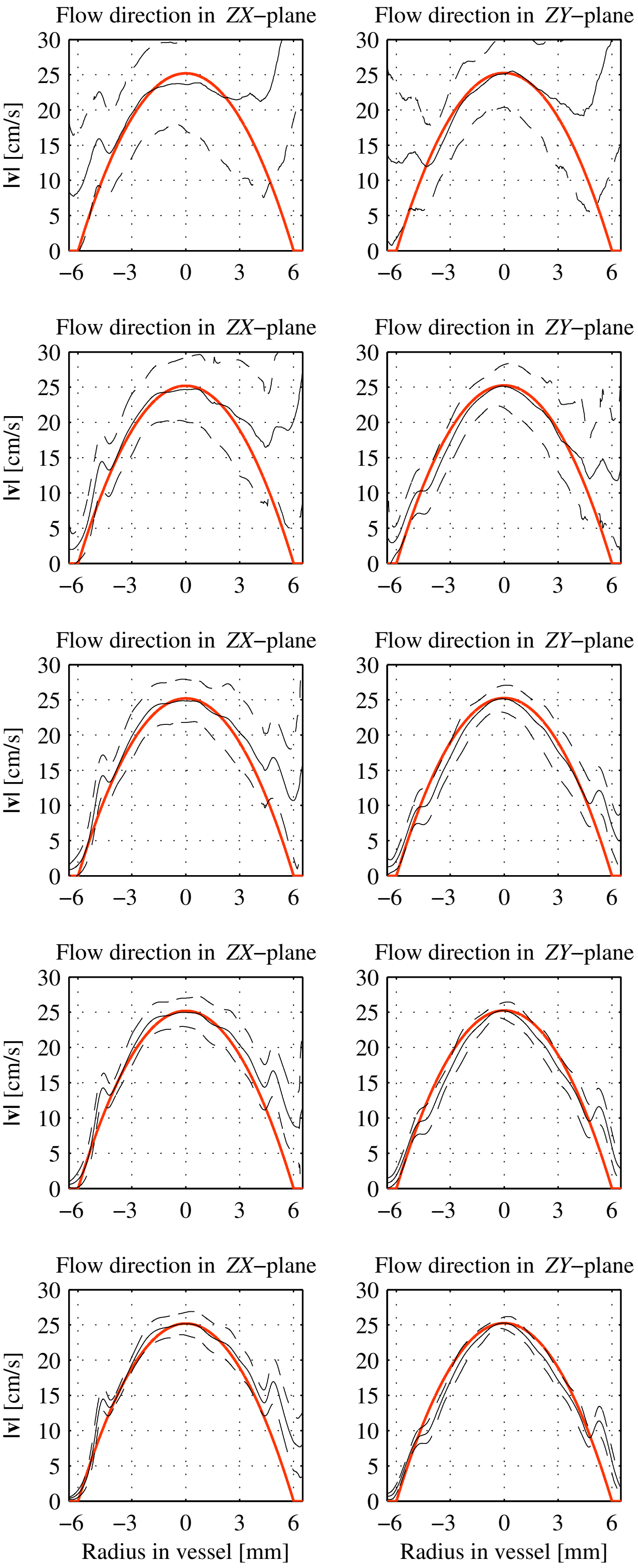

Figure 7.15 Mean and standard deviation of the measured velocity magnitude profiles as a function of ensemble length. From top to bottom: 8, 16, 32, 64, and 128 emissions per velocity estimate. Thick lines indicate the expected velocity profile, thin lines indicate the mean of the profiles, and dashed lines the range of one standard deviation.

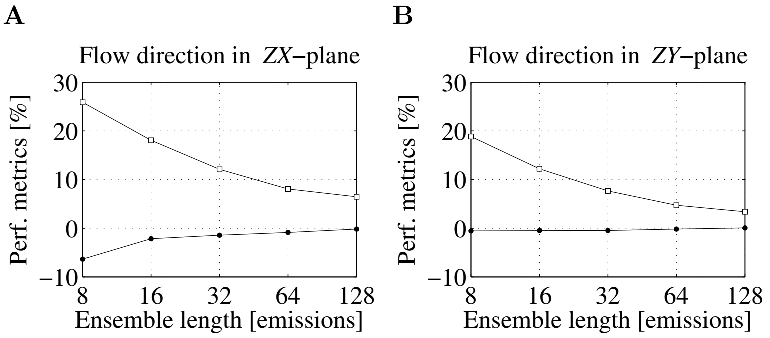

Figure 7.16 Performance metrics for the estimated velocity magnitude at the center of the vessel for the flow direction confined to **A** the ZX-plane and **B** the ZY-plane. (□) denotes the relative standard deviation and ($\cdot$) the relative bias.

simulations where the added noise was white zero-mean Gaussian noise. That is a positive result, and therefore, it is expected that the performance will be improved in a commercial implementation where systems usually suffer less from noise and the transducer manufacturing process is more streamlined.

7.7 3D vector flow imaging

This section presents the preliminary results of 3D vector flow images obtained in a cross-section of a vessel. The measurement setup differs slightly compared with the previous sections. These differences are highlighted below. Afterwards, the results are presented and discussed.

7.7.1 Measurement setup

The beams are steered radially, hence, the estimated axial velocity, v_a, the transverse velocity, v_t, and the elevation velocity, v_e, must be rotated and scan converted to obtain v_x, v_y and v_z. The velocity estimation of $v_{x'}$, $v_{y'}$, and $v_{z'}$ is the same as Section 6.4.3.

Velocities are measured in the flow-rig system. The transducer was aligned so that the scan plane was a cross-sectional plane of the vessel. This is illustrated in Figure 7.17. The velocity was set to be approximately 1.0 m/s to mimic the velocities of the blood in the carotid artery. The pulse repetition frequency was 2.4 kHz.

Ten frames of 3D vector flow images are acquired in a cross-sectional plane of the vessel orthogonal to the length axis, which coincides with the

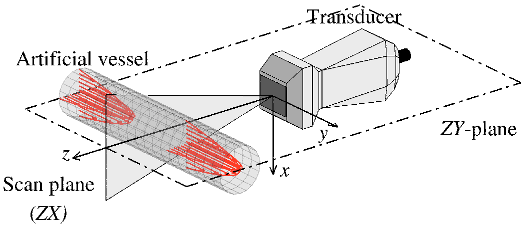

Figure 7.17 Illustration of the measurement setup. The transducer is placed above the vessel. Data are obtained along the z-axis (vertically) and in the ZX-plane.

y-axis and the flow direction. Each frame consists of 31 flow lines steered from -15° to 15° in steps of 1° in the ZX plane. For the center line, 3200 emissions are obtained yielding 100 M-mode lines The scan plane is the ZX plane, and thereby, the expected flow direction is $\mathbf{v}/|\mathbf{v}| = (0, 1, 0)$ in (x, y, z). Hence, only out of plane motion is expected, which cannot be measured by current commercial scanners.

7.7.2 Post processing

After matched filtration, the data are beamformed offline using the Beamformation Toolbox 3. Mean stationary echo cancelling (clutter filtering) is performed by subtracting the mean ensemble value from the 32 M-mode lines prior to the velocity estimation. The estimated transverse and axial velocities have to be rotated as they are obtained orthogonal to or along, respectively, the steered beams. The rotation of the axial, v_a, and the transverse, v_t, velocity components to obtain v_z and v_x is

$$\begin{pmatrix} v_z \\ v_x \end{pmatrix} = \begin{pmatrix} \cos\theta_{zx} & -\sin\theta_{zx} \\ \sin\theta_{zx} & \cos\theta_{zx} \end{pmatrix} \begin{pmatrix} v_{z'} \\ v_{x'} \end{pmatrix}$$

where θ_{zx} is the steering angle in the ZX plane. Due to the position of the scan plane, the elevation velocities, $v_{y'}$, are equal to v_y. Before displaying the 3D vector flow images, the velocities and the B-mode image are scan converted according to the steering angle of the lines from radial coordinates to Cartesian coordinates.

7.7.3 Measurement results and discussion

Figure 7.18 shows the velocity profiles for the three velocity components v_x, v_y, and v_z and the velocity magnitude obtained for M-mode lines along the diameter of the vessel. The mean of 100 velocity profiles along with the range of one standard deviation is displayed. The mean of the velocities follow the expected profiles. At the center of the vessel, the mean of the measured velocity vector along with the expected velocity and the resulting bias is

$$\bar{\mathbf{v}} = \begin{pmatrix} \bar{v}_x \\ \bar{v}_y \\ \bar{v}_z \end{pmatrix} = \begin{pmatrix} -0.03 \\ 95. \\ 1.0 \end{pmatrix} \pm \begin{pmatrix} 9. \\ 6. \\ 0.8 \end{pmatrix} \text{cm/s},$$

The expected velocities were

$$\mathbf{v}_{\text{exp}} = \begin{pmatrix} 0. \\ 96. \\ 0. \end{pmatrix} \text{cm/s},$$

yielding a bias of

$$\mathbf{B}_{\mathbf{v}} = \begin{pmatrix} -0.03 \\ -0.8 \\ -1. \end{pmatrix} \text{cm/s}.$$

The results demonstrate the performance of the estimator and that the method is capable of estimating 3D velocities.

The above results and Figure 7.18 demonstrate the performance of the 3D TO estimator using the given measurement equipment. As the results show, the standard deviation is higher for v_x compared with v_y. This is due to the transducer inaccuracies discussed above—such as phase aberrations and short-circuited elements—and the system noise, which especially affects elements and channels used for estimating v_x compared with the ones used for v_y. Nonetheless, the results presented above demonstrate the performance of the estimator, and that the method is capable of estimating 3D velocities.

Frames of 3D vector flow images in the 2D scan plane forming a cross section of the vessel are acquired. Due to the flow direction, no in plane velocity is expected. Hence, conventional 1D or even 2D velocity estimators would not measure any velocity. One of the ten 3D vector flow image frames is visualized in Figure 7.19. The figure displays the color flow images for the three velocity components and the absolute velocity magnitude. The velocity

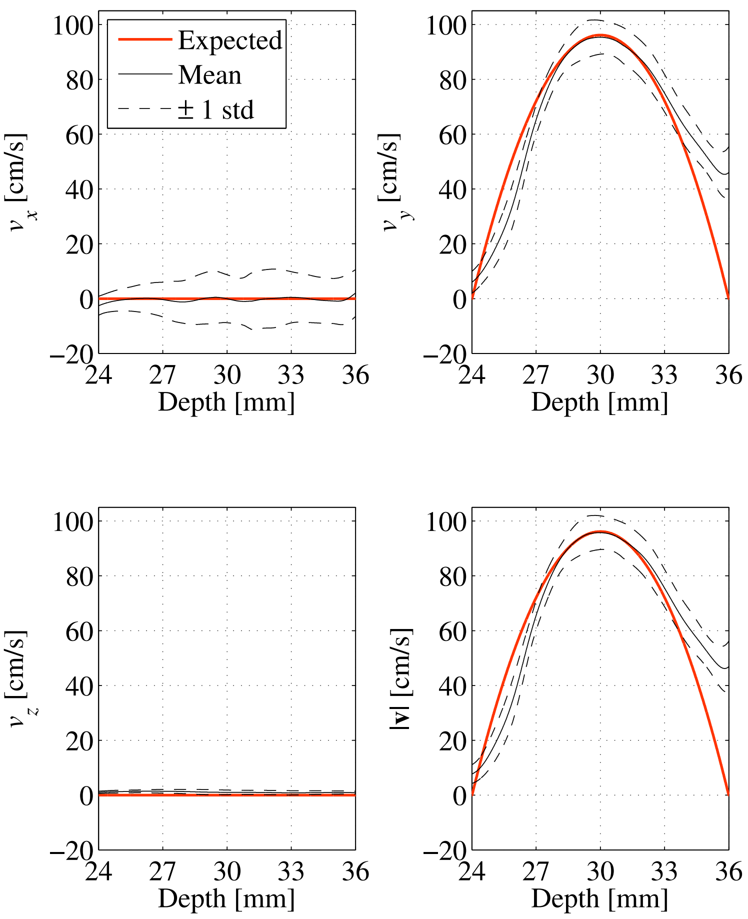

Figure 7.18 The mean and the range of one standard deviation as well as the expected profiles are plotted for the three velocity components and the resulting velocity magnitude through the center of the vessel.

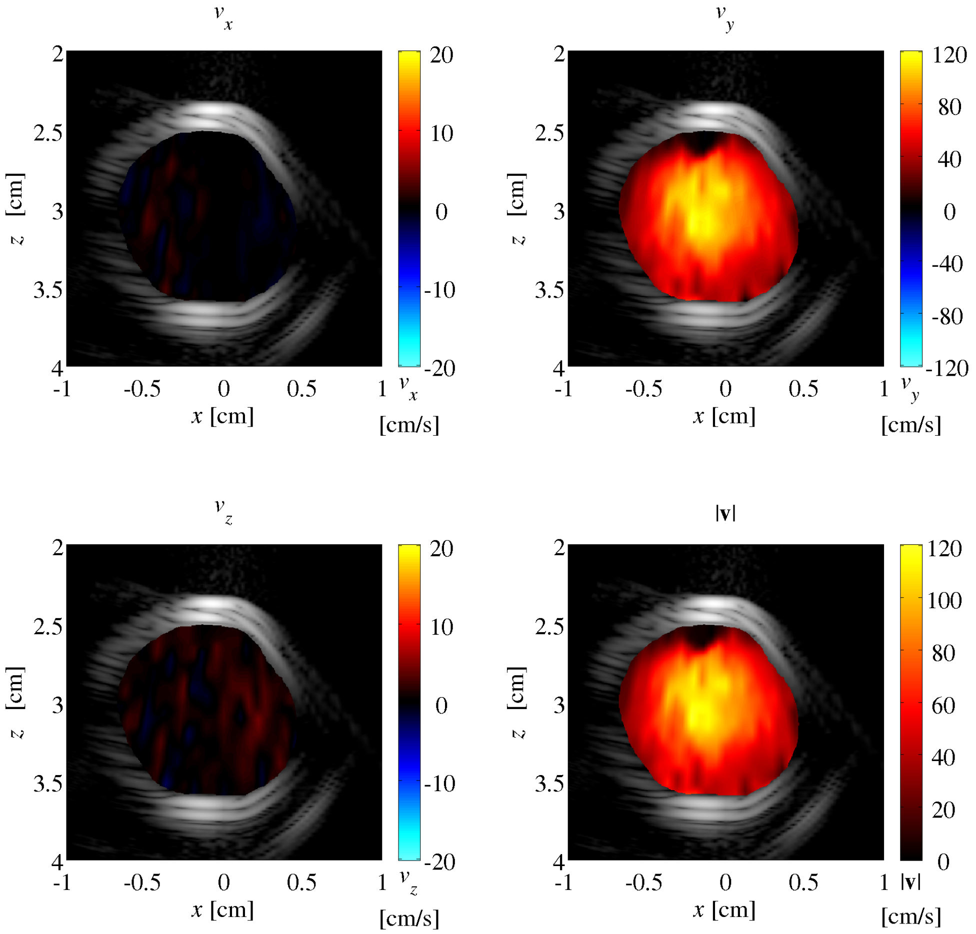

Figure 7.19 Measured 3D vector flow images in a 2D scan plan for the three scan converted velocity components v_x, v_y, and v_y and the velocity magnitude $|\mathbf{v}|$. The scan plan is orthogonal to the flow direction. Please note the different scaling of the colorbars. The mask for mapping the flow data was created by manually selecting the outline of the inner lumen based on the B-mode image (70 dB dynamic range). The black area in the top of the vessel lumen is due to clipping in the sampled channel data because of the strong reflections at the top of the vessel.

components v_x and v_z are almost zero in the scan plane as expected due to the flow direction. For v_y, the velocity is highest at the center of the vessel and lower at the vessel boundaries. Same appearance is found for the velocity magnitude $|\mathbf{v}|$. The shape is similar to the expected circular-symmetric 2D parabolic velocity profile.

7.8 Conclusion and perspectives

Based on the results it can be concluded that the 3D velocity vector estimates the 3D velocity vector. The measured and the simulated TO fields demonstrate that the 3D TO approach generates the spatial IQ pairs in the transverse and the elevation direction as hypothesized. Based on the simulated TO spectra, the mean spatial wavelengths in the transverse and elevation direction can be calculated and used in the subsequent beamforming and the velocity estimation.

Three-dimensional velocity estimates are obtained through experimental measurements and simulations of steady flow. The velocity profiles of the three components v_x, v_y, and v_z follow the expected profiles with a bias at the center ranging from -0.6 to 1 cm/s. Hence, using the simulated mean spatial wavelengths instead of the theoretically derived wavelengths in the beamforming and velocity estimation stages practically eliminates the bias otherwise present.

Using the same parameters and under similar conditions, the measurements and the simulations yield comparable results. Thereby, the validity of the simulation results presented here and previously reported has been verified.

Three-dimensional vector flow images using the 3D TO method has been presented, and they demonstrate the feasibility of using the method for 3D vector flow imaging. With the 3D TO method, the full 3D velocity vector—including the out of plane motion—and the correct velocity magnitude can be measured in e.g. cross sections of blood vessel. Conventional and even 2D methods would fail to estimate any velocity in the presented 3D vector flow images. The correct velocity magnitude can be obtained regardless of the orientation of the transducer, and therefore, operator independent. Additionally, the simultaneous calculation of the three velocity components is important for visualizing complex flow patterns. Hence, it will be possible to measure and visualize the full 3D vortices and rotational flow as found for instance in the carotid artery—particularly at the bifurcation or at stenoses.

Perspectives

With a 2D array it is possible to estimate the full 3D velocities. Furthermore, the 3D TO method can estimate the velocities in a volume, and hence provide volumetric 3D vector velocity images. This will pose a challenge in terms of visualizing these seven-dimensional data sets, where three dimensions are for the position, three for the velocity vector, and one is for time. As a first approach, image planes can be displayed with the in-plane velocities visualized as for instance arrows and colors—as has been done in the commercial implementation of 2D TO method. Rendering of semi-transparent stream lines in a volume is another approach used for instance to visualize volumetric 3D velocities obtained with MRI. The increasing power and use of graphical processing units may allow real-time rendering of the volumetric 3D velocity data. A third option could be to use holographic projections to display the velocity information in 3D.

Another challenge lies in the number of channels used in this work, where single channel data from 1024 tranducer elements were sampled. In a longer time frame, this will probably not pose a problem as the channel capacities of modern scanner constantly increase. Meanwhile, clever multiplexing and pre-beamforming may reduce the required number of channels. Additionally, besides employing piezo-electric transducers as in this thesis, capacitive micromachined ultrasonic transducers (CMUTs) are under development. CMUTs are micromachined devices, and it should be easier (when the technology is ripe) to construct 2D CMUT arrays compared with manufacturing large 2D piezo-electric arrays. CMUTs also allow the application of integrated circuits which will make various pre-beamforming schemes possible.

Finally, and more importantly, the clinical perspectives are multiple. It will be possible to obtain simultaneous estimates of the 3D velocity vectors, and thereby visualize and measure hemodynamic phenomena and complex flow patterns. In other words, it will be possible to measure the full 3D vortices and rotational flow as found for instance in the carotid artery—particularly at the bifurcation or at stenoses. The data can be obtained in real-time and for a much lower cost compared with MRI. The method may also be employed in screenings, as the full 3D velocity vector—and hence, the correct velocity magnitude—can be readily obtained independent of the operator. This may allow for larger screenings of increased peak systolic velocities in the carotid artery for detecting early indications of stenoses caused by atherosclerosis. These measurements could be conducted by less experienced sonographers or other medical personnel for screening purposes, yielding indicators for referral to further diagnosing.

3D vector velocity imaging may also provide additional insight for other cardiovascular diseases. Especially, a very interesting perspective would be the application of 3D velocity methods in cardiac imaging, where the actual vectors and magnitudes may contribute to a better understanding of normal and pathological flow patterns in the heart.

The clinical potential has still to be determined, and further development and investigation are required including phantom measurement and *in vivo* studies, yet, this thesis has served as a proof of concept for 3D vector velocity estimation and 3D vector flow imaging using the 3D Transverse Oscillation method.

8

Project conclusion

The main objective of this project has been to develop a method capable of estimating 3D velocities. The method will make use of a 2D phased array transducer and should be implementable on a commercial scanner. Chapter 4 demonstrates how it is possible to use the TO method on a commercial scanner to estimate 2D velocity vectors. It also shows that if the TO fields are poorly defined, the resulting velocities are biased. Bias compensation can remove this, but preferably, the method should be optimized to reduce the bias.

As an intermediate step, the method is expanded to a 1D phased array transducer. A new beamforming strategy and performance metrics to ease the optimization of the TO fields are suggested in Chapter 5, and it is demonstrated that these performance metrics are correlated with the standard deviation and the bias of the velocity estimates.

In Chapter 6, a method for estimating 3D vector velocities is proposed. The method is based on the TO approach and employs a 2D matrix array. The velocity estimation is decoupled into estimating the three velocity components. The velocity estimation is based on beamforming five lines from the same received data, and hence, the three velocity components are estimated simultaneously. Calculations of the number of operations needed, demonstrate that the required number of flops are within the capability of modern scanners. Simulations of parabolic flow demonstrate the feasibility of the method, where the mean spatial wavelengths were applied instead of the theoretical spatial wavelengths in the velocity estimation yielding a relative mean bias around 0 %. The relative mean standard deviations were less than 5 %. The flow angle was estimated without bias and with 95 % of the estimates within ±8.4°.

The proposed 3D TO method is investigated experimentally in Chapter 7. Measurements are acquired using a 32x32 element 2D transducer connected to the 1024 channels on the experimantel research scanner SARUS. Pulse-echo measurements are performed in a scanning tank using a hydrophone as a point target. The two pairs of TO fields are to a large extend 90° phase-shifted compared with each other, and the results exhibit similar performance compared with the simulated TO fields. The simulated mean spatial wavelengths were used in the following beamforming and velocity estimation. Experimental results are obtained in a flow-rig system with steady flow. The results demonstrate that the estimated velocity components follow the expected profiles, and that v_x and v_y can be separated. The bias is approximately 0 m/s, whereas the relative standard deviations for the transverse and elevation velocity components range from 8–12 %. The results are comparable with the simulated results obtained under similar conditions. The experimental velocities verify the previous simulated results and validate the capability of the method for 3D vector velocity estimation.

Subsequently, 3D velocities are obtained in a cross-sectional plane of the vessel. As expected, both v_x and v_z are practically 0 m/s, and only the out of plane velocity components are present. Thereby, also the true full velocity magnitude is estimated. Both v_y and the $|\mathbf{v}|$ exhibit the expected 2D circular-symmetric parabolic profile. The results demonstrate that the 3D TO method is suitable for 3D vector flow imaging.

8.1 Perspectives and future work

During this project a method for estimating 3D vector velocities has been developed, and it has been demonstrated that the method is suitable for 3D vector flow imaging. The estimation of the three velocity components makes it possible to estimate the true velocity magnitude independent of transducer orientation and operator angle-compensation. This has been demonstrated in a 2D plane, and the next step is to measure the 3D velocities in a volume. The potential of this is automated peak velocity estimation in use for improved diagnosis or even screening of carotid artery stenosis.

The estimation of 3D velocities in a 3D volume will give rise to new issues in terms of displaying the three dimensional volumetric data set with one 3-D velocity vector associated with each voxel as a function of time. The data to display will therefore have three spatial coordinates, the three velocity components, and time.

The simultaneous estimation of the 3D velocity vector components is important for estimating complex 3D flow patterns in planes and volumes. Here, further research include measurements on realistic flow phantoms of e.g. the carotid artery bifurcation with and without stenosis under pulsatile flow conditions. Obtained velocities may also be compared with CFD modelling or MRI measurements in terms of velocities or volume flow. The 3D velocities can also be used as input to CFD models or for validation purposes.

The requirements of the method are within the capabilities of modern scanners which is an advantage in terms of the clinical impact. 3D vector flow imaging may aid and provide new information in e.g. cardiac imaging and in the diagnosis of cardiovascular diseases as stenosis or malfunctioning valves. The proposed 3D TO method has this potential.

Bibliography

Please note that the (page) numbers appearing at the end of each bibliography entry link to the page(s) with the reference.

[1] E. G. Grant et al. Carotid artery stenosis: Gray-scale and Doppler US diagnosis - society of radiologists in ultrasound consensus conference. *Radiology*, 229(2):340–346, 2003. 1, 16

[2] C. Arning, B. Widder, G. M. von Reutern, H. Stiegler, and M. Görtler. Revison of DEGUM Ultrasound Criteria for Grading Internal Carotid Artery Stenoses and Transfer to NASCET Measurement. *Ultraschall in Med.*, 31 (3):251–257, 2010. 1, 16

[3] D. J. Phillips, K. W. Beach, J. Primozich, and D. E. Strandness. Should results of ultrasound Doppler studies be reported in units of frequency or velocity? *Ultrasound Med. Biol.*, 15:205–212, 1989. 1, 18, 84

[4] K. L. Hansen, J. Udesen, F. Gran, J. A. Jensen, and M. B. Nielsen. In-vivo examples of complex flow patterns with a fast vector velocity method. *Ultraschall in Med.*, 30:471–476, 2009. 1, 18, 20, 84

[5] M. M. Wood, L. E. Romine, Y. K. Lee, K. M. Richman, M. K. O'Boyle, D. A. Paz, P. K. Chu, and D. H. Pretorius. Spectral Doppler signature waveforms in ultrasonography: A review of normal and abnormal waveforms. *Ultrasound Q.*, 26(2):83–99, 2010. 1

[6] L. J. Frazin, G. Lanza, M. Vonesh, F. Khasho, C. Spitzzeri, S. McGee, D. Mehlman, K. B. Chandran, J. Talano, and D. McPherson. Functional chiral asymmetry in descending thoracic aorta. *Circulation*, 82(6):1985–1994, 1990. 1

[7] P. Tortoli, V. Michelassi, G. Bambi, F. Guidi, and D. Righi. Interaction between secondary velocities, flow pulsation and vessel morphology in the common carotid artery. *Ultrasound Med. Biol.*, 29(3):407–415, 2003. 1

[8] P. J. Kilner, G. Z. Yang, R. H. Mohiaddin, D. N. Firmin, and D. B. Longmore. Helical and retrograde secondary flow patterns in the aortic arch studied by three-directional magnetic resonance velocity mapping. *Circulation*, 88(5):2235–2247, 1993. 1

[9] M. Markl, M. T. Draney, M. D. Hope, J. M. Levin, F. P. Chan, M. T. Alley, N. J. Pelc, and R. J. Herfkens. Time-resolved 3-dimensional velocity

mapping in the thoracic aorta: Visualization of 3-directional blood flow patterns in healthy volunteers and patients. *J. Comput. Assist. Tomogr.*, 28(4):459–468, 2004.

[10] A. Harloff, F. Albrecht, J. Spreer, A. F. Stalder, J. Bock, A. Frydrychowicz, J. Schollhorn, A. Hetzel, M. Schumacher, J. Hennig, and M. Markl. 3D blood flow characteristics in the carotid artery bifurcation assessed by flow-sensitive 4D MRI at 3T. *Magn. Reson. Med.*, 61(1):65–74, 2009. 1

[11] C.A. Taylor, T.J.R. Hughes, and C.K. Zarins. Finite element modeling of blood flow in arteries. *Comput. Methods Appl. Mech. Engrg.*, 158(1): 155–196, 1998. 1

[12] D. A. Steinman, J. B. Thomas, H. M. Ladak, J. S. Milner, B. K. Rutt, and J. D. Spence. Reconstruction of carotid bifurcation hemodynamics and wall thickness using computational fluid dynamics and MRI. *Magn Reson Med*, 47(1):149–159, 2002.

[13] I. Marshall, S. Zhao, P. Papathanasopoulou, P. Hoskins, and X. Y. Xu. MRI and CFD studies of pulsatile flow in healthy and stenosed carotid bifurcation models. *J. Biomech.*, 37:679–687, 2004.

[14] A. Swillens, L. Løvstakken, J. Kips, H. Torp, and P. Segers. Ultrasound simulation of complex flow velocity fields based on computational fluid dynamics. *IEEE Trans. Ultrason., Ferroelec., Freq. Contr.*, 56(3):546–556, 2009. doi: 10.1109/TUFFC.2009.1071. 1

[15] J.S. Milner, J.A. Moore, B.K. Rutt, and D.A. Steinman. Hemodynamics of human carotid artery bifurcations: Computational studies with models reconstructed from magnetic resonance imaging of normal subjects. *J. Vasc. Surg.*, 28(1):143–156, 1998. 1

[16] A. M. Malek, S. L. Alper, and S. Izumo. Hemodynamic shear stress and its role in atherosclerosis. *JAMA*, 282(21):2035–2042, 1999. 1

[17] M. J. Thubrikar. *Vascular Mechanics and Pathology.* Springer, New York, NY, 2007. 1

[18] S.-W. Lee, L. Antiga, J. D. Spence, and D. A. Steinman. Geometry of the carotid bifurcation predicts its exposure to disturbed flow. *Stroke*, 39: 2341–2347, 2008. 1

[19] P. M. Hansen, M. M. Pedersen, K. L. Hansen, M. B. Nielsen, and J. A. Jensen. Demonstration of a vector velocity technique. *Ultraschall in Med.*, 32:213–215, 2011. 1, 36

[20] J. A. Jensen and P. Munk. A New Method for Estimation of Velocity Vectors. *IEEE Trans. Ultrason., Ferroelec., Freq. Contr.*, 45:837–851, 1998. 2, 25, 28, 30, 31, 37, 42, 84

[21] M. C. Hemmsen, S. I. Nikolov, M. M. Pedersen, M. J. Pihl, M. S. Enevoldsen, J. M. Hansen, and J. A. Jensen. Implementation of a versatile research data acquisition system using a commercially available medical ultrasound scanner. *IEEE Trans. Ultrason., Ferroelec., Freq. Contr.*, 59(7):1487–1499, 2012. 3, 39, 41

[22] J. A. Jensen. Medical ultrasound imaging. *Prog. Biophys. Mol. Biol.*, 93: 153–165, 2007. 9, 10

[23] P. N. T. Wells. Ultrasonic color-flow imaging. *Phys. Med. Biol.*, 39(12): 2113–2145, Dec 1994. 10, 13

[24] B. Dunmire and K. W. Beach. A Brief History of Vector Doppler. In *Proc. SPIE Med. Imag.*, volume 4325, pages 200–214, Feb. 2001. 10, 12, 18

[25] D. H. Evans, J. A. Jensen, and M. B. Nielsen. Ultrasonic colour Doppler imaging. *Interface Focus*, 1(4):490–502, August 2011. 10, 15, 16

[26] D. H. Evans, W. N. McDicken, R. Skidmore, and J. P. Woodcock. *Doppler Ultrasound, Physics, Instrumentation, and Clinical Applications.* John Wiley & Sons, New York, 1989. 10

[27] J. A. Jensen. *Estimation of Blood Velocities Using Ultrasound: A Signal Processing Approach.* Cambridge University Press, New York, 1996. 10, 12, 13, 14, 16, 44, 69

[28] D. H. Evans and W. N. McDicken. *Doppler Ultrasound, Physics, Instrumentation, and signal processing.* John Wiley & Sons, New York, 2000. 10, 11, 13, 18, 20

[29] S. Satomura. Ultrasonic Doppler method for the inspection of cardiac functions. *J. Acoust. Soc. Am.*, 29:1181–1185, 1957. 12

[30] C. Kasai, K. Namekawa, A. Koyano, and R. Omoto. Real-Time Two-Dimensional Blood Flow Imaging using an Autocorrelation Technique. *IEEE Trans. Son. Ultrason.*, 32:458–463, 1985. 14, 15, 91

[31] D. Dotti, E. Gatti, V. Svelto, A. Uggè, and P. Vidali. Blood flow measurements by ultrasound correlation techniques. *Energia Nucleare*, 23:571–575, 1976. 15

[32] O. Bonnefous and P. Pesqué. Time domain formulation of pulse-Doppler ultrasound and blood velocity estimation by cross correlation. *Ultrason. Imaging*, 8:73–85, 1986. doi: 10.1016/0161-7346(86)90001-5. 15

[33] S. G. Foster, P. M. Embree, and W. D. O'Brien. Flow velocity profile via time-domain correlation: Error analysis and computer simulation. *IEEE Trans. Ultrason., Ferroelec., Freq. Contr.*, 37:164–175, 1990. 15

[34] K. Namekawa, C. Kasai, M. Tsukamoto, and A. Koyano. Realtime bloodflow imaging system utilizing autocorrelation techniques. In R.A Lerski and P. Morley, editors, *Ultrasound '82*, pages 203–208, New York, 1982. Pergamon Press. 15

[35] T. Loupas, J. T. Powers, and R. W. Gill. An axial velocity estimator for ultrasound blood flow imaging, based on a full evaluation of the Doppler equation by means of a two-dimensional autocorrelation approach. *IEEE Trans. Ultrason., Ferroelec., Freq. Contr.*, 42:672–688, 1995. 15, 33, 90, 91

[36] T. Loupas, R. B. Peterson, and R. W. Gill. Experimental evaluation of velocity and power estimation for blood flow imaging, by means of a two-dimensional autocorrelation approach. *IEEE Trans. Ultrason., Ferroelec., Freq. Contr.*, 42:689–699, 1995. 15

[37] Y. Miyagi, H. Masaoka, N. Akamatsu, and K. Sekiba. Development of a three-dimensional color Doppler system. *Med. Prog. Technol.*, 18(4): 201–208, 1992. 15

[38] P. A. Picot, D. W. Ricky, R. Mitchell, R. N. Rankin, and A. Fenster. Three-dimensional colour Doppler imaging. *Ultrasound Med. Biol.*, 19:95–104, 1993. 15

[39] T. R. Nelson and D. H. Pretorius. Three-dimensional ultrasound imaging. *Ultrasound Med. Biol.*, 24:1243–1270, 1998. 16

[40] S. Berg, H. Torp, B. O. Haugen, and S. Samstad. Volumetric blood flow measurement with the use of dynamic 3-dimensional ultrasound color flow imaging. *J. Am. Soc. Echocardiog.*, 13(5):393–402, 2000. 16

[41] J. Pemberton, X. Li, A. Kenny, C. H. Davies, M. S. Minette, and D. J. Sahn. Real-time 3-dimensional Doppler echocardiography for the assessment of stroke volume: An in vivo human study compared with standard 2-dimensional echocardiography. *J. Am. Soc. Echocardiog.*, 18(10):1030–1036, 2005. 16

[42] H. Torp. Clutter Rejection Filters in Color Flow Imaging: A Theoretical Approach. *IEEE Trans. Ultrason., Ferroelec., Freq. Contr.*, 44(2):417–424, 1997. 16

[43] S. Bjærum, H. Torp, and K. Kristoffersen. Clutter filter design for ultrasound colour flow imaging. *IEEE Trans. Ultrason., Ferroelec., Freq. Contr.*, 49: 204–209, 2002. 16

[44] S. Bjærum, H. Torp, and K. Kristoffersen. Clutter filters adapted to tissue motion in ultrasound color flow imaging. *IEEE Trans. Ultrason., Ferroelec., Freq. Contr.*, 49(6):693–704, June 2002. 16, 20

[45] V. L. Newhouse, D. Censor, T. Vontz, J. A. Cisneros, and B. B. Goldberg. Ultrasound Doppler probing of flows transverse with respect to beam axis. *IEEE Trans. Biomed. Eng.*, BME-34:779–788, 1987. 18

[46] B. Dunmire, K. W. Beach, K-H Labs., M. Plett, and D. E. Strandness. Cross-beam vector Doppler ultrasound for angle independent velocity measurements. *Ultrasound Med. Biol.*, 26:1213–1235, 2000. 18, 22

[47] K. Fahrbach. Ein Beitrag Zur Blutgeschwindigkeitsmessung unter Anwendung des Dopplereffektes. *Elektromedizin*, 15(1):26–36, 1970. 18

[48] L. Capineri, M. Scabia, and L. Masotti. A Doppler system for dynamic vector velocity maps. *Ultrasound Med. Biol.*, 28(2):237–248, 2002. 19

[49] P. Tortoli, G. Bambi, and S. Ricci. Accurate Doppler angle estimation for vector flow measurements. *IEEE Trans. Ultrason., Ferroelec., Freq. Contr.*, 53(8):1425–1431, Aug. 2006. 19

[50] S. Ricci, S. Diciotti, L. Francalanci, and P. Tortoli. Accuracy and reproducibility of a novel dual-beam vector Doppler method. *Ultrasound Med. Biol.*, 35(5):829–838, 2009. 19

[51] M. Arigovindan, M. Sühling, C. Jansen, P. Hunziker, and M. Unser. Full motion and flow field recovery from echo Doppler data. *IEEE Trans. Med. Imag.*, 26(1):31–45, 2007. 19

[52] W. Li, C.T. Lancée, E. Ignacio Céspedes, A.F.W. Van Der Steen, and N. Bom. Decorrelation of intravascular echo signals: Potentials for blood velocity estimation. *J. Acoust. Soc. Am.*, 102:3785–3794, 1997. 19

[53] L. N. Bohs, S. C. Gebhart, M. E. Anderson, B. J. Geiman, and G. E. Trahey. 2-d motion estimation using two parallel receive beams. *IEEE Trans. Ultrason., Ferroelec., Freq. Contr.*, 48:392–408, 2001. 19

[54] J. A. Jensen. Directional velocity estimation using focusing along the flow direction: I: Theory and simulation. *IEEE Trans. Ultrason., Ferroelec., Freq. Contr.*, 50:857–872, 2003. 19

[55] J. A. Jensen and R. Bjerngaard. Directional velocity estimation using focusing along the flow direction: II: Experimental investigation. *IEEE Trans. Ultrason., Ferroelec., Freq. Contr.*, 50:873–880, 2003. 19

[56] J. A. Jensen and S. I. Nikolov. Directional synthetic aperture flow imaging. *IEEE Trans. Ultrason., Ferroelec., Freq. Contr.*, 51:1107–1118, 2004. 19

[57] J. Kortbek and J. A. Jensen. Estimation of velocity vector angles using the directional cross-correlation method. *IEEE Trans. Ultrason., Ferroelec., Freq. Contr.*, 53:2036–2049, 2006. 19

[58] L. Henze, I. K. Holfort, J. Kortbek, and J. A. Jensen. Transverse Correlation: An Efficient Transverse Flow Estimator – Initial Results. In *Proc. IEEE Ultrason. Symp.*, pages 1619–1622, 2008. 19

[59] G. E. Trahey, J. W. Allison, and O. T. von Ramm. Angle independent ultrasonic detection of blood flow. *IEEE Trans. Biomed. Eng.*, BME-34: 965–967, 1987. 20

[60] G. E. Trahey, S. M. Hubbard, and O. T. von Ramm. Angle independent ultrasonic blood flow detection by frame-to-frame correlation of B-mode images. *Ultrasonics*, 26:271–276, 1988. 20

[61] L. N. Bohs and G. E. Trahey. A novel method for angle independent ultrasonic imaging of blood flow and tissue motion. *IEEE Trans. Biomed. Eng.*, 38:280–286, 1991. 20

[62] L. N. Bohs, B. H. Friemal, B. A. McDermott, and G. E. Trahey. A real-time system for quantifying and displaying two-dimensional velocities using ultrasound. *Ultrasound Med. Biol.*, 19:751–761, 1993. 20

[63] L. N. Bohs, B. J. Geiman, K. R. Nightingale, C. D. Choi, B. H. Friemel, and G. E. Trahey. Ensemble tracking: a new method for 2D vector velocity measurement. In *Proc. IEEE Ultrason. Symp.*, pages 1485–1488, 1995. 20

[64] L. N. Bohs, B. J. Geiman, S. M. Breit, and G. E. Trahey. Ensemble tracking for 2D vector velocity measurement: experimental and initial clinical results. *IEEE Trans. Ultrason., Ferroelec., Freq. Contr.*, 45:912–924, 1998. 20

[65] L. Sandrin, S. Manneville, and M. Fink. Ultrafast two-dimensional ultrasonic speckle velocimetry: A tool in flow imaging. *Appl. Phys. Lett.*, 78(8):1155–1157, 2001. 20

[66] J. Udesen, F. Gran, K. L. Hansen, J. A. Jensen, C. Thomsen, and M. B. Nielsen. High frame-rate blood vector velocity imaging using plane waves: Simulations and preliminary experiments. *IEEE Trans. Ultrason., Ferroelec., Freq. Contr.*, 55(8):1729–1743, 2008. 20

[67] M. Crapper, T. Bruce, and C. Gouble. Flow field visualization of sediment-laden flow using ultrasonic imaging. *Dynam. Atmos. Oceans*, 31(1-4): 233–245, 2000. 20

[68] B. A. Lin, S. Einav, and M. Gharib. Digital ultrasound speckle image velocimetry for quantitative cardiovascular flow visualization. In *ASME Summer Bioengineering Conference*, pages 0163–0164, 2003.

[69] M. Gharib and M. Beizaie. Correlation between negative near-wall shear stress in human aorta and various stages of congestive heart failure. *Ann. Biomed. Eng.*, 31:678–685, 2003.

[70] H. B. Kim, J. R. Hertzberg, and R. Shandas. Development and validation of echo PIV. *Exp. Fluids*, 36:455–462, 2004.

[71] L. Liu, H. Zheng, L. Williams, F. Zhang, R. Wang, J. Hertzberg, and R. Shandas. Development of a custom-designed echo particle image velocimetry system for multi-component hemodynamic measurements: System characterization and initial experimental results. *Phys. Med. Biol.*, 53:1397–1412, 2008. 20

[72] C. E. Willert and M. Gharib. Digital particle image velocimetry. *Exp. Fluids*, 10(4):181–193, 1991. 20

[73] R. Y. Chiao, L. Y. Mo, A. L. Hall, S. C. Miller, and K. E. Thomenius. B-mode blod flow (B-flow) imaging. In *Proc. IEEE Ultrason. Symp.*, pages 1677–1680, 2000. 20

[74] L. Løvstakken, S. Bjærum, D. Martens, and H. Torp. Blood flow imaging - a new real-time, 2-D flow imaging technique. *IEEE Trans. Ultrason., Ferroelec., Freq. Contr.*, 53(2):289–299, February 2006. 20

[75] Løvstakken, K. S. Ibrahim, N. Vitale, S. T. Henriksen, I. Kirkeby-Garstad, H. Torp, and R. Haaverstad. Blood flow imaging: A new two-dimensional ultrasound modality for enhanced intraoperative visualization of blood flow patterns in coronary anastomoses. *J. Am. Soc. Echocardiog.*, 21(8):969–975, 2008. 20

[76] N. Oddershede, L. Løvstakken, H. Torp, and J. A. Jensen. Estimating 2-D vector velocities using multidimensional spectrum analysis. *IEEE Trans. Ultrason., Ferroelec., Freq. Contr.*, 55(8):1744–1754, 2008. 21

[77] A. Marion and D. Vray. Spatiotemporal filtering of sequences of ultrasound images to estimate a dense field of velocities. *Pattern Recogn.*, 42(11):2989–2997, 2009. 21

[78] Vernon L. Newhouse, Keith S. Dickerson, D. Cathignol, and J.-Y. Chapelon. Three-dimensional vector flow estimation using two transducers and spectral width. *IEEE Trans. Ultrason., Ferroelec., Freq. Contr.*, 41:90–95, 1994. 21

[79] A. McArdle, V.L. Newhouse, and K.W. Beach. Demonstration of three-dimensional vector flow estimation using bandwidth and two transducers on a flow phantom. *Ultrasound Med. Biol.*, 21:679–692, 1995. 21

[80] R. E. Daigle, C. W. Miller, M. B. Histand, F. D. McLeod, and D. E. Hokanson. Nontraumatic aortic blood flow sensing by use of an ultrasonic esophageal probe. *J. Applied Phys.*, 38:1153–1160, 1975. 22

[81] M. D. Fox. Multiple crossed-beam ultrasound Doppler velocimetry. *IEEE Trans. Son. Ultrason.*, SU-25:281–286, 1978. 22

[82] M. D. Fox and W. M. Gardiner. Three-dimensional Doppler velocimetry of flow jets. *IEEE Trans. Biomed. Eng.*, 35:834–841, 1988. 22

[83] J. R. Overbeck, K. W. Beach, and D. E. Strandness. Vector Doppler: Accurate measurement of blood velocity in two dimensions. *Ultrasound Med. Biol.*, 18:19–31, 1992. 22

[84] D. W. Rickey, P. A. Picot, D. W. Holdsworth, M. Drangova, D. J. M. Miller, R. N. Rankin, and A. Fenster. Quantitative three-dimensional true velocity colour Doppler imaging. In *Proc. IEEE Ultrason. Symp.*, pages 1277–1280, 1991. 22

[85] J. M. Rubin, T. A. Tuthill, and J. B. Fowlkes. Volume flow measurement using doppler and grey-scale decorrelation. *Ultrasound Med. Biol.*, 27: 101–109, 2001. 22

[86] T.A. Tuthill, J.M. Rubin, and J.B. Fowlkes. Three-dimensional flow vectors from RF ultrasound signals. In *Proc. SPIE Med. Imag.*, volume 4687, pages 210–217, 2002. 22

[87] O. Bonnefous. Measurement of the complete (3D) velocity vector of blood flows. In *Proc. IEEE Ultrason. Symp.*, pages 795–799, 1988. 22

[88] I. A. Hein. Triple-beam lens transducers for three-dimensional ultrasonic fluid flow estimation. *IEEE Trans. Ultrason., Ferroelec., Freq. Contr.*, 42: 854–869, 1995. 23

[89] I. A. Hein. 3-D flow velocity vector estimation with a triple-beam lens transducer — experimental results. *IEEE Trans. Ultrason., Ferroelec., Freq. Contr.*, 44:85–95, 1997. 23

[90] J. A. Jensen and S. I. Nikolov. A method for real-time three-dimensional vector velocity imaging. In *Proc. IEEE Ultrason. Symp.*, pages 1582–1585, 2003. 23

[91] L. N. Bohs, B. J. Geiman, M. E. Anderson, S. C. Gebhart, and G. E. Trahey. Speckle tracking for multi-dimensional flow estimation. *Ultrasonics*, 38: 369–375, 2000. 23

[92] J. Meunier. Tissue motion assessment from 3D echographic speckle tracking. *Phys. Med. Biol.*, 43:1241–1254, 1998. 23

[93] X. Chen, H. Xie, R. Erkamp, K. Kim, C. Jia, J. M. Rubin, and M. O'Donnell. 3-D correlation-based speckle tracking. *Ultrason. Imaging*, 27(1):21–36, 2005. 23

[94] C. Poelma, J. M. Mari, N. Foin, M.-X. Tang, R. Krams, C. G. Caro, P. D. Weinberg, and J. Westerweel. 3D flow reconstruction using ultrasound PIV. *Exp. Fluids*, 50(4):777–785, 2011. 23

[95] G. R. Bashford and O. T. von Ramm. Ultrasound three-dimensional velocity measurements by feature tracking. *IEEE Trans. Ultrason., Ferroelec., Freq. Contr.*, 43(3):376–384, 1996. 23

[96] A. A. Morsy and O. T. von Ramm. FLASH correlation: A new method for 3-D ultrasound tissue motion tracking and blood velocity estimation. *IEEE Trans. Ultrason., Ferroelec., Freq. Contr.*, 46:728–736, 1999. 23

[97] Y. Ogura, K. Katakura, and M Okujima. A method of ultrasonic 3-D computed velocimetry. *IEEE Trans. Biomed. Eng.*, 44(9):823–830, 1997. 23

[98] P. Munk and J. A. Jensen. Performance of a vector velocity estimator. In *Proc. IEEE Ultrason. Symp.*, pages 1489–1493, 1998. 25

[99] P. Munk. Estimation of the 2-D flow vector in ultrasonic imaging: A new approach. Master's thesis, Department of Information Technology, Technical University of Denmark, 1996. 25

[100] M. E. Anderson. Spatial quadrature: a novel technique for multi-dimensional velocity estimation. In *Proc. IEEE Ultrason. Symp.*, volume 45, pages 1233–1238, 1997. 25

[101] M. E. Anderson. Multi-dimensional velocity estimation with ultrasound using spatial quadrature. *IEEE Trans. Ultrason., Ferroelec., Freq. Contr.*, 45:852–861, 1998. 25, 31

[102] M. E. Anderson and R. F. Kerr. In vivo lateral flow estimation with spatial quadrature. In *Proc. IEEE Ultrason. Symp.*, volume 2, pages 1445–1449, 2001. 25

[103] C. Sumi. Displacement vector measurement using instantaneous ultrasound signal phase - multidimensional autocorrelation and Doppler methods. *IEEE Trans. Ultrason., Ferroelec., Freq. Contr.*, 55(1):24–43, 2008. 25

[104] P. Munk. *Estimation of blood velocity vectors using ultrasound.* PhD thesis, Department of Information Technology, Technical University of Denmark, Lyngby, Denmark, 2000. 26, 28, 31, 37, 54

[105] J. Udesen. *2-D blood vector velocity estimation using a phase shift estimator.* PhD thesis, Ørsted•DTU, Technical University of Denmark, 2800, Lyngby, Denmark, 2005. 26, 27, 28, 37

[106] P. Munk and J. A. Jensen. Performance of velocity vector estimation using an improved dynamic beamforming setup. In *Proc. of SPIE: Progress in biomedical optics and imaging*, volume 4325, pages 227–241, 2001. 26

[107] J. A. Jensen. A New Estimator for Vector Velocity Estimation. *IEEE Trans. Ultrason., Ferroelec., Freq. Contr.*, 48(4):886–894, 2001. 26, 31, 32, 33, 90

[108] J. Udesen and J. A. Jensen. Investigation of Transverse Oscillation Method. *IEEE Trans. Ultrason., Ferroelec., Freq. Contr.*, 53:959–971, 2006. 26, 28, 31, 44, 46, 112

[109] J. Udesen, M. B. Nielsen, K. R. Nielsen, and J. A. Jensen. Examples of in-vivo blood vector velocity estimation. *Ultrasound Med. Biol.*, 33:541–548, 2007. 26

[110] J. A. Jensen. Apparatus and method for determining movements and velocities of moving objects, International patent PCT/DK97/00287, 1996. 26

[111] J. A. Jensen. An estimator for vector velocity estimation, International patent, 2000. 26

[112] H. Liebgott, J. Fromageau, J. E. Wilhjelm, D. Vray, and P. Delachartre. Beamforming scheme for 2D displacement estimation in ultrasound imaging. *EURASIP J. Adv. Signal Process.*, 2005(8):1212–1220, 2005. 26

[113] H. Liebgott, J. Wilhjelm, J. A. Jensen, D. Vray, and P. Delachartre. PSF dedicated to estimation of displacement vectors for tissue elasticity imaging with ultrasound. *IEEE Trans. Ultrason., Ferroelec., Freq. Contr.*, 54(4): 746–756, 2007. 26

[114] H. Liebgott, A. Basarab, S. Marincas, O. Bernard, and D. Friboulet. Tangential oscillations for motion estimation in echocardiography. In *Proc. IEEE Ultrason. Symp.*, pages 1761–1764, nov. 2008. 26

[115] H. Liebgott, A. Ben Salem, A. Basarab, Hang Gao, P. Claus, J. D'hooge, P. Delachartre, and D. Friboulet. Tangential sound field oscillations for 2D motion estimation in echocardiography. In *Proc. IEEE Ultrason. Symp.*, pages 498–501, Sept. 2009. 26

[116] H. Liebgott, A. Basarab, P. Gueth, C. Cachard, and P. Delachartre. Lateral RF image synthesis using a synthetic aperture imaging technique. *IEEE Trans. Ultrason., Ferroelec., Freq. Contr.*, 55(9):2097–2103, 2008. 26

[117] A. Basarab, P. Gueth, H. Liebgott, and P. Delachartre. Phase-based block matching applied to motion estimation with unconventional beamforming strategies. *IEEE Trans. Ultrason., Ferroelec., Freq. Contr.*, 56(5):945–957, 2009. 26

[118] J. W. Goodman. *Introduction to Fourier optics*. McGraw Hill Inc., New York, second edition, 1996. 28, 29

[119] S. M. Gehlbach and R. E. Alvarez. Digital ultrasound imaging techniques using vector sampling and raster line reconstruction. *Ultrason. Imaging*, 3 (1):83–107, 1981. 30

[120] G. R. Lockwood, P-C. Li, M. O'Donnell, and F. S. Foster. Optimizing the radiation pattern of sparse periodic linear arrays. *IEEE Trans. Ultrason., Ferroelec., Freq. Contr.*, 43:7–14, 1996. 30

[121] M. E. Anderson. Vector flow estimator isomorphism and wall filter requirements. In *Proc. SPIE Med. Imag.*, volume 4325, pages 215–226, 2001. 31

[122] J. Udesen, M. B. Nielsen, K. R. Nielsen, and J. A. Jensen. Examples of in-vivo blood vector velocity estimation. *Ultrasound Med. Biol.*, 33:541–548, 2007. 33

[123] J. Udesen, M. B. Nielsen, K. R. Nielsen, and J. A. Jensen. Blood vector velocity estimation using an autocorrelation approach: In vivo investigation. In *Proc. IEEE Ultrason. Symp.*, pages 162–166, 2005. 33

[124] J. A. Jensen, O. Holm, L. J. Jensen, H. Bendsen, H. M. Pedersen, K. Salomonsen, J. Hansen, and S. Nikolov. Experimental ultrasound system for real-time synthetic imaging. In *Proc. IEEE Ultrason. Symp.*, volume 2, pages 1595–1599, 1999. 33

[125] K. L. Hansen, J. Udesen, N. Oddershede, L. Henze, C. Thomsen, J. A. Jensen, and M. B. Nielsen. In-vivo evaluation of three ultrasound vector velocity techniques with MR angiography. In *Proc. IEEE Ultrason. Symp.*, pages 1060–1063, 2008. 33

[126] K. L. Hansen, J. Udesen, C. Thomsen, J. A. Jensen, and M. B. Nielsen. In vivo validation of a blood vector velocity estimator with MR angiography. *IEEE Trans. Ultrason., Ferroelec., Freq. Contr.*, 56(1):91–100, 2009.

[127] K. L. Hansen, J. Udesen, N. Oddershede, L. Henze, C. Thomsen, J. A. Jensen, and M. B. Nielsen. In vivo comparison of three ultrasound vector velocity techniques to MR phase contrast angiography. *Ultrasonics*, 49: 659–667, 2009. 33

[128] M. J. Pihl. Investigation of ultrasound vector flow imaging on a commercial platform. Master's thesis, DTU Elektro, Technical University of Denmark, Lyngby, Denmark, 2009. 34

[129] M. M. Pedersen, M. J. Pihl, P. Haugaard, J. M. Hansen, K. L. Hansen, M. B. Nielsen, and J. A. Jensen. Comparison of real-time in vivo spectral and vector velocity estimation. *Ultrasound Med. Biol.*, 38(1):145–151, 2012. 34

[130] M. M. Pedersen. *Quantification of In Vivo 2D Vector Flow Ultrasound*. PhD thesis, Department of Radiology, Copenhagen University Hospital, Denmark, October 2011. 34, 35, 36

[131] M. M. Pedersen, M. J. Pihl, P. Haugaard, M. B. Nielsen, and J. A. Jensen. Quantification of complex blood flow using real-time in vivo vector flow ultrasound. In *Proc. IEEE Ultrason. Symp.*, pages 1088–1091, 2010. 34

[132] P. M. Hansen, M. M. Pedersen, K. L. Hansen, M. B. Nielsen, and J. A. Jensen. Examples of vector velocity imaging. In *15. Nordic-Baltic Conf. Biomed. Eng. and Med. Phys.*, 2011. 36

[133] M. M. Pedersen, M. J. Pihl, J. M. Hansen, P. M. Hansen, P. Haugaard, M. B. Nielsen, and J. A. Jensen. Secondary arterial blood flow patterns visualised with vector flow ultrasound. In *Proc. IEEE Ultrason. Symp.*, pages 1242–1245, 2011. 36

[134] J. A. Jensen, O. Holm, L. J. Jensen, H. Bendsen, S. I. Nikolov, B. G. Tomov, P. Munk, M. Hansen, K. Salomonsen, J. Hansen, K. Gormsen, H. M. Pedersen, and K. L. Gammelmark. Ultrasound Research Scanner for Real-time Synthetic Aperture Image Acquisition. *IEEE Trans. Ultrason., Ferroelec., Freq. Contr.*, 52 (5):881–891, May 2005. 39

[135] K. V. Ramnarine, D. K. Nassiri, P. R. Hoskins, and J. Lubbers. Validation of a new blood mimicking fluid for use in Doppler flow test objects. *Ultrasound Med. Biol.*, 24:451–459, 1998. 44

[136] J. A. Jensen. Field: A program for simulating ultrasound systems. *Med. Biol. Eng. Comp.*, 10th Nordic-Baltic Conference on Biomedical Imaging, Vol. 4, Supplement 1, Part 1:351–353, 1996. 45

[137] J. A. Jensen and N. B. Svendsen. Calculation of Pressure Fields from Arbitrarily Shaped, Apodized, and Excited Ultrasound Transducers. *IEEE Trans. Ultrason., Ferroelec., Freq. Contr.*, 39:262–267, 1992. 45

[138] G. E. Tupholme. Generation of acoustic pulses by baffled plane pistons. *Mathematika*, 16:209–224, 1969. 45

[139] P. R. Stepanishen. Transient radiation from pistons in an infinite planar baffle. *J. Acoust. Soc. Am.*, 49:1629–1638, 1971. 45

[140] B. J. Oosterveld, J. M. Thijssen, and W. A. Verhoef. Texture of B-mode echograms: 3-D Simulations and experiments of the effects of diffraction and scatterer density. *Ultrason. Imaging*, 7(2):142–160, Apr. 1985. 61

[141] J. A. Jensen, M. Hansen, B. G. Tomov, S. I. Nikolov, and H. Holten-Lund. System architecture of an experimental synthetic aperture real time ultrasound system. In *Proc. IEEE Ultrason. Symp.*, pages 636–640, Oct. 2007. 71

[142] J. A. Jensen, H. Holten-Lund, R. T. Nielson, B. G. Tomov, M. B. Stuart, S. I. Nikolov, M. Hansen, and U. D. Larsen. Performance of SARUS: A Synthetic Aperture Real-time Ultrasound System. In *Proc. IEEE Ultrason. Symp.*, pages 305–309, Oct. 2010.

[143] M. B. Stuart, B. G. Tomov, and J. A. Jensen. Performance evaluation of a synthetic aperture real-time ultrasound system. In *IFMBE Proceedings; 34*, pages 160–163, Jun. 2011. 71

[144] J. M. Hansen, M. C. Hemmsen, and J. A. Jensen. An object-oriented multi-threaded software beamformation toolbox. In *Proc. SPIE Med. Imag.*, volume 7968, pages 79680Y 1–9, March 2011. URL `http://dx.doi.org/10.1117/12.878178`. 74

[145] J. Marcher. Vector velocity imaging using a commercial scanner - implementation of the transverse oscillation method using a phased array transducer. Master's thesis, Center for Fast Ultrasound Imaging, Department of Electrical Engineering, Technical University of Denmark, Lyngby, Denmark, March 2012. 81

[146] J. Marcher, M. J. Pihl, and J. A. Jensen. The transverse oscillation method using a phased array transducer. In *Proc. IEEE Ultrason. Symp.*, pages 1890–1893, 2012. 81

[147] M. E. Anderson. A heterodyning demodulation technique for spatial quadrature. In *Proc. SPIE Med. Imag.*, pages 1487–1490, 2000. 90, 91, 112

Paper I

Performance of the Transverse Oscillation Method using Beamformed Data from a Commercial Scanner

Michael Johannes Pihl, Svetoslav Nikolov, Per Haugaard,
Martin Christian Hemmsen, and Jørgen Arendt Jensen

Proceedings of the IEEE International Ultrasonics Symposium

Presented in Rome, Italy, 2009

Performance of the Transverse Oscillation Method using Beamformed Data from a Commercial Scanner

Michael Johannes Pihl[1], Svetoslav Nikolov[2], Per Haugaard[2], Martin Christian Hemmsen[1,2], and
Jørgen Arendt Jensen[1]

[1]Center for Fast Ultrasound Imaging, Department of Electrical Engineering,
Technical University of Denmark, DK-2800 Kgs. Lyngby, Denmark

[2]BK Medical ApS, Mileparken 34, DK-2730 Herlev, Denmark

Abstract— **Blood velocity estimates using conventional color flow imaging (CFI) or Doppler techniques are angle dependent. One of the proposed techniques to overcome this limitation is the Transverse Oscillation (TO) method, which also estimates the lateral velocity components. The performance of this is evaluated on a commercial platform. Beamformed data are acquired using a commercial BK Medical scanner as opposed to the previously reported results obtained with the experimental scanner RASMUS. The implementation is evaluated using an in-house circulating flow rig by calculating the relative mean standard deviation and bias of the velocity components. The relative mean standard deviation decreases as the number of shots per estimate increases and a value of 5% is obtained for 64 shots per estimate. For a center frequency of 5 MHz at 60°, 75°, and 90°, the relative mean bias varies from 21% to 27% and is lowest at a transmit focal depth close to the center of the vessel. The present performance is comparable with the results from the experimental scanner and simulations. It is obtained with only few changes to the conventional CFI setup and further optimization can improve the performance. This illustrates the feasibility of implementing the TO method on a commercial platform for real-time estimation.**

I. INTRODUCTION

Medical ultrasound is widely used to study blood flow dynamics in the human circulatory system. For instance, the estimation of blood flow velocities plays a key role in diagnosing major diseases in the carotid arteries [1]. However, blood velocity estimates using conventional color flow imaging (CFI) or Doppler techniques are angle dependent. That is a major limitation, and poses a huge challenge for quantitatively estimating the magnitude of the blood velocity. Present conventional techniques for estimating the magnitude of the velocity (as in spectral Doppler) are based on operator-based angle estimations, yet it is often difficult to predict flow direction and compensate for it [2]. It also strongly limits the possibility of visualizing complicated flow patterns like disturbed flow and vortices [3], which potentially carry pathological information about e.g. stenoses and malfunctioning valves.

Several techniques have been proposed to compensate for the inherent angle dependency problem. Fox [4] suggested a multibeam method, Trahey *et al.* [5] a speckle tracking technique, Newhouse *et al.* [6] an approach based on the transit-time spectral broadening effect, and Bonnefous [7] suggested using a number of beamformers working in parallel. Another method is the directional beamforming suggested by Jensen [8] or the Plane Wave Excitation method as recently suggested by Udesen *et al.* [9]. Another recent method using a cross correlation approach was proposed by Henze *et al.* [10]. Most of the above mentioned techniques have limitations in either geometry, computational load of the estimator, inherent noise, or heavy computational demands on beamformation.

Jensen and Munk [11] suggested the Transverse Oscillation (TO) method. Anderson [12] suggested a similar approach. The TO method has demonstrated promising *in vivo* results [13], [14]. However, the previously reported results have been obtained using the experimental scanner RASMUS [15], [16].

The purpose of this paper is to demonstrated the feasibility of a commercial implementation of the TO method for clinical use. The implementation is tested in a flow rig with a parabolic flow profile. Statistical measures are computed to evaluate and compare the performance to previously reported results with focus on the lateral velocity component.

The following section describes the methods employed, and the results are presented and discussed in Section III.

II. METHODS

A. TO implementation

The basic idea in the TO method is to create a double oscillating field by using special apodization profiles in receive. Two lines with a lateral displacement of a quarter spatial wavelength, corresponding to a 90° phase shift, are beamformed simultaneously in receive. A center line is also beamformed for traditional axial velocity estimation. For a description and derivation of the estimator, the reader is referred to Jensen [17].

Beamformed data are acquired using a BK Medical (Herlev, Denmark) 2202 Pro Focus scanner, a BK8812 linear array transducer, and a BK UA2227 research interface connected to a standard PC through a DALSA (Waterloo, ON, Canada) X64-CL Express camera link. Only minor changes to the conventional CFI setup, including adjusting the apodization and delay profiles in receive, are necessary to obtain the required data.

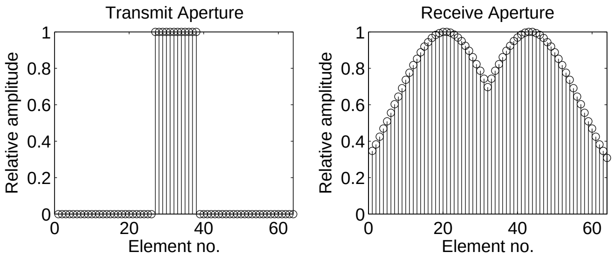

Fig. 1. The transmit and receive aperture for the TO estimator with a transmit focal depth at 15 mm. The transmit aperture is rectangular, and the F-number is 4. The receive aperture is the TO apodization.

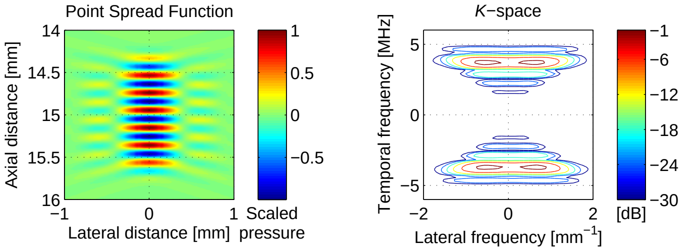

Fig. 2. The pulse-echo field (or point spread function) at the focal depth calculated based on the used transmit and receive apertures (left). The 2D-Fourier transform of the pulse-echo field, *i.e.* k-space representation (right)

The transmit and receive aperture functions used in this paper are illustrated in Fig. 1. A narrow transmit aperture produces a broad transmit field. The relative high apodization values in the receive aperture increases the signal-to-noise-ratio (SNR). The point spread function (PSF) is calculated using Field II [18], [19] and is depicted in Fig. 2, which also illustrates the 2D-Fourier transform of the pulse echo-field, *i.e.* the k-space representation. From Fig. 2 it can be noted that the transverse oscillations are 14 dB lower compared to the main lobe. They are lower compared to the ones presented by Udesen *et al.* [13], [14] where side lobes were around 2 dB down. This can also be observed from the k-space representation where the distinction of the two lateral peaks is poorer. The differences in PSFs affects the estimator.

Due to limitations in the current scanner setup, the TO apodization profile is kept constant over depth. This increases the spatial wavelength over depth. Therefore, the lateral velocity sensitivity changes over depth. This poses an optimization challenge, but does not affect the proof of concept.

The parameters for the measurements are shown in Table I. The table includes the physical setup of the flow rig, fixed scanner parameters, and the parameters that were varied in this study.

TABLE I

Parameters for the experimental flow rig measurements. Values marked with **bold face** denotes the reference setup.

Flow Rig Setup	Value
Vessel radius	5.7 mm
Center of vessel	16 mm
Peak velocity of flow, v_0	0.215 m/s
Fixed Scanner Parameters	Value
Distance between aperture peaks	6.6 mm
Pulse repetition frequency	1.3 kHz
Speed of sound	1480 m/s
Averaging length	1 pulse length **(2.4 mm)**
Number of transmit cycles	6
Transverse lag	1
Varied Scanner Parameter	Value
Number of shots per estimate	[4 8 **16** 31 61]
Transmit focus depth	[10 **15** 20 25 30] mm
Beam-to-flow angle	[60 **75** 90]°
Center frequency of CFI pulses	[**3.75** 5] MHz

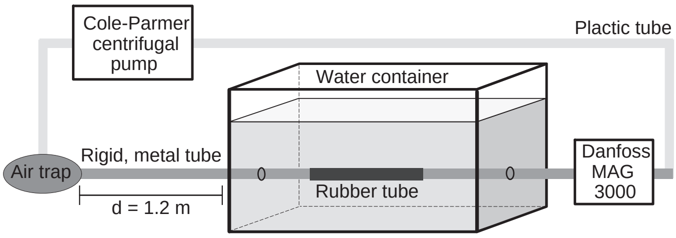

Fig. 3. The flow rig setup with a Cole-Parmer centrifugal pump, an air entrapment device, a water container with a rubber tube, and a Danfoss MAG 3000 magnetic flow meter. Notice that this figure is not to scale, and that the entrance length of the tube is more than 1.2 m, enough to ensure fully developed laminar flow. A fixture can be placed in the water container to keep the transducer fixed at a known beam-to-flow angle.

B. *Flow rig setup*

Velocity measurements are performed using an in-house circulating flow rig to evaluate the TO method. The setup consists of a long rigid tube replaced by a rubber tube inside a water filled container as illustrated in Fig. 3. The tube is filled with a blood mimicking fluid [13]. A Cole-Parmer (Vernon Hills, IL) 75211-60 centrifugal pump controls the fluid flow, and a Danfoss (Sønderborg, Denmark) MAG 3000 magnetic volume flow meter is used to measure the actual volume flow. The transducer can be placed in a fixture and the beam-to-flow angle can be set to a known value. The fixture can then be placed in the water container prior to the measurements.

C. *Statistics*

To investigate the performance of the method, a statistical analysis is performed on the data collected from the flow rig setup. It is assumed that the velocity estimates are independent between depths and between velocity profiles, and that the volume flow is constant over a measurement sequence.

At each discrete depth in the vessel, the velocity is estimated from a number of emissions. The average, $\bar{v}(z_k)$, of N estimates and the estimated standard deviation, $\sigma(z_k)$, is calculated at each discrete depth as

$$\bar{v}(z_k) = \frac{1}{N}\sum_{i=1}^{N} v_i(z_k) \qquad (1)$$

$$\sigma(z_k) = \sqrt{\frac{1}{N-1}\sum_{i=1}^{N}\left(v_i(z_k)-\bar{v}(z_k)\right)^2}, \qquad (2)$$

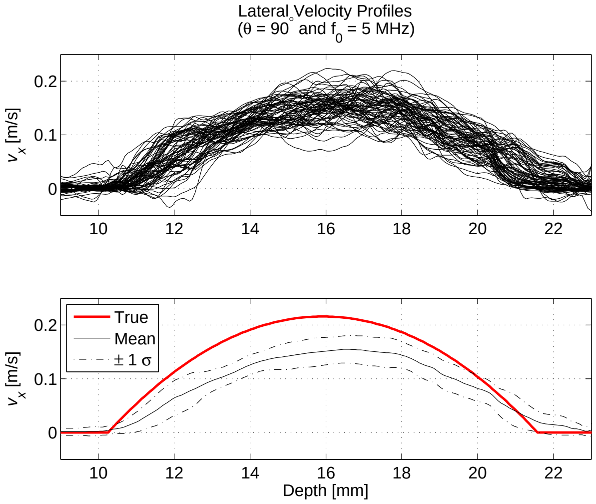

Fig. 4. TO estimated lateral velocities for 75 flow profiles with a beam-to-flow angle of 90° and a center frequency of 5 MHz (top). Mean estimate ± one standard deviation and expected theoretical velocity profile. No attempt has been made to suppress false velocity estimates at the vessel wall and in the surrounding water (bottom). Here, $\tilde{B}_{v_x}$ is 21% and $\tilde{\sigma}_{v_x}$ is 11%.

where $v_i(z_k)$ is the ith velocity estimate at the discrete depth z_k.

To determine the accuracy of the method, the bias, B, between the mean estimated velocity and the expected velocity, $v_\mu(z_k)$, at each depth can be calculated as

$$B = \bar{v}(z_k) - v_\mu(z_k). \tag{3}$$

For better and more straightforward comparison of various parameter settings, two single measures for the bias and the estimated standard deviation for a specific velocity profile are preferred. In order to do so, the estimated variance and the absolute bias are averaged over the entire vessel and divided by the peak velocity, v_0. The two quantities, the relative mean absolute bias, $\tilde{B}$, and the estimated relative mean standard deviation, $\tilde{\sigma}$, are given by

$$\tilde{B} = \frac{1}{v_0 \cdot N_{z_k}} \sum_{z_k=1}^{N_{z_k}} |B(z_k)| \tag{4}$$

$$\tilde{\sigma} = \frac{1}{v_0} \sqrt{\frac{1}{N_{z_k}} \sum_{z_k=1}^{N_{z_k}} \sigma(z_k)^2}, \tag{5}$$

where N_{z_k} is the number of discrete samples within the vessel. These measures can be used to describe the performance of the TO estimator.

III. RESULTS AND DISCUSSION

To address the feasibility of a commercial implementation of the TO method, the obtained results are compared with those from a simulation study and from the experimental scanner RASMUS, as previously reported [13], [20]. However, some parameters as well as the reference setup from the present study differ from the previous investigations.

Fig. 4 shows the estimated lateral velocity component of the flow profiles for 75 measurements at a beam-to-flow angle of 90° and at a center frequency of the transmitted pulse of 5 MHz. It also indicates the mean estimate ± one standard deviation and the expected true velocity. The TO method is clearly able to estimate the lateral velocity component, which is not possible with conventional estimators. As expected, the estimated lateral velocity profile has a parabolic shape. However, the TO estimator underestimates the velocity. With the parameter settings given in Table I the relative mean bias, $\tilde{B}_{v_x}$, is 21% and the relative standard deviation, $\tilde{\sigma}_{v_x}$, is 11%.

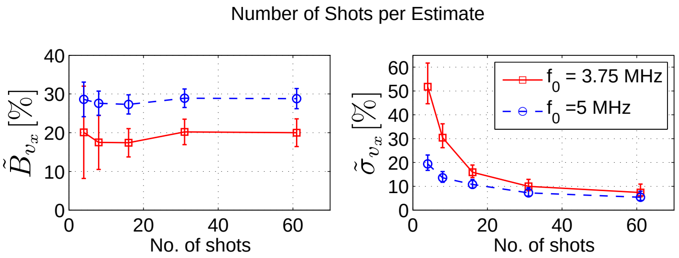

Fig. 5. The relative mean estimated bias, $\tilde{B}_{v_x}$, and relative mean estimated standard deviation, $\tilde{\sigma}_{v_x}$, for the lateral velocity component for center frequencies of 3.75 and 5 MHz. The error bars indicate the 95% confidence interval on $\tilde{B}_{v_x}$ and $\tilde{\sigma}_{v_x}$, respectively.

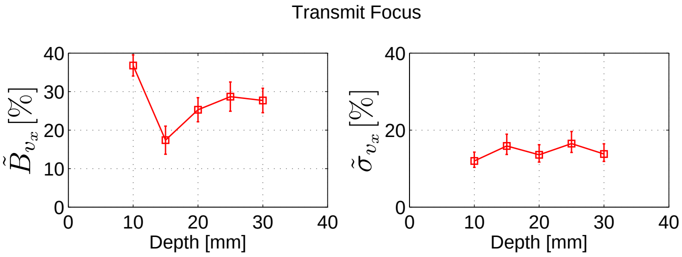

Fig. 6. $\tilde{B}_{v_x}$ and $\tilde{\sigma}_{v_x}$ for the lateral velocity component as a function of transmit focal depth (N=75).

A. Number of shots per estimate

When the number of shots per estimate is increased, $\tilde{\sigma}_{v_x}$ decreases, as expected, with approximately $\sqrt{N}$ as illustrated in Fig. 5. $\tilde{\sigma}_{v_x}$ is lower for 5 MHz than for 3.75 MHz. Conversely, $\tilde{B}_{v_x}$ is more or less constant, and somewhat larger for 5 MHz than for 3.75 MHz.

The results for the relative bias and standard deviation, when increasing the number of shots per estimate, show the same trend as the previously reported simulations [13]. The simulation results have lower values, but they are simulated with an infinite SNR, which is not the case in a real measurement situation. At 32 shots per estimate the simulated results had a relative standard deviation of 6% at 70°, where this study showed values of 7% and 10% at 75° with center frequencies at 5 MHz and 3.75 MHz, respectively. This demonstrates a similar performance, where it should be noted that the simulated results were obtained with a center frequency of 7 MHz and a different PSF.

B. Transmit focus

Varying the transmit focus from 10 to 30 mm in 5 mm increments yields the results shown in Fig. 6, where the F-

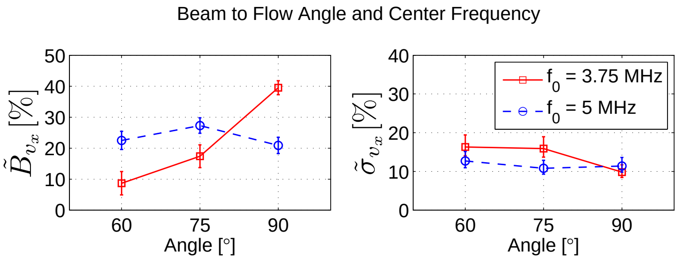

Fig. 7. $\tilde{B}_{v_x}$ and $\tilde{\sigma}_{v_x}$ as a function of beam-to-flow angle and for center frequencies of 3.75 and 5 MHz (N=75).

number is held constant at 4.0. $\tilde{B}_{v_x}$ has a minimum at 15 mm of 17%, whereas $\tilde{\sigma}_{v_x}$ shows no clear significant variation.

The obtained results for changing the transmit focus depth, show that for the given setup and a specific vessel location, the lowest bias is obtained with a focus depth of 15 mm. The 15 mm is close to the center of the vessel at 16 mm.

Comparing the results for different transmit focal depths with the simulations, the trends in the results are comparable. The optimal depth is a trade off between having a relative broad lateral extend when focusing beyond the vessel, and not reducing the SNR by emitting energy over a large area [13].

C. Beam-to-flow angle

Measurements were performed at three different beam-to-flow angles: 60°, 75°, and 90°. The resulting statistical measures are shown in Fig. 7.

For a center frequency at 3.75 MHz, the bias increases with increasing angle, whereas the standard deviation slightly decreases. For 5 MHz, the bias peaks at 75°, while the standard deviation is constant. A constant bias over the range of angles would be desirable, because it would then be possible to correct for the underestimation with a fixed scaling factor.

The beam-to-flow angle affects the magnitude of the axial and lateral velocity components. It also effects the bias and the standard deviation. The simulation results showed almost constant relative bias from 60° to 90°, whereas the relative standard deviation dropped from about 7% to 5%. The flow rig results in Udesen *et al.* [13] showed the same trend with a relative bias around 10% and a relative standard deviation from 4-7% for 32 shots per estimate and a center frequency of 7 MHz.

Comparing with the present study, $\tilde{\sigma}_{v_x}$ was more or less constant around 11% (5 MHz), and decreasing from 17 to 10% for 3.75 MHz both with 16 shots per estimate. This corresponds to the simulations and the results obtained with the experimental scanner, especially when taking the difference in number of shots and the variation in PSFs into account.

IV. CONCLUSION

The Transverse Oscillation method has been investigated using data from a commercial BK scanner. The implementation was evaluated and the results were compared to previously reported results from an experimental scanner. The results were found comparable having the differences in PSFs in mind. The performance can be improved by introducing a dynamic receive aperture, by further optimizations of the PSF, and a potential bias calibration. Hence, the feasibility of a commercial implementation for real-time estimations of blood flow vector velocity has been demonstrated.

ACKNOWLEDGEMENTS

This work was supported by grant 26-04-0024 from the Danish Science Foundation and by BK Medical Aps, Denmark.

REFERENCES

[1] E. G. Grant et al., "Carotid artery stenosis: Gray-scale and doppler us diagnosis - society of radiologists in ultrasound consensus conference," *Radiology*, vol. 229, no. 2, pp. 340–346, 2003.

[2] D. J. Phillips, K. W. Beach, J. Primozich, and D. E. Strandness, "Should results of ultrasound Doppler studies be reported in units of frequency or velocity?," *Ultrasound Med. Biol.*, vol. 15, pp. 205–212, 1989.

[3] K.L. Hansen, J. Udesen, F. Gran, J. A. Jensen, and M. B. Nielsen, "*In-vivo* examples of flow patterns with a fast vector velocity ultrasound method," *Ultraschall in Med.*, 2009. Accepted for publication.

[4] M. D. Fox, "Multiple crossed-beam ultrasound Doppler velocimetry," *IEEE Trans. Son. Ultrason.*, vol. SU-25, pp. 281–286, 1978.

[5] G. E. Trahey, J. W. Allison, and O. T. von Ramm, "Angle independent ultrasonic detection of blood flow," *IEEE Trans. Biomed. Eng.*, vol. BME-34, pp. 965–967, 1987.

[6] V. L. Newhouse, D. Censor, T. Vontz, J. A. Cisneros, and B. B. Goldberg, "Ultrasound doppler probing of flows transverse with respect to beam axis," *IEEE Trans. Biomed. Eng.*, vol. 34, pp. 779–789, 1987.

[7] O. Bonnefous, "Measurement of the complete (3D) velocity vector of blood flows," in *Proc. IEEE Ultrason. Symp.*, 1988, pp. 795–799.

[8] J. A. Jensen, "Directional velocity estimation using focusing along the flow direction: I: Theory and simulation," *IEEE Trans. Ultrason., Ferroelec., Freq. Contr.*, pp. 857–872, 2003.

[9] J. Udesen, F. Gran, K. L. Hansen, J. A. Jensen, C. Thomsen, and M. B. Nielsen, "Examples of *In Vivo* blood vector velocity estimation," *IEEE Trans. on Ultrason., Ferroelec., Freq. Contr.*, vol. 55, no. 8, pp. 1729–1743, 2008.

[10] L. Henze, I. K. Holfort, J. Kortbek, and J. A. Jensen, "Transverse Correlation: An Efficient Transverse Flow Estimator – Initial Results," in *Proc. IEEE Ultrason. Symp.*, 2008, pp. 1619–1622.

[11] J. A. Jensen and P. Munk, "A new method for estimation of velocity vectors," *IEEE Trans. Ultrason., Ferroelec., Freq. Contr.*, vol. 45, pp. 837–851, 1998.

[12] M. E. Anderson, "Multi-dimensional velocity estimation with ultrasound using spatial quadrature," *IEEE Trans. Ultrason., Ferroelec., Freq. Contr.*, vol. 45, pp. 852–861, 1998.

[13] J. Udesen and J. A. Jensen, "Investigation of transverse oscillation method," *IEEE Trans. Ultrason., Ferroelec., Freq. Contr.*, vol. 53, pp. 959–971, 2006.

[14] J. Udesen, M. B. Nielsen, K. R. Nielsen, and J. A. Jensen, "Examples of *In Vivo* blood vector velocity estimation," *Ultrasound in Med. & Biol.*, vol. 33, no. 4, pp. 541–548, 2007.

[15] J. A. Jensen, O. Holm, L. J. Jensen, H. Bendsen, H. M. Pedersen, K. Salomonsen, J. Hansen, and S. Nikolov, "Experimental ultrasound system for real-time synthetic imaging," in *Proc. IEEE Ultrason. Symp.*, 1999, vol. 2, pp. 1595–1599.

[16] J. A. Jensen, O. Holm, L. J. Jensen, H. Bendsen, S. I. Nikolov, B. G. Tomov, P. Munk, M. Hansen, K. Salomonsen, J. Hansen, K. Gormsen, H. M. Pedersen, and K. L. Gammelmark, "Ultrasound research scanner for real-time synthetic aperture image acquisition," *IEEE Trans. Ultrason., Ferroelec., Freq. Contr.*, vol. 52 (5), pp. 881–891, May 2005.

[17] J. A. Jensen, "A new estimator for vector velocity estimation," *IEEE Trans. Ultrason., Ferroelec., Freq. Contr.*, vol. 48, no. 4, pp. 886–894, 2001.

[18] J. A. Jensen, "Field: A program for simulating ultrasound systems," *Med. Biol. Eng. Comp.*, vol. 10th Nordic-Baltic Conference on Biomedical Imaging, Vol. 4, Supplement 1, Part 1, pp. 351–353, 1996.

[19] J. A. Jensen and N. B. Svendsen, "Calculation of pressure fields from arbitrarily shaped, apodized, and excited ultrasound transducers," *IEEE Trans. Ultrason., Ferroelec., Freq. Contr.*, vol. 39, pp. 262–267, 1992.

[20] J. Udesen, *2-D blood vector velocity estimation using a phase shift estimator.*, Ph.D. thesis, Ørsted●DTU, Technical University of Denmark, 2800, Lyngby, Denmark, 2005.

Paper II

Transverse Oscillations for Phased Array Vector Velocity Imaging

Michael Johannes Pihl and Jørgen Arendt Jensen

Proceedings of the IEEE International Ultrasonics Symposium

Presented in San Diego, California, United States, 2010

Transverse Oscillations for Phased Array Vector Velocity Imaging

Michael Johannes Pihl and Jørgen Arendt Jensen

Center for Fast Ultrasound Imaging, Department of Electrical Engineering,
Technical University of Denmark, DK-2800 Kgs. Lyngby, Denmark

***Abstract*— Medical ultrasound imaging is widely used to visualize blood flow in the human circulatory system. However, conventional methods are angle dependent. The Transverse Oscillation (TO) method is able to measure the lateral velocity component, and it has been demonstrated in *in vivo* measurements of superficial blood vessels. To broaden the usability of the method, it should be expanded to a phased array geometry enabling vector velocity imaging of the heart. Therefore, the scan depth has to be increased to 10-15 cm. This paper presents suitable pulse echo fields (PEF). Two lines are beamformed in receive to obtain lateral spatial in-phase and quadrature components. The relative mean bias and standard deviation of the lateral velocity component are computed as performance measures. For the PEF, the coefficient of variance, *CV*, of the spectral frequencies, and the energy ratio, *ER*, of leakage into negative frequencies are used as metrics to assess estimator performance. At 10 cm's depth for an initial setup, the relative mean bias and standard deviation are 9.1% and 9.5%, respectively. At a depth of 15 cm, the values are 20% and 13%, respectively. The PEF metric *ER* can be used to assess the bias (correlation coefficient, R: -0.76), and therefore predict estimator performance. *CV* is correlated with the standard deviation (R=0.74). The results demonstrate the potential for using a phased array for vector velocity imaging at larger depths, and potentially for imaging the heart.**

I. INTRODUCTION

Medical ultrasound is widely used to image blood flow. For instance, the estimation of blood velocities plays a key role in diagnosing carotid artery stenosis [1]. However, blood velocity estimates using conventional color flow imaging or Doppler techniques are angle dependent. This poses a huge challenge for quantitatively measuring the magnitude (and direction) of the blood's velocity. Several techniques have been proposed to remedy this. The Transverse Oscillation (TO) method by Jensen and Munk [2] and the similar approach by Andersen [3] are two of them. The TO method has shown intriguing *in vivo* results of blood vector velocities in superficial vessels using linear arrays [4], and is a technique close to a commercial breakthrough [5]. However, the current implementation limits the scan depth, and hence, prevents imaging of deeper lying vessels and organs, e.g. the heart. To broaden its usability, the method should be expanded to phased arrays enabling vector velocity imaging of the heart. Therefore, suitable pulse-echo fields (PEFs) with transverse oscillations have to be designed for depths up to 10-15 cm, and velocity measurements have to be performed.

The purpose of this paper is to expand the TO method to a phased array allowing blood flow measurements down to 10 to 15 cm. The theory of the method is briefly stated in Section II including the application of the technique for a phased array. The section also includes a description of measures to evaluate the performance of the estimator and metrics to evaluate PEFs. The simulation setup is described in Section III followed by the obtained results in Section IV. The results are discussed in Section V and the conclusions stated in Section VI.

II. THEORY

This section describes the theoretical background of the Transverse Oscillation method for a phased array along with performance measures and pulse echo field metrics.

A. Transverse Oscillation method

In the following, the generated pressure field using a phased array is described, followed by beamforming approaches, and the velocity estimation.

1) Field generation and beamforming: The basic idea in the TO method is to create a double oscillating pulse-echo field as illustrated in Fig. 1. This is accomplished by using special apodization profiles in receive, whereas the transmitted beam is similar to the one used in conventional velocity estimation. A derivation of the required apodization functions and a description of the respective generated fields for the linear array can be found in [2], [6].

Using the Fraunhofer approximation, the relation between the lateral spatial wavelength, λ_x, and the apodization function is

$$\lambda_x = \frac{2\lambda_z z_0}{d}, \tag{1}$$

where d is the distance between the two peaks in the apodization function, z_0 is depth, and λ_z is the axial wavelength.

As (1) shows, the lateral wavelength increases as the depth increases, if the apodization function is kept constant (d is constant). To keep a constant lateral wavelength, the aperture must expand width depth. Using a phased array, the width is often limited, so instead the spacing between the two beamformed lines can be increased through depth. Keeping the apodization function fixed, the two lines can be beamformed with a fixed angle.

Using the tangent-relation (see Fig. 2) and (1), the angle between the two lines can be derived as

$$\theta/2 = \arctan\frac{\lambda_x/8}{z_0} = \arctan\frac{\lambda_z}{4d}. \tag{2}$$

The transverse oscillations are created in receive, and two lines are beamformed simultaneously to get the spatial lateral

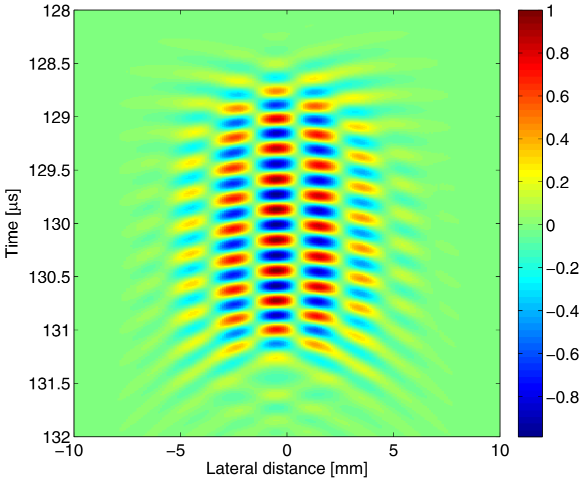

Fig. 1. Pulse-echo field for the left beam in normalized pressure for the reference simulation point at a depth of 10 cm.

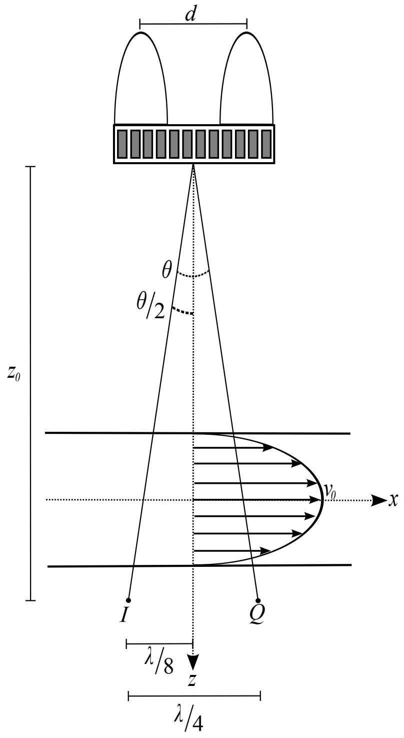

Fig. 2. Beamforming approach based on a fixed aperture function with a fixed angle between beamformed lines corresponding to the increasing spatial lateral wavelength over depth. The location of the simulation phantom with a parabolic flow profile and peak velocity, v_0, is also indicated.

in-phase (I) and quadrature (Q) components (left and right beam on Fig. 2). The spatial IQ samples, r_{IQ}, are obtained by

$$r_{IQ} = r_I + jr_Q, \tag{3}$$

where r_I and r_Q are the samples from the left and right beam, respectively.

For a spacing of 20 mm of the apodization peaks, a center frequency of 3.5 MHz and c = 1540 m/s, the angle between the two lines will be 0.63°. At a depth of 10 cm this corresponds to $\lambda_x/4$ = 1.1 mm. The $\lambda_x/4$ spacing results in spatial IQ sampling for the particular modulation frequency.

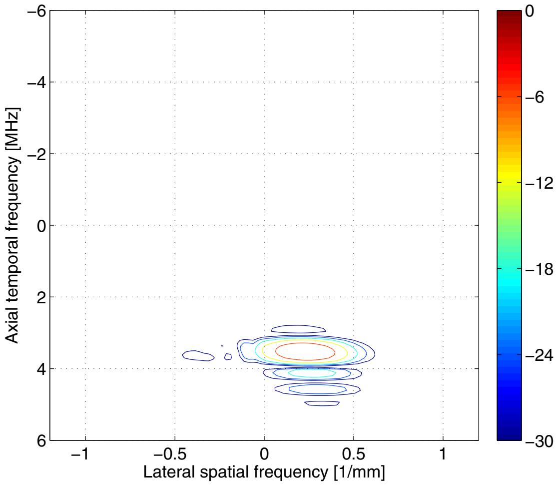

Fig. 3. The spatio-temporal frequency spectrum (k-space) for the spatio-temporal IQ pulse-echo field. Shown as a contour plot of the normalized amplitude spectrum with 6 dB between contours. Note that the spectrum's energy mainly is located in one quadrant.

Along with the two TO lines, a center line can be beamformed for conventional axial velocity estimation.

2) Velocity estimation: For a description and derivation of the estimator used for subsequent calculations, the reader is referred to [7]. Prior to the velocity estimation, the data are matched filtered by convolving with the time inverted excitation pulse. This is followed by stationary echo canceling, where the mean of N emitted signal is subtracted from each emission. No discrimination has been performed to distinguish between the stationary and the moving scatterers.

B. *Statistical performance measures*

To investigate the performance of the method, a statistical analysis is performed on the simulated data. It is assumed that the velocity estimates are independent.

At each discrete depth in the vessel, the velocity is estimated from a number of emissions. The mean, $\bar{v}(z_k)$, of N estimates and the estimated standard deviation, $\sigma(z_k)$, is calculated at each discrete depth.

For better and more straightforward comparison of various parameter settings, two single measures for the bias and the estimated standard deviation for a specific velocity profile are computed. In order to do so, the estimated variance and bias are averaged over the entire vessel and divided by the peak velocity, v_0. The two quantities, the relative mean bias, $\tilde{B}$, and the estimated relative mean standard deviation, $\tilde{\sigma}$, are given by

$$\tilde{B} = \frac{1}{v_0 N_{z_k}} \sum_{z_k=1}^{N_{z_k}} B(z_k) \tag{4}$$

$$\tilde{\sigma} = \frac{1}{v_0} \sqrt{\frac{1}{N_{z_k}} \sum_{z_k=1}^{N_{z_k}} \sigma(z_k)^2}, \tag{5}$$

where N_{z_k} is the number of discrete samples within the vessel. These measures can to some extend be used to describe the performance of the TO estimator.

C. *PEF metrics*

The simulations take a long time to perform to obtain enough estimates for evaluating the performance of the estimator. Therefore, it would be desirable if the performance to some extend could be predicted from the spatio-temporal frequency spectrum. Two metrics are suggested as described in the following.

Ideally, the lateral spatial frequencies of the two added signals should yield a narrow one-sided spectrum (see Fig. 3) in the lateral dimension of the 2D spatio-temporal spectrum. Using temporal IQ sampled data, or the Hilbert transform, the spectrum will already be one-sided in the axial dimension.

The mean spatial frequency depends on the aperture function, *i.e.* the spacing of the two apodization peaks. The width of the apodization peaks determine the frequency spread in the spatio-temporal spectrum, $S(f)$.

One of the metrics used to evaluate the designed PEFs is the coefficient of variation, CV, of the spectral frequencies

$$CV = \frac{\sigma_{fx}}{\bar{f}_x} = \frac{\sqrt{\frac{\int_{-\infty}^{\infty}(f_x-\bar{f}_x)^2 S(f_x,f_0)^2 df_x}{\int_{-\infty}^{\infty} S(f_x,f_0)^2 df_x}}}{\frac{\int_{-\infty}^{\infty} f_x S(f_x,f_0)^2 df_x}{\int_{-\infty}^{\infty} S(f_x,f_0)^2 df_x}} \quad (6)$$

where CV is computed at the (temporal) center frequency, f_0, $\bar{f}_x$ is the mean spectral (lateral) frequency, and σ_{f_x} is the spatial standard deviation. It is hypothesized that this terms is related to the standard deviation of the velocity estimates.

Furthermore, the estimated mean spatial frequency can be used in the estimator to yield a more unbiased estimate. This is due to the fact that the Fraunhofer approximation is not 100% valid.

The second metric is the energy ratio, ER, computed as

$$ER = \frac{\displaystyle\int_{-\infty}^{0} S(f_x,f_0)^2 df_x}{\displaystyle\int_{-\infty}^{\infty} S(f_x,f_0)^2 df_x} \quad (7)$$

at the center frequency, f_0. This provides information of the energy leak into the other half of the spatio-temporal frequency spectrum, e.g. looking at Fig. 3 from positive spatial frequencies to negative. It is hypothesized that this gives an estimate of the bias of the velocity profiles. When the value of ER is 50% the energy is evenly distributed between both quadrants, and velocity estimation is expected to be compromised.

III. SIMULATION SETUP

The ultrasound simulation program Field II [8], [9] was used for the simulation study. A phased array transducer with the characteristics shown in Table I was emulated. A blood vessel (as illustrated in Fig. 2) was modeled as a cylindrical volume (radius = 6 mm) of moving scatterers surrounded by a block of stationary scatters in a 2x2x2 cm scatter block. The number of scatterers was 6726 to obtain 10 scatterers per resolution cell. The flow angle was set to be perpendicular to the depth axis to obtain purely transverse flow at a scan angle of 0 degrees. When scanning at angles different from zero the scatter block was translated to the new position (not rotated).

TABLE I

SIMULATION SETUP

Transducer parameter	Value
Transducer	Phased array
Number of elements	128
Pitch	0.220 mm
Kerf	0.022 mm
Center frequency	3.5 MHz
Sampling frequency	100 MHz
Fixed simulation parameter	**Value**
Pulse repetition frequency	5 kHz
Speed of sound	1540 m/s
Maximum velocity of blood	1.0 m/s
No. of transmit cycles in pulse	8
Transmit focus (radial depth)	10 cm
Signal-to-noise ratio (SNR)	∞

TABLE II

VARIED SIMULATION PARAMETERS

Parameter	Value
Center of vessel	2 3 4.5 7.5 **10** 15 [°]
Scan angle	-30 -15 **0** 15 30 [degrees]
F# in transmit	4 6 8 **10** 12
Transmit apodization shape	**Hanning**, Tukey, Rectangular
Receive apodization shapes	**Hanning**, Tukey, Rectangular
Space between peaks	16 48 80 **96** 112
Apodization width	8 16 **32** 64
Number of shots per estimate	4 8 16 **32** 64
Transverse lag in estimator	**1** 2 3 4 5

The fixed simulation parameters are listed in Table I as well. To investigate the performance under optimal conditions, no noisy was added to the simulated data, hence the SNR of ∞.

Table II lists the parameters that where varied in the simulation study. A number of initial conditions were used to form a starting point in parameter space as indicated with bold face in Table II. During this study, the different parameters were kept fixed at their starting point (unless otherwise stated), and only the parameter under investigation was varied. Every simulation setup was repeated 20 times.

For the apodization shapes, the Hanning, the Tukey, and the rectangular shapes can be modeled as Tukey windows with ratio of tapers as 1, 0.5, and 0, respectively. When testing the space between the receive apodization peaks, the apodization width was set to 16 elements instead of 32 elements as in the rest of the study in order to increase the possible spacing. At a depth of 10 cm these spacings, [16 48 80 96 112] elements, correspond to λ_x = [25 8.3 5.0 4.2 3.6] mm. When testing the width of the receive apodization peaks, the spacing between the peaks was set to 64 instead of the 96 in the rest of the study, as there is only 128 elements in the transducer.

The flow was modeled to be laminar with a parabolic flow profile (see Fig. 2) given by

$$v(r) = \left(1 - \frac{r^2}{R^2}\right) v_0, \quad (8)$$

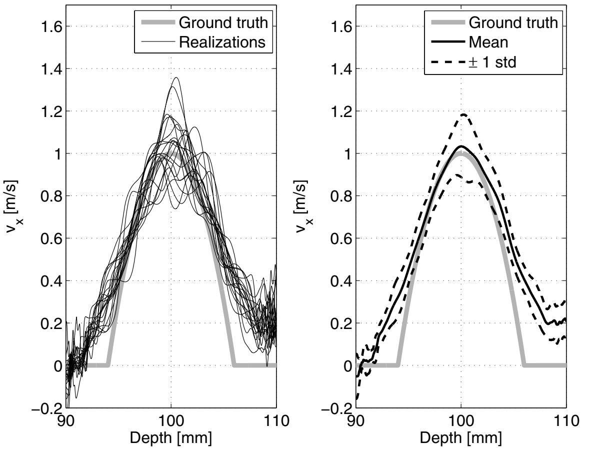

Fig. 4. [Left] Transverse velocity estimates from 20 realizations. [Right] the mean estimate plus/minus one standard deviation. Note that no effort has been made to remove the estimates outside the vessel

where r denotes the radial position, R is the radius of the tube, and v_0 is the maximum velocity at the centre of the tube.

The beamformed data are matched filtered and mean stationary echo canceling is performed prior to velocity estimation as previously described.

IV. RESULTS

A. Initial point

Initially, the simulation phantom is positioned at a (radial) depth of 10 cm at a scan angle of 0°. The transmit apodization of the transducer is a Hanning function with a width corresponding to a F-number of 10. The two receive apodization shapes are two Hanning functions with widths of 32 elements (7.0 mm) spaced 96 elements (21 mm) apart. The number of shots per estimate, N, and the transverse lag, k, are parameters that only affect the estimator itself, and they are 32 and 1, respectively.

The lateral velocity estimates, v_x, from the 20 realizations are shown in Fig. 4 on the left. The 20 realizations closely follow the ground truth, as illustrated on the right panel showing the mean of the 20 realizations plus/minus one standard deviation. With these settings the relative mean bias, $\tilde{B}_{v_x}$, is 9.1% and the relative standard deviation, $\tilde{\sigma}_{v_x}$, is 9.5%.

B. Parameter study

1) Physical parameters: The effect on performance measures when changing the position of the phantom in terms of (radial) scan depth and scan angle is illustrated in Fig. 5. $\tilde{B}_{v_x}$ is closet to zero at a depth of 7.5 cm. With the given setup, the estimator underestimates velocity at low depths, and overestimates at large depths. $\tilde{\sigma}_{v_x}$ increases with depth. For $\tilde{B}_{v_x}$, the performance decreases when steering the beam away from 0°.

2) Transmit parameters: On the transmit side, the F-number and the shape of the apodization has been varied. There is no real difference between the performance measures for the different transmit types. For the given setup, the most accurate and precise velocities estimates are obtained with a F-number of 6 as shown in Fig. 6.

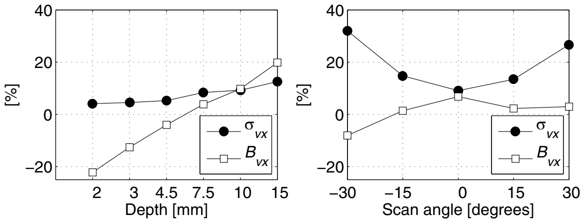

Fig. 5. Performance measures for different scan depths and scan angles.

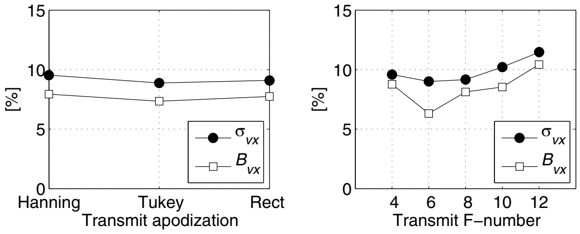

Fig. 6. Performance measures for transmit apodization type and F-number.

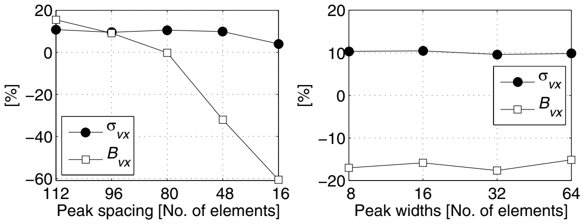

Fig. 7. Performance measure for receive apodization peak spacing and width.

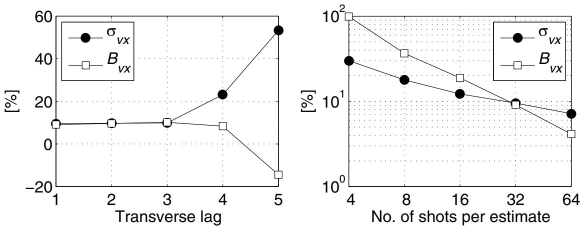

Fig. 8. Performance measures for transverse lag and no. of shots per estimate.

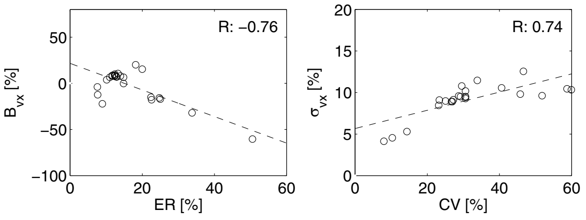

Fig. 9. Scatter plot of PEF metrics and performance measures for ER & $\tilde{B}_{v_x}$ [left] and CV & $\tilde{\sigma}_{v_x}$ [right]. The correlation values are -0.76, and 0.74, respectively.

3) Receive parameters: As mentioned, the receive apodization creates the transverse oscillations in the pulse-echo field. The result of changing apodization functions, width, and position is depicted in Fig. 7. Decreasing the peak spacing below a certain point yields a significant degradation of $\tilde{B}_{v_x}$, illustrating that the estimator gets increasingly biased, and is unable to estimate the velocity accurately. However, $\tilde{\sigma}_{v_x}$ is not affected. For the given reference setup (at 10 cm's depth), changing the width of the peak has no influence on the two performance measures. Using different receive types yielded the same trends as for the transmit case (data not shown).

4) Estimator parameters: As Fig. 8 illustrates, increasing the number of shots per estimate decreases $\tilde{\sigma}_{v_x}$ with approximately the expected $1/\sqrt{N}$. Also $\tilde{B}_{v_x}$ decreases. The transverse lag can be increased to k = 3 without affecting performance, thereafter aliasing increasingly occurs.

C. Performance measures

To test the hypothesis whether there are a correlation between the PEF metrics and performance measures, the values are plotted in Fig. 9. The correlation coefficients are -0.76 for ER and $\tilde{B}_{v_x}$. For CV & $\tilde{\sigma}_{v_x}$ the value is 0.74. In both cases, the values indicate that there is a correlation. For the latter, 2 outliers have been removed. The criteria is the energy ratio, *i.e.* the energy leak. The cut-off is set remove data points where $ER >$33%. When 50%, the energy is located in both halves of the spectrum. A value slightly lower than this is selected to ensure that energy leak into the other quadrant is limited, so that the velocity is estimated without too much bias.

The correlation coefficients indicate that there is a correlation between the PEF metrics and the performance measures. Hence, the PEF metrics can be used as an initial assessment of the expected estimator performance. The PEF metrics can be readily computed opposed to the simulated velocity data and the derived performance measures.

V. DISCUSSION

As the depth increases, the transverse spatial frequency decreases and thereby affecting the precision of the estimator. The bias is negative at low depths and positive at large depths for the current setup. A more unbiased estimate might be obtained, if the actual spatial wavelength was used and not the theoretically derived one, either by estimating it or deriving it from the pulse-echo field. Furthermore, training the estimator on data set could provide bias correction terms for different setups. The underlying assumption is that the bias is constant and deterministic for a given spatial location with a specific setup.

There are some performance issues at increasing steering angle, but they might be resolved with further optimization of the pulse-echo field taking the increasing steering angle under consideration.

It can be noted that the transmit F-number can be optimized for the depth. The apodization types (transmit and receive) did not significantly affect performance. However, the different combinations should be investigated, especially having two rectangular apodizations. The larger the area under the apodization functions, the better SNR can be obtained in a noisy environment.

Performance decreases when peak separation in receive decreases, due to a lower spatial frequency. Additionally, a poorer spatial resolution is obtained. The apodization width affects CV, however, does not seem to affect $\tilde{\sigma}_{v_x}$.

Because of the decreasing spatial frequency through depth, the velocity range increases with depth. However, the estimator appears to be unaffected within its velocity range.

The PEF metric ER is correlated with $\tilde{B}_{v_x}$ and can be used to predict when the performance of the estimator will deteriorate due to a poor PEF and corresponding spatio-temporal spectrum. CV can to some extend give a hint of the magnitude of $\tilde{\sigma}_{v_x}$.

Overall, the estimator is not very sensitive to small changes in parameter settings. In some cases the performance degrades in the sense that the velocities are not estimated correctly, however, this is done consistently as the standard deviation is not affected. In some cases, the degradation can be predicted by calculating ER of the PEF. In general, a lot can be learned by investigating the PEF prior to simulation and optimizing it.

VI. CONCLUSION

Various parameters have been investigated around a reference point at 10 cm's depth where $\tilde{B}_{v_x}$ is 9.1% and $\tilde{\sigma}_{v_x}$ is 9.5%. Overall, the estimator is not very sensitive to minor changes in the setup. At a depth of 15 cm, it was possible to estimate the lateral velocity with $\tilde{B}_{v_x}$ and $\tilde{\sigma}_{v_x}$ being 20% and 13%, respectively. This demonstrates that in simulation without noise, the velocity can be estimated at 10-15 cm's depth with standard deviations on par with conventional estimators.

The results are encouraging for further development and for obtaining measured velocity data. And potentially, for imaging the heart with phased array vector velocity imaging.

ACKNOWLEDGMENTS

This work was supported by grant 024-2008-3 from the Danish Advanced Technology Foundation and BK Medical Aps, Denmark.

REFERENCES

[1] E. G. Grant *et al.*, "Carotid artery stenosis: Gray-scale and doppler us diagnosis - society of radiologists in ultrasound consensus conference," *Radiology*, vol. 229, no. 2, pp. 340–346, 2003.

[2] J. A. Jensen and P. Munk, "A New Method for Estimation of Velocity Vectors," *IEEE Trans. Ultrason., Ferroelec., Freq. Contr.*, vol. 45, pp. 837–851, 1998.

[3] M. E. Anderson, "Multi-dimensional velocity estimation with ultrasound using spatial quadrature," *IEEE Trans. Ultrason., Ferroelec., Freq. Contr.*, vol. 45, pp. 852–861, 1998.

[4] K. L. Hansen, J. Udesen, C. Thomsen, J. A. Jensen, and M. B. Nielsen, "In-vivo validation of transverse oscillation vector velocity estimation with MR angiography," *IEEE Trans. Ultrason., Ferroelec., Freq. Contr.*, vol. 56, no. 1, pp. 91–100, 2009.

[5] M. J. Pihl, S. Nikolov, P. Haugaard, M. C. Hemmsen, and J. A. Jensen, "Performance of the transverse oscillation method using beamformed data from a commercial scanner," in *Proc. IEEE Ultrason. Symp.*, 2009, p. Accepted.

[6] J. Udesen and J. A. Jensen, "Investigation of Transverse Oscillation Method," *IEEE Trans. Ultrason., Ferroelec., Freq. Contr.*, vol. 53, pp. 959–971, 2006.

[7] J. A. Jensen, "A New Estimator for Vector Velocity Estimation," *IEEE Trans. Ultrason., Ferroelec., Freq. Contr.*, vol. 48, no. 4, pp. 886–894, 2001.

[8] J. A. Jensen, "Field: A Program for Simulating Ultrasound Systems," *Med. Biol. Eng. Comp.*, vol. 10th Nordic-Baltic Conference on Biomedical Imaging, Vol. 4, Supplement 1, Part 1, pp. 351–353, 1996.

[9] J. A. Jensen and N. B. Svendsen, "Calculation of Pressure Fields from Arbitrarily Shaped, Apodized, and Excited Ultrasound Transducers," *IEEE Trans. Ultrason., Ferroelec., Freq. Contr.*, vol. 39, pp. 262–267, 1992.

Paper III

Phased Array Vector Velocity Estimation using Transverse Oscillations

Michael Johannes Pihl, Jønne Marcher, and
Jørgen Arendt Jensen

IEEE Transactions on Ultrasonics, Ferroelectrics, and Frequency Control

Accepted for publication, August 2012

Phased Array Vector Velocity Estimation using Transverse Oscillations

Michael Johannes Pihl, *Student Member, IEEE*, Jønne Marcher, and Jørgen Arendt Jensen, *Fellow, IEEE*

***Abstract*— A method for estimating the 2D vector velocity of blood using a phased array transducer is presented. The approach is based on the Transverse Oscillation (TO) method. The purpose of this work is to expand the TO method to a phased array geometry. The purpose is to broaden the potential clinical applicability of the method. A phased array transducer has a smaller footprint and a larger field of view compared to a linear array, and is therefore more suited for e.g. cardiac imaging. The method relies on suitable transverse oscillating fields, and a beamforming strategy employing diverging TO beams is proposed. The implementation of the TO method on a phased array transducer for vector velocity estimation is evaluated using Field II simulations and flow-rig measurements acquired using the experimental scanner SARUS. The vast number of calculations needed to perform flow simulations makes the optimizing of the TO fields a cumbersome process. Therefore, three performance metrics are proposed. They are calculated based on the complex TO spectrum of the combined TO fields. It is hypothesized that the performance metrics are related to the performance of the velocity estimates. The simulations show that the squared correlation values range from 0.79 to 0.92 indicating a correlation between the performance metrics of the TO spectrum and the velocity estimates. As these performance metrics are much more readily computed, the TO fields can be optimized faster for improved velocity estimation of both simulations and measurements. For simulations of a parabolic flow at a depth of 10 cm, a relative (to the peak velocity) bias and standard deviation of 4% and 8%, respectively, are obtained. Overall, the simulations show that the TO method implemented on a phased array transducer is robust with relative standard deviations around 10% in most cases. The flow-rig measurements show similar results. At a depth of 9.5 cm using 32 emissions per estimate, the relative standard deviation is 9% and the relative bias -9%. At the center of the vessel, the velocity magnitude is estimated to be 0.25 ± 0.023 m/s compared to an expected peak velocity magnitude of 0.25 m/s and the beam-to-flow angle is calculated to be $89.3 \pm 0.77^\circ$ compared to an expected angle value between 89° and 90°. For steering angles up to ± 20 degrees, the relative standard deviation is below 20%. The results also show, that a 64 element transducer implementation is feasible, but with a poorer performance compared to a 128 element transducer. The simulation and experimental results demonstrate that the TO method is suitable for use in conjunction with a phased array transducer, and that 2D vector velocity estimation is possible down to a depth of 15 cm.**

I. INTRODUCTION

For decades medical ultrasound imaging has been used to image blood flow in the human circulatory system, and measurements of the blood velocity play a key role in diagnosing various cardiovascular diseases [1]. Clinical diagnostics, however, are still based on angle-dependent 1D velocity estimates.

Moreover, it is important to bear in mind that blood flow directions in the human blood vessel rarely (if ever) are constant over time, as the velocities vary as a function of time and space as exemplified by the results presented in [2].

Several techniques have been proposed to remedy the angle dependency. Fox suggested a multibeam method [3], and variations of this methods by other authors have been reviewed by Dunmire et al. [4]. The multibeam methods often struggle with small angle differences at larger depths. More recently, Tortoli et al. [5] suggested a method for estimating the Doppler angle for angle compensation of the velocity estimates. This method assumes the same flow angle throughout the region of interest. The speckle tracking technique suggested by Trahey et al. [6] has been widely used for motion estimation. This method is computationally very demanding. Newhouse et al. proposed an approach based on the transit-time spectral broadening effect [7], but this method has difficulties finding the lateral velocity component reliably. Bonnefous suggested using a number of beamformers working in parallel [8], however, this method degrades when the flow is not parallel to the beamformed lines. Jensen [9], [10], therefore, suggested a directional beamforming approach, but this method is computationally demanding as well. Another method proposed for estimating both the axial and the lateral velocity component is the Transverse Oscillation (TO) method suggested by Jensen and Munk [11]. This method introduces a lateral oscillation in the receive field, which allows the estimation of the transverse velocity component. A similar lateral modulation approach was suggested by Anderson [12], and more recently, Sumi has described another lateral modulation approach [13]. The TO method has been investigated using a linear array [14] and *in vivo* examples of blood vector velocities in superficial vessels using a linear array have been demonstrated [15]. The applicability for a commercial implementation has been demonstrated [16], and 2D velocity data from a commercial implementation has been used for investigating flow patterns in various vessels [2]. So far, only experiments on linear arrays have been conducted. Liebgott et al. [17] have used the TO method in combination with a phased array transducer for estimating tissue motion for elastography, whereas the focus of this paper is vector velocity imaging, where the motion is much larger.

The aim of this paper is to expand the TO method for velocity estimation to a phased array and to increase the penetration depth of the method. The paper also suggests a

---

Manuscript received February 20, 2012; accepted August 11, 2012.

This work was supported by grant 024-2008-3 from the Danish Advanced Technology Foundation and BK Medical ApS, Denmark.

The authors are with the Center for Fast Ultrasound Imaging, Department of Electrical Engineering at the Technical University of Denmark, DK-2800 Kgs. Lyngby, Denmark. Email of corresponding author: mjp@elektro.dtu.dk.

Digital Object Identifier: xxxx

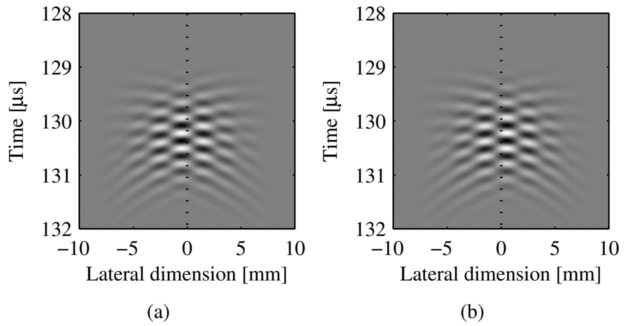

Fig. 1. PEFs in normalized pressure at a fixed depth of 100 mm when the steering angle of the transmitted beam is 0° (see Fig. 2). (a) is for the left TO beam: $h_{\mathrm{pe,left}}(x,t)$. (b) is for the right TO beam: $h_{\mathrm{pe,right}}(x,t)$. Note that a conventional PEF for axial velocity estimation will not have oscillations in the lateral dimension. $h_{\mathrm{pe,left}}(x,t)$ and $h_{\mathrm{pe,right}}(x,t)$ are defined in Section II-B and calculated using Field II with the standard parameter settings described in Section IV-A.

number of performance measures to evaluate the performance of the TO method. The initial work of this paper was presented in [18]. This paper presents a more thorough investigation of the suggested performance measures, and uses larger data sets to obtain the conclusions.

Expanding the TO method to a phased array geometry requires suitable pulse-echo fields (PEFs) with transverse oscillations. Three performance measures are suggested to evaluate the created double-oscillating fields, and they are compared with performance measures of the velocity estimates.

The important theoretical concepts are briefly stated in Section II including the application of the technique for a phased array. Section III describes the measures used to describe the performance of the TO estimator, and the measures used to evaluate the designed PEFs. Simulations are performed to demonstrate the feasibility of the implementation and are presented in Section IV. Measurement setup and results are described in Section V. The simulation and measurement results are discussed in Section VI, and the conclusion is given in Section VII.

II. THE TRANSVERSE OSCILLATION METHOD

This section provides a brief description of the TO method for 2D velocity estimation using a phased array transducer.

A. A Double Oscillating Field

The basic mechanism that allows the traditional estimation of axial velocities, is the axial oscillations in the transmitted ultrasonic pulse. Using the same principle, an introduction of a transverse oscillation in the ultrasound field generates received signals that depend on the transverse oscillation, *i.e.* the lateral modulation. If this lateral modulation frequency is known, the velocity can be estimated. An example of a PEF with oscillations in both the axial and the transverse direction is illustrated in Fig. 1.

B. Field Generation and Beamforming

The pulse-echo field is the combined transmit-receive pressure field. It depends on the transducer geometry, the transducer impulse response, the excitation waveform, the transmit apodization, and the receive apodization. The field can be obtained in the focus or in the far field by means of the Fraunhofer approximation that relates the aperture functions to the field. Alternatively, as in this paper, the ultrasound simulation tool Field II [19], [20] was used.

To create the double oscillating pulse-echo fields in Fig. 1, only the receive apodization has been changed into special receive apodization profiles compared to a typical setup for conventional axial velocity estimation. What characterizes the receive apodization are two peaks (in some shape) spaced a given distance apart, as exemplified in Fig. 2.

The transmitted beam is a standard focused beam with eight cycles in the excitation pulse. The transmit apodization is practically the same as the one used in conventional axial velocity estimation using a phase shift estimator, *e.g.* a rectangular or a Hanning apodization of the transmitting aperture.

A derivation of the required apodization functions and a description of the respective generated fields for the linear array can be found in [11], [14], [21], which states that the transverse oscillation period is given by

$$\lambda_x = 2\lambda_z \frac{z_0}{d}, \tag{1}$$

where z_0 is the depth, d the distance between the two peaks in the aperture function, and λ_z is the axial wavelength. It should be noted, that when the steering angle, θ_0, is different from 0°, the effective aperture width and d decreases with a factor of $\cos\theta_0$. This is taken into consideration when evaluating (1), although the effect is small for small steering angles.

Two beams are beamformed in parallel in receive from one emission as depicted in Fig. 2. To obtain a spatial quadrature signal for transverse velocity estimation, the two lines are separated by a distance of $\lambda_x/4$. Considering (1), it is clear that the theoretically derived λ_x increases with depth, unless d increases accordingly. While increasing d in the receive apodization function to maintain a constant λ_x often is possible for a linear transducer at shallower depths, the width of a phased array transducer is limited. In addition, the best performance at each depth is obtained by separating the TO peaks as much as possible, which yields the smallest transverse wavelength and best spatial resolution. In the case where the apodization function is kept constant (i.e. d is constant), the lateral wavelength increases with depth, however, at each depth, the best possible transverse wavelength is obtained. Keeping the apodization function fixed, the two TO lines can be beamformed with a fixed angle instead of a fixed lateral distance.

Using the tangent-relation (see Fig. 2) and (1), the angle, θ_{TO}, between the two lines can be derived as

$$\theta_{TO} = 2\arctan\frac{\lambda_x/8}{z_0} = 2\arctan\frac{\lambda_z}{4d_e}, \tag{2}$$

where d_e is the effective distance between the TO peaks in the apodization function calculated as $d_e = d\cos\theta_0$. So for

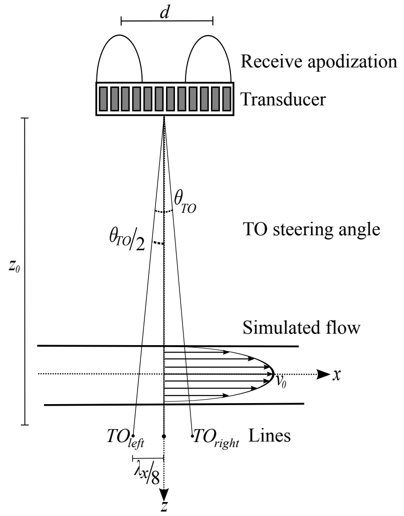

Fig. 2. Beamforming approach based on a fixed receive apodization function with a fixed angle between beamformed lines. This angle corresponds to the increase of the spatial lateral wavelength with depth. The simulation phantom with a parabolic flow profile and peak velocity magnitude, v_0, is also indicated. For the simulations described in Section IV, the vessel direction is changed, so that the flow direction by default is perpendicular to the steered beam, i.e. the vessel is only parallel to the transducer surface in the case above where the steered beam coincides with the z-axis. This means, that only the transverse velocity component contributes to the velocity magnitude as the axial velocity is 0 m/s. On the other hand, when investigation the effect of different beam-to-flow angles, the vessel was rotated around its center, so that an axial velocity component is present for beam-to-flow angles different than 90°. In the measurements presented in Section V, however, the vessel is fixed and parallel to the transducer regardless of the direction of the steered beam (contrary to the simulations). Therefore, the axial velocity component contributes to the velocity magnitude, when the steering angle is different than 0°.

the phased array, instead of beamforming the TO lines with a fixed lateral distance, they diverge with a fixed angle.

The two TO lines are beamformed in parallel with dynamic focusing in receive, as opposed to the triangular focusing profiles originally presented in [21], where the focusing was obtained by steering plane waves so that they intersected at the point of interest by means of triangular delay curves.

Often, a center line will be beamformed in parallel as well for conventional axial velocity estimation.

With the two TO beams beamformed at $\lambda_x/4$, the spatial quadrature signal is given by [22]

$$r_{\mathrm{sq}}(t) = r_{\mathrm{left}}(t) + \mathrm{j}r_{\mathrm{right}}(t),$$

where r_{left} and r_{right} are the samples at time t from the left (TO_{left}) and right (TO_{right}) beams, respectively. To obtain the corresponding temporal quadrature signal, r_{tq}, the data can either be sampled as in-phase and quadrature components directly, or by using the temporal Hilbert transform ($\mathscr{H}\{\bullet\}$) on r_{sq}

$$r_{\mathrm{tq}}(t) = \mathscr{H}\{r_{\mathrm{sq}}\} = \mathscr{H}\{r_{\mathrm{left}}(t)\} + \mathrm{j}\mathscr{H}\{r_{\mathrm{right}}(t)\}.$$

Similarly, the PEFs at a given depth of interest for the left and the right TO beam are $h_{\mathrm{pe,left}}(x,t)$ and $h_{\mathrm{pe,right}}(x,t)$, and

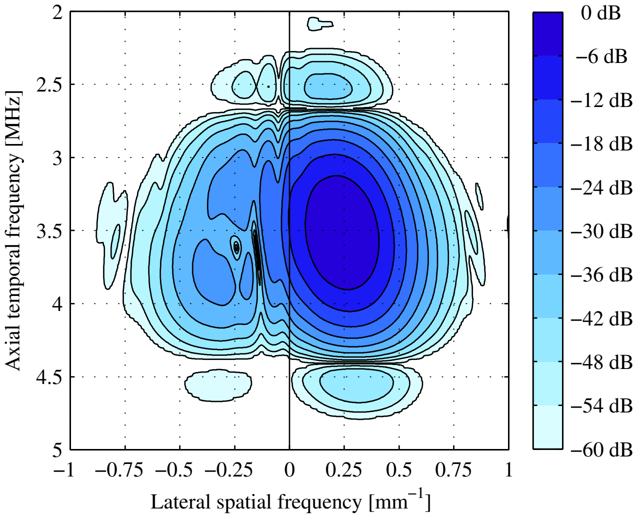

Fig. 3. The amplitude spectrum of the 2D spatio-temporal frequency spectrum, $S(f_x, f_t)$, of the PEFs in Fig. 1 when combined as described in (3). Note that the energy is mainly located in the fourth quadrant. The first and second quadrant are not shown, as the energy is zero for negative temporal frequencies due to the analytical signal by use of the Hilbert transform.

the combined field is calculated as

$$\begin{aligned} &h_{\mathrm{pe,comb}}(x,t) = \\ &\qquad h_{\mathrm{pe,left}}(x,t) + \mathrm{j}\mathscr{H}\{h_{\mathrm{pe,left}}(x,t)\} \\ &\qquad + \mathrm{j}\left(h_{\mathrm{pe,right}}(x,t) + \mathrm{j}\mathscr{H}\{h_{\mathrm{pe,right}}(x,t)\}\right). \end{aligned} \tag{3}$$

The 2D spatio-temporal frequency spectrum is then calculated as

$$S(f_x, f_t) = \mathscr{F}_{\mathrm{2D}}\{h_{\mathrm{pe,comb}}(x,t)\},$$

where f_x and f_t are the spatial (transverse) and temporal (axial) frequencies, and $\mathscr{F}_{\mathrm{2D}}\{\bullet\}$ denotes the 2D Fourier transform. The amplitude spectrum of $S(f_x, f_t)$ for the PEFs given in Fig. 1 is illustrated in Fig. 3.

Based on $S(f_x, f_t)$ an estimated value of the mean transverse wavelength, $\bar{\lambda}_x$, at the given depth of interest can be obtained as $1/\bar{f}_x$, where $\bar{f}_x$ can be computed as

$$\bar{f}_x = \frac{\displaystyle\int_{-f_s/2}^{f_s/2}\int_{-f_{ss}/2}^{f_{ss}/2} f_x S(f_x,f_t)^2 \,\mathrm{d}f_x \mathrm{d}f_t}{\displaystyle\int_{-f_s/2}^{f_s/2}\int_{-f_{ss}/2}^{f_{ss}/2} S(f_x,f_0)^2 \,\mathrm{d}f_x \mathrm{d}f_t} \tag{4}$$

where f_s is the temporal sampling frequency and f_{ss} is the spatial sampling frequency.

Additionally, $\bar{\lambda}_x = 1/\bar{f}_x$ from (4) can be used instead of λ_x from (1) in (2), however, it requires that $\bar{\lambda}_x$ has been estimated prior to the beamforming stage.

C. Velocity Estimation

The estimation of the transverse velocity, v_x, follows the one presented in [22]. Based on the spatial quadrature, r_{sq}, and temporal quadrature, r_{tq}, signals, two new signals, r_1 and r_2, can be generated

$$r_1(t) = r_{\text{sq}}(t) + \mathrm{j}r_{\text{tq}}(t),$$
$$r_2(t) = r_{\text{sq}}(t) - \mathrm{j}r_{\text{tq}}(t).$$

The transverse velocity is then calculated by

$$v_x = \frac{\lambda_x}{2\pi 2kT_{\text{prf}}} \times \arctan\left(\frac{\Im\{R_1(k)\}\Re\{R_2(k)\} + \Im\{R_2(k)\}\Re\{R_1(k)\}}{\Re\{R_1(k)\}\Re\{R_2(k)\} - \Im\{R_1(k)\}\Im\{R_2(k)\}}\right), \tag{5}$$

where T_{prf} is the time between two emissions, $R_1(k)$ is the complex lag k autocorrelation value for $r_1(k)$, and $R_2(k)$ is the complex lag autocorrelation k value for $r_2(k)$. $\Re\{\bullet\}$ denotes the real part, and $\Im\{\bullet\}$ the imaginary part. The complex autocorrelation is estimated over N emissions. RF averaging is performed by averaging the autocorrelation estimate over the length of the excitation pulse [22], [23].

The aliasing limit of the transverse velocity is

$$v_{x,\text{max}} = \frac{1}{4}\frac{\lambda_x}{kT_{prf}}. \tag{6}$$

The axial velocity component is calculated using an autocorrelation estimator as suggested by Loupas et al. [23] with RF averaging as

$$v_z = -\frac{\lambda_z}{2\pi 2kT_{\text{prf}}} \arctan\left(\frac{\Im\{R(k)\}}{\Re\{R(k)\}}\right),$$

where $R(k)$ is the autocorrelation of the center line at lag k.

III. PERFORMANCE MEASURES

This section describes the performance measures used to evaluate the TO estimator based on the velocity estimates and the designed PEFs.

A. Velocity Estimates

To investigate the performance of the TO method, the average behaviour over a number of velocity estimates is investigated. It is assumed that the velocity estimates are independent.

At each discrete depth, z_k, in the vessel, the velocity is estimated from a number of emissions. The mean, $\bar{v}(z_k)$, and the estimated standard deviation, $\sigma(z_k)$, of N estimates are computed at each discrete depth. Also, the bias, $B(z_k)$, and the root mean square error, $E_{\text{RMS}}(z_k)$, are calculated as

$$B(z_k) = \bar{v}(z_k) - v_t(z_k),$$
$$E_{\text{RMS}}(z_k) = \sqrt{\frac{1}{N}\sum_{i=1}^{N}(v_i(z_k) - v_t(z_k))^2},$$

where $v_i(z_k)$ is the *i*th estimated velocity profile and v_t is the true velocity profile.

For a better and more straightforward comparison of various parameter settings, three single measures for the bias, the standard deviation, and the root mean square error are computed. Therefore, B, σ, and E_{RMS} are averaged over the entire vessel and divided by the peak velocity magnitude, v_0. The three non-dimensional quantities, the relative mean bias, $\tilde{B}$, the relative mean standard deviation, $\tilde{\sigma}$, and the relative root mean square error, $\tilde{E}_{\text{RMS}}$, are given by

$$\tilde{B} = \frac{1}{v_0 N_{z_k}} \sum_{z_k=1}^{N_{z_k}} B(z_k),$$
$$\tilde{\sigma} = \frac{1}{v_0}\sqrt{\frac{1}{N_{z_k}} \sum_{z_k=1}^{N_{z_k}} \sigma(z_k)^2},$$
$$\tilde{E}_{\text{RMS}} = \frac{1}{v_0}\sqrt{\frac{1}{N_{z_k}} \sum_{z_k=1}^{N_{z_k}} E_{\text{RMS}}(z_k)^2},$$

where N_{z_k} is the number of discrete samples within the vessel. These measures are used to describe the performance of the TO estimator.

B. 2D Spatio-Temporal Frequency Spectrum

If the performance of the velocity estimator can be predicted from the spatio-temporal frequency spectrum, the design of suitable PEFs will be made easier. Three metrics are suggested to characterize the combined PEFs based on the corresponding 2D spatio-temporal Fourier domain.

The advantage of the suggested performance metrics based on the TO fields and their corresponding TO spectrum is that they can be more readily obtained. They can be obtained based on the TO fields which require much less calculations compared to a simulation study of moving scatterers. The TO fields can be estimated based on 100 points (scatterers) for each TO line, whereas a speckle phantom may require a factor of 100 or 1000 more scatterers for just one TO line for one emission. This number must then be multiplied with the number of emissions per estimate and the desired velocity profiles. Therefore, it preferable to optimize the TO method based on these performance metrics compared to on the obtained velocity estimates. For this to work, the performance metrics from the TO fields must be correlated to the performance of the velocity estimator. The following defines and describes the three performance metrics and states what performance measure of the velocity estimates that they are hypothesized to correlate with.

Ideally, the lateral spatial frequencies of the 2D spatio-temporal frequency spectrum, $S(f_x, f_t)$, should yield a narrow one-sided spectrum (see Fig. 3) in the lateral dimension of $S(f_x, f_t)$. Using temporal IQ sampled data or the Hilbert transform to generate analytical signals, the spectrum will already be one-sided in the axial dimension.

The mean spatial frequency depends on the aperture function, i.e. the spacing of the two apodization peaks as described in (1). The width of the apodization peaks determine the frequency spread in the spatio-temporal spectrum, $S(f_x, f_z)$.

One of the measures used to evaluate the designed PEFs is the coefficient of variation, c_v, of the spatial lateral frequencies, f_x,

$$c_v = \frac{\sigma_{fx}}{\bar{f}_x}$$

where $\bar{f}_x$ is the mean spatial (lateral) frequency given in (4), and σ_{f_x} is the standard deviation of the spatial frequency given by

$$\sigma_{f_x} = \sqrt{\frac{\int_{-f_s/2}^{f_s/2}\int_{-f_{ss}/2}^{f_{ss}/2}(f_x-\bar{f}_x)^2 S(f_x,f_0)^2\,\mathrm{d}f_x\mathrm{d}f_t}{\int_{-f_s/2}^{f_s/2}\int_{-f_{ss}/2}^{f_{ss}/2} S(f_x,f_0)^2\,\mathrm{d}f_x\mathrm{d}f_t}}.$$

It is hypothesized that c_v is related to the standard deviation of the velocity estimates, where an increase in c_v should result in an increase in standard deviations.

Based on the simulated $\bar{\lambda}_x = 1/\bar{f}_x$ and the theoretically predicted lateral wavelength given in (1), the relative bias of λ_x can be estimated as

$$B_{\lambda_x} = \frac{\bar{\lambda}_x - \lambda_x}{\lambda_x}.$$

This bias arises due to the fact that the Fraunhofer approximation is not entirely valid. A positive bias is expected to induce a negative bias on the velocity estimates. The mean transverse wavelength, $\bar{\lambda}_x$, can be used in the estimator to yield a more unbiased estimate. Furthermore, $\bar{\lambda}_x$ instead of λ_x can be used in (2) to expectedly reduce the bias on the velocity estimates.

The third measure is the energy ratio, E_r, computed as

$$E_r = \frac{\int_{-f_s/2}^{f_s/2}\int_{-f_{ss}/2}^{0} S(f_x,f_t)^2\,\mathrm{d}f_x\mathrm{d}f_t}{\int_{-f_s/2}^{f_s/2}\int_{-f_{ss}/2}^{f_{ss}/2} S(f_x,f_t)^2\,\mathrm{d}f_x\mathrm{d}f_t}.$$

This provides information of the energy leak from the right half plane to the left half plane of the 2D frequency spectrum. Fig. 3 serves as an illustration of the energy leak from positive spatial frequencies to negative spatial frequencies. It is hypothesized, that this gives an estimate of the overall performance of the TO velocity estimator. If the value of E_r approaches 50%, the amount of energy in both quadrants is increasingly the same, and velocity estimation is expected to be compromised, because the spatial quadrature approach has failed. Therefore, it is hypothesized that the relative mean standard deviation and $\tilde{E}_{\mathrm{RMS}}$ increase as E_r increases.

IV. SIMULATIONS

Simulated data are used to evaluate the implementation of the TO method on a phased array. First, an initial example is constructed with a sensible choice of parameter settings. Afterwards, several parameter settings are varied around this initial operating point to investigate their effect on the performance of the estimator, which will provide an indication of the robustness of the method.

This section presents the simulation setup, the data generation and processing, and the results.

A. Simulation Setup

The ultrasound simulation program Field II [19], [20] was used for the simulation study. A phased array transducer with the characteristics shown in Table I was emulated. A blood vessel, as illustrated in Fig. 2, was modeled as a circular cylindrical volume (radius = 6 mm, length = 20 mm) of moving scatterers surrounded by a block of stationary scatterers in a 20 mm × 20 mm × 20 mm volume.

TABLE I
TRANSDUCER PARAMETERS

Parameter	Value
Transducer type	Phased array
Number of elements	128
Pitch	0.220 mm
Kerf	0.022 mm
Element height	15 mm
Center frequency	3.5 MHz
Impulse response	3 cycle sinusoid (Hanning windowed)
Elevation focus	85 mm

TABLE II
FIXED SIMULATION PARAMETERS

Parameter	Value
Sampling frequency	100 MHz
Pulse repetition frequency	5 kHz
Speed of sound	1540 m/s
Maximum velocity of blood	1.0 m/s
No. of transmit cycles in excitation pulse	8 cycles
Transmit excitation window	Hanning
Transmit focus (radial depth)	10 cm

The flow was modeled to be laminar with a parabolic flow profile given by

$$v(r) = \left(1 - \frac{r^2}{R^2}\right)v_0, \tag{7}$$

where r denotes the radial position, R is the radius of the tube, and v_0 is the maximum velocity at the center of the tube.

The resolution cell size was conservatively calculated as $\lambda_z \cdot \mathrm{FWHM}_y \cdot \lambda_x/4$, where the full-width-half-max (FWHM) in the elevation direction was calculated as $\mathrm{FWHM}_y = \lambda_z F^{\#}$, yielding approximately $1.2\,\mathrm{mm}^3$. Consequently, the number of scatterers was set to 80 000 to obtain at least 10 scatterers per resolution cell, which ensures fully developed speckle signals [24]. The flow angle was set to be perpendicular (90°) to the depth axis to obtain purely transverse flow at a steering angle of 0°. When scanning at steering angles different from 0°, the scatterer block was rotated around $(x, y, z) = (0, 0, 0)\,\mathrm{m}$ according to the steering angle - i.e. even at steering angles different than 0° no axial velocity component was present. However, at beam-to-flow angles different from 90°, an axial velocity component was present. See also explanation in Fig. 2.

The fixed simulation parameters are listed in Table II. At a depth of 10 cm, the lateral wavelength was 4.1 mm, and the maximal detectable velocity with the given pulse repetition frequency was 5.15 m/s using (6). The peak velocity of 1 m/s was therefore only at about 20% of the aliasing limit.

Table III lists the parameters that were varied in the simulation study. A number of initial conditions were used to form a

TABLE III
VARIED SIMULATION PARAMETERS

Parameter	Value
Scan depth (transmit focus at scan depth)	2.5 5 7.5 **10** 12.5 15 [cm]
Scan depth (fixed transmit focus at 10 cm)	2.5 5 7.5 **10** 12.5 15 [cm]
Steering angle	[-45:5:45] (**0**) [°]
Beam-to-flow angle	[60:5:120] (**90**) [°]
F# in transmit	4 6 8 **10** 12
Transmit apodization shape	**Hanning**, Tukey, Rect
Receive apodization shapes	**Hanning**, Tukey, Rect
Spacing between TO apodization peaks	33 49 65 81 **97** [elements]
Width of TO apodization peaks	8 16 **32** 64 [elements]
Number of emissions per estimate	4 8 16 **32** 64 [emissions]
Lag in acquisition time	**1** 2 3 4 5
SNR	-3 0 3 6 9 12 ∞ [dB]

starting point in the parameter space as indicated with boldface in Table III. During this study, the different parameters were kept fixed at their starting point (unless otherwise stated), and only the parameter under investigation was varied. Each simulation setup was repeated 100 times with random initial scatterer positions.

A few comments to some of the parameters in Table III is given here: For the different scan depths, the center of the vessel was placed at the given scan depths. In one case, the transmit focus depth was the same as the scan depth, and in the other, the transmit focus depth was fixed at 10 cm for all scan depths. For the apodization shapes, the Tukey window had a ratio of taper of 0.5. At a depth of 10 cm, the spacing of [33 49 65 81 97] elements corresponded to λ_x = [12.1 8.2 6.2 5.0 4.1] mm. For the TO apodization peak width investigation, the spacing was 65 elements (not 97), so that a TO peak width of 64 elements could be obtained. The lag in acquisition corresponded to effectively lowering the pulse repetition frequency by the given factor. According to the previous calculation of the aliasing limit, the peak velocity, v_0, with the given lag values, was at approximately [20 40 60 80 100] % of the aliasing limit of the transverse velocity estimator. As default, the SNR was ∞, i.e. no noise was added. When changing the SNR, zero mean white Gaussian noise was added to the beamformed RF signals prior to the matched filtration. The matched filter improved the SNR by 18 dB, and the resulting SNR after matched filtration is listed in the table.

B. Data Generation and Processing

M-mode lines were simulated with Field II. The flow lines were matched filtered by convolving them with the time-reversed excitation pulse, and, if echo cancelling was enabled, mean stationary echo canceling was performed by subtracting the ensemble mean of N flow lines. Afterwards, the velocity estimation with RF averaging was employed as described in Section II-C. In addition, the PEF was simulated and the 2D spatio-temporal frequency spectrum was calculated.

Subsequently, the performance measures listed in Section III were computed for both the velocity estimates and the 2D spatio-temporal Fourier domain. For the velocity estimates, the relative mean bias and standard deviations were averaged over the entire vessel - expect for the outer 1 mm at either end of the vessel to reduce edge effects.

C. Simulation Results

Initially, the simulated flow phantom was positioned at a (radial) depth of 10 cm at a steering angle of 0°. The transmit apodization of the transducer aperture was a Hanning function with a width corresponding to a F-number of 10. The two receive apodization shapes were two Hanning functions each 32 elements (7.0 mm) wide, and spaced 96 elements (21 mm) apart. These parameters affected the beamforming of the flow lines. The number of emissions per estimate, N, and the acquisition lag (i.e. the lag in the pulse repetition frequency), k_{prf}, are parameters that only affected the velocity estimator, and they were 32 and 1, respectively. Similarly, changing the flow angle only affected the estimated velocities.

The estimates of the transverse, v_x, and axial, v_z, velocity components from the 100 realizations are shown in Fig. 4. The velocity is fully transverse, hence, no axial velocity is present. This is reflected in the figure. The axial velocity component is estimated using a conventional axial velocity estimator, and is therefore not investigated further. With the standard settings, the relative mean bias, $\tilde{B}_{v_x}$, was -5.0% and the relative standard deviation, $\tilde{\sigma}_{v_x}$, was 7.9% without echo cancelling. With echo cancelling, $\tilde{B}_{v_x}$, was 3.8% and $\tilde{\sigma}_{v_x}$, was 7.8%. Although not considered further, for comparison it can be noted that no axial bias is present, and that the standard deviations for the axial velocity estimates are about an order of magnitude smaller than for the transverse velocity estimates.

The effect on the performance measures when changing the position of the simulated phantom in terms of (radial) scan depth is illustrated in Figs. 5a and 5b. Fig. 5a shows the result when the transmit focal depth follows the phantom position, and Fig. 5b the results of having a fixed transmit focus at a depth of 10 cm. No large difference between the two types of focusing exists. The relative mean standard deviation increases with depth, and also the relative mean bias is depth dependent. With echo cancelling $\tilde{B}_{v_x}$ increases, whereas without echo cancelling $\tilde{B}_{v_x}$ is closest to 0% at around 75 mm for both transmit foci. As the depth increases, an increasing difference between $\tilde{B}_{v_x}$ with and without echo cancelling is visible.

At a depth of 15 cm, $\tilde{B}_{v_x}$ and $\tilde{\sigma}_{v_x}$ was 8.5% and 10%, with echo cancelling and transmit focus at 15 cm. For the fixed transmit focus at 10 cm and using echo cancelling, $\tilde{B}_{v_x}$ was 14% and $\tilde{\sigma}_{v_x}$ was 11%.

The effect of changing the steering angle (and also rotating the phantom), is visible in Fig. 5c. The $\tilde{\sigma}_{v_x}$ is lowest at a steering angle of 0 degrees with a value of 8.1% and increases with increasing steering angle. At ±45° $\tilde{\sigma}_{v_x}$ is 11%. Without echo cancelling $\tilde{B}_{v_x}$ ranges from -1% to -7% without a clear trend. However, with echo cancelling, $\tilde{B}_{v_x}$ is 3.3% at 0° and increases to 17% at ±45°. The difference between the relative mean bias with and without echo cancelling increases when steering away from 0°.

Regarding the beam-to-flow angle, the results are shown in Fig. 5d. The relative mean standard deviation is lowest at 90° (8.3%) and highest at either 60 or 120° with an approximate

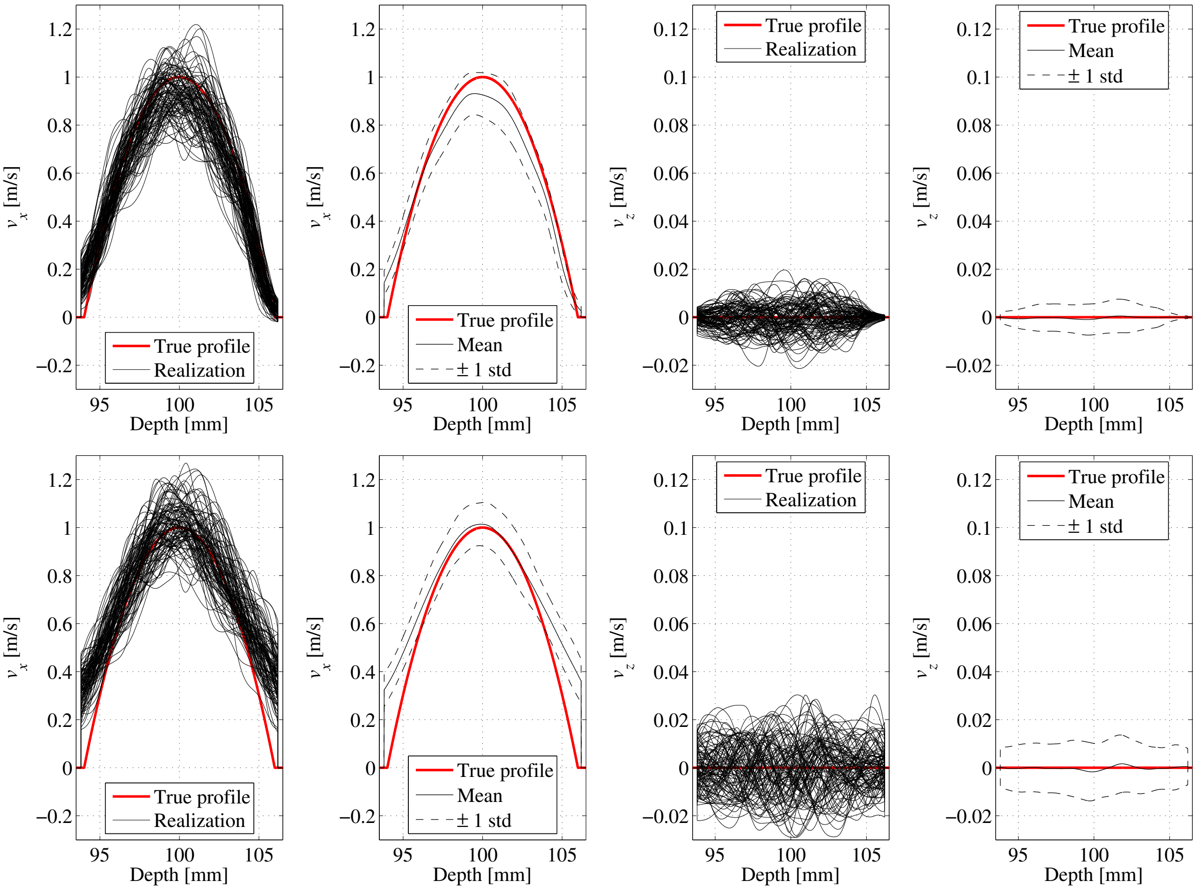

Fig. 4. Transverse, v_x, and axial, v_z, velocity estimates from 100 simulated realizations (column 1 and 3) and the mean and the standard deviation (column 2 and 4). Top panels (row 1) are results without echo cancelling, and bottom panels (row 2) with echo cancelling. Note that the velocity range on the y-axis has been decreased with a factor 10 for the axial velocities (column 3 and 4) compared to the transverse velocities (column 1 and 2).

value of 23%. The relative mean biases are more or less the same with and without echo cancelling except at values close to 90°. At 90° the difference is largest. Without echo cancelling there is no large variation in $\tilde{B}_{v_x}$, whereas with echo cancelling, a noticeable jump at a beam-to-flow angle of 90% can be observed.

On the transmit side, the F-number of the transmitting aperture was varied. The results can be seen in Fig. 5e, which shows that the F-number has only a small effect on both $\tilde{B}_{v_x}$ and $\tilde{\sigma}_{v_x}$. The best performance is obtained at a transmit F-number of 6.

Combining the three different apodization shapes for the transmit aperture and receive aperture yields the results shown in Fig. 5f. With the given (reference) spacing of the TO peaks, the apodization type does not affect $\tilde{\sigma}_{v_x}$ or $\tilde{B}_{v_x}$.

As mentioned, the receive TO apodization creates the transverse oscillations in the PEF. The result of changing the TO apodization peak spacing and width provides the results presented in Fig. 5g and Fig. 5h, respectively. Increasing the spacing between the two TO apodization peaks reduces $\tilde{\sigma}_{v_x}$ with and without echo cancelling and $\tilde{B}_{v_x}$ with echo cancelling. The performance increase (reduction in $\tilde{\sigma}_{v_x}$) is larger when the spacing is lower than 64 elements. With a spacing of 32 elements, only 64 elements are used in receive with $\tilde{\sigma}_{v_x}$ being 25% and $\tilde{B}_{v_x}$ being 33%. These values are most likely not optimal for a 64-element transducer, where a smaller width of the TO apodization peak, and hence larger spacing of the TO apodization peak, is expected to be better.

As Fig. 5i illustrates, increasing the number of emissions per estimate decreases $\tilde{\sigma}_{v_x}$ with approximately $1/\sqrt{N}$ as expected. Without echo cancelling, $\tilde{B}_{v_x}$ is not affected, however, with echo cancelling, $\tilde{B}_{v_x}$ drops from 33% to -1.2%.

Changing the acquisition lag (i.e. lowering the effective pulse repetition frequency) lowers the relative standard deviation, because the peak velocity gets closer to the aliasing limit. This can be observed from Fig. 5j. When k_{prf} = 4, v_0 is at about 80% of the aliasing limit. For k_{prf} = 5, v_0 is at about 100% of the aliasing limit, and therefore, aliasing occurs, which affects both $\tilde{\sigma}_{v_x}$ and $\tilde{B}_{v_x}$ and results in a decreased performance.

Fig. 5k displays the results of varying the SNR of the beamformed RF data. The matched filter improved the SNR by 18 dB. It can be observed that the echo cancelling (mean subtraction of ensemble values) improves the performance when the SNR is below 6 dB. The results also demonstrate, that when the SNR is below 3 dB, the performance degrades rapidly. Without echo cancelling the relative mean standard deviation is 22% and 50% at 3 dB and 0 dB, respectively,

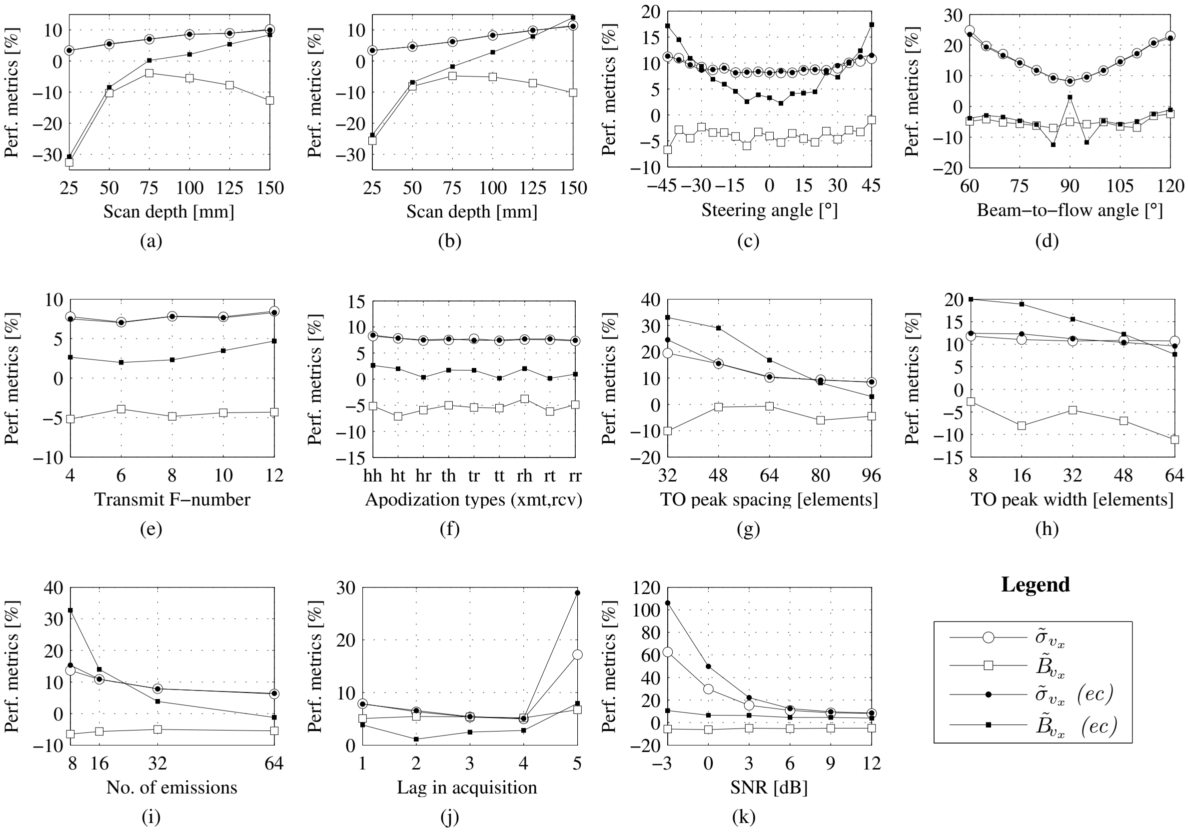

Fig. 5. Performances measures ($\tilde{\sigma}_{v_x}$ and $\tilde{B}_{v_x}$) with and without echo cancelling (ec) for (see legend at the bottom): (a) different scan depths with transmit focus at the given scan depth; (b) different scan depths with fixed transmit focus at 10 cm; (c) a number of steering angles; (d) a number of beam-to-flow angles; (e) various F-numbers in transmit; (f) the nine combinations of Hanning [h], Tukey [t], and rectangular [r] apodized aperture functions in transmit & receive; (g) different spacings between the two TO apodization peaks in receive; (h) different widths of the two TO apodization peaks in the receive; (i) varying the number of emissions per estimate; (j) five different lag values, k_{prf}, in the acquisition, so the pulse repetition frequency effectively is $5/k_{prf}$ kHz; and finally, (k) the performance depending on the SNR.

whereas with echo cancelling the values are 15% and 30%. The relative mean bias is unaffected with and without echo cancelling.

Overall it can be noted that echo cancelling does not affect $\tilde{\sigma}_{v_x}$. However, $\tilde{B}_{v_x}$ is affected, but primarily when the beam-to-flow angle is close to 90°.

To test the hypothesis that a correlation between the performance measures of the PEFs and the performance measures velocity estimates exist, pair-wise values are plotted in Fig. 6. For these plots all the varied parameter values are included except the variation of the beam-to-flow angle, the number of emissions per estimate, and the acquisition lag, as these parameters do not affect the PEF. For the velocity estimates, only the values without echo cancelling are investigated, as the echo cancelling affects the performance of the estimator.

Fig. 6a demonstrates the correlation between the coefficient of variation, c_v, of the transverse wavelength in the PEF and the relative mean standard deviation of the velocity estimates. The correlation value of 0.96 indicates a strong relation. Fig. 6b presents the correlation between the bias of the mean transverse wavelength based on the simulated PEF compared to the relative mean bias of the velocity estimates. The correlation value is -0.91 indicating that a positive bias of the mean wavelength leads to a negative bias on the velocity estimates. In Fig. 6c the relation between the energy leak, E_r, and the relative mean RMS error shows a correlation of 0.43. This indicates some relation between the two, however, the results tend to group into two trends, which lowers the correlation value. A smaller group, where the same value of E_r results in different values for $\tilde{E}_{\text{RMS}}$, and a larger group where a linear relation is observed. Therefore, E_r only to some extend can predict $\tilde{E}_{\text{RMS}}$. Finally, Fig. 6d indicates the correlation between the energy leak and the relative mean standard deviation. The correlation value is 0.89.

V. MEASUREMENTS

To complement the findings from the simulations, measurements were conducted in a similar environment to the simulation study.

A. Measurements Setup

The experimental ultrasound scanner SARUS [25] was used to acquire data together with a transducer with the same parameters as the ones listed in Table I.

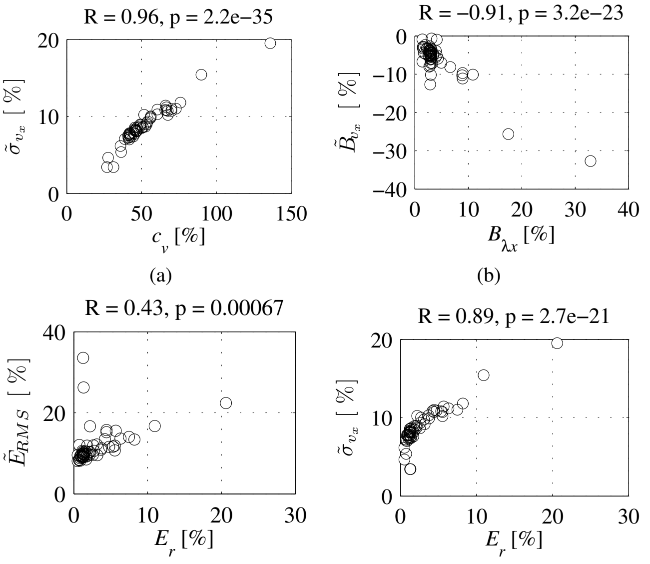

(a) (b) (c) (d)

Fig. 6. Correlation between the performance measures for the 2D spatio-temporal frequency spectrum and the performance measures for the velocity estimates. R indicates the correlation value, and p is the p-value for testing the hypothesis R=0. (a) is for the coefficient of variance, c_v, of the 2D spectrum compared to the relative mean standard deviation, $\tilde{\sigma}_{v_x}$. (b) Is the bias of the transverse wavelength, B_{λ_x}, in the 2D spectrum versus the bias of the velocity estimates, $\tilde{B}_{v_x}$. (c) is the energy ratio of energy leakage, E_r, in the 2D spectrum compared to the relative mean root-mean-square error, $\tilde{E}_{\text{RMS}}$, of the velocity estimates. (d) is E_r versus $\tilde{\sigma}_{v_x}$.

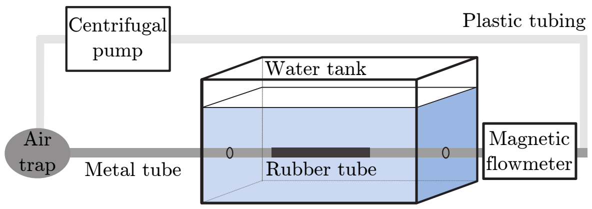

Fig. 7. Illustration of the flow-rig system. It consists of a centrifugal pump, an air trap, a long rigid metal tube extending into a water tank followed by a magnetic flow meter. The tubing inside the water tank is replaced with rubber penetrable to ultrasound waves. A transducer fixation device can be lowered into the water tank at adjustable beam-to-flow angles. The radius of the metal tube and the rubber tube is 6 mm.

TABLE IV
Fixed Parameters for Measurements

Parameter	Value
Sampling frequency	70 MHz
Number of channels	128
Pulse repetition frequency	1.25 kHz
Speed of sound	1480 m/s
Maximum velocity of blood mimicking fluid	0.25 m/s
No. of transmit cycles in pulse	8 [cycles]
Transmit focus (radial depth)	10 cm
Transmit F-number	6
Center of vessel	9.5 cm
Vessel orientation compared to transducer surface	Parallel

TABLE V
Varied Parameters for Measurements

Parameter	Value
Number of emissions per estimate	8 16 **32** 64
Steering angle	-30:5:30, **(0)** [degrees]
Spacing between TO apodization peaks	33 49 65 81 **97** [elements]
Width of TO apodization peak	8 16 **32** 64 [elements]
Optimal TO apodization peak spacing	64 80 96 112 120

The measurements were performed on an in-house built flow-rig system as depicted in Fig. 7. A Cole-Parmer (Vernon Hills, IL, US) centrifugal pump circulates a blood-mimicking fluid in a closed loop circuit. Part of the circuit is contained inside a tank filled with demineralized water, where part of the tubing is replaced with a heat-shrink tube, which is penetrable to ultrasound. The internal radius, R, is 6.0 mm, the thickness of heat-shrink tube is 0.5 mm, and the length of the metal tube prior to the rubber tube is 1.2 m to ensure fully developed laminar flow with a parabolic flow profile. The fluid volume flow, Q, was measured with a MAG 3000 flow meter (Danfoss, Hasselager, Danmark).

The blood-mimicking fluid (Danish Phantom Design, Frederikssund, Denmark) contained 5 micron orgasol, glycerol, detergent, and demineralized water in its concentrated form [26]. It was diluted 1:20 with demineralized water, and dextran was added to obtain a viscosity, μ, of 3.9 mPa·s. The density, ρ, was 1.0×10^3 kg/m^3.

The peak velocity in the tube was set to 0.25 m/s in contrast to the 1 m/s in the simulations. This velocity was chosen to assure laminar and fully developed flow. The pulse repetition frequency was adjusted accordingly with a factor of four. With this setting, the peak velocity of 0.25 m/s was at approximately 20% of the aliasing limit.

The vessel was parallel to the transducer surface, and the center of the vessel was located 9.5 cm below the transducer. The parameters that were fixed for the measurements are listed in Table IV, and the varied parameters are listed in Table V. The standard settings are typed in boldface. For the investigation of the TO apodization peak width, the spacing between the TO apodization peaks was 65 elements. For the optimal TO apodization peak spacing, the width of the TO apodization peaks are adjusted accordingly, so a spacing of [64 80 96 112 120] elements goes with TO apodization peak widths of [64 48 32 16 8] elements, respectively.

B. Data Acquisition and Processing

Using SARUS, data were sampled with 12 bits at 70 MHz from each transducer channel. The fixed measurement parameters are listed in Table I. After data acquisition, the channel data were filtered with a matched filter designed as the time-reversed excitation pulse. The RF data were beamformed using the Beamformation Toolbox 3 [27]. Echo canceling was performed by subtracting the mean of an assemble of emissions in the same direction. As part of the velocity estimation, RF averaging was performed with a window length equal to the excitation pulse length.

C. Experimental Results

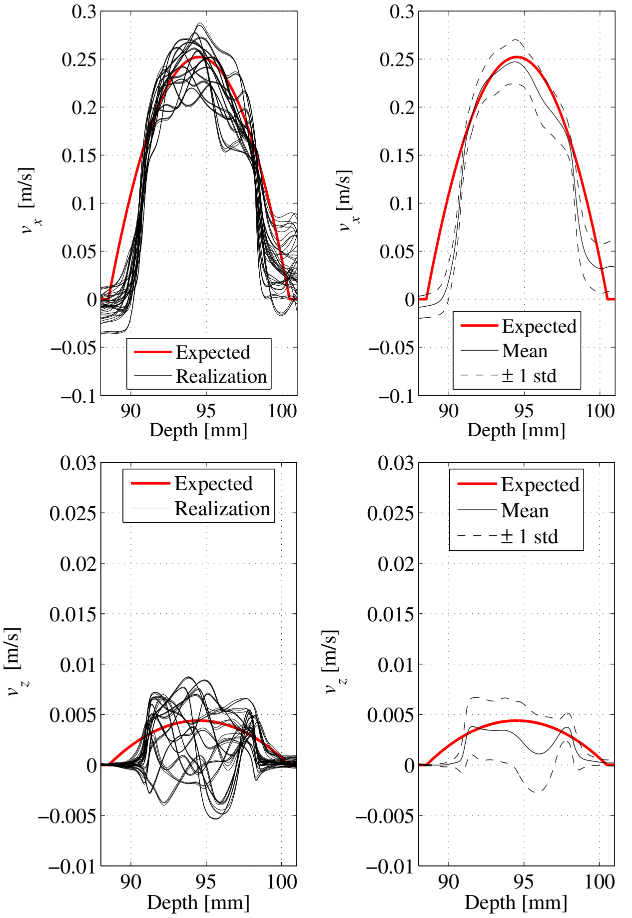

Fig. 8. Measured transverse, v_x, and axial, v_z, velocity components at a beam-to-flow angle of approximately 89° in the experimental flow-rig system. The left panels show the result of 45 estimated realizations of the velocity profiles using the standard settings and the expected parabolic profiles. The right panels show the expected profiles, the mean of the estimated velocities plus/minus one standard deviation. The underestimation at the vessel boundaries is due to clipping in the sampled RF signals from the vessel walls. This was only a issues at beam-to-flow angle close to 90° (see Section VI for more details). Note that the velocity range on the y-axis for the axial velocities (bottom panels) are reduced with a factor 10 compared to the transverse velocities (top panels).

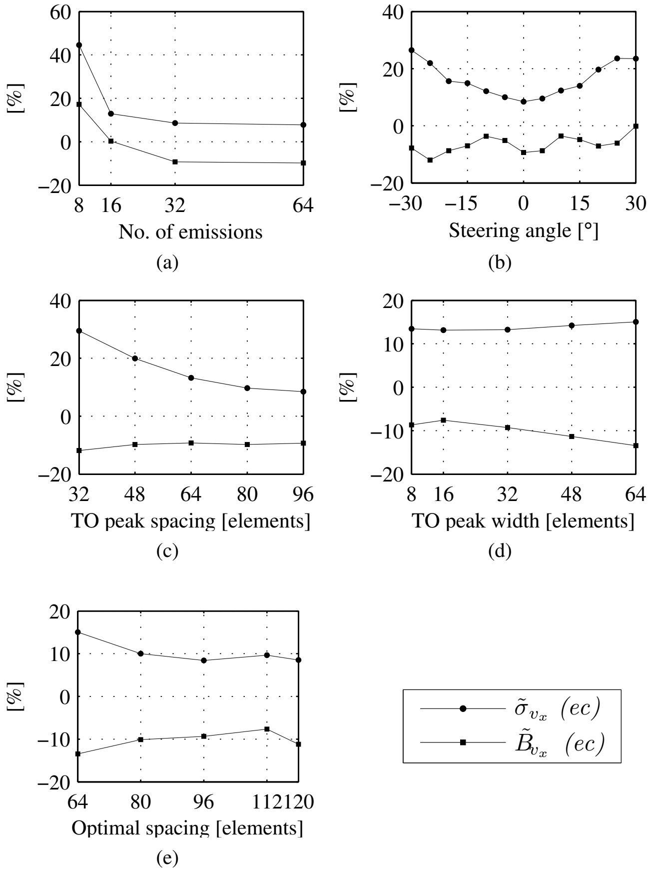

Fig. 9. Illustrates the mean relative standard deviation and the relative mean bias with echo cancelling for: (a) changing the number of emissions per estimate, (b) varying the steering angle, (c) changing the TO peak spacing, (d) changing the TO peak width, and (e) optimizing the TO peak spacing.

Estimated transverse and axial velocities based on experimental flow-rig measurements are shown in Fig. 8. Using the (default) parameters listed in Table IV and V, 45 velocity profiles are obtained for each velocity component. The expected profiles of the velocity components are illustrated as well. They are obtained based on the volume flow, the vessel radius, and an estimate of the beam-to-flow angle. The beam-to-flow angle was estimated to be approximately 89-90° based on B-mode images. For the transverse velocity components, it can be observed, that the mean profile follows the expected parabolic profile. For these data, the relative standard deviation and bias were 8.6 % and −9.2 %, respectively. As Fig. 8 illustrates, the axial velocity component is very small due to a beam-to-flow angle of almost 90°. As well known, it would not be possible to obtain the correct velocity magnitude based on the axial velocity alone as small changes in the estimated beam-to-flow angle would result in large changes of the estimated velocity magnitude due to the division by the $\cos\theta$-term.

Based on the estimated velocity components at the center of the vessel, the mean velocity magnitude over the 45 profiles is 0.247±0.023 m/s compared to an expected peak velocity magnitude of 0.252 m/s. The beam-to-flow angle is calculated to be 89.3±0.77°. Excluding the almost zero velocities at the vessel boundaries, the mean angle off all estimates at all depths inside the vessel is 89.3±0.85°.

In Fig. 9 the result of varying the different parameters listed in Table V is illustrated. Fig. 9a demonstrates the results of increasing the number of emissions per estimate. Both $\tilde{\sigma}_{v_x}$ and $\tilde{B}_{v_x}$ decrease with increasing numbers. The negative $\tilde{B}_{v_x}$ is due to clipping in the RF signals from the vessel walls.

In Fig. 9b the effect of changing the steering angle is illustrated. However, it must be noted that this differs from the simulations in the regard that the vessel was parallel to the transducer surface for all steering angles, and not rotated as the simulation phantom was. In the simulations, a beam-to-flow angle of 90° was maintained for all steering angles, yielding full transverse flow and no axial velocity component. For the measurements, the vessel was perpendicular to the transducer surface for all steering angles. Therefore, the beam-to-flow angle was 90° + θ_0. Hence, for a steering angle different than 0°, the beam-to-flow was no longer 90° resulting in a reduced transverse velocity component and an increase in the the axial velocity component. Additionally, the vessel location (radially) was farther away from the transducer as the steering angle is moved away from 0°. With that in mind, the results still demonstrate that larger steering angles results in larger standard deviations, however, if the angle is below ±20 degrees, the relative standard deviation remains below 20%.

The effect of changing the TO peak spacing in the receive beamforming is illustrated in Fig. 9c. As the spacing increases, $\tilde{\sigma}_{v_x}$ decreases, whereas $\tilde{B}_{v_x}$ is practically unaffected.

Fig. 9d shows the effect of changing the peak width. The effect on $\tilde{\sigma}_{v_x}$ is small, but there is an effect on $\tilde{B}_{v_x}$.

Finally, Fig. 9e demonstrates the effect of using an optimal TO peak spacing based on the different TO peak widths. Both $\tilde{\sigma}_{v_x}$ and $\tilde{B}_{v_x}$ are affected by this.

VI. DISCUSSION

This section covers the discussion of the results from the simulations and the results obtained form flow-rig measurements, and the results are compared to the theory when applicable.

From (1) the transverse spatial wavelength, λ_x, increases as a function of depth, and therefore, the velocity range of the TO estimator increases in accordance with (6). The simulations show that the relative mean standard deviation, $\tilde{\sigma}_{v_x}$, increased with depth (Figs. 5a & 5b). Two factors can explain this. First, c_v was observed to increase with depth. Secondly, the simulated peak velocity was kept constant, and as λ_x increases, the velocities get further and further away from the aliasing limit, and therefore, the standard deviation on the velocity estimates increases. Both factors are suspected to contribute to the observed increase in relative standard deviation as the depth increases. The latter reason is supported by Fig. 5j. This demonstrates, that it is important to adjust the pulse repetition frequency to match the expected peak velocity. In the reference setup, the peak velocity was at approximately 20% of the aliasing limit of the TO estimator at a depth of 10 cm. When the velocity was at 80% of the aliasing limit, $\tilde{\sigma}_{v_x}$ was 5.1% (see Fig. 5j).

The bias in the velocity estimates arises from the discrepancy between the mean transverse wavelength in the PEF, and the theoretically derived wavelength. As the simulations results have demonstrated a difference in the relative mean bias depending on whether echo cancelling was used or not exists. This demonstrates that the echo cancelling filter biases the velocity estimates towards an overestimation. However, as Fig. 5d demonstrates, this only happens in the simulations when the beam-to-flow-angle is close to 90°, and is expected to be a consequence of the lack of axial motion when employing the echo cancelling filter. It is expected that better echo cancelling filters can remedy or improve this.

Both simulations and measurements (Figs. 5c & 9b) show that the performance degrades as the steering angle increases. Several factors come into play: 1) The effective aperture decreases, hence, the lateral wavelength increases with the same effect as described above. 2) In the measurements, the angle sensitivity of the elements influence the SNR and therefore the performance of the TO estimator. 3) The radial depth for the measurements increases with the steering angle due the fixed positions of the vessel and the transducer.

The bias for the measurements depending on the steering angle have a minimum at a steering angle of 0° where the beam-to-flow angle is 90° (Fig. 9b). As mentioned this is a consequence of clipping in the RF signals originating from the vessel wall. A large part of the signal energy was reflected at the incident angle of 90°. At the same time, the gain was set too high, so that the sampled signals were saturating the analog-to-digital converter. This was the case for the signals originating from the vessel wall, but due to the 8 cycles in the transmitted pulse, the clipping also occurred inside the vessel wall drowning the additional small signal amplitudes from the scatterers in the fluid. Therefore, the sampled and beamformed signals at those depths were constant over time, leading to an estimated velocity of 0 m/s. On that account, the minimum around 0° is expected to be an artifact. Also, the different values for $\tilde{B}_{v_x}$ arise due to different PEFs and radial vessel location when steering the beam. Therefore, the results in Fig. 5c cannot be directly compared to the results in Fig. 9b.

The results demonstrate that it is important to estimate the true wavelength for a given setup, so the TO angle in the beamforming step can be adjusted. Alternatively, the velocity estimates can be bias compensated based on the difference in wavelengths. As Fig. 6b indicates, a 10% bias in wavelength, corresponds to approximately a -10% relative mean bias in the velocity estimates from the simulations. This relation is an approximation. Yet, if the actual transverse wavelength is 10% larger than expected, then an underestimation of 10% is not surprising if using a transverse wavelength in (5) that is 10% too small.

The results also indicate, that the bias is a function of depth depending on the parameter settings. For optimal bias compensation, this function has to be derived for a given setup. The true transverse wavelength can be estimated based on simulations or hydrophone measurements, yet, the process of optimizing the actual (mean) transverse wavelength in the PEF and the TO angle is a recursive process, because the estimated $\hat{\lambda}_x$ influences the TO angle, θ_{TO}, which again affects PEFs, and therefore, the estimation of $\hat{\lambda}_x$.

The transmit F-number should be optimized for the given field of view for the velocity estimates. The transmitted field must be broad enough to cover the diverging TO beams. The optimal F-number is 6 for the standard simulation setup. This value was used in the measurements.

Varying the apodization types (either in transmit or in receive) did not affect performance (Fig. 5f). The larger the area under the apodization functions, the better SNR can be obtained in a noisy environment, and therefore, rectangular or Tukey-windowed apodizations may be advantageous at low SNRs.

Performance decreases when peak separation in receive decreases (Figs. 5g & 9c), due to a lower spatial frequency. Additionally, a poorer spatial resolution is obtained. If the larger standard deviation is accepted, an implementation on a 64 element transducer is possible. Fig. 5h indicates that increasing the TO apodization peak widths decreases $\tilde{\sigma}_{v_x}$, although the effect is small. Broader TO peaks increases the SNR. The results in Fig. 9d show a slight increases in $\tilde{\sigma}_{v_x}$ when increasing the width. The SNR in the flow-rig measurement is large due to practically no attenuation in water, so the effect may be different in tissue. The results from the TO apodization peak width and peak distance, Fig. 9e, shows the optimal (for these two parameters only) combination of width and spacing. Again, these results may be different when the SNR is low. As the results in Fig. 5k demonstrate, the performance of the estimator degrades rapidly when the SNR decreases below 3 dB. So, in cases where the SNR is low, and increased amount of receive energy is expected to be beneficial and outweigh the drawback of increasing the apodization peaks and thereby also reduce the TO spacing.

The correlation coefficient between the PEF metrics and the performance measure indicate that correlations between the PEF metrics and the performance measures exist. The PEF metric c_v is related to $\tilde{\sigma}_{v_x}$. There is also a relation between the bias, B_{λ_x}, of the mean transverse wavelength compared to the theoretical wavelength and the relative mean bias, $\tilde{B}_{v_x}$, of the velocity estimates. A relation between the energy leak, E_r, and the $\tilde{\sigma}_{v_x}$ exists, but the relation between E_r and $\tilde{E}_{\text{RMS}_{v_x}}$ is not as clear.

VII. CONCLUSION

In general, a lot can be learned by investigating and optimizing the PEF prior to performing velocity simulations. In other words, the PEF metrics can be used as an initial assessment of the expected estimator performance. The PEF metrics can be readily computed opposed to the simulated velocity data and the derived performance measures.

Various parameters have been investigated in a simulation study around a reference point at 10 cm's depth, where the relative mean bias, $\tilde{B}_{v_x}$, was estimated to 7.8% and the relative mean standard deviation, $\tilde{\sigma}_{v_x}$, was estimated to 3.8% with echo cancelling. At a depth of 15 cm, it was possible to estimate the lateral velocity in the simulations using echo cancelling with $\tilde{B}_{v_x}$ and $\tilde{\sigma}_{v_x}$ being 8.5% and 10%, respectively.

The flow-rig measurements resulted in $\tilde{\sigma}_{v_x}$ equal to 8.3% and $\tilde{B}_{v_x}$ equal to 11% at a depth of 9.5 cm with 32 shots per estimate. At the center of the vessel, the velocity magnitude was estimated to be 0.247 ± 0.023 m/s compared to an expected peak velocity magnitude of 0.252 m/s and the beam-to-flow angle was calculated to be $89.3 \pm 0.77^\circ$ compared to an expected value between 89° and 90°. For steering angles up to ± 20 degrees, $\tilde{\sigma}_{v_x}$ was below 20%. The results also showed, that a 64 element transducer implementation is feasible, but with a poorer performance compared to a 128 element transducer.

Overall, the estimator is robust with values of $\tilde{\sigma}_{v_x}$ less than 10% for most parameter settings. Additionally, methods to reduce the bias have been demonstrated.

The simulation and measurement results demonstrate that the TO method is suitable for use in conjunction with a phased array transducer, and that 2D vector velocity estimation is possible down to a depth of 15 cm.

REFERENCES

[1] D. H. Evans, J. A. Jensen, and M. B. Nielsen, “Ultrasonic colour Doppler imaging,” *Interface Focus*, vol. 1, no. 4, pp. 490–502, August 2011.

[2] P. M. Hansen, M. M. Pedersen, K. L. Hansen, M. B. Nielsen, and J. A. Jensen, “Demonstration of a vector velocity technique,” *Ultraschall in Medicine*, vol. 32, pp. 213–5, 2011.

[3] M. D. Fox, “Multiple crossed-beam ultrasound Doppler velocimetry,” *IEEE Trans. Son. Ultrason.*, vol. SU-25, pp. 281–286, 1978.

[4] B. Dunmire, K. W. Beach, K.-H. Labs., M. Plett, and D. E. Strandness, “Cross-beam vector Doppler ultrasound for angle independent velocity measurements,” *Ultrasound Med. Biol.*, vol. 26, pp. 1213–1235, 2000.

[5] P. Tortoli, G. Bambi, and S. Ricci, “Accurate doppler angle estimation for vector flow measurements,” *IEEE Trans. Ultrason., Ferroelec., Freq. Contr.*, vol. 53, no. 8, pp. 1425 – 1431, Aug. 2006.

[6] G. E. Trahey, J. W. Allison, and O. T. von Ramm, “Angle independent ultrasonic detection of blood flow,” *IEEE Trans. Biomed. Eng.*, vol. BME-34, pp. 965–967, 1987.

[7] V. L. Newhouse, D. Censor, T. Vontz, J. A. Cisneros, and B. B. Goldberg, “Ultrasound Doppler probing of flows transverse with respect to beam axis,” *IEEE Trans. Biomed. Eng.*, vol. BME-34, pp. 779–788, 1987.

[8] O. Bonnefous, “Measurement of the complete (3D) velocity vector of blood flows,” in *Proc. IEEE Ultrason. Symp.*, 1988, pp. 795–799.

[9] J. A. Jensen, “Directional velocity estimation using focusing along the flow direction: I: Theory and simulation,” *IEEE Trans. Ultrason., Ferroelec., Freq. Contr.*, vol. 50, pp. 857–872, 2003.

[10] J. A. Jensen and R. Bjerngaard, “Directional velocity estimation using focusing along the flow direction: II: Experimental investigation,” *IEEE Trans. Ultrason., Ferroelec., Freq. Contr.*, vol. 50, pp. 873–880, 2003.

[11] J. A. Jensen and P. Munk, “A New Method for Estimation of Velocity Vectors,” *IEEE Trans. Ultrason., Ferroelec., Freq. Contr.*, vol. 45, pp. 837–851, 1998.

[12] M. E. Anderson, “Multi-dimensional velocity estimation with ultrasound using spatial quadrature,” *IEEE Trans. Ultrason., Ferroelec., Freq. Contr.*, vol. 45, pp. 852–861, 1998.

[13] C. Sumi, “Displacement vector measurement using instantaneous ultrasound signal phase - multidimensional autocorrelation and Doppler methods,” *IEEE Trans. Ultrason., Ferroelec., Freq. Contr.*, vol. 55, no. 1, pp. 24–43, 2008.

[14] J. Udesen and J. A. Jensen, “Investigation of Transverse Oscillation Method,” *IEEE Trans. Ultrason., Ferroelec., Freq. Contr.*, vol. 53, pp. 959–971, 2006.

[15] J. Udesen, M. B. Nielsen, K. R. Nielsen, and J. A. Jensen, “Examples of in-vivo blood vector velocity estimation,” *Ultrasound Med. Biol.*, vol. 33, pp. 541–548, 2007.

[16] M. J. Pihl, S. Nikolov, P. Haugaard, M. C. Hemmsen, and J. A. Jensen, “Performance of the transverse oscillation method using beamformed data from a commercial scanner,” in *Proc. IEEE Ultrason. Symp.*, 2009.

[17] H. Liebgott, A. Basarab, S. Marincas, O. Bernard, and D. Friboulet, “Tangential oscillations for motion estimation in echocardiography,” in *IEEE Ultrasonics Symposium*, nov. 2008, pp. 1761 –1764.

[18] M. J. Pihl and J. A. Jensen, “Transverse oscillations for phased array vector velocity imaging,” in *Proc. IEEE Ultrason. Symp.*, 2010, pp. 1323–27.

[19] J. A. Jensen, “Field: A Program for Simulating Ultrasound Systems,” *Med. Biol. Eng. Comp.*, vol. 10th Nordic-Baltic Conference on Biomedical Imaging, Vol. 4, Supplement 1, Part 1, pp. 351–353, 1996.

[20] J. A. Jensen and N. B. Svendsen, “Calculation of Pressure Fields from Arbitrarily Shaped, Apodized, and Excited Ultrasound Transducers,” *IEEE Trans. Ultrason., Ferroelec., Freq. Contr.*, vol. 39, pp. 262–267, 1992.

[21] P. Munk, “Estimation of blood velocity vectors using ultrasound,” Ph.D. dissertation, Department of Information Technology, Technical University of Denmark, Lyngby, Denmark, 2000.

[22] J. A. Jensen, “A New Estimator for Vector Velocity Estimation,” *IEEE Trans. Ultrason., Ferroelec., Freq. Contr.*, vol. 48, no. 4, pp. 886–894, 2001.

[23] T. Loupas, J. T. Powers, and R. W. Gill, “An axial velocity estimator for ultrasound blood flow imaging, based on a full evaluation of the Doppler equation by means of a two-dimensional autocorrelation approach,” *IEEE Trans. Ultrason., Ferroelec., Freq. Contr.*, vol. 42, pp. 672–688, 1995.

[24] B. Osterveld, J. Thijssen, and W. Verhoef, “Texture of B-mode echograms: 3-D Simulations and experiments of the effects of diffraction and scatterer density,” *Ultrason. Imaging*, vol. 7, no. 2, pp. 142–160, Apr. 1985.

[25] J. A. Jensen, H. Holten-Lund, R. T. Nielson, B. G. Tomov, M. B. Stuart, S. I. Nikolov, M. Hansen, and U. D. Larsen, "Performance of SARUS: A Synthetic Aperture Real-time Ultrasound System," in *Proc. IEEE Ultrason. Symp.*, Oct. 2010, pp. 305–309.

[26] K. V. Ramnarine, D. K. Nassiri, P. R. Hoskins, and J. Lubbers, "Validation of a new blood mimicking fluid for use in Doppler flow test objects," *Ultrasound Med. Biol.*, vol. 24, pp. 451–459, 1998.

[27] J. M. Hansen, M. C. Hemmsen, and J. A. Jensen, "An object-oriented multi-threaded software beam formation toolbox," in *Proc. SPIE - Medical Imaging - Ultrasonic Imaging and Signal Processing*, vol. 7968, 2011, p. 79680Y.

Paper IV

3D Vector Velocity Estimation using a 2D Phased Array

Michael Johannes Pihl and Jørgen Arendt Jensen

Proceedings of the IEEE International Ultrasonics Symposium

Presented in Orlando, Florida, United States, 2011

3D Vector Velocity Estimation using a 2D Phased Array

Michael Johannes Pihl and Jørgen Arendt Jensen
Center for Fast Ultrasound Imaging, Department of Electrical Engineering,
Technical University of Denmark, DK-2800 Kgs. Lyngby, Denmark

***Abstract*—A method to estimate the three dimensional (3D) velocity vector is presented is this paper. 3D velocity vector techniques are needed to measure the full velocity and characterize the complicated flow patterns in the human body. The Transverse Oscillation (TO) method introduces oscillations transverse to the ultrasound beam, which enables the estimation of the transverse velocity. To expand the method from 2D to 3D, it is proposed to decouple the velocity estimation into separate estimates of v_x, v_y, and v_z in combination with a 2D phased matrix array. Through simulations the feasibility of using the TO method for estimation 3D velocity vectors, and the proposed decoupling is demonstrated. A 64x64 and a 32x32 elements transducer are emulated using Field II. Plug flow with a speed of 1 m/s in a small region is rotated in the XY-plane. A binary flow example with [v_x,v_y]=[1,0] and [0,1] m/s shows, that the velocity estimation can be decoupled into the transverse and elevation velocity components. This is substantiated by the results for seven different angles, where the mean and the standard deviation of the estimated speed are 0.97±0.05 m/s and of the angle bias are -0.73±3.3° for the 64x64 matrix transducer. For the 32x32 transducer, the mean and standard deviation for the speed are 0.94± 0.11 m/s and for the angle bias -0.48±7.7°. The simulation study clearly demonstrates, that the new method can be used to estimate the 3D velocity vector using a 2D phased matrix array, and that the velocity vector estimation can be decoupled into separate estimates of v_x, v_y, and v_z.**

I. INTRODUCTION

Measurements of the blood velocity in the human body play a key role in diagnosing various cardiovascular diseases [1], however, the complicated flow patterns in the circulatory system yet have to be fully characterized. Conventional methods only estimate velocities in one dimension. As the velocities vary as a function of time and space [2], [3], 3D techniques need to be employed to fully estimate and characterize the complicated flow patterns.

Different approaches have been proposed for 2D velocity estimation. A multibeam approach was suggested by Fox [4] where the velocity components are estimated using trigonometry. Speckle tracking (normalized cross-correlation) proposed by Trahey *et al.* [5] finds the velocity vector by searching for the best match between a kernel and a search region. The directional beamforming approach by Jensen [6] estimates the velocity by cross correlating lines that are beamformed in the direction of the flow.

The Transverse Oscillation method is another technique that solves the angle-dependency problem in traditional ultrasonic flow estimation. The technique was suggested by Jensen and Munk [7], and *in vivo* examples were demonstrated in [2]. A similar approach was suggested by Anderson [8].

So far, the technique has only been used for 2D velocity estimation. Expanding the method from 2D to 3D, it is proposed to estimate v_x, v_y, and v_z separately, *i.e.* to decouple the velocity estimation of v_x and v_y as well as v_z. That is contrary to the other methods mentioned above, where the velocity components cannot be decoupled.

This paper will demonstrate the feasibility of using the TO method on simulated data for estimating 3D velocity vectors using a 2D matrix phased array. Furthermore, the purpose is to demonstrate that the velocity estimation can be decoupled into estimating the three velocity components v_x, v_y, and v_z separately. A simulation study will serve as a proof of concept. The results are presented in Section IV, followed by a discussion and a conclusion.

II. THE TRANSVERSE OSCILLATION METHOD

The basic mechanism, that allows the traditional estimation of axial velocities, is the oscillations in the transmitted ultrasonic pulse. Using the same principle, an introduction of a transverse oscillation in the ultrasound field generates received signals that depend on the transverse motion, and the velocity can be estimated.

A. 3D Velocity Estimation

For the 2D case, a derivation of the required apodization functions and a description of the respective generated fields for the linear array can be found in [7], [9]. A thorough description and derivation of the velocity estimator used for each decoupled transverse or elevation velocity component is given in [10].

In the 3D case, it is assumed that the velocity estimates can be decoupled into three independent velocity components: the axial, v_z, the transverse, v_x, and the elevation v_y. The estimated velocity components v_x and v_y are orthonormal to the scan line. In the setup as illustrated in Fig. 1, the scan line and the z-axis coincides, and the velocity components are v_x, v_y, and v_z.

In terms of beamforming, a center line for axial velocity v_z, two lines in the XZ-plane for the transverse velocity v_x, and two lines in the YZ-plane for the elevation velocity v_y as demonstrated in Fig. 1. As a result, the velocity estimation is decoupled into the three components. The pairwise TO beams are steered at specific fixed angles, such that the spacing is a

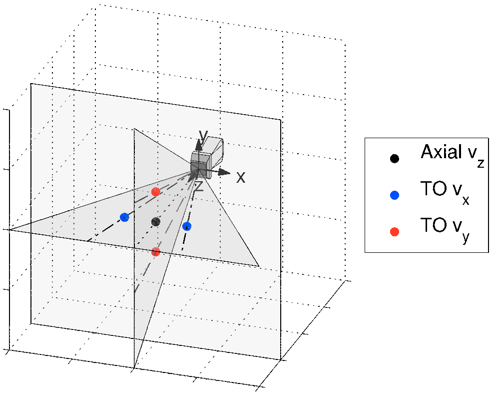

Fig. 1. Beamforming approach for 3D velocity estimation using a 2D matrix phased array transducer. The coordinate system of the transducer is (x,y,z). The dotted line indicates the scan angle, here coinciding with the z-axis. Spheres indicate beamformed samples at a given depth: A center line is beamformed for conventional axial velocity v_z estimation (black), and two pairwise TO lines are beamformed for estimation of the transverse and elevation velocities v_x and v_y (blue and red, respectively). The steering angles have been exaggerated for illustration purposes; for the 64x64 transducer, they are 0.6° with respect to the z-axis. The gray shaded areas illustrate the XY-, XZ-, and YZ-planes.

quarter spatial wavelength at every sample depth, because the lateral wavelength increases with depth.

The axial velocity can also be estimated by use of the conventional autocorrelation approach [11]. For the transverse velocity v_x the TO method is employed as done previously [12] in 2D although the apodizations are adapted to the 2D phased array. As the transverse and elevation velocity components can be decoupled, the field generation, the beamforming approach, and the velocity estimation are identical for v_x and v_y, and follow [12], and is therefore omitted here.

The novelty is that the velocity component in the elevation direction, v_y, can be measured when using a 2D phased array. Essentially, the process of estimating v_y is the same for v_x. The only difference is that the apodization profiles are rotated 90 degrees.

All five lines are beamformed in parallel in receive based on the same transmission, so only five beamformers in receive are required. However, the method may be expanded to beamform several flow lines in parallel. As the lines are beamformed in parallel, the three velocity components are estimated simultaneously.

III. Simulations Setup

The simulations are performed using the ultrasound simulation program Field II [13], [14]. The sampling frequency is 120 MHz, and the speed of sound is set to 1480 m/s.

A 64x64 elements 2D phased array is simulated, however, only 1024 active channels are used. The center frequency is 3 MHz, the pitch $\lambda/2$ mm and the kerf $\lambda/100$ mm. The transducer impulse response is simulated as a 3 cycle pulse at the center frequency multiplied with a Hanning window. A second transducer is simulated with 32x32 elements, but otherwise with the same characteristics.

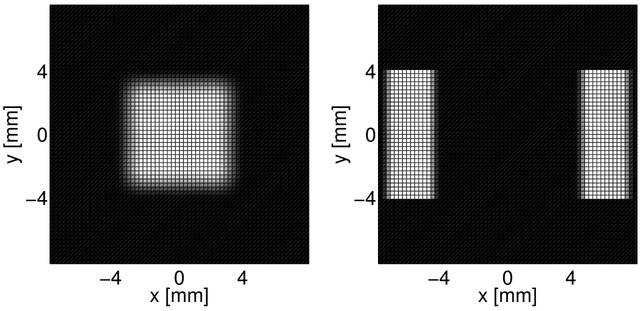

(a) 64x64 transmit (b) 64x64 receive

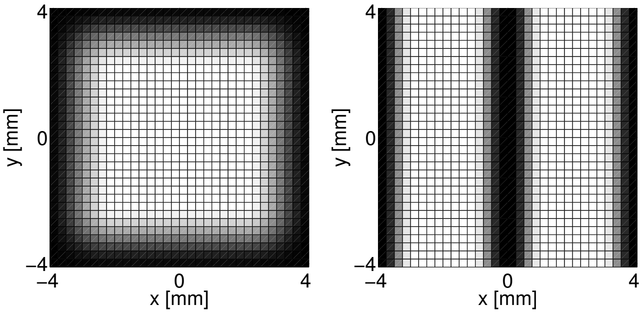

(c) 32x32 transmit (d) 32x32 receive

Fig. 2. Apodization functions in transmit and receive for the 64x64 and 32x32 apertures. Colorbar: Black→white = 0→1. Each small square represents an element. For all four apertures, 1024 active channels are used. The transmit apodizations are the same for each receive line, whereas the depicted receive apertures are for the estimation of v_x.

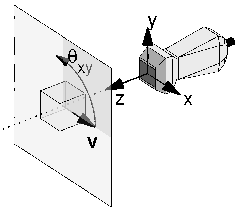

Fig. 3. Illustration of the simulation setup for the 2D transducer. The dotted line is the scan line (here coinciding with the z-axis). The light gray shaded plane is orthonormal to the scan line. The cube represents the flow phantom and the black arrow the velocity vector $\mathbf{v}$. In the simulations, the cube is rotated around the z-axis at different angles, θ_{xy}, within the darker shaded quadrant.

In transmit, only the center 32x32 elements of the 64x64 transducer is used, *i.e.* 1024 active channels. The focal point is set to 25 mm, whereas the point of interest is at 15 mm. For the 32x32 transducer, the transmit apodization is identical to the center 32x32 elements of the 64x64 transducer, whereas the focus point is moved to 100 mm to increase the beam width at 15 mm. The transmit apodizations are illustrated in Fig. 2a and 2c. The transmitted pulse is a 8 cycle sinusoid at the center frequency windowed with a Tukey window with a ratio of taper of 0.75.

For receive, also only 1024 active channels are used. To increase the spatial transverse wavelength, the apodization peaks are placed as far as part as possible. This gives the transducer apodizations as demonstrated in Figs. 2b and 2d.

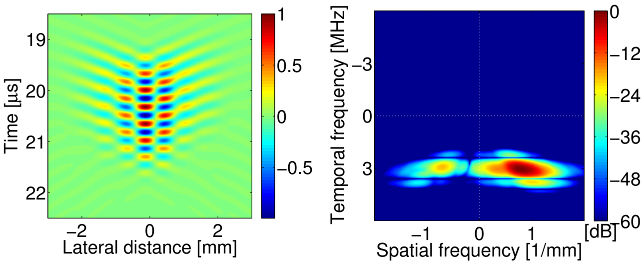

(a) (b)

Fig. 4. (a) Pulse-echo field in normalized pressure for the left TO beam (PEF$_{\text{left}}$) in both the XZ- and YZ-plane. (b) The amplitude spectrum of the 2D spatio-temporal Fourier transform of PEF$_{\text{left}}$+j·PEF$_{\text{right}}$, where both PEFs are complex signals obtained using the Hilbert transform.

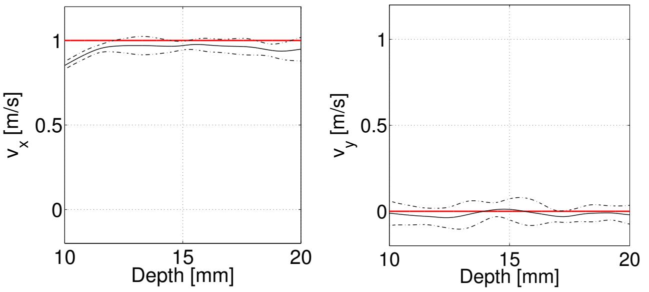

(a) θ_{xy} = 0 degrees (b) θ_{xy} = 0 degrees

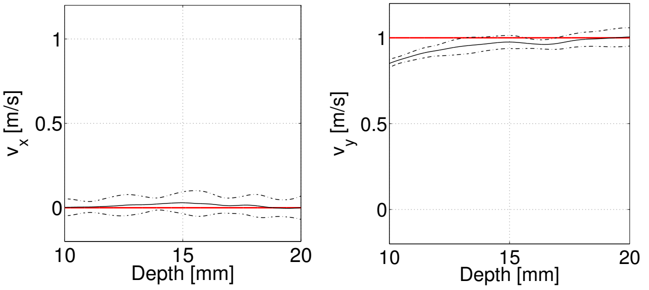

(c) θ_{xy} = 90 degrees (d) θ_{xy} = 90 degrees

Fig. 5. Velocity estimates of v_x and v_y as a function of θ_{xy}. Thick red line indicates simulated velocity, thin black line the mean of 10 profiles and dot-dashed lines the standard deviation.

The receive apodizations are for the two lines in the XZ-plane used for estimating v_x.

Flow motion is simulated in a 10x10x10 mm^3 cube centered at [x,y,z]=[0,0,15] mm with plug flow as illustrated in Fig. 3. 10 000 scatterers with a Gaussian scattering amplitude distribution with zero mean value and unit variance are randomly, uniformly distributed in the volume. The simulations are performed with a constant speed of 1 m/s and a varying angle, θ_{xy}, for the vector flow. The plug flow is rotated around the z-axis (*i.e.* rotations in the XY-plane) as shown in Fig. 3.

IV. RESULTS

A. The Pulse-Echo Field and its Fourier Domain

To investigate how well defined the transverse oscillations are, the pulse-echo fields (PEFs) are calculated with Field II, and the 2D Fourier domain is investigated. The obtained pulse-echo field for the 64x64 transducer with the specified apodizations is illustrated in Fig. 4.

The 2D temporal and spatial Fourier domain is calculated based on the imaginary field obtained when the left beam is the real part, and the right is the imaginary part. The obtained amplitude spectrum is shown in Fig. 4b. The theoretical lateral spatial frequency is 0.85 mm^{-1}, whereas the mean frequency is 0.80 mm^{-1}. This gives a bias of -6% between the theoretical and the mean of the simulated spatial frequencies. For the 32x32 transducer, the values are 3.4 and 4.2 mm^{-1} for the mean and theoretical spatial frequencies, respectively. The bias is -20%.

To investigate how well the TO method performs as spatial IQ, the energy should mainly be concentrated in the 4th quadrant. In Fig.4b there is no energy in the 1st and 2nd quadrant, indicating that the Hilbert transform works for all frequencies. For the lateral spatial frequencies, there is an energy leak into the 3rd quadrant, and it is calculated as $E_l = E_{3q}/E_{total}$, where E_{3q} is the energy in the 3rd quadrant and E_{total} is the total energy. In this case, E_l is 1.1% for the 64x64 transducer and 5.8% for the 32x32 transducer. The coefficient of variation is calculated as $COV = \bar{f}_x/D(f_x)$, where $\bar{f}_x$ is the estimated mean lateral frequency and D the dispersion of f_x. COV is 13.4% and 40.3% for the 64x64 and 32x32 transducers, respectively. These numbers indicate that the spatial distribution of frequencies is more biased, and less well defined for the 32x32 transducer compared to the 64x64. Therefore, it is expected that the velocity estimates for the 32x32 transducer will be poorer than for the 64x64.

B. Velocity Estimates

Before the velocity estimation, a matched filtration is performed using the time reversed transmitted pulse. No stationary echo cancelling is performed. To obtain temporal IQ data, the Hilbert transform is used to create the analytical signal. RF averaging is performed on the autocorrelation estimates as suggested in [15]. The velocities are estimated based on 32 shots, and for each flow angle the simulations are repeated 10 times. No bias compensation is performed in the velocity estimations.

Only velocities in the XY-plane are simulated as illustrated in Fig. 3, hence, the results from the estimation of the axial velocity is omitted.

When the simulated velocity is “binary”, *i.e.* [v_x,v_y]=[1,0] m/s or [0,1] m/s (corresponding to θ_{xy} = 0 or 90°, respectively), the estimated velocities for the 64x64 transducer are shown in Fig. 5. As the figure demonstrates, the estimated velocities closely follow the expected value for both angles.

The flow angle is varied from 0 to 90 degrees in steps of 15 degrees in the XY-plane. The velocity components v_x and v_y at depth 15 mm are estimated for each angle, and the mean and the standard deviation of the transverse velocity components are calculated. The results for the seven different angles are shown in Fig. 6 for the 64x64 and the 32x32 transducer, respectively.

The average performance for all 70 estimates at 15 mm

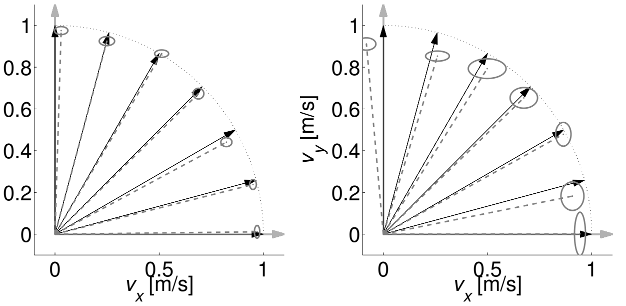

(a) 64x64 (b) 32x32

Fig. 6. Velocity estimates as a function of flow angle θ for the two transducers, respectively. Black arrows (solid) indicate simulated velocities, gray vectors (dashed) the estimated velocities, and gray ellipses (solid) the standard deviations for v_x and v_y, respectively.

TABLE I
OVERALL PERFORMANCE OF THE ESTIMATOR

Statistics	64x64	32x32
Mean speed [m/s]	0.97 ± 0.047	0.94 ± 0.11
Mean angle bias [°]	-0.73 ± 3.3	-0.48 ± 7.7

depth is shown in Table I for the two transducers. The estimated mean and standard deviation of all speeds and of all biases between the estimated and simulated angle, where the flow angle can be estimated by $\hat{\theta} = \arctan(v_y/v_x)$, are listed.

V. DISCUSSION

Fig. 5 with its almost "binary" velocity estimates demonstrates, that it is possible to decouple the transverse velocity estimations into v_x and v_y and estimate them separately. Fig. 6 substantiates this for a number of flow angles. Fig. 6 also shows that the velocity estimates are more uncertain and biased for the 32x32 than for the 64x64 transducer, as expected from the PEF and the amplitude spectrum of the 2D spatio-temporal Fourier domain mentioned in the last paragraph of Section IV-A. This is due to the smaller distance between the aperture peaks for the 32x32 transducer. These findings are more quantitatively illustrated in Table I, where the biases and the standard deviations are higher for the 32x32 compared to the 64x64 array. A better match between the theoretical and mean simulated wavelength, will decrease the bias. Optimization of the PEFs is also exptected to reduce the biases and standard deviations.

On average, the standard deviations for the transverse velocities are about 5% and 10% for the 64x64 and the 32x32 array, respectively, compared to a standard deviation around 1% for the axial velocity component (not shown). That, however, should be seen in the light of that the conventional axial estimator would wrongfully estimate the speed to be 0 m/s, when it actually is 1 m/s as correctly estimated with the proposed 3D TO method.

The simulations demonstrate that the new method can be used to estimate the 3D velocity vector when using a 2D phased array. The beamforming is within the capabilities of modern 3D scanners and the estimators for the three velocity components are on the order of the conventional autocorrelation approach with RF averaging making it suitable for commercial implementations. With clever channel multiplexing the number of active channels needed can also be reduced.

VI. CONCLUSION

The simulation study demonstrates, that the TO method can be used to estimate the 3D velocity vector within 5%. The requirements are a 2D phased array, five parallel beamformers, and 1024 active channels. Additionally, the results confirm that the velocity vector estimation can be decoupled into separate and simultaneous estimates of v_x, v_y, and v_z.

ACKNOWLEDGMENTS

This work was supported by grant 024-2008-3 from the Danish Advanced Technology Foundation and BK Medical Aps, Denmark.

REFERENCES

[1] D. H. Evans, J. A. Jensen, and M. B. Nielsen, "Ultrasonic colour Doppler imaging," *Interface Focus*, vol. 1, no. 4, pp. 490–502, August 2011.

[2] J. Udesen, M. B. Nielsen, K. R. Nielsen, and J. A. Jensen, "Examples of in-vivo blood vector velocity estimation," *Ultrasound Med. Biol.*, vol. 33, pp. 541–548, 2007.

[3] K. L. Hansen, J. Udesen, F. Gran, J. A. Jensen, and M. B. Nielsen, "In-vivo examples of complex flow patterns with a fast vector velocity method," *Ultraschall in Med*, vol. 30, pp. 471–476, 2009.

[4] M. D. Fox, "Multiple crossed-beam ultrasound Doppler velocimetry," *IEEE Trans. Son. Ultrason.*, vol. SU-25, pp. 281–286, 1978.

[5] G. E. Trahey, J. W. Allison, and O. T. von Ramm, "Angle independent ultrasonic detection of blood flow," *IEEE Trans. Biomed. Eng.*, vol. BME-34, pp. 965–967, 1987.

[6] J. A. Jensen, "Directional velocity estimation using focusing along the flow direction: I: Theory and simulation," *IEEE Trans. Ultrason., Ferroelec., Freq. Contr.*, vol. 50, pp. 857–872, 2003.

[7] J. A. Jensen and P. Munk, "A New Method for Estimation of Velocity Vectors," *IEEE Trans. Ultrason., Ferroelec., Freq. Contr.*, vol. 45, pp. 837–851, 1998.

[8] M. E. Anderson, "Multi-dimensional velocity estimation with ultrasound using spatial quadrature," *IEEE Trans. Ultrason., Ferroelec., Freq. Contr.*, vol. 45, pp. 852–861, 1998.

[9] J. Udesen and J. A. Jensen, "Investigation of Transverse Oscillation Method," *IEEE Trans. Ultrason., Ferroelec., Freq. Contr.*, vol. 53, pp. 959–971, 2006.

[10] J. A. Jensen, "A New Estimator for Vector Velocity Estimation," *IEEE Trans. Ultrason., Ferroelec., Freq. Contr.*, vol. 48, no. 4, pp. 886–894, 2001.

[11] C. Kasai, K. Namekawa, A. Koyano, and R. Omoto, "Real-Time Two-Dimensional Blood Flow Imaging using an Autocorrelation Technique," *IEEE Trans. Son. Ultrason.*, vol. 32, pp. 458–463, 1985.

[12] M. J. Pihl and J. A. Jensen, "Transverse oscillations for phased array vector velocity imaging," in *Proc. IEEE Ultrason. Symp.*, 2010, pp. 1323–27.

[13] J. A. Jensen, "Field: A Program for Simulating Ultrasound Systems," *Med. Biol. Eng. Comp.*, vol. 10th Nordic-Baltic Conference on Biomedical Imaging, Vol. 4, Supplement 1, Part 1, pp. 351–353, 1996.

[14] J. A. Jensen and N. B. Svendsen, "Calculation of Pressure Fields from Arbitrarily Shaped, Apodized, and Excited Ultrasound Transducers," *IEEE Trans. Ultrason., Ferroelec., Freq. Contr.*, vol. 39, pp. 262–267, 1992.

[15] T. Loupas, J. T. Powers, and R. W. Gill, "An axial velocity estimator for ultrasound blood flow imaging, based on a full evaluation of the Doppler equation by means of a two-dimensional autocorrelation approach," *IEEE Trans. Ultrason., Ferroelec., Freq. Contr.*, vol. 42, pp. 672–688, 1995.

Paper V

A method for estimation of three-dimensional velocity vectors in ultrasound

Michael Johannes Pihl and Jørgen Arendt Jensen

Journal of the Acoustical Society of America

Under review – submitted June 2012

A method for estimation of three-dimensional velocity vectors in ultrasound[a)]

Michael Johannes Pihl[b)] and Jørgen Arendt Jensen
Center for Fast Ultrasound Imaging, Department of Electrical Engineering, Technical University of Denmark, Ørsteds Plads, Bldg. 349, DK-2800 Kgs. Lyngby, Denmark

(Dated: June 22, 2012)

The presented method is based on the Transverse Oscillation approach and synthesizes two double-oscillating ultrasonic fields. It employs a 2D phased array matrix transducer and decouples the velocity estimation into three orthogonal velocity components, which are estimated simultaneously. The suggested spatial quadrature sampling approach requires 5:1 parallel receive beamforming. To investigate the method, the ultrasound simulation tool Field II is used. A proof of concept study demonstrates that the velocity estimation can be decoupled. For a simulated flow phantom emulating a blood vessel and a 32x32 transducer, the average velocity at the center is (v_x, v_y, v_z)=(1.00,0.0091,0.00058)±(0.059,0.083,0.0053) m/s compared to the expected velocity of (1,0,0) m/s. The results are based on 100 flow lines with 32 emissions per estimate. In the XY-plane, the flow angle is estimated without bias with 95 % of the estimates within 8.4°. A parameter study demonstrates that the method is robust in terms of transverse and elevation wavelengths and signal-to-noise ratio (SNR). Adding noise yielding a SNR of 0 dB, the standard deviations increase with approximately a factor of 2. Besides requiring a 2D transducer, the complexity and the number of calculations of the 3D Transverse Oscillation method is within the capabilities of modern scanners.

PACS numbers: 43.35.Yb
Keywords: Ultrasound, Velocity estimation, 3D velocity vectors, Transverse oscillations

I. INTRODUCTION

For decades, velocity estimation of the blood has been an important diagnostic tool in the clinic. For instance, velocity estimation in the carotid artery is a main diagnostic criteria in assessing the degree of stenosis[1,2]. Hemodynamic studies have shown that the blood flow is far from unidirectional, rather on the contrary. It exhibits complex flow patterns, and the velocity has components in all three dimensions as ultrasound measurements[3–5] as well as MRI[6,7] and computational fluid dynamics modelling[8] have shown.

As pointed out, the velocity vector is three-dimensional, and the above underlines the need for methods that can estimate the three-dimensional (3D) velocity vector. The purpose of this paper is to develop an approach that can estimate the full 3D velocity vector in real-time. The 3D Transverse Oscillation (TO) method estimates the two transverse velocity components based on two double-oscillating fields and spatial quadrature sampling. With the 3D TO method, the velocity estimation is decoupled into the three velocity components, which are obtained simultaneously. The feasibility of the method is demonstrated in a simulation study. Initial proof of concept results have previously been presented at a conference[9]. Those results are summarized here. Further results are presented including an approach to optimize the method and results form a parameter study. It is also illustrated that the method is implementable on modern scanners. The physical requirements are limited to a 2D matrix array transducer, and the number of calculations needed are within the capability of modern scanners making a real-time implementation possible.

The presented method is based on the same principle as the Transverse Oscillation (TO) method suggested by Jensen and Munk[10], and the similar approach by Anderson[11]. The TO method in combination with a 1D linear arrays has been investigated[12] and *in vivo* examples of blood vector velocities in superficial vessels have been presented[13]. The applicability for a commercial implementation of the 2D TO method has been demonstrated[14], and 2D velocity data from a commercial implementation have been used for investigating flow patterns in various vessels[15]. Furthermore, the method has been expanded to a 1D phased array geometry[16].

Methods have been suggested that provide the axial velocity component as color Doppler in a 3D volume[17]. However, methods that estimate the full 3D velocity vector are needed, and multiple approaches have been suggested to obtain true 3D velocity estimates. Of these, the cross-beam vector Doppler methods employing single-element transducers[18–20] are not suited for obtaining 3D velocity vector estimates over an entire volume. The elements in the esophageal probe by Daigle et al.[18] had one point of beam convergence and had to be operated sequantially over several cardiac cycles. The system developed by Fox[19,21] for obtaining calibrated 3D Doppler velocimetry information employed continous-wave transmit/receivers sacrificing depth information, and the sys-

---

[a)] Portions of this work were presented in "3D velocity estimation using a 2D phased array", *Proc. IEEE Ultrason. Symp.*, Orlando, FL, October 2011

[b)] Author to whom correspondence should be addressed. Electronic mail: `mjp@elektro.dtu.dk` tem had to be manually adjust for a specific area of interest. The five-transducer system proposed by Dunmire et al. had similar challenges[20]. Newhouse et al.[22] suggested a two-transducer system that estimated the 3D velocity based on a combination of the two Doppler mean frequencies and the Doppler spectral bandwidth. The main disadvantages are the assumption of only one velocity in the region of interest and the dependence on the spectral broadening effect.

Several authors have suggested methods employing beamforming several lines and using cross-correlation to track the motion. The method by Bonnefous[23] requires a 2D array transducer and five beamformers in parallel to obtain the velocity vector by means of five 1D cross-correlations. The method works for transverse motions, but breaks down if axial motion is present as it will dominate the signal change. The approach by Hein[24] employing a triple-beam lens transducer requires detailed consideration of beamwidth and beam separation, and suffers from low signal-to-noise ratio (SNR). The directional beamforming approach by Jensen et al.[25,26] estimates the velocity by beamforming lines in the direction of the flow. The flow direction and the velocity is found by using cross-correlation estimators. The drawback of this approach is the larger number of calculations needed for 3D velocity estimation.

Bohs et al.[27] suggested a speckle tracking method for multi-dimensional flow estimation. tracking. However, results from non-invasive speckle tracking for 3D flow estimation have yet to be presented. Speckle or particle tracking is also used in the more recent ultrasonic particle image velocimetry (PIV) approach[28,29], but this approach requires that a contrast agent is injected into the blood stream. Reconstructed 3D flow using ultrasound PIV has been reported[30], but results from estimating the full 3D velocity vectors have yet to be reported. In general, the challenge with speckle tracking techniques, especially in 3D, is the fairly high number of calculations needed. Another approach is to apply feature tracking in 3D[31], however, the approaches are limited by uncertainty in especially the transverse localization of the peak, false peak detection, and the duration of the tracked feature. All of the above methods still have to demonstrate their clinical and commercial applicability for 3D vector flow imaging.

The outline of the paper is as follows: The Transverse Oscillation method and the 3D approach is presented in Section II. Section III presents performance metrics used to evaluate the method. The simulation environment is explained in Section IV as well as the post processing. A proof of concept is presented in Section V, and an approach to optimize the method employed in Section VI. The simulation results and the discussion of the parameter study can be found in Section VII, and the conclusions are stated in Section VIII.

II. THE TRANSVERSE OSCILLATION METHOD

The idea in the Transverse Oscillation method is to introduce a double-oscillating field, which generates received signals affected by both the axial and the transverse oscillations. The following describes the basic concept of the TO method, briefly refers to the important papers for the 2D TO method, and states the theory of 3D TO method.

A. The basic concept

The axial oscillations in the emitted ultrasound beam are conventionally used for estimating the axial movement by use of an autocorrelation or a cross-correlation approach. Based on this property, the TO method generates an artificial transverse oscillation in the ultrasound field by applying special apodization functions to the receiving aperture[10]. The received signals are modulated both by the axial and the transverse oscillations. Using an estimator as the one presented by Jensen[32], the axial and the transverse modulations can be separated, and the axial and the transverse velocity estimation can be estimated.

B. Velocity estimation in 2D

For the 2D case, a derivation of the required apodization functions and a description of the respective generated ultrasound fields for a linear array transducer can be found in the work by Jensen and Munk[10] and by Jensen and Udesen[12]. Jensen[32] provides a thorough description and derivation of the velocity estimator used for estimation of the transverse velocity. A phased array implementation of the Transverse Oscillation method for vector velocity estimation has been described by the authors[16]. The transverse spatial wavelength is given by[10,12,16]

$$\lambda_x = 2\lambda_z \frac{z_0}{d_x \cos\theta_{zx}}, \qquad (1)$$

where λ_z is the axial wavelength, z_0 is the depth, d_x the distance between the two peaks in the aperture function, and the $\cos\theta_{zx}$-term accounts for the steering angle in the azimuth (ZX) plane. This is due to the decrease in effective aperture width. The synthesized oscillations are perpendicular (transverse) to the steered beam. Two lines are then beamformed with a separation of $\lambda_x/4$ to obtain spatial IQ pairs. Using the TO velocity estimator[32], the transverse velocity component can be estimated.

C. 3D TO vector velocity estimation

The following describes the concept, the beamforming approach, and the velocity estimation of 3D velocity vectors using a Transverse Oscillation approach.

1. The concept

In the 3D case, the concept is to create two double oscillating fields perpendicular to each other. By employing special receive apodizations, the synthesized fields

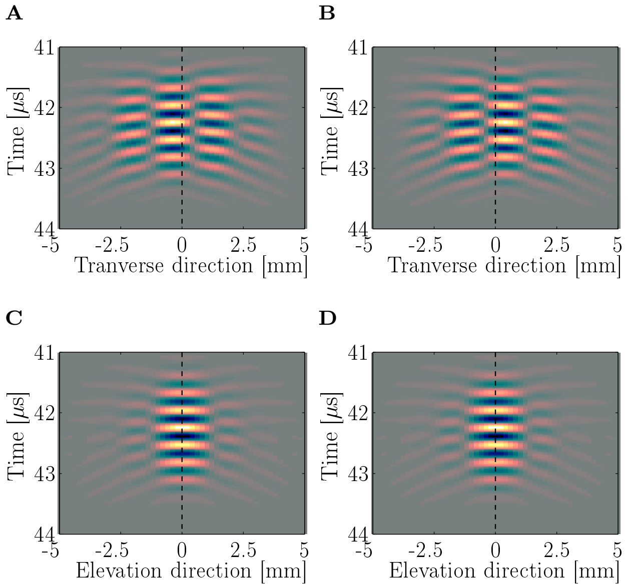

Figure 1. (Color online) Transverse oscillating pulse-echo fields simulated at a depth of 30 mm across 10 mm in either the transverse direction (**A** and **B**) or the elevation direction (**C** and **D**). **A** and **C** are for the left beam in the transverse (ZX) plane and **B** and **D** are for right beam in the transverse (ZX) plane. Transverse oscillations are only present in the transverse direction, and the oscillations for the left and right beams in the transverse direction are shifted by 1/4 of a spatial transverse wavelength. In the elevation direction, there are no oscillations for the left and the right beams in the ZX-plane. This example illustrates that the transverse fields in the ZX-plane oscillate only in the transverse direction and not in the elevation direction. There is a 90° spatial phase shift between the TO fields in the transverse directions, and none in the elevation direction. The opposite is the case for the two TO beams in the ZY-plane, where the TO fields oscillate only in the elevation direction and not in the transverse direction (not shown).

should oscillate only in one direction. This is illustrated in Fig. 1, where transverse oscillations are only present in the transverse (x-direction) when beamforming the two TO lines in transverse (ZX) plane, whereas there are no oscillations in the elevation direction. The opposite (not shown) holds for the two TO lines beamformed in the elevation plane (ZY).

Furthermore, it is assumed that the velocity estimation can be decoupled into estimating three independent velocity components: The axial, v_z, the transverse, v_x, and the elevation, v_y, velocity component. The three estimated velocity components can be obtained, so that they are orthogonal in a primed coordinate system (x',y',z'), which depends on the direction of the steered beam. If the steered beam z'-axis coincides with the z-axis, $v_{x'}$, $v_{y'}$, and $v_{z'}$ are equal to v_x, v_y, and v_z, respectively. This is illustrated in Fig. 2 where the sampled signals for the estimation of v_x, v_y and v_z are orthogonal, and where the axial velocity, v_z, is along the beam axis.

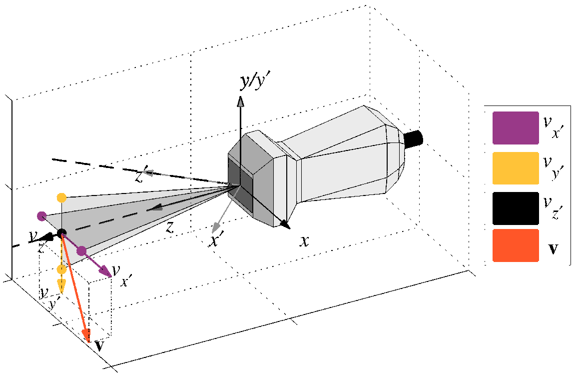

Figure 2. (Color online) Beamforming approach for 3D velocity estimation using a 2D matrix phased array transducer. The estimation of the 3D velocity vector is decoupled into three components orthogonal to each other. The coordinate system of the transducer is (x,y,z), and the sampling coordinate system along the direction of the steered beam is (x',y',z'). The dashed lines indicate two different steered beam lines: One coinciding with the z-axis and the other is steered in the ZX-plane with an angle θ_{zx}. Spheres indicate beamformed samples at a given depth: A center line is beamformed for conventional axial velocity $v_{z'}$ estimation, and two pairwise TO lines are beamformed for estimation of the transverse and elevation velocities $v_{x'}$ and $v_{y'}$. They are pairwise steered at specific fixed angles, $\theta_{TO_{zx}}$ and $\theta_{TO_{zy}}$, such that the spacing is a quarter spatial wavelength at every sample depth. For illustration purposes, $\theta_{TO_{zx}}$ and $\theta_{TO_{zy}}$ have been exaggerated. For a 64x64 transducer, they are 0.6° with respect to the z-axis. The gray shaded areas illustrate the $Z'X'$- and $Z'Y'$-planes here coinciding with the ZX-, and the ZY-planes.

With the 3D TO method, the velocity component in the elevation direction, v_y, is obtained by creating an oscillation in the elevation direction perpendicular to the ultrasound beam. The elevation wavelength is given by

$$\lambda_y = 2\lambda_z \frac{z_0}{d_y \cos\theta_{zy}}, \tag{2}$$

where d_y is the distance between the apodization peaks in the y-direction of the transducer and the $\cos\theta_{zy}$-term accounts for the steering angle in the elevation (ZY) plane. This can be obtained using a 2D phased array. Essentially, the process of estimating v_y is the same as for v_x, except for a rotation of the steered beams and the receiving aperture of 90 degrees in the transducers XY-plane.

2. *Beamforming in 3D*

The beamforming approach is illustrated in Fig. 2. For each sample depth, five samples are beamformed. One along the center axis for conventional axial estimation r_c, and two pairs of the left and right TO samples for spatial IQ in both transverse, r_{left_x} and r_{right_x}, and elevation, r_{left_y} and r_{right_y}, direction. These signals can be combined to

$$r_{\text{sq}_x}(i) = r_{\text{left}_x}(i) + \text{j}r_{\text{right}_x}(i)$$
$$r_{\text{sq}_y}(i) = r_{\text{left}_y}(i) + \text{j}r_{\text{right}_y}(i),$$

where i is the pulse number of N_i emissions. Taking the temporal Hilbert transform or sampling temporal IQ data directly, one obtains

$$\begin{aligned} r_{\mathrm{sqh}_x}(i) &= \mathcal{H}\{r_{\mathrm{sq}_x}(i)\} \\ r_{\mathrm{sqh}_y}(i) &= \mathcal{H}\{r_{\mathrm{sq}_y}(i)\}. \end{aligned}$$

To create one flow line with the 3D velocity vectors along it, five lines are beamformed per emission as illustrated in Fig. 2. A center line along the beam axis is beamformed for use in estimating the axial velocity, $v_{z'}$, and two TO lines are beamformed in the $Z'X'$-plane for estimation of the transverse velocity, $v_{x'}$. These are the same as for the 2D case using a 1D transducer. In the 3D case, two additional TO lines are beamformed. They are steered in the $Z'Y'$-plane for the estimation of the elevation velocity $v_{y'}$. The velocity vector estimation is, thus, decoupled into these three components, as illustrated in Fig. 1 and 2.

In transmit, the emitted ultrasound pulse may be focused, a plane wave, or unfocused, but it is crucial that beam is broad enough to cover all lines and the two transverse oscillating fields. On the receive side, the five lines are beamformed dynamically in parallel. The center line is in the direction of the transmitted beam axis. The pairwise TO beams are beamformed, so that they are spaced a quarter of the respective lateral spatial wavelength apart. Thereby, spatial IQ pairs can be obtained in both the transverse and the elevation directions. In the transverse (azimuth) plane, this distance is determined by (1), and in the elevation plane by (2). Because of the limited width of the 2D phased array transducer, lines are beamformed radially. The width also limits the use of an expanding aperture to keep λ_x and λ_y constant. Consequently, the transverse and elevation wavelength increase with depth as apparent from (1) and (2). As a result, the TO lines must be beamformed with an increase in spacing as a function of depth, so that their spacing matches the increasing spatial wavelengths. This can be obtained by beamforming the TO beams with a fixed angle, so that they diverge radially. The angle, θ_{TO}, between the two TO lines can be derived as[16]

$$\theta_{TO_{zx}} = 2\arctan\frac{\lambda_x/8}{z_0} = 2\arctan\frac{\lambda_z}{4d_e}, \qquad (3)$$

where d_e is the effective distance between the TO peaks in the apodization function calculated as $d_e = d_x\cos\theta_{zx}$. Thus, instead of beamforming the TO lines with a fixed lateral distance over depth, they diverge with a fixed angle. When beamforming the other pair of TO lines, $\theta_{TO_{zy}}$ is calculated in the same manner.

The receive apodization for the TO lines will typically be two peaks with a given width, and a given spacing, d_x or d_y. The two pairs of TO lines are beamformed orthogonal to each other, and therefore, the required apodization functions are merely the same except for a rotation of 90°.

All five lines are beamformed in parallel in receive based on the same transmission, so only five beamformers in receive are required. However, the method may be expanded to beamform several flow lines in parallel. As the lines are beamformed in parallel, the three velocity components are estimated simultaneously.

3. Velocity estimation

The estimation of the transverse and elevation velocity components, $v_{x'}$ and $v_{y'}$, follows the one presented by Jensen[32]. The velocity estimation is the same for $v_{x'}$ and $v_{y'}$, each based on one pair of the four TO lines. Based on the spatial quadrature, $r_{\mathrm{sq}}(i)$, and temporal quadrature, $r_{\mathrm{sqh}}(i)$, signals in the ZX-plane, two new signals, $r_1(i)$ and $r_2(i)$, can be generated. Similarly, two new signals in the ZY-plane $r_3(i)$ and $r_4(i)$ are generated. The four new signals are given by

$$\begin{aligned} r_1(i) &= r_{\mathrm{sq_x}}(i) + \mathrm{j}r_{\mathrm{sqh_x}}(i) = \exp(j2\pi i T_{\mathrm{prf}}(f_{x'} + f_p)) \\ r_2(i) &= r_{\mathrm{sq_x}}(i) - \mathrm{j}r_{\mathrm{sqh_x}}(i) = \exp(j2\pi i T_{\mathrm{prf}}(f_{x'} - f_p)) \\ r_3(i) &= r_{\mathrm{sq_y}}(i) + \mathrm{j}r_{\mathrm{sqh_y}}(i) = \exp(j2\pi i T_{\mathrm{prf}}(f_{y'} + f_p)) \\ r_4(i) &= r_{\mathrm{sq_y}}(i) - \mathrm{j}r_{\mathrm{sqh_y}}(i) = \exp(j2\pi i T_{\mathrm{prf}}(f_{y'} - f_p)), \end{aligned}$$

where the frequency f_p is due to the axial pulse modulation, $f_{x'}$ is due to the spatial transverse modulation, and $f_{y'}$ is due to the spatial elevation modulation. The transverse, $v_{x'}$, and the elevation velocity, $v_{y'}$, are then calculated by

$$v_{x'} = \frac{\lambda_x}{2\pi 2kT_{\mathrm{prf}}} \times \arctan\left(\frac{\Im\{R_1(k)\}\Re\{R_2(k)\}+\Im\{R_2(k)\}\Re\{R_1(k)\}}{\Re\{R_1(k)\}\Re\{R_2(k)\}-\Im\{R_1(k)\}\Im\{R_2(k)\}}\right) \qquad (4)$$

$$v_{y'} = \frac{\lambda_y}{2\pi 2kT_{\mathrm{prf}}} \times \arctan\left(\frac{\Im\{R_3(k)\}\Re\{R_4(k)\}+\Im\{R_4(k)\}\Re\{R_3(k)\}}{\Re\{R_3(k)\}\Re\{R_4(k)\}-\Im\{R_3(k)\}\Im\{R_4(k)\}}\right), \qquad (5)$$

where T_{prf} is the time between two emissions, $R_m(k)$ is the complex lag k autocorrelation value of $r_m(k)$ for $m = 1, \ldots, 4$. $\Re\{\bullet\}$ denotes the real part, and $\Im\{\bullet\}$ the imaginary part. The complex autocorrelation is estimated over N_i emissions. RF averaging is performed by averaging the autocorrelation estimate over the length of the excitation pulse[32,33]. Both λ_x and λ_y can be calculated theoretically using (1) and (2) based on the given sampling depth, z. Bias compensation may be performed by substituting λ_x and λ_y with for instance the mean lateral wavelengths, $\bar{\lambda}_x$ and $\bar{\lambda}_y$, which can be estimated based on simulations or measurements.

As an alternative to the method described above, a heterodyning demodulation approach[34] can be applied. In that case, the following signals are formed

$$\begin{aligned} r_{12}(i) &= r_1(i) \times r_2(i) = \exp(j2\pi i T_{\mathrm{prf}}2f_{x'}) \\ r_{12^*}(i) &= r_1(i) \times r_2^*(i) = \exp(j2\pi i T_{\mathrm{prf}}2f_p) \\ r_{34}(i) &= r_3(i) \times r_4(i) = \exp(j2\pi i T_{\mathrm{prf}}2f_{y'}) \\ r_{34^*}(i) &= r_3(i) \times r_4^*(i) = \exp(j2\pi i T_{\mathrm{prf}}2f_p). \end{aligned}$$

In stead of calculating the phase change in the complex signals over time directly[34], we apply an autocorrelation approach[35] with RF averaging[33] to estimate the phase change. The estimation of the transverse and elevation velocity components then becomes

$$v_{x',\text{het}} = \frac{\lambda_x}{2\pi 2kT_\text{prf}} \arctan\left(\frac{\Im\{R_{12}(k)\}}{\Re\{R_{12}(k)\}}\right) \tag{6}$$

$$v_{y',\text{het}} = \frac{\lambda_x}{2\pi 2kT_\text{prf}} \arctan\left(\frac{\Im\{R_{34}(k)\}}{\Re\{R_{34}(k)\}}\right), \tag{7}$$

where $R_{12}(k)$ and $R_{34}(k)$ are the complex lag k autocorrelation values of $r_{12}(k)$ and $r_{34}(k)$, respectively. Because this approach multiplies the generated signals $r_1(k)$ and $r_2(k)$ directly prior to the autocorrelation, it is suspected that this approach will be more susceptible to noise compared to the TO approach, which estimates the autocorrelations first prior to the pairwise multiplication of the autocorrelation values.

The axial velocity component is calculated using an autocorrelation estimator[35] with RF averaging[33] as

$$v_{z'} = -\frac{\lambda_z}{2\pi 2kT_\text{prf}} \arctan\left(\frac{\Im\{R_c(k)\}}{\Re\{R_c(k)\}}\right),$$

where $R_c(k)$ is the autocorrelation of the center line at lag k.

Because the velocity estimations are based on autocorrelation approaches, the aliasing limit of the axial, transverse, and elevation velocity components is

$$v_{z',\max} = \frac{1}{4}\frac{\lambda_z}{kT_\text{prf}},$$
$$v_{x',\max} = \frac{1}{4}\frac{\lambda_x}{kT_\text{prf}}$$
$$v_{y',\max} = \frac{1}{4}\frac{\lambda_y}{kT_\text{prf}}.$$

D. Number of operations

The number of operations needed (both additions and multiplications) for the 3D velocity estimation is calculated in the following. The calculation assumes that the temporal quadrature data have already been obtained either by IQ sampling or by means of the Hilbert transform.

Per set of four samples used for estimating $v_{x'}$ and $v_{y'}$, the following number of operations are required

$$N_{c,\text{TO}} = 2 \cdot \left(2 \cdot (10+1+2) + \frac{7}{N_i}\right),$$

where the first 2 is for v_x and v_y, the second 2 is for two autocorrelation functions per velocity component, 10 is the number of operations to calculate one autocorrelation value in $R_i(1)$, the +1 for summing the autocorrelation values, and the +2 is for the adding the latest value and subtracting the oldest in the RF averaging. For every N_i emissions, the final velocity calculation as described in (4) is performed. This requires additional 5 multiplications, 2 additions and one arctan look-up.

The required floating point operations per second (flops) can be calculated as

$$f_\text{flops} = N_c \cdot f_s \cdot p_v,$$

where p_v is fraction of time used for velocity estimation. Assuming N_i is 16, the sampling frequency is 15 MHz, and 80 % of the time is used for flow estimation, the required flops for estimating v_x and v_y are

$$f_\text{flops,TO} \approx 53 \cdot 15\,\text{MHz} \cdot 0.8 = 0.64\,\text{Gflops}.$$

The amount of floating point operations per seconds is within the capabilities of standard CPUs, whose capabilities are at least 1 Gflops.

For comparison, the number of calculations needed by the conventional axial velocity estimator is

$$N_{c,\text{conv}} = (6+1+2) + \frac{1}{N_i}.$$

Consequently, the flops for the autocorrelation estimator in the given examples are

$$f_\text{flops,conv} \approx 9 \cdot 15\,\text{MHz} \cdot 0.8 = 0.11\,\text{Gflops}.$$

As it can be observed, the number of calculations required for the two transverse velocities is approximately a factor of 6 larger than for the conventional estimator. For a realistic example, the combined flops required for estimating v_x, v_y, and v_z are 0.75 Gflops. This is less than 1 Gflops, which is a lower limit of the capabilities of standard CPUs today. Based on the above, it is concluded that the 3D TO method is suitable for a real-time implementation on a modern scanner.

III. PERFORMANCE METRICS

This section introduces two groups of metrics for evaluating performance. The first group evaluates the obtained double-oscillating pulse-echo field and the corresponding TO spectrum, and the second evaluates the quality of the obtained velocity estimates.

A. The spectrum of the TO fields

It has previously been demonstrated that several metrics used to evaluate the double oscillating pulse-echo fields (PEFs) and the beamforming were correlated with the subsequent performance of the velocity estimation[16]. The following metrics are used to evaluate the TO field and the beamforming: The mean lateral wavelengths, $\bar{\lambda}_x$ or $\bar{\lambda}_y$; the bias, B_λ, between the mean lateral wavelength and the theoretical wavelength; the coefficient of variance, c_v, of the dispersion of the spatial lateral frequencies, f_x or f_y about their mean; and the energy ratio, E_r, of the TO spectrum.

The metrics are all calculated based on the TO spectrum. The TO spectrum is obtained by first constructing the combined TO pulse-echo field, $h_\text{TO}(x, y, t)$, by summing the pulse-echo fields from the left, $h_\text{l}(x, y, t)$, and the right, $h_\mathrm{r}(x,y,t)$, TO lines from either the ZX- or the ZY-plane as

$$h_\mathrm{TO}(x,y,t) = h_\mathrm{l}(x,y,t) + \mathrm{j}\mathcal{H}\{h_\mathrm{l}(x,y,t)\} + h_\mathrm{r}(x,y,t) + \mathrm{j}\mathcal{H}\{h_\mathrm{r}(x,y,t)\},$$

where $\mathcal{H}\{\bullet\}$ denotes the temporal Hilbert transform. For use with the stated metrics, the TO spectra are calculated in 2D in either the ZX- or the ZY-plane as

$$S(f_x,f_t) = \mathcal{F}_\mathrm{2D}\{h_\mathrm{TO}(x,y,t)|_{y=0}\}$$
$$S(f_y,f_t) = \mathcal{F}_\mathrm{2D}\{h_\mathrm{TO}(x,y,t)|_{x=0}\},$$

where $\mathcal{F}_\mathrm{2D}\{\bullet\}$ denotes the 2D Fourier transform. Because the emulated transducer layout is the same in both the x-direction and the y-direction, only the performance metrics for the ZX-plane is considered in the following. The obtained results will be same for the ZY-plane.

Based on $S(f_x,f_t)$, an estimated value of the mean transverse wavelength, $\bar{\lambda}_x$, at the given depth of interest can be obtained as $1/\bar{f}_x$, where $\bar{f}_x$ can be computed as

$$\bar{f}_x = \frac{\int_{-f_s/2}^{f_s/2}\int_{-f_{ss}/2}^{f_{ss}/2} f_x S(f_x,f_t)^2 \,\mathrm{d}f_x\mathrm{d}f_t}{\int_{-f_s/2}^{f_s/2}\int_{-f_{ss}/2}^{f_{ss}/2} S(f_x,f_t)^2 \,\mathrm{d}f_x\mathrm{d}f_t} \quad (8)$$

where f_s is the temporal sampling frequency and f_{ss} is the spatial sampling frequency.

Additionally, $\bar{\lambda}_x = 1/\bar{f}_x$ from (8) can be used instead of λ_x in (1) and (3) when beamforming to yield a less biased velocity estimate. The bias of the spatial wavelength in the TO spectrum is calculated as

$$B_{\lambda_x} = \frac{\lambda_x - \bar{\lambda}_x}{\bar{\lambda}_x}. \quad (9)$$

A negative bias will result in velocity estimates that have lower (absolute) values than expected. Most often the bias is negative because the mean spatial frequency, e.g. $\bar{f}_x = 1/\bar{\lambda}_x$ is lower than expected from (1), because the energy in the other half of the TO spectrum lowers the mean. The actual mean spatial wavelength in the TO fields is, thus, larger than theoretically expected. Because the TO spectrum is rather broad band, it does not affect the velocity estimation as such (if the discrepancy is not too large), but the wavelength used when scaling the velocities is then too small, and hence, the velocity estimates are biased in a negative direction. It should be noted, that echo cancelling as observed previously by the authors[16] also affected the bias in some cases by biasing the velocity estimates towards higher values.

To evaluate the frequency spread around the mean spatial wavelength in the TO spectrum, the coefficient of variation, c_v, is calculated as

$$c_v = \frac{\sigma_{fx}}{\bar{f}_x} \quad (10)$$

where $\bar{f}_x$ is the mean spatial (lateral) frequency given in (8), and σ_{f_x} is the frequency dispersion about the mean spatial frequency, $\bar{f}_x$, given by

$$\sigma_{f_x} = \sqrt{\frac{\int_{-f_s/2}^{f_s/2}\int_{-f_{ss}/2}^{f_{ss}/2} (f_x - \bar{f}_x)^2 S(f_x,f_t)^2 \,\mathrm{d}f_x\mathrm{d}f_t}{\int_{-f_s/2}^{f_s/2}\int_{-f_{ss}/2}^{f_{ss}/2} S(f_x,f_t)^2 \,\mathrm{d}f_x\mathrm{d}f_t}}.$$

It has been shown that increases in c_v leads to increases in the standard deviation of the velocity estimates[16]. This is in accordance with the fact that the velocity estimator is an autocorrelation estimator, which performs best in narrow frequency band conditions.

The last metric is the energy ratio, E_r, computed as

$$E_r = \frac{\int_{-f_s/2}^{f_s/2}\int_{-f_{ss}/2}^{0} S(f_x,f_t)^2 \,\mathrm{d}f_x\mathrm{d}f_t}{\int_{-f_s/2}^{f_s/2}\int_{-f_{ss}/2}^{f_{ss}/2} S(f_x,f_t)^2 \,\mathrm{d}f_x\mathrm{d}f_t}. \quad (11)$$

This provides information about the energy leak from the right half plane to the left half plane of the 2D TO frequency spectrum. This value is related to the standard deviation of the velocity estimates[16]. If the value of E_r approaches 0 dB, the amount of energy in both quadrants is increasingly the same, and velocity estimation is expected to be compromised, because the spatial quadrature approach has failed. This energy ratio is therefore used as a criteria for optimization of the TO field to match $\bar{\lambda}_x$ in the TO field with λ_x used in the beamforming.

B. Velocity estimates

The performance of the TO method for 3D velocity vector estimation is determined by the accuracy and precision of the estimated velocities. Therefore, the average of N_p velocity profiles is investigated. In the calculations of the relative mean biases and relative mean standard deviations, it is assumed that the velocity estimates are independent.

At each discrete depth, z_n, the velocity is estimated from a number of emissions, N_i. The mean, $\bar{v}(z_n)$, and the estimated standard deviation, $\sigma(z_n)$, of N_p estimates are computed at each discrete depth. Also, the bias, $B(z_n)$, is calculated as

$$B(z_n) = \bar{v}(z_n) - v_t(z_n),$$

where v_t is the true velocity profile.

To provide a straightforward comparison of various parameter settings, two non-dimensional parameters are calculated based on the biases and the standard deviations for the N_p profiles as

$$\tilde{B} = \frac{1}{v_0 N_{z_n}} \sum_{z_n=1}^{N_{z_n}} B(z_n) \quad (12)$$

$$\tilde{\sigma} = \frac{1}{v_0}\sqrt{\frac{1}{N_{z_n}} \sum_{z_n=1}^{N_{z_n}} \sigma(z_n)^2}, \quad (13)$$

where v_0 is the peak velocity and N_{z_n} is the number of discrete samples within the region of interest. The relative mean bias, $\tilde{B}$, the relative mean standard deviation, $\tilde{\sigma}$, are thus used to describe the performance of the 3D TO velocity vector estimator.

IV. SIMULATION ENVIRONMENT AND POST PROCESSING

The simulation studies performed to investigate the TO method for 3D velocity vector estimation uses the ultrasound simulation program Field II[36,37]. The simulation environment, the parameters, and the post processing are described in the following.

A. Simulation setup

The simulation and post processing environments consist of a number of parameters. They are listed below along with their default value. The variables in the parameter study are mentioned, and their respective values are listed in Table I. Bold face values correspond to the reference setup. For all the simulations, the sampling frequency, f_s, was set to 100 MHz, and the speed of sound, c, was set to 1480 m/s to mimic the speed of sound in water.

A transducer was emulated as a 2D matrix array with a center frequency, f_0, of 3.5 MHz. The array had 32x32 elements with a pitch in both dimensions of 300 μm. The kerfs were set to $\lambda/100$, where λ is the wavelength of the ultrasound pulse in water. The one-way impulse response of the transducer was defined as a 2 cycle Hanning windowed pulse at the center frequency yielding a 6 dB bandwidth of 96%. A second transducer with 64x64 elements, but otherwise the same characteristics, was emulated as well. For this transducer, the number of active channels was limited to 1024.

The emitted pulse for the velocity vector estimation was an 8 cycle Hanning windowed sinusoid at the center frequency. The emitted ultrasound beam was a plane wave. As default, it was steered in the direction of the z-axis, but the steering angles, θ_{zx} and θ_{zy}, were varied in the parameter study. All 1024 channels were used for transmitting the pulse. The default was an apodization of 1 for all elements (rectangular). The receive aperture for the conventional axial velocity estimation was apodized with a circular symmetrical Hamming window. The receive apodization for both pairs of TO lines were two peaks with widths of w and spaced a given distance d apart. The apodization of the TO peaks was varied in both dimensions, *i.e.* in the direction with oscillations (osc.) and in the direction without oscillations (non-osc.). The difference between the pair of TO lines in the x-direction and the y-direction was merely a 90° rotation.

As part of the parameter study, the number of emissions per estimate, and the SNR was varied. As default, an ensemble length of 32 emissions was used, and no noise was added to the simulated RF signals. When testing the effect of varying the signal-to-noise ratio (SNR), zero mean white Gaussian noise was added to the beamformed RF-data prior to the match filtration. The amplitude of the noise was varied to obtain different SNR values. The matched filtration improved the SNR by 18 dB. The SNR values after the matched filtration are listed in Table I. The default value used in the simulations unless otherwise stated is ∞, i.e. no noise was added.

Two flow phantoms were simulated: A 10 mm x 10 mm x 10 mm block of scatterers moving as a plug flow, and a 20x20x20 mm cube with a cylinder with a length l of 20 mm and a radius r of 6 mm centered inside the block — mimicking e.g. the carotid artery. The scatterers inside the cylinder was moving with a circular symmetric parabolic velocity profile, and the scatterers outside the cylinder were stationary. The simulations were performed with a constant peak speed $|\vec{v}_0|$ of 1 m/s, whereas the direction of the flow $\vec{v}_0/|\vec{v}_0|$ was varied by rotating the block of scatterers. As default, the center of the plug flow phantom was located at a depth of $(x, y, z) = (0,0,15)$ mm, and the parabolic flow phantom was located at $(x, y, z) = (0,0,30)$ mm. The steering direction and the radial depth were varied. Depending on this, the block of scatterers were rotated and translated accordingly to obtain velocity vectors orthogonal to the ultrasound beam. The plug flow phantom was used for a simple proof of concept, whereas the parabolic flow phantom was used in the parameter study.

B. Post processing

In the post processing step, matched filtration was used by convolving the calculated RF signals with the time reversed emitted pulse, $g(-n)$, as

$$r_m(n) = r_s(n) * g(-n),$$

where $r_s(n)$ is the received sampled signal at time n.

When clutter filtering (stationary echo cancelling) was applied, it was performed by subtracting the mean ensemble value of N_i emissions by

$$r_{cf}(n, i) = r_m(n, i) - \sum_{i=1}^{N_i} r_m(n, i),$$

where i is the emission number. Afterwards, the velocities were estimated as described in Section II.C.

C. Proof of concept study

The plug flow phantom was used as a simple case for validating the concept. The 32x32 and the 64x64 element transducers were used in this case. Compared to the reference setup, the following parameters differed in this proof of concept setup: The center frequency was 3 MHz, the pitch was $\lambda/2$, and the transducer impulse response was a 3 cycle sinusoid at the center frequency.

In this case, 10 realizations for each parameter setting were simulated. The scatterers were initialized with random positions and amplitudes between each realization.

Table I. Variables in the parameter study

Parameter	Values
Steering angle θ_{zx} [°]	**0**,5,. . . ,45
Steering angle θ_{zy} [°]	**0**,5,. . . ,45
Transmit apodization (in 2D)	Hanning, Tukey, **Rect**
TO peak apod. (osc. direction)	Hanning, Tukey, **Rect**
TO peak apod. (non-osc. direction)	Hanning, Tukey, **Rect**
No. of elements in TO peak spacing	8,12,16,20,**24**
No. of elements in TO peak width	2,4,**8**,12,16
Flow direction ϕ_{xy} [°]	**0**,15,. . . ,90
Flow direction ϕ_{zy} [°]	0,15,. . . ,**90**
Flow direction ϕ_{zx} [°]	0,15,. . . ,**90**
No. of emissions per estimate	8,16,**32**,64
SNR [dB]	-6,-3,. . . ,12,∞

D. Parameter study

The parameters varied in the study are summarized in Table I with their respective values. The reference point in parameter space is highlighted with bold face. For the SNR, ∞ is the default value. In this study, the velocity profile had a circular-symmetrical parabolic shape. For each parameter value, 100 realizations, N_p, were performed with random scatterer initialization in terms of position and amplitude.

V. PROOF OF CONCEPT

This section presents results from the initial proof of concept simulations. The results have been part of a conference contribution[9]. Before the velocity estimation, a matched filtration was performed using the time reversed transmitted pulse. No stationary signal was added in this case, and hence, no stationary echo cancelling was performed. To obtain temporal IQ data, the Hilbert transform was used to create the analytical signal. The velocities were estimated based on 32 emissions, and for each flow angle the simulations were repeated 10 times. No bias compensation was performed in the velocity estimations.

The center of the plug flow phantom was placed at $(x, y, z) = (0{,}0{,}15)$ mm. Only velocities in the XY-plane were simulated, hence, the results from the estimation of the axial velocity are not shown. The estimated velocities for flow in the x-direction (ϕ_{xy} equal to 0°) and y-direction (ϕ_{xy} equal 90°) for the 64x64 transducer are shown in Fig. 3. The true velocities are $(v_x,v_y) = (1{,}0)$ m/s and $(v_x,v_y) = (0{,}1)$ m/s for the two flow directions, respectively. The figure demonstrates the agreement between the theoretical profiles and the obtained velocity estimates, v_x and v_y, from the simulations at both flow angles. At 15 mm, v_x was 0.97 ± 0.026 m/s and v_y was 0.011 ± 0.061 m/s for flow in the x-direction ($\phi_{xy} = 0°$). For flow in the y-direction where ϕ_{xy} is 90°, v_x was 0.029 ± 0.065 m/s and v_y was 0.98 ± 0.038 m/s.

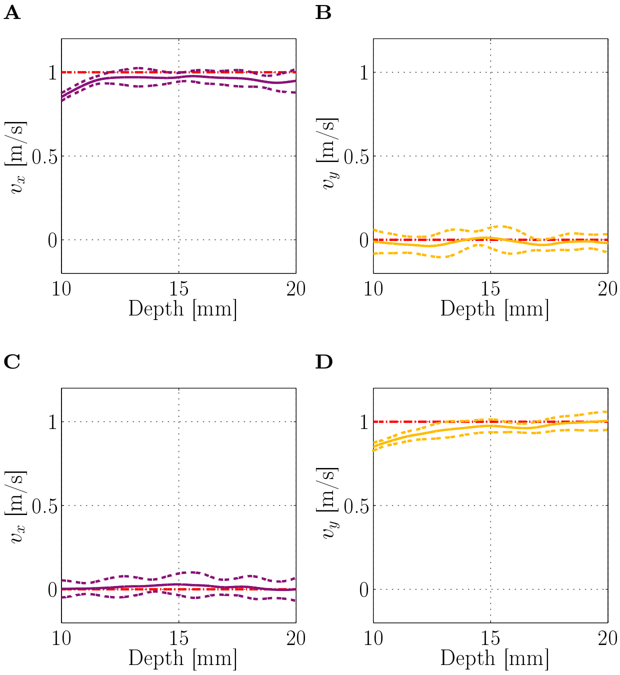

Figure 3. (Color online) Velocity estimates of v_x and v_y for flow in the XY-plane orthogonal to the ultrasound beam. The results are for the 64x64 transducer. Dot-dashed lines indicates true velocity, solid lines the mean of 10 profiles, and dashed lines one standard deviation.In **A** and **B** ϕ_{xy} is 0°, and ϕ_{xy} is 90° for **C** and **D**.

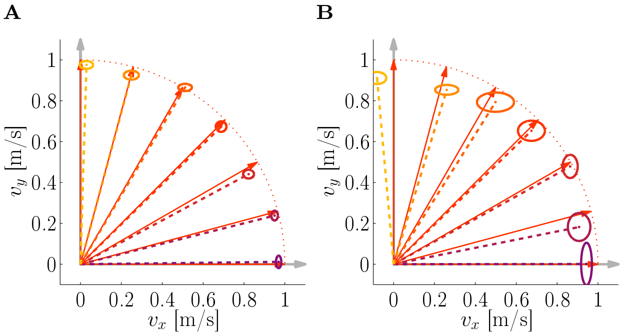

Figure 4. (Color online) Velocity estimates for flow in the XY-plane orthogonal to the ultrasound beam as a function of flow angle ϕ_{xy}. **A** is for the 64x64 transducer and **B** for the 32x32 transducer. Thin solid arrows indicate the true simulated velocities, dashed lines the estimated velocity vectors, and the ellipses (solid) the standard deviations for v_x and v_y, respectively.

The flow angle in the XY-plane, ϕ_{xy}, was varied from 0 to 90° in steps of 15°. The velocity components v_x and v_y at depth 15 mm were estimated for each angle, and the mean and the standard deviation of the transverse velocity components were calculated. The results for the seven different angles are shown in Fig. 4 for the 64x64 and the 32x32 transducer, respectively.

The average performance for all 70 estimates at 15 mm depth is shown in Table II for the two transducers. Listed

Table II. Overall performance of the estimator at the center of the vessel for the proof of concept study.

Metric	64x64	32x32
Mean $\lvert\mathbf{v}\rvert$ [m/s]	0.97± 0.047	0.94± 0.11
Mean $B_{\hat{\phi}}$ [°]	-0.73±3.3	-0.48±7.7

are the mean speed, $\lvert\mathbf{v}\rvert$, and the standard deviation of all speeds as well as the mean estimated angle bias, $B_{\hat{\phi}}$, between the true angles and the estimated flow angles, which are estimated by

$$\hat{\phi}_{xy} = \arctan \frac{v_y}{v_x}. \tag{14}$$

From the results it can be observed, that the bias and the standard deviation is higher when using the 32x32 compared to the 64x64 transducer. This is expected, because d is smaller for the 32x32 transducer compared to the 64x64 transducer, and hence, the transverse wavelength is larger for the 32x32 transducer than for the 64x64 transducer. Consequently, the velocity range is larger for the 32x32 transducer compared to the 64x64 transducer. And as the velocity and f_{prf} are the same in the two cases, the velocity estimates for the 32x32 transducer will have higher standard deviations compared to the 64x64 transducer. In addition, the separation between the peaks is smaller for the 32x32 transducer compared to the 64x64 transducer, which results in a poorer defined TO field which affects both bias and standard deviation. This also indicates that the TO field should be optimized for a given setup.

The results shown in Fig. 3 and 4 demonstrate that the 3D TO method can estimate v_x and v_y, and that the estimation is decoupled. The relative bias is -3% & -6% and the relative standard deviation is 5% & 11% for the 64x64 & 32x32 transducer, respectively. The estimated angle is practically unbiased, and the relative standard deviation of the angle is 1% and 2%, respectively. Therefore, the results serve as proof of concept.

VI. OPTIMIZING THE METHOD

A part of optimizing the TO method is to ensure a good agreement between the transverse wavelength, λ_x, used when beamforming the TO lines and the resulting $\bar{\lambda}_x$ in the combined TO field. This section presents and discusses results that illustrate how the bias arising from the mismatch between λ_x and $\bar{\lambda}_x$ can be eliminated.

A. Investigation of the TO spectrum

Based on the 32x32 transducer and the default parameters given in the previous section, the PEFs are simulated with a range of λ_x. Based on the combined TO spectrum, the resulting $\bar{\lambda}_x$ and the corresponding bias between the theoretical and the estimated mean wavelength is calculated using (8) and (9), respectively. Furthermore, the coefficient of variation, c_v, is calculated based on (10), and the energy ratio, E_r, is computed using (11).

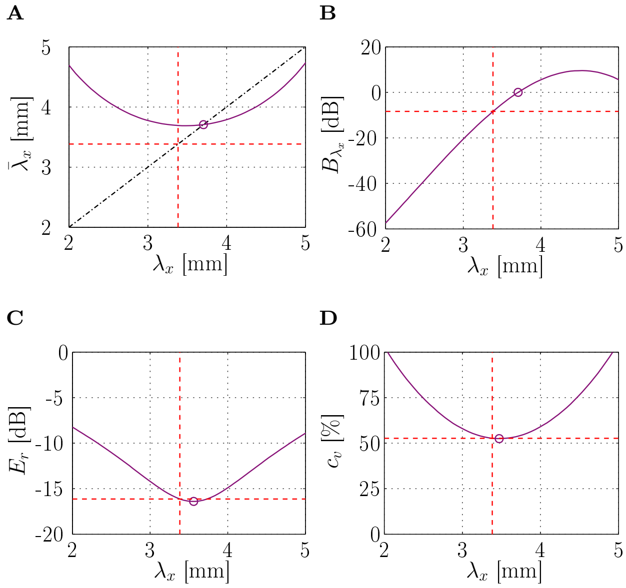

Figure 5. (Color online) Illustrates the effect of varying the transverse wavelength in the beamforming stage on the TO spectrum. Solid lines indicate the input/output relation, dashed lines the values for the theoretical wavelength, circles the optimal point, and the dot-dashed line indicates the output=input curve. **A** Shows the mean estimated transverse wavelength as a function of input λ_x in the beamforming of the TO lines, **B** depicts the corresponding bias between the theoretical and the mean wavelength, **C** displays E_r as a function of λ_x, and **D** shows c_v a function of λ_x.

The effect of varying λ_x in the beamforming stage on $\bar{\lambda}_x$ is displayed in Fig. 5A. The transverse wavelength is used when calculating $\theta_{TO_{zx}}$ with (3). The theoretically calculated λ_x is 3.38 mm for the given parameters. The optimal point where the input λ_x equals the output $\bar{\lambda}_x$ occurs at a transverse wavelength of 3.71 mm. It can also be noted that the shape of the mean transverse wavelength as a function of the transverse wavelength in the beamforming is a flat parabola. The minimum value of $\bar{\lambda}_x$ based on the TO spectrum is 3.69 mm. This value is obtained when a value of λ_x of 3.38 mm is used in the beamforming stage.

Fig. 5B shows B_{λ_x} corresponding to the wavelengths shown in Fig. 5A. Consequently, the optimal point where the bias is 0 is at λ_x=3.71 mm. B_{λ_x} is -8.35 % at the theoretical value of λ_x.

The energy ratio of the energy in the left versus the right of the TO spectrum is shown in part Fig. 5C. The lower the value the better. At the theoretical λ_x, E_r is -16.1 dB, and at the optimal point E_r is -16.4 dB for λ_x equal to 3.56 mm.

In Fig. 5D c_v is shown. The optimal point is at 3.47 mm with a value of 52.4 %. For the theoretical value of λ_x, c_v is 52.7 %.

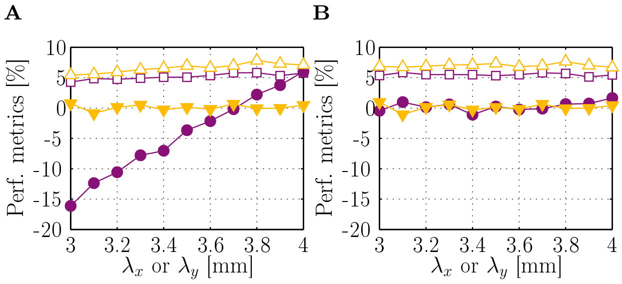

Figure 6. (Color online) Performance metrics of the velocity estimates as a function of λ_x: The relative mean standard deviations $\tilde{\sigma}_{v_x}$ (□) and $\tilde{\sigma}_{v_y}$ (△), and the relative mean biases $\tilde{B}_{v_x}$ (●) and $\tilde{B}_{v_y}$ (▼). **A** The relative mean and standard deviation of the velocity estimates, when the transverse wavelength used in the beamforming (x-axis) is used in the velocity estimation as well. **B** The mean TO wavelengths are used in the velocity estimation. They are calculated based on the TO fields, which are simulated for the different wavelengths (x-axis) used in the beamforming stage.

The above results demonstrate that the optimal value for λ_x in the beamforming in terms of bias is 3.71 mm, whereas when considering c_v and E_r the value is a little lower. The results also demonstrate, that there is little difference when operating around the optimal point. So it is not crucial that λ_x in the beamforming stage is exactly the same as $\bar{\lambda}_x$. However, the estimated $\bar{\lambda}_x$ should be used in the velocity estimation instead of the theoretical λ_x to reduce the bias. In this case this value is approximately 3.7 mm. The flat parabolic shape of $\bar{\lambda}_x$ in Fig. 5A indicates that it is not crucial to optimize the λ_x-$\bar{\lambda}_x$-relation in this case, but it suffices to estimate $\bar{\lambda}_x$ based on TO spectrum obtained when using the theoretical λ_x in the beamforming.

B. Bias compensation of velocity estimates

The predictions based on the performance metrics are tested in a simulation of velocities using the standard parameters previously described, where the velocity is in the x-direction. In these simulations the transverse and elevation wavelengths, λ_x and λ_y, used in the beamforming is varied from 3.0 mm to 4.0 mm in steps of 0.1 mm. Afterwards, the velocity estimation is performed in two different ways. To quantize the effect of varying the velocity estimation, the relative mean bias, $\tilde{B}_{v_x}$, and the relative mean standard deviation, $\tilde{\sigma}_{v_x}$, are calculated for each set of 100 velocity profiles. No echo cancelling is used in this case.

Fig. 6A shows the relative mean biases and standard deviations when the transverse and elevation wavelengths used in the velocity estimation are the same as the ones used for beamforming. In Fig. 6B the mean transverse and and elevation wavelengths calculated based on the TO spectrum are used in the velocity estimation. In both cases, the relative mean standard deviations, $\tilde{\sigma}_{v_x}$ and $\tilde{\sigma}_{v_y}$, are practically unaffected by varying the wavelengths, and they are approximately 5–7 % and 4–6 %, respectively. In addition, the relative mean bias $\tilde{B}_{v_y}$ is practically constant at approximately 0 % for the range of the elevation wavelengths, λ_y. Considering the relative mean bias $\tilde{B}_{v_x}$, it increases from -16 % to 6 % and is 0.001 % at 3.7 mm in Fig. 6A. In Fig. 6B the metric is more or less constant at values of approximately 0 %.

These results illustrate that the bias is not an offset, but rather reflects a wrong scaling factor of the velocity estimates, and that this wrong scaling factor is determined by the mismatch between the theoretically derived spatial wavelengths and the actual mean spatial wavelengths in the TO fields.

If mean stationary echo cancelling is applied prior to the velocity estimation, the trends of the results are the same as for the results presented in Fig. 6, and therefore, the results are not shown, but the differences are stated here. The relative mean standard deviation $\tilde{\sigma}_{v_x}$ is unaffected and the relative mean standard deviation $\tilde{\sigma}_{v_y}$ is 1–2 percentage points larger. In terms of the relative mean biases, $\tilde{B}_{v_y}$ is unaffected, whereas $\tilde{B}_{v_x}$ is offset with approximately 2 percentage points in all cases. However, it should be noted that simulation results previously reported by the authors[16] indicated that this offset was only present at beam-to-flow angles close to 90°. A main contribution to the increase in $\tilde{B}_{v_x}$ comes from the clutter filter that gives rise to edge effects, where the velocity is overestimated at the vessel boundaries.

In conclusion, it is beneficial to optimize the TO field based on one of the optimization criteria. Additionally, bias compensation should be addressed. In this case, neither E_r nor c_v were far from their optimal points when using the theoretical wavelength. This illustrates that the method is robust in terms of TO wavelengths. The velocity estimations were improved by compensating for the bias. This was achieved by substituting the theoretical TO wavelengths, λ_x and λ_y, with the mean TO wavelength, $\bar{\lambda}_x$ and $\bar{\lambda}_y$, in (4) and (5), respectively.

VII. PARAMETER STUDY

This section presents results from the parameter study and discusses them. Firstly, examples of estimated 3D velocities at the reference point are presented. Secondly, the mean and standard devations of 3D velocity vectors obtained by varying the flow angle are visualized. Subsequently, the results of varying the parameters are investigated in terms of the relative mean bias and the relative mean standard deviation of the velocity profiles.

A. 3D velocities at reference point

With the reference parameter values, 3200 emissions were simulated where the motion followed a circular symmetric parabolic profile. The flow direction was in the x-direction with a peak velocity of 1 m/s. The steering angles were both 0°.

One hundred estimates of the velocity components were estimated based on 32 emissions per estimate. Clutter filtering was applied. The results for v_x, v_y, and v_z

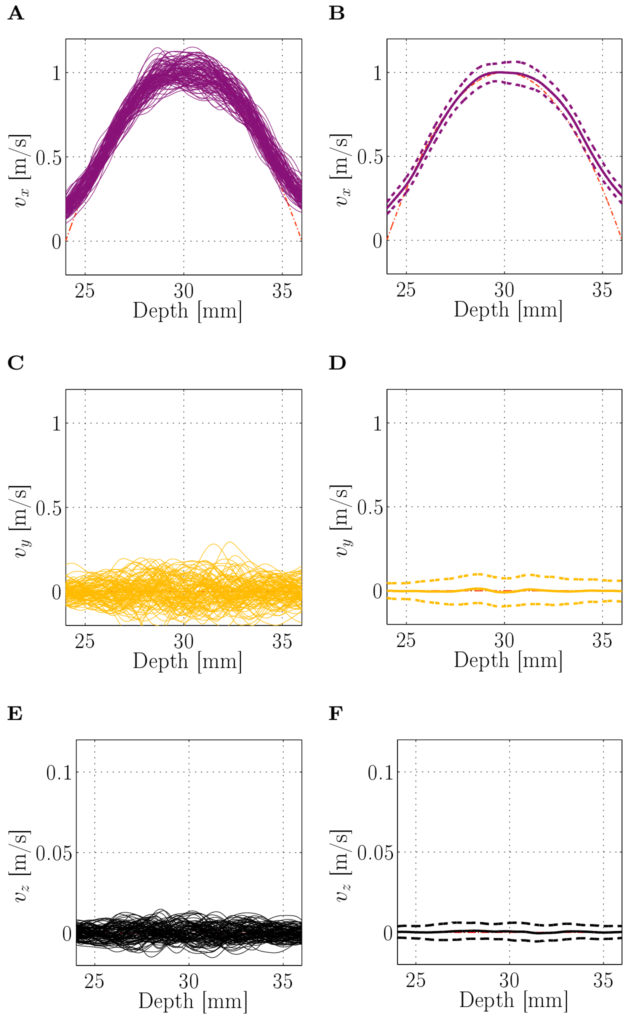

Figure 7. (Color online) Velocity estimates of v_x, v_y, and v_z where ϕ_{xy} is 0°. Thin dot-dashed lines indicate the true velocity, thin solid lines individual estimates, thick solid lines the mean of the 100 profiles, and dashed lines one standard deviation. **A**, **C**, and **E** show 100 estimated velocity profiles. **B**, **D**, and **F** show the mean and standard deviations of the profiles. Note, that the velocity range for v_z has been reduced with a factor of 10 compared to v_x and v_y.

are displayed in Fig. 7. The left panels show the 100 estimated velocity profiles, and the right panels the mean and standard deviation. Both the transverse and elevation velocities were bias compensated as discussed in Section VI, e.g. λ_x equal to 3.4 mm was substituted with $\bar{\lambda}_x$ equal to 3.7 mm in (4).

At the center of the vessel at 30 mm, the average velocity was

$$\bar{\mathbf{v}} = \begin{pmatrix} \bar{v}_x \\ \bar{v}_y \\ \bar{v}_z \end{pmatrix} = \begin{pmatrix} 1.00 \\ -0.0091 \\ 0.00059 \end{pmatrix} \pm \begin{pmatrix} 0.059 \\ 0.083 \\ 0.0053 \end{pmatrix} \text{m/s},$$

where the true velocity was $(v_x, v_y, v_z) = (1{,}0{,}0)$ m/s. At this position and normalized with the speed, the relative biases were smaller than 1 %, and the relative standard deviations were 6 %, 8 %, and 0.5 %, respectively.

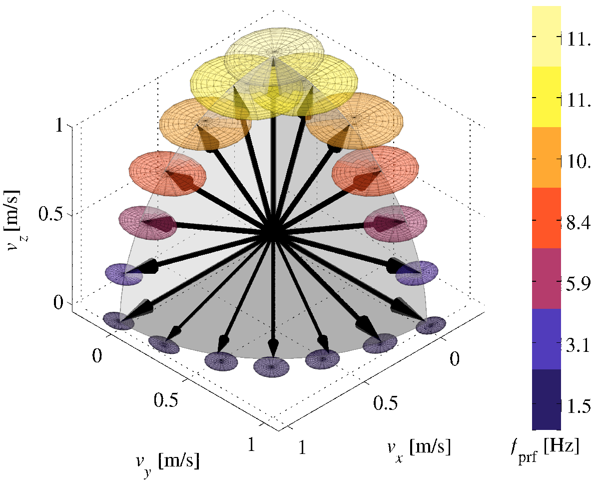

Figure 8. (Color online) The average of the estimated 3D velocity vectors at the center of the vessel for different flow angles in the ZX-, ZY-, and XY-plane. Black arrows indicate the true flow direction. Ellipsoids represent estimated velocities. The center of the ellipsoids is the mean of the 100 estimates, and the the three radii of the ellipsoids are one standard deviation for v_x, v_y, and v_z, respectively. Note, that the pulse repetition frequency, f_{prf}, had to be increased with an increasing axial velocity component (see color coding of the colorbar). This resulted in higher standard deviations on the transverse and elevation velocity estimates. The ellipsoids appear to be discs because the standard deviation of the axial velocities are about an order of magnitude smaller compared to the transverse and elevation velocities. The results are shown in 2D in Fig. 9.

Table III. Overall performance of the estimator at the center of the vessel for the parameter study.

Metric / Plane	ZX	ZY	XY
Mean $\lvert\mathbf{v}\rvert$ [m/s]	1.01 ± 0.093	1.00 ± 0.098	1.03 ± 0.083
Mean $B_{\hat{\phi}}$ [°]	0.92±8.9	1.4±9.2	-0.14±4.2

B. Visualization of estimated flow directions

The flow directions contained in either the ZX-, the ZY-, or the XY-plane were investigated. The flow angle in the individual planes were varied from 0° to 90° in steps of 15°. As in the above case, the mean velocity vector at the center of the vessel was calculated for each variation, and the results are presented in 3D in Fig. 8. For clarity, the pair-wise velocity components in the ZX-, the ZY-, and the XY-plane are presented in Fig. 9. The overall performance of the mean speed, $|\mathbf{v}|$, and the mean estimated angle bias, $B_{\hat{\phi}}$, at the center of the vessel for all angles in the three respective planes are summarized in Table III.

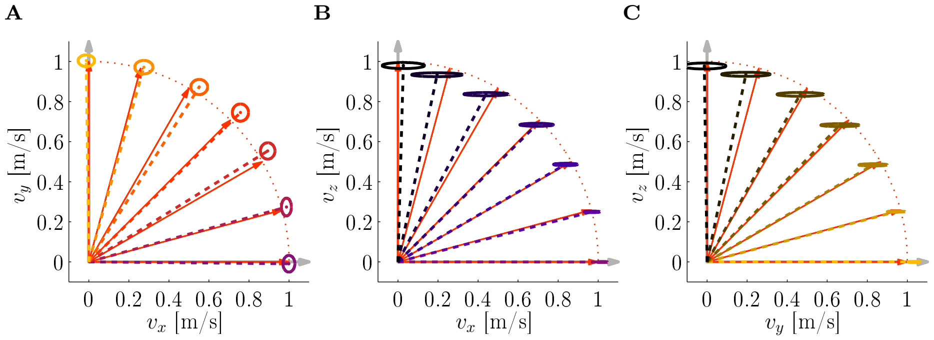

Figure 9. (Color online) 3D velocity estimates as shown in Fig. 8 displayed here as the velocity components in **A** the ZX-plane, **B** the ZY-plane, and **C** the XY-plane. Thin solid arrows indicate the true simulated velocity vectors at the center of the vessel, dashed lines the estimated mean velocity vectors, and ellipses (solid) the standard deviations for pairs of v_x, v_y, or v_z, respectively.

The results show that in the XY-plane the velocity in either the x- or y-direction is determined without bias, whereas at angles around 45°, there is a positive bias of 6 %. Overall, for all seven angles, the relative bias of the speed at the center of the vessel is 3 %. The corresponding relative standard deviation is 8 %. For comparison, the relative bias of the average speed is 1 % and 0 % for the ZX- and the ZY-plane. The mean angle bias is -0.14±4.2° in the XY-plane, and in the ZX- and the ZY-plane the bias is less than 1.4° with standard deviations less than 10°.

It should be noted, that with an increasing axial velocity component, it is necessary to increase the pulse repetition frequency, f_{prf}, to avoid aliasing. It is increased, so that the axial velocity component is maintained at 80 % of the aliasing limit. As a consequence, the aliasing limit for the transverse and elevation velocity components increases, and the poorer use of the velocity range results in the increased standard deviations observed for v_x and v_y. However, this drawback is to some degree alleviated by the fact that most vessels run more or less parallel to the skin surface, and hence, the transducer surface. Additionally, it can be observed that the standard deviations for the conventionally estimated axial velocity are about an order of magnitude smaller than for the transverse and elevation velocity components.

Based on the results shown in Fig. 8, Fig. 9, and Table III, it can be concluded that the speed and the angle of the peak velocity in the XY-plane on average are determined practically without bias, and that 95 % of the estimates are within 8.4°, which is 2.3 % of 360°. For the ZX- and the ZY-plane the performance is comparable, but slightly worse because of the increasing mismatch between the magnitude of the transverse and elevation velocity components and the corresponding aliasing limits.

C. Varying the parameters

The previous paragraphs demonstrated the ability of the 3D TO method to estimate 3D velocity vectors. The following presents the results of varying the previously outlined parameters. In the parameter study, the relative mean bias and relative mean standard deviations are computed according to (12) and (13) for each set of mean velocity profiles for the various parameter settings. This allows for a more straight-forward comparison of the performance over the different parameters and their values. To reduce the effect of the vessel boundaries, the performance metrics are calculated over the entire vessel except for the outer most 1 mm at either end. As default, the flow in is the x-direction, unless the flow angle is changed.

To recapitulate the results from Section VII.B in the framework of the parameter study, the relative mean bias and standard deviations for v_x and v_y are shown in Fig. 10A–10C for the velocities with flow angles ϕ_{zx}, ϕ_{zy}, and ϕ_{xy}, respectively. From Figs. 10A and 10B it is obvious that the relative mean biases, $\tilde{B}_{v_x}$ and $\tilde{B}_{v_y}$, are more or less unaffected, whereas the relative standard deviations, $\tilde{\sigma}_{v_x}$ and $\tilde{\sigma}_{v_y}$, increase as the flow angle decreases and the axial velocity components increases. As previously mentioned, this is due to the increase in the pulse repetition frequency. The shape of the curves is similar to the increase in f_{prf} (see values in Fig. 8). The relative increase in the relative mean standard deviations is largest at large flow angles, which reflects that the largest relative increase in f_{prf} occurs when going from a flow angle of 90° to 80°.

The results in Fig. 10C show that the relative mean standard deviation for v_x increases from about 6 % to about 8 % as the flow angle, ϕ_{xy}, is increased from 0 to 90°. As the angle increases, the transverse velocity component decreases from 1 m/s to 0 m/s. The opposite is the case for the elevation velocity component. The results show that the relative mean standard deviation increases as the magnitude of the velocity component decreases. The relative mean biases for v_x and v_y have a parabolic shape. The values are between 0% and 2% at 0° and 90°, and 4% at 45°. This was also apparent from Fig. 9C.

The number of emissions per velocity estimate affects the performance. The results are shown in Fig. 10D. As the number of emissions increases, the relative mean

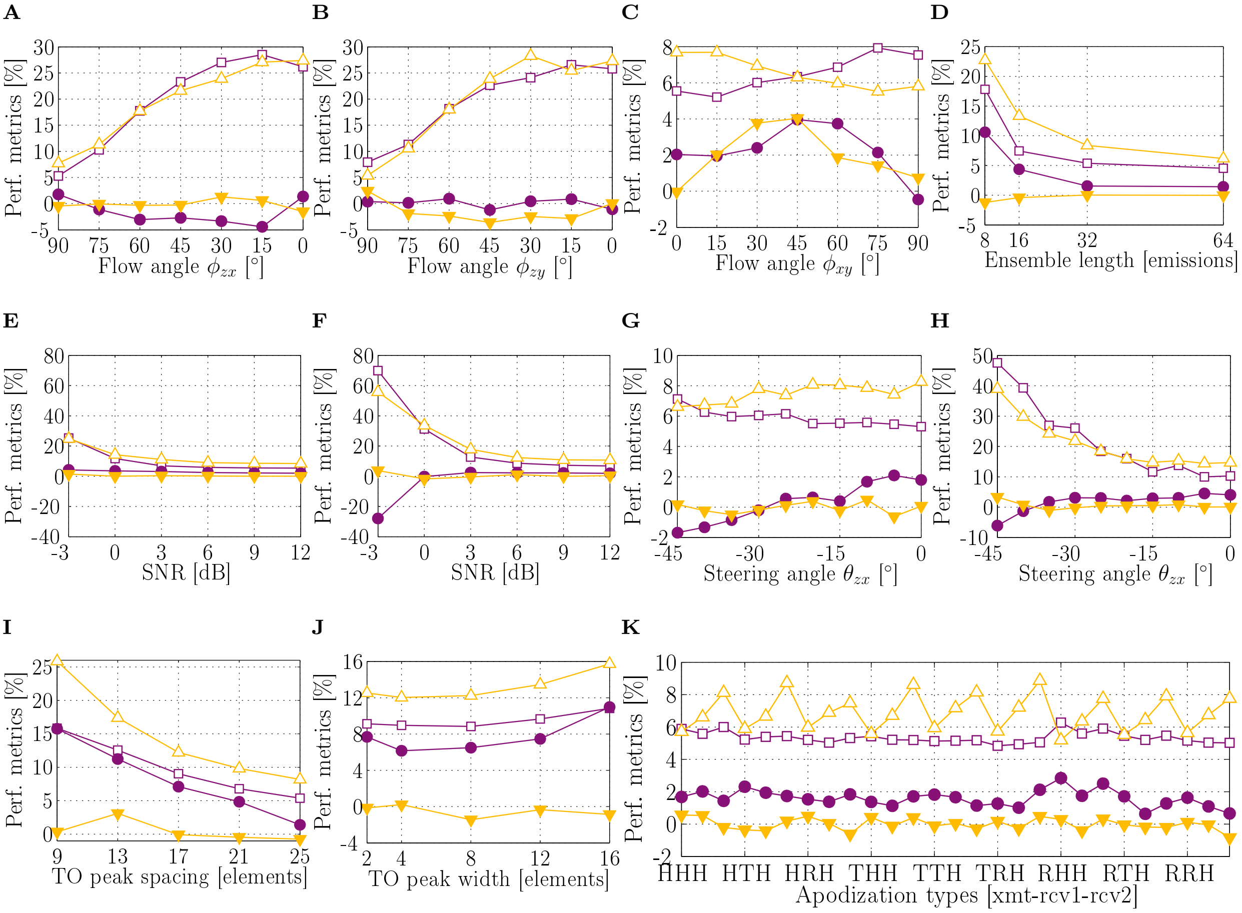

Figure 10. (Color online) Performance metrics as a function of various parameter settings and their values: The relative mean standard deviations $\tilde{\sigma}_{v_x}$ (□) and $\tilde{\sigma}_{v_y}$ (△), and the relative mean biases $\tilde{B}_{v_x}$ (●) and $\tilde{B}_{v_y}$ (▼). The reader is referred to the text for details.

standard deviation decreases, e.g. when the ensemble length is increased from 16 to 64, $\tilde{\sigma}_{v_x}$ and $\tilde{\sigma}_{v_y}$ decrease from 7.4 % and 13 % to 4.5 % and 6.2 %, respectively. The decrease in standard deviation is expected, because the standard deviation should decrease with a factor of $1/\sqrt{N_e}$, if the N_e signals are uncorrelated. The relative mean bias for v_x decreases from 10 % to 1.5 %, whereas the relative mean bias for v_y is unaffected.

The effect of varying the SNR is demonstrated in Fig. 10E and 10F. Fig. 10E shows the result of using the TO estimator — Eqs. (4) and (5) — compared to the heterodyning approach — Eqs. (6) and (7) — in Fig. 10F. For the TO approach with a SNR of ∞ and 0 dB, the relative mean biases for v_x and v_y are increased from 5 % to 12 % and from 8 % to 14 %, respectively. For the heterodyning approach[34], the relative mean standard deviations increase from 7 % to 31 % for v_x and from 10 % to 34 % for v_y when the SNR is changed from ∞ to 0 dB. The difference is more than a factor of 2. In addition, the heterodyning approach breaks down with a SNR between 0 dB and -3 dB, whereas the TO approach first breaks down with a SNR between -6 dB and -3 dB. The results confirm the suspicion raised in Section II.C.3 that the heterodyning approach is more susceptible to noise compared to the TO approach. This observation is in agreement with the results reported by Udesen and Jensen[12].

Fig. 10G show the result of changing the steering angle θ_{zx}. The results for θ_{zy} are similar and are therefore not shown. As the results indicate, the relative standard deviation is almost unaffected with values between 5 % and 7 %. The relative mean biases vary from -2 % to 2 %. These values are obtained by using the theoretically calculated transverse and elevation wavelengths based on (1) and (2) in the beamforming. The values for λ_x and λ_y increase as a function of steering angle because of the $\cos\theta$-term. However, the most accurate velocity estimates (with the smallest bias) were obtained using $\bar{\lambda}_x$ and $\bar{\lambda}_x$ calculated at steering angles of 0° in the velocity estimation. That observation and the low values for especially the relative mean standard deviations were surprising. It was expected that steering the beam would degrade the performance of the velocity estimator. An explanation may reside in the ideal conditions of the Field II simulation environment, and the fact that no noise is added. Hence the drop in SNR due to the angular sensitivity has not been captured. To test this hypothesis, the velocity estimation was repeated with white Gaussian noise added, so that the SNR was changed to 0 dB at a steering angle of 0°. The noise amplitude is kept constant for all steering angles. The result can be observed in Fig. 10H. When the steering angle increases, the received energy is lower, and hence the SNR decreases if the noise is constant. The decrease in SNR degrades the performance and the relative mean standard deviations increases. The relative mean bias is only affected at large steering angles. The results thereby confirm the hypothesis, that noise degrades the performance when steering the beam.

The result of changing the spacing of the TO peaks is illustrated in Fig. 10I. As the spacing increases, the relative mean standard deviations decrease. The relative mean bias for v_y is 0 % for almost all settings, but decreases for v_x. Fig. 10J shows the effect of changing the TO peak width. Increasing the TO peak width slightly increases the relative mean standard deviations. The relative mean bias for v_x has a flat parabolic shape. For v_y, the relative mean bias is unaffected.

Fig. 10K presents the results of combining various apodization shapes. Three different apodization shapes are used: A Hanning window, a Tukey window with a ratio of taper of 0.5, and a rectangular window. These windows are applied to the transmitting aperture, the receive aperture with the TO peaks in the transverse oscillating direction, and with apodizations across the TO peaks in the non-oscillating direction. All e27 combinations are investigated. The first data point in Fig. 10K is denoted HHH. It is an abbreviation for applying Hanning, Hanning, and Hanning windowing in transmit, receive (oscillation direction), and receive (non-oscillation direction), respectively. The next point is HHT denoting Hanning, Hanning, and Tukey, and the third data point is HHR, denoting Hanning, Hanning, and Rect. The fourth data point is HTH, and the pattern is repeated. The results indicate that the relative mean biases are practically unaffected as well as the relative mean standard deviation for v_x. For v_y, however, the relative mean standard deviation has a serrated appearance. The relative standard deviation is around 7 % when the apodization in the non-oscillating direction is a rectangular window, and it is about 5 % when it is Hanning apodized.

When deciding on which apodization to use, it is important to remember that the SNR is proportional with the area under the apodization functions. The consideration of SNR and the area under the apodization functions is also important when considering the peak width. The results indicate, that in a noisy environment, there will be a trade-off between the TO spacing, the TO peak width, and the apodization functions where the SNR affects the optimal setting.

Overall, the parameter study demonstrates that the TO method is robust in terms of creating the TO fields and the appertaining transverse and elevation wavelengths. The theoretical values of the TO wavelengths can be used, but for bias optimization, the mean TO wavelengths based on the TO fields should be computed. Additionally, the TO fields themselves should be optimized by means of the performance metrics to reduce the bias and standard deviations of the velocity estimates. Furthermore, the TO method is less susceptible to noise compared to the heterodyning approach.

VIII. CONCLUSION

A method for estimation of 3D velocity vectors using the Transverse Oscillation approach is presented in Section II.C. Initial results from the plug flow simulation presented in Section V serve as a proof of concept, and demonstrate that the estimation of the velocity vector is decoupled into v_x, v_y, and v_z. It is further demonstrated that it is beneficial to optimize the TO method and to perform bias compensation by estimating the mean TO wavelengths based on the TO fields as described in Section VI.

As demonstrated in Section VII, velocity estimates are obtained with relative mean biases around 0% and relative mean standard deviations less than 5% when optimized. The mean speed at the center of the vessel is estimated with a relative bias less than 3% and a relative standard deviation less than 10%. In the XY-plane, the flow angle is estimated without bias, and with 95% of the estimates within 8.4°. For the given reference setup with a SNR of 0 dB, the parameter study presented in Section VII.C shows that the relative mean standard deviation is increased from 5 % to 12 %. In the presence of noise, the performance degrades as the steering angles are increased, and at high levels of noise, the method breaks down. Overall, the results demonstrate that 3D TO method is able to estimate the three velocity components under various parameter settings, and that the method is robust in terms of the transverse and elevation wavelengths.

The simulation results presented are promising, and they warrant further investigation and experimental verification. Besides requiring a 2D phased array matrix transducer, the complexity of the 3D TO method is within the capabilities of modern scanners. With measurements of 3D velocity vectors, it will be possible to measure the full 3D vortices and rotational flow as found for instance in the carotid artery.

Acknowledgments

This work was supported by grant 024-2008-3 from the Danish Advanced Technology Foundation and BK Medical ApS, Denmark.

[1] E. G. Grant, C. B. Benson, G. L. Moneta, A. V. Alexandrov, J. D. Baker, E. I. Bluth, B. A. Carroll, M. Eliasziw, J. Gocke, B. S. Hertzberg, S. Katanick, L. Needleman, J. Pellerito, J. F. Polak, K. S. Rholl, D. L. Wooster, and E. Zierler, "Carotid artery stenosis: Gray-scale and doppler us diagnosis - society of radiologists in ultrasound consensus conference", Radiology **229**, 340–346 (2003).

[2] C. Arning, B. Widder, G. M. von Reutern, H. Stiegler, and M. Görtler, "Revison of DEGUM Ultrasound Criteria for Grading Internal Carotid Artery Stenoses and Transfer to NASCET Measurement", Ultraschall in Med **31**, 251–257 (2010).

[3] L. J. Frazin, G. Lanza, M. Vonesh, F. Khasho, C. Spitzzeri, S. McGee, D. Mehlman, K. B. Chandran, J. Talano, and D. McPherson, "Functional chiral asymmetry in descending thoracic aorta", Circulation **82**, 1985–97 (1990).

[4] P. Tortoli, V. Michelassi, G. Bambi, F. Guidi, and D. Righi, "Interaction between secondary velocities, flow pulsation and vessel morphology in the common carotid artery", Ultrasound in Med. & Biol. **29**, 407–15 (2003).

[5] K. L. Hansen, J. Udesen, F. Gran, J. A. Jensen, and M. B. Nielsen, "In-vivo examples of complex flow patterns with a fast vector velocity method", Ultraschall in Med **30**, 471–476 (2009).

[6] P. J. Kilner, G. Z. Yang, R. H. Mohiaddin, D. N. Firmin, and D. B. Longmore, "Helical and retrograde secondary flow patterns in the aortic arch studied by three-directional magnetic resonance velocity mapping", Circulation **88**, 2235 – 2247 (1993).

[7] A. Harloff, F. Albrecht, J. Spreer, A. F. Stalder, J. Bock, A. Frydrychowicz, J. Schollhorn, A. Hetzel, M. Schumacher, J. Hennig, and M. Markl, "3D blood flow characteristics in the carotid artery bifurcation assessed by flow-sensitive 4D MRI at 3T", Magn Reson Med **61**, 65–74 (2009).

[8] C. A. Taylor, T. J. R. Hughes, and C. K. Zarins, "Finite element modeling of blood flow in arteries", Comput. Methods Appl. Mech. Engrg. **158**, 155–196 (1998).

[9] M. J. Pihl and J. A. Jensen, "3D velocity estimation using a 2D phased array", in *Proc. IEEE Ultrason. Symp.*, 430–433 (2011).

[10] J. A. Jensen and P. Munk, "A New Method for Estimation of Velocity Vectors", IEEE Trans. Ultrason., Ferroelec., Freq. Contr. **45**, 837–851 (1998).

[11] M. E. Anderson, "Multi-dimensional velocity estimation with ultrasound using spatial quadrature", IEEE Trans. Ultrason., Ferroelec., Freq. Contr. **45**, 852–861 (1998).

[12] J. Udesen and J. A. Jensen, "Investigation of Transverse Oscillation Method", IEEE Trans. Ultrason., Ferroelec., Freq. Contr. **53**, 959–971 (2006).

[13] J. Udesen, M. B. Nielsen, K. R. Nielsen, and J. A. Jensen, "Examples of in-vivo blood vector velocity estimation", Ultrasound Med. Biol. **33**, 541–548 (2007).

[14] M. J. Pihl, S. Nikolov, P. Haugaard, M. C. Hemmsen, and J. A. Jensen, "Performance of the transverse oscillation method using beamformed data from a commercial scanner", in *Proc. IEEE Ultrason. Symp.* (2009).

[15] P. M. Hansen, M. M. Pedersen, K. L. Hansen, M. B. Nielsen, and J. A. Jensen, "Examples of vector velocity imaging", in *15. Nordic-Baltic Conf. Biomed. Eng. and Med. Phys.* (2011).

[16] M. J. Pihl, J. Marcher, and J. A. Jensen, "Phased array vector velocity estimation using tranverse oscillations", IEEE Trans. Ultrason., Ferroelec., Freq. Contr. **In press** (2012).

[17] P. A. Picot, D. W. Ricky, R. Mitchell, R. N. Rankin, and A. Fenster, "Three-dimensional colour Doppler imaging", Ultrasound Med. Biol. **19**, 95–104 (1993).

[18] R. E. Daigle, C. W. Miller, M. B. Histand, F. D. McLeod, and D. E. Hokanson, "Nontraumatic aortic blood flow sensing by use of an ultrasonic esophageal probe", J. Applied Phys. **38**, 1153–1160 (1975).

[19] M. D. Fox, "Multiple crossed-beam ultrasound Doppler velocimetry", IEEE Trans. Son. Ultrason. **SU-25**, 281–286 (1978).

[20] B. Dunmire, K. W. Beach, K.-H. Labs., M. Plett, and D. E. Strandness, "Cross-beam vector Doppler ultrasound for angle independent velocity measurements", Ultrasound Med. Biol. **26**, 1213–1235 (2000).

[21] M. D. Fox and W. M. Gardiner, "Three-dimensional Doppler velocimetry of flow jets", IEEE Trans. Biomed. Eng. **35**, 834–841 (1988).

[22] V. L. Newhouse, K. S. Dickerson, D. Cathignol, and J.-Y. Chapelon, "Three-dimensional vector flow estimation using two transducers and spectral width", IEEE Trans. Ultrason., Ferroelec., Freq. Contr. **41**, 90–95 (1994).

[23] O. Bonnefous, "Measurement of the complete (3D) velocity vector of blood flows", in *Proc. IEEE Ultrason. Symp.*, 795–799 (1988).

[24] I. Hein, "Triple-beam lens transducers for three-dimensional ultrasonic fluid flow estimation", IEEE Trans. Ultrason., Ferroelec., Freq. Contr. **42**, 854–869 (1995).

[25] J. A. Jensen, "Directional velocity estimation using focusing along the flow direction: I: Theory and simulation", IEEE Trans. Ultrason., Ferroelec., Freq. Contr. **50**, 857–872 (2003).

[26] J. A. Jensen and S. I. Nikolov, "A method for real-time three-dimensional vector velocity imaging", in *Proc. IEEE Ultrason. Symp.*, 1582–1585 (2003).

[27] L. N. Bohs, B. J. Geiman, M. E. Anderson, S. C. Gebhart, and G. E. Trahey, "Speckle tracking for multi-dimensional flow estimation", Ultrasonics **38**, 369–375 (2000).

[28] H. B. Kim, J. R. Hertzberg, and R. Shandas, "Development and validation of echo PIV", Exp. in Fluids **36**, 455–462 (2004).

[29] L. Liu, H. Zheng, L. Williams, F. Zhang, R. Wang, J. Hertzberg, and R. Shandas, "Development of a custom-designed echo particle image velocimetry system for multi-component hemodynamic measurements: System characterization and initial experimental results", Phys. Med. Biol. **53**, 1397–1412 (2008).

[30] C. Poelma, J. M. Mari, N. Foin, M. Tang, R. Krams, C. G. Caro, P. D. Weinberg, and J. Westerweel, "3D flow reconstruction using ultrasound PIV", Exp. Fluids **50**, 777–785 (2011).

[31] G. R. Bashford and O. T. von Ramm, "Ultrasound three-dimensional velocity measurements by feature tracking", IEEE Trans. Ultrason., Ferroelec., Freq. Contr. **43**, 376–384 (1996).

[32] J. A. Jensen, "A New Estimator for Vector Velocity Estimation", IEEE Trans. Ultrason., Ferroelec., Freq. Contr. **48**, 886–894 (2001).

[33] T. Loupas, J. T. Powers, and R. W. Gill, "An axial velocity estimator for ultrasound blood flow imaging, based on a full evaluation of the Doppler equation by means of a two-dimensional autocorrelation approach", IEEE Trans. Ultrason., Ferroelec., Freq. Contr. **42**, 672–688 (1995).

[34] M. E. Anderson, "A heterodyning demodulation technique for spatial quadrature", in *Proc. SPIE - med. imag.*, 1487–1490 (2000).

[35] C. Kasai, K. Namekawa, A. Koyano, and R. Omoto, "Real-Time Two-Dimensional Blood Flow Imaging using an Autocorrelation Technique", IEEE Trans. Son. Ultrason. **32**, 458–463 (1985).

[36] J. A. Jensen, "Field: A Program for Simulating Ultrasound Systems", Med. Biol. Eng. Comp. **10th Nordic-Baltic Conference on Biomedical Imaging, Vol. 4, Supplement 1, Part 1**, 351–353 (1996).

[37] J. A. Jensen and N. B. Svendsen, "Calculation of Pressure Fields from Arbitrarily Shaped, Apodized, and Excited Ultrasound Transducers", IEEE Trans. Ultrason., Ferroelec., Freq. Contr. **39**, 262–267 (1992).

Paper VI

Experimental investigation of three-dimensional velocity vector estimation

Michael Johannes Pihl and Jørgen Arendt Jensen

Journal of the Acoustical Society of America

Submitted August 2012

Experimental investigation of three-dimensional velocity vector estimation

Michael Johannes Pihl[a)] and Jørgen Arendt Jensen
Center for Fast Ultrasound Imaging, Department of Electrical Engineering, Technical University of Denmark, Ørsteds Plads, Bldg. 349, DK-2800 Kgs. Lyngby, Denmark

(Dated: August 13, 2012)

Experimentally obtained estimates of three-dimensional (3D) velocity vectors using the 3D Transverse Oscillation (TO) method are presented. The velocities are measured along the diameter of a vessel in a steady flow phantom. Experimental ultrasound measurements using the SARUS scanner validates recently reported results of 3D velocity vectors obtained through simulations. The method employs a 2D transducer and synthesizes two double-oscillating fields in receive to obtain the axial, transverse, and elevation velocity components simultaneously. These TO fields are investigated in an experimental setup. The results demonstrate that the created fields only oscillate in the axial plus either the transverse or the elevation direction. Velocity measurements of steady flow in two different directions (mainly in x or y-direction) are conducted in an experimental flow-rig. All three velocity components are measured with relative biases and standard deviations (normalized to expected value) below 5 % and 12 %, respectively. For an expected velocity magnitude of 25.2 cm/s, the method estimates 24.4±3.1 cm/s and 25.1±1.9 cm/s for the two directions. Under similar conditions, the simulations yield 25.1±1.5 cm/s and 25.4±1.6 cm/s. The experimental results validate the results obtained through simulations and verify that the 3D TO method estimates the full 3D velocity vectors and the correct velocity magnitudes.

PACS numbers: 43.35.Yb
Keywords: Ultrasound, velocity estimation, 3D velocity vectors, transverse oscillations, experimental measurements

I. INTRODUCTION

Ultrasonic velocity estimation has come far since the first measurements of were conducted[1]. Yet, the conventional methods in commercial scanners estimate the axial velocity component only. This is the case despite the fact that studies have shown that the velocity vectors have components in all three spatial dimensions and vary as a function of time and space[2–4]. Several ultrasound methods have been proposed for measuring three-dimensional (3D) velocities over the past decades. These includes cross-beam methods[5–7], speckle or feature tracking methods[8–10], transverse Doppler methods using the spectral broadening effect[11,12], decorrelation based techniques[13–15], cross-correlation of beams[16–18], or particle imaging velocimetry[19–21]. However, the various techniques have individual limitations such as limited field of view, high computational demands, or the need for contrast agents. So far, none of these techniques have produced *in-vivo* 3D vector flow images and none of the techniques have been adopted by commercial manufactures.

Recently, the authors suggested an approach for estimating 3D velocity vectors by means of two transverse oscillating fields, spatial quadrature sampling, and the use of a 2D phased array transducer[22]. Simulation results demonstrated that the 3D Transverse Oscillation (TO) method has the ability to estimate 3D velocity vectors. This paper presents the first experimentally obtained 3D vector velocities measured in a steady flow-rig system using the 3D TO method to validate the previously reported findings. This is attained by measuring the transverse oscillating fields and by measuring 3D velocity profiles through an artificial vessel in an flow-rig system using an experimental research scanner and a 2D matrix array. To underline the validity of the previously reported simulation results, the experimentally obtained measurement results are compared to results from simulations.

To achieve the objective, the paper briefly refers to the 3D Transverse Oscillation method in the next section and describes the materials and methods used in Section III. Section IV presents the experimental measurement results, and Section V the simulation results. The discussion can be found in Section VI, and the conclusion in Section VII.

II. THE 3D TRANSVERSE OSCILLATION METHOD

A method employing transverse oscillations for 3D velocity vector estimation has recently been suggested by the authors[22]. The following serves as a brief summary.

The 3D TO method employs a Transverse Oscillation approach as suggested by Jensen and Munk[23], where Anderson[24] proposed a similar method. The 3D Transverse Oscillation method estimates the two transverse velocity

---

[a)] Author to whom correspondence should be addressed. Electronic mail: `mjp@elektro.dtu.dk`

components based on two double-oscillating fields and spatial quadrature sampling by employing a 2D matrix array transducer. The double oscillating fields are synthesized in receive by applying special apodization functions. To obtain the oscillations in the transverse direction, the receive aperture is modulated in the transverse direction. Conversely, the oscillations in the elevation direction are obtained by modulating the receive aperture in the elevation direction. The fields are created so that they do not oscillate in the perpendicular direction. Thereby, the velocity estimation is decoupled into three orthogonal velocity components, and the components are estimated simultaneously. Note that both fields are synthesized in receive from the same data and all components of the velocity vector are obtained simultaneously.

The creation of the transverse (and the elevation) double-oscillating fields is combined with spatial quadrature sampling. The spatial quadrature data are obtained by sampling the field at four positions that pairwise are 90° phase-shifted. This is obtained by sampling the field at four points that pairwise are spaced a quarter spatial wavelength apart. For a range of depths, this is achieved by steering four beams radially, so that they diverge from each other. The spatial wavelengths can be determined theoretically[23,25]. Alternatively, and with improved performance, the wavelengths can be determined as the mean transverse wavelength, $\bar{\lambda}_x$, and the mean elevation wavelength, $\bar{\lambda}_y$, based on the TO spectra[23,25]. The latter is applied in this paper, and it is further described in Section III.E. Besides the four TO lines, an additional axial line is beamformed for conventional axial velocity estimation.

After the beamforming, the velocity estimation utilizes the estimator suggested by Jensen[26]. The velocity estimation is the same for v_x and v_y, each based on one pair of the four TO lines. The axial velocity component is calculated using a conventional autocorrelation estimator[27] with RF averaging[28]. The three estimated velocity components, v_x, v_y and v_z, are orthogonal, and they are estimated simultaneously by the 5:1 parallel beamforming in receive.

The originally proposed TO method for 2D velocity estimation employed linear array transducers, and experimentally obtained *in vivo* results using the TO method for 2D vector velocity imaging have been presented[29]. Furthermore, the 2D method has been implemented on a commercial scanner and FDA approved for clinical use, and clinical *in vivo* vector flow images obtained using the commercial scanner have been presented[30]. The feasibility of a phased array implementation for 2D velocity estimation has also been demonstrated[25]. Therefore, the 3D TO method is a strong candidate for a commercial implementation of 3D vector velocity imaging.

III. MATERIALS AND METHODS

The following describes the materials and methods used including the measurement equipment, the simulation framework, general settings, the performed measurements and simulations, the data processing, and the performance metrics used.

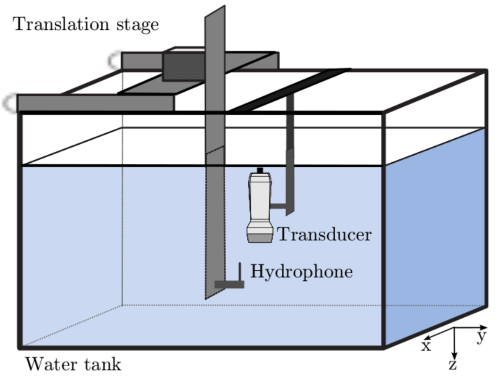

Figure 1. (Color online) The scanning tank system with mounted hydrophone and 2D transducer.

A. Measurement equipment

This section describes the equipment used for performing pulse-echo measurements in a scanning tank and velocity measurements in a flow-rig system.

The 3D Transverse Oscillation method requires a 2D transducer. A 3.5 MHz 32x32 element 2D matrix array transducer (Vermont S.A., Tours, France) is used. The pitch of the transducer is 0.3 mm. The transducer consists of four blocks of 8x32 elements. These four blocks are stacked together separated by an inactive row of elements, hence, the element layout of the transducer differs in the x- and the y-direction.

At a sampling frequency of 70 MHz, data from all the 1024 active elements are acquired simultaneously through 1024 channels connected to the 1024 channels on the synthetic aperture real-time ultrasound system (SARUS)[31]. Data are stored for offline processing. Signals from a hydrophone can be sampled by SARUS as well.

A hydrophone is mounted in an AIMS III Scanning Tank (Onda, Sunnyvale, CA), which can control the position of the hydrophone in all three dimensions. The setup is illustrated in Fig. 1. The hydrophone is a HGL-0400 capsule hydrophone (Onda, Sunnyvale, CA), and it is connected through a preamplifier to either a digital oscilloscope or to SARUS. SARUS and the scanning tank system can be controlled from MATLAB to ensure synchronized data acquisition.

The in-house built flow-rig system is illustrated in Fig. 2. It is a closed loop circuit and consists of a Cole-Parmer (Vernon Hills, IL) centrifugal pump, an air-trap, a long (>1.2 m) metal tube, which is replaced by a rubber (heat-shrink material) tube penetrable to ultrasound inside a tank filled with demineralized water, a calibrated magnetic MAG1100 (Danfoss, Nordborg, Denmark) flowmeter, and plastic tubing to connect the parts. The internal radius, r, of both the metal and the rubber tube is 6 mm, and the wall thickness of the rubber tube is 0.5 mm. The length is long enough to ensure fully developed laminar flow, which has a parabolic flow profile.

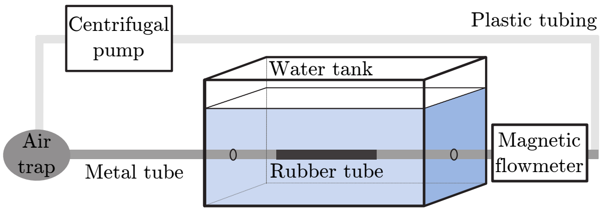

Figure 2. (Color online) The in-house flow-rig. It is a closed loop circuit driven by a centrifugal pump. The volume flow rate can be read out from a calibrated magnetic flowmeter. Inside the water tank, the metal tube is replaced by a rubber tube penetrable to ultrasound. A transducer fixation device, can be lowered into the tank at adjustable beam-to-flow angles.

The flow-rate, Q, is measured by the flowmeter. The centrifugal pump circulates a blood-mimicking fluid (Danish Phantom Design, Frederikssund, Denmark). In its concentrated form, the fluid contains 5 μm orgasol, glycerol, detergent, and demineralized water. It is diluted 1:20 with demineralized water, and dextran is added to obtain a viscosity, μ, of 3.9 mPa·s. The density, ρ, is $1.0 \times 10^3\,\text{kg/m}^3$. A transducer fixation device can be lowered into the water tank at adjustable beam-to-flow angles.

B. Simulation environment

Simulations are performed in order to compare the measurement results with the simulated results. This is performed because the physical transducer differs slightly in layout compared to the previously reported simulation results[32]. Single channel data are obtained using the ultrasound simulation program Field II[33,34]. The general parameter settings for both measurements and simulations are described below. The flow phantom mimicking the experimental flow-rig system is designed as a $20 \times 20 \times 20\,\text{mm}^3$ cube of scatterers. At the center, the vessel is modelled as a cylinder of length of 20 mm and a radius of 6 mm. The velocity profile inside the vessel is a circular-symmetric two-dimensional parabolic profile. The number of scatterers in the total volume is 80,000, and they were initialized with uniformly distributed random positions and random zero-mean Gaussian amplitudes.

In the simulations, plane waves were emulated for both the simulations of the TO fields and flow phantom.

C. General settings

This section describes the general settings that apply to both the measurements and the simulations. The parameters with their values are listed in Table I. These values are used unless stated otherwise.

A few of the parameters are explained in more detail in the following. The layout of the 2D transducer has been described above. The transmit apodization value is listed as “Hamming(32x32)”, which means that a 1x32 samples long Hamming signal is repeated 32x1 times. It is then multiplied (element-wise) with it transposed counterpart. The receive TO apodization in the x-direction is two rectangular functions (2x8 elements) separated by

Table I. Default parameter settings for the measurements and the simulations.

Parameter	**Value**
Transducer	
Geometry [elements]	35x32
Active elements	32x32
Rows of inactive elements (by design)	3×32
Pitch [mm]	0.3
Center frequency [MHz]	3.5
Bandwidth (two-way) [%]	67
System	
Sampling freq. (simulations) [MHz]	100
Sampling freq. (measurements) [MHz]	70
Speed of sound [m/s]	1480
Number of receive channels (SARUS)	1024
Emitted pulse	
Center frequency [MHz]	3.5
No. of cycles	8
Windowing of emitted pulse	Hanning
Focal depth [mm]	30
Steering angle in azimuth plane, θ_{zx} [°]	0
Steering angle in elevation plane, θ_{zy} [°]	0
Transmit apodization	
Transmit apodization	Hamming(32x32)
Receive apodization	
Center line	Hanning(32x32)
TO peak apod. (osc. direction)	Rectangular
TO peak apod. (non-osc. direction)	Rectangular
TO distance d_x [elements]	25
TO distance d_y [elements]	28
TO window width [elements]	8
Flow settings	
Flow angle ϕ_{xy} [°]	0 or 90
Beam-to-flow angle ϕ_{zx} [°]	80 or 90
Beam-to-flow angle ϕ_{zy} [°]	90 or 80
Peak speed [m/s]	0.253
Flow profile	Parabolic
Data acquisition	
No. of emissions	3200
Pulse repetition frequency [Hz]	600
Post processing	
Matched filter	Time-reversed excitation pulse
Clutter filtering	Mean subtraction
Velocity estimator	
Ensemble length [emissions]	32
SNR [dB]	7-10

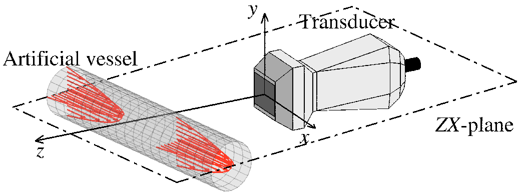

Figure 3. (Color online) Illustration of the flow phantom for measurements and simulations. The beam-to-flow angle ϕ_{ZX} is 80° as one of the two cases of flow directions.

16 elements. Hence, the distance of the TO functions is 25 elements. This is repeated along the non-oscillating (non-osc.) direction, which in this case is the y-direction. The TO apodization for flow estimation in the y-direction is merely a 90° rotation of the TO apodization in the x-direction, except for that fact that the distance of the centers of the TO function is 28, because of the three inactive rows.

The peak velocity is calculated based on the volume flow rate from the flow-meter and the radius of the vessel. The velocity was set to be approximately 0.25 m/s, because the pump cannot deliver a steady flow at high velocities. The same velocity was used in the simulations. The pulse-repetition frequency was set low accordingly. If the velocity was approximately 1 m/s as e.g. in the carotid artery, the pulse repetition frequency should just be increased to 2.4 kHz.

In the beamforming, the receiving aperture for the TO lines in the ZY-plane consisted of the two 32x8 rectangles, where center points were separated by 28 elements. For the ZX-plane, the receiving aperture consisted of two 8x16 rectangles, centered in the y-direction and with 25 elements between the centers. This difference was applied due to transducer inaccuracies affecting the two velocity components differently. In the simulations, the geometrical layout of the physical transducer was emulated, and the measured transducer impulse-response was used.

D. Performed measurements and simulations

Pulse-echo measurements are performed in the scanning tank. First, the hydrophone is aligned under the transducer in the XY-plane at a depth of 30 mm. Second, the hydrophone is used as a point source and the transmit-receive pulse-echo field is sampled at various positions in the field. For these measurements, plane waves where emitted instead of a focused beam.

Flow measurements were conducted with two different flow directions in regard to the transducer. The direction of the velocity vectors were either approximately $(v_x, v_y, v_z)/|\mathbf{v}| = (0.986, 0, 0.168)$ or $(v_x, v_y, v_z)/|\mathbf{v}| = (0, 0.986, 0.168)$ relative to the transmitted beam, which was along the z-axis. The one case is illustrated in Fig. 3. In the measurements, these flow directions were obtained by adjusting the transducer $z-$axis-to-flow angle to 80°, and letting the transducer x-axis point in the direction of the flow. In the other case the transducer was rotated 90°, so that the flow was in the y-direction.

For both cases, 1600 emissions with a pulse repetition frequency of 600 Hz were obtained.

Pulse-echo simulations and flow phantom simulations corresponding to the measurements were performed using Field II. Simulations with flow were conducted with the same flow directions as for the measurements.

E. Data processing

The data processing was performed offline. The individual channel data sampled with SARUS or obtained through the simulations were matched filtered with the time-reversed excitation pulse prior to the beamforming stage. The beamforming was performed using the Beamformation Toolbox III[35].

The measurement system inherently introduces noise to the measurements. In SARUS, the noise level varies over various channels. Therefore, channels with high noise levels were removed in the beamforming. The standard deviation over 100 emissions are calculated for each sample covering the vessel wall (300 samples in total). For each channel, the mean of the standard deviations is calculated. Now, the mean and standard deviations across the channels are computed. Channels were the mean standard deviation is higher than the mean of all channels plus 2 standard deviations (i.e. above the 95% interval) are removed. In all, 33 channels were removed.

The amount of noise in the system affects the signal-to-noise ratio (SNR). This parameter that affects the performance of the velocity estimator. The SNR of the beamformed RF data inside the vessel was calculated based on 100 emissions where the flow has been turned off. The SNR is calculated as

$$\mathrm{SNR}_{\mathrm{dB}}(n) = 10\log_{10}\frac{\sum\limits_{n=-N_s/2}^{N_s/2} s^2(n)}{\sum\limits_{n=-N_s/2}^{N_s/2} n_s^2(n)},$$

where n denotes discrete time samples, $s(n)$ is the received sampled signals, $n_s(n)$ is calculated as the residuals after subtracting the average of $s(n)$ over the 100 emissions from $s(n)$, and N_s is the number of samples in one excitation pulse. The final value of the SNR is averaged over the 100 emissions, and over the vessel lumen. For the simulation of velocities, zero mean Gaussian white noise was added to the individual channels prior to matched filtration and beamforming. The noise amplitude was adjusted to obtain the desired SNR.

To obtain the TO fields, the temporal IQ data are obtained by use of the Hilbert transform on the time-sampled signals. Then the signals from the left and right beams are combined to create the complex TO fields[25]. The corresponding TO spectrum is obtained by applying a Fourier transform on the complex TO fields. Ideally, if the spatial IQ process worked for all spatial frequencies, the TO spectra should be one-sided in the oscillating direction and symmetrical around 0 mm^{-1} in the non-oscillating direction. A performance metric to evaluate how well the spatial IQ process has worked is the ratio of energy at negative spatial frequencies over the ratio of energy at positive spatial frequencies denoted E_r.[25]

Before the velocity estimation was performed, clutter filtering was applied by subtracting the mean ensemble value of N_i emissions as

$$r_{cf}(n,i) = r_m(n,i) - \sum_{i=1}^{N_i} r_m(n,i),$$

where $r_m(n,i)$ are the matched filtered received signals and i is the emission number.

To improve the performance of the velocity estimates, the mean transverse wavelength, $\bar{\lambda}_x$, and the mean elevation wavelength, $\bar{\lambda}_y$, were used in both the beamforming stage and in the velocity estimation. This lowers the standard deviation, and reduces the bias.[25] The estimated mean values are determined from simulations, and the mean wavelengths and theoretically determined wavelengths are stated in Section V.A. To obtain the TO spectra, however, the theoretical values were used in both measurements and simulations.

IV. MEASUREMENTS RESULTS

This section presents the results obtained from measuring the TO fields and velocities in the flow-rig.

A. Measurements of the TO fields

The TO method depends on creating the two double-oscillating fields that oscillate in the axial and in either the transverse (x) direction or the elevation (y) direction.

The double-oscillating pulse-echo fields are investigated using the scanning tank system, and data are obtained using SARUS. Fig. 4 presents the result of performed measurements. The signals displayed in the figure were averaged over 8 emissions at each position and they are normalized to the overall maximum signal value. Fig. 4A shows the sampled left and right beams in the ZX-plane for a specific time instance for a point target (the hydrophone), which is moved in the x-direction between emissions. Hence, the positions of the point target were $(x, y, z) = (x_i, 0, 30)$ mm, where $x_i = -5, -4.5, \ldots, 5$ mm. The dashed line in Fig. 4A shows the Hilbert transform of the left beam. Ideally, the right beam should overlap with the Hilbert transform of the left beam for the spatial IQ to work perfectly. As it can be observed from the figure, this is the case for the most part of the signals.

Fig. 4B shows the left and right beam in the ZY-plane, for the point target moved in the x-direction. In this case, there should not be a 90° phase-shift between the left and the right beam as the TO oscillations are in the y-direction, and the point target was moved in the x-direction. As Fig. 4B demonstrates, there is no 90° phase-shift between the left and the right beam.

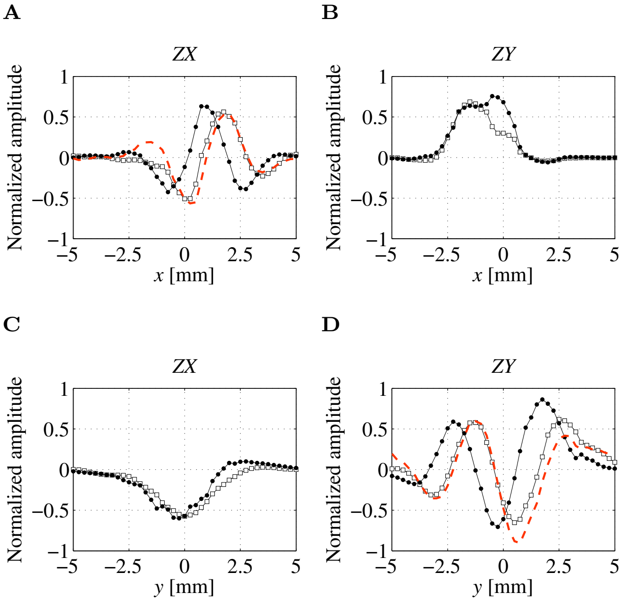

Figure 4. (Color online) Pulse-echo measurements of the TO fields at a depth of 30 mm for a specific time instance across either the transverse x-direction (**A** and **B**) or the elevation y-direction (**C** and **D**). Dots ($\cdot$) denotes samples for the left beam, and squares (□) denotes samples for the right beam. **A** and **C** is for the two beam in the ZX-plane. **B** and **D** is for the beams in the ZY-plane. The dashed line is the Hilbert transform of the left beam (in **A** and **D**).

For the results in Fig. 4C and 4D, the point target was moved in the y-direction. Therefore, the obtained results are the opposite of the results in Fig. 4A and 4B. Fig. 4C shows the left and the right beam in the ZX-plane. As can be observed, the two signals almost coincide: The phase of the signals are the same with some small differences in amplitude. Conversely, the left and the right beam in the ZY-plane shown in Fig. 4D exhibits the same trends as for the signals in Fig. 4A: The right beam and the Hilbert transform of the left beam overlap for part of the signals, and else, they have the same phase but different amplitudes. On a side note, the signals in the x-direction (Fig. 4A and B) are slightly off the center axis.

The results presented in Fig. 4 were the sampled signals at one specific time instance. The results in Fig. 5 shows the results of the TO spectra, for the four cases shown in Fig. 4. It is expected that Fig. 5A and D should have one-sided spectra, i.e. the main energy located within the positive frequencies, whereas Fig. 5B and C should be symmetric around 0 mm^{-1}. This is also the case, although the spectra in both Fig. 5B and C are a little off the center axis.

The mean transverse wavelength, $\bar{\lambda}_x$, and mean elevation wavelength, $\bar{\lambda}_y$, calculated based on the TO spectra (Fig. 5A and D) are 8.0 mm and 5.4 mm, respectively. In terms of frequency, this corresponds to 0.124 mm^{-1} and 0.186 mm^{-1}. The peaks are located at 4.2 mm (0.240 mm^{-1}) and 4.9 mm (0.203 mm^{-1}). The energy ratio, E_r, is -14 dB for Fig. 5A and -8.5 dB for

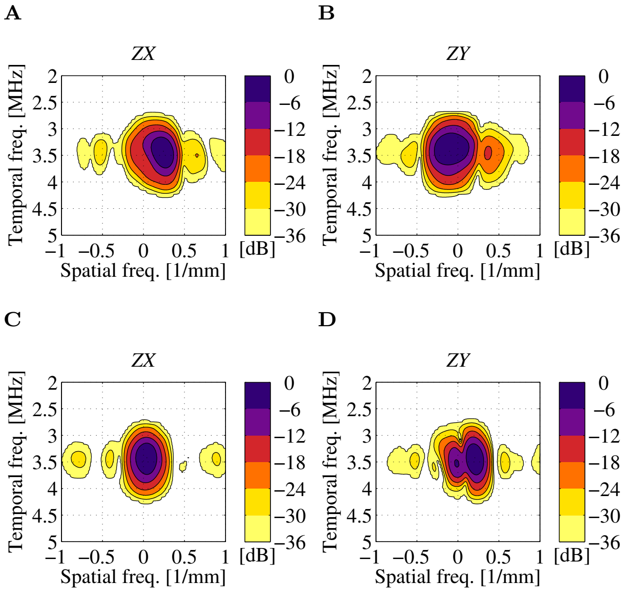

Figure 5. (Color online) The TO spectra corresponding to the TO fields in Fig. 4.

Fig. 5D.

For Fig. 5B and C the mean frequencies are -0.031 mm^{-1} and -0.0021 mm^{-1}. The energy ratios are 4.5 dB and -3.2 dB for Fig. 5B and Fig. 5C, respectively.

The discussion of the presented results and the differences between the theoretical and measured mean wavelengths as well as a comparison to the obtained simulation data is deferred to Section VI.

B. Flow-rig measurements

Measurements were performed in a flow-rig with steady flow to evaluate the performance of the estimator. As default, 32 emissions per estimate were used yielding 50 velocity profiles of the three velocity components v_x, v_y, and v_z as demonstrated in Fig. 6. The left panels are for a flow direction expectedly confined to the ZX-plane. The transducer was placed inside the water tank with an expected beam-to-flow angle ϕ_{ZX} of 80° and an expected flow angle ϕ_{ZY} of 0°, i.e. a flow direction confined inside the ZX-plane. The actual beam-to-flow angle was determined to be 78° by use of the mean axial velocity profile. The low standard deviation of the conventionally estimated axial velocities allows for this determination of the beam-to-flow angle. Note, that this is done without considering either v_x or v_y. For v_y, the velocities were expected to be 0 m/s. The actual value of ϕ_{ZX} is within the expected uncertainty of the transducer fixation devices.

The right panels in Fig. 6 are the results for a flow direction confined inside the ZY-plane. In the same way as above, ϕ_{ZX} was determined to be 79° and ϕ_{ZX} to be 90°. Comparing the velocity profiles for v_x and v_y, it can be observed, that several of the flow lines for v_x have higher fluctuations than for v_y. The reasons for this will be discussed later. Compared to v_x and v_y, the variance of the estimated axial velocities is 5–8 times smaller. This is determined by investigating the mean and standard deviations of the estimated velocity profiles.

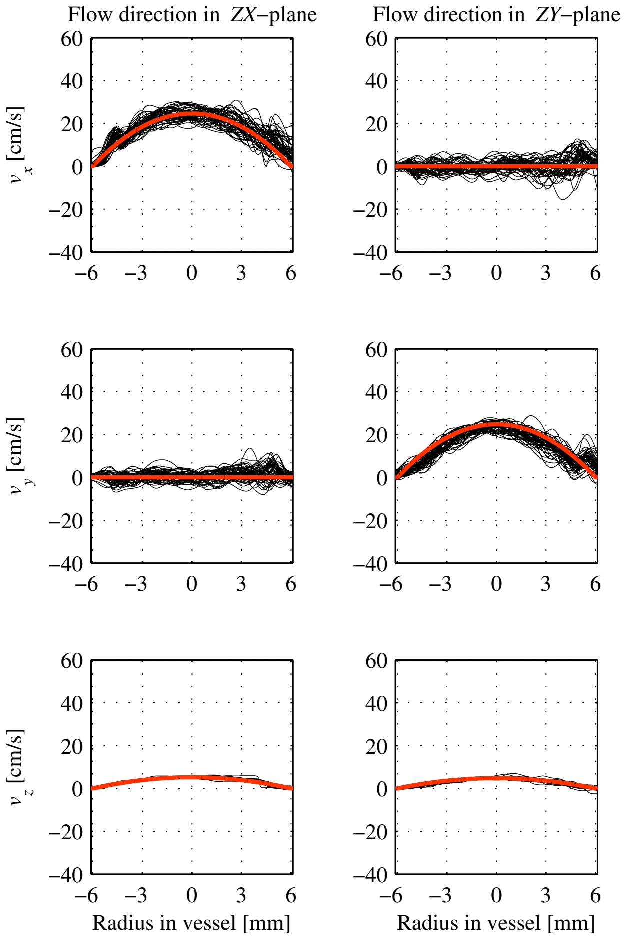

Figure 6. (Color online) Estimated velocity profiles of the three components v_x, v_y, and v_z based on experimental measurements in a flow-rig. The center of the vessel was located at an axial depth of 30 mm. Left panels are for a flow direction primarily in the ZX-plane. Right panels are for a flow direction in the ZY-plane. Thin lines represents individual estimated profiles, and thick lines represent the expected flow profiles.

The estimated mean and standard deviation for v_x, v_y, and v_z for the two cases are displayed in Fig. 7. In all the six subplots, the mean of the estimated velocity components follows the expected profiles. At the center of the vessel at 30 mm, the average velocity for the two cases with the flow direction confined to the ZX-plane or the ZY-plane were

$$\bar{\mathbf{v}}_{\mathbf{ZX}} = \begin{pmatrix} \bar{v}_x \\ \bar{v}_y \\ \bar{v}_z \end{pmatrix} = \begin{pmatrix} 24.4 \\ -0.21 \\ 5.22 \end{pmatrix} \pm \begin{pmatrix} 2.6 \\ 2.1 \\ 0.31 \end{pmatrix} \text{cm/s}$$

$$\bar{\mathbf{v}}_{\mathbf{ZY}} = \begin{pmatrix} \bar{v}_x \\ \bar{v}_y \\ \bar{v}_z \end{pmatrix} = \begin{pmatrix} 0.25 \\ 23.5 \\ 4.92 \end{pmatrix} \pm \begin{pmatrix} 2.5 \\ 2.1 \\ 0.39 \end{pmatrix} \text{cm/s.}$$

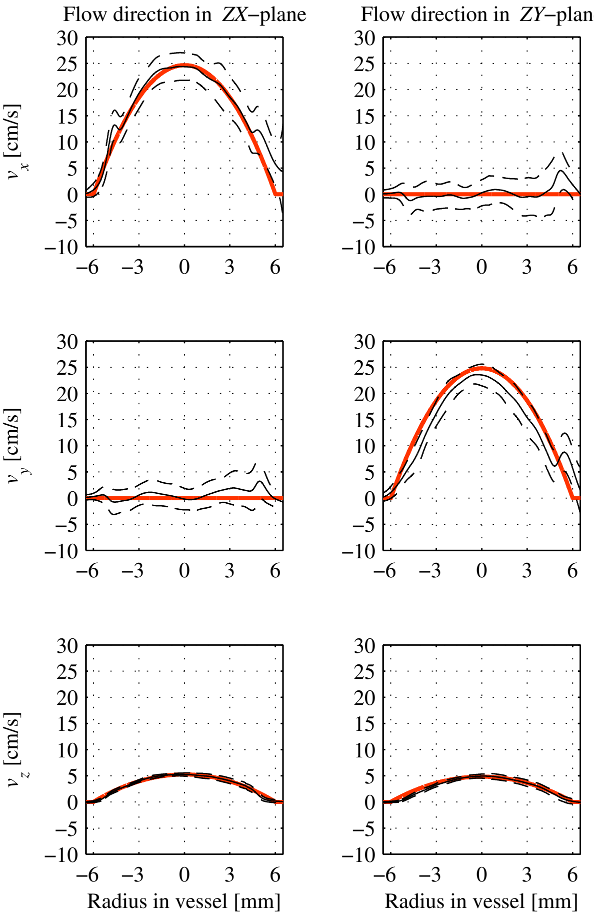

Figure 7. (Color online) Mean and the range of one standard deviation of the 50 measured velocity profiles for the three estimated velocity components. Thick lines indicate the expected velocity profile, thin lines indicates the mean of the profiles, and dashed lines one standard deviation. Compare to the simulated results in Fig. 12.

The expected velocities in the two cases were

$$\mathbf{v}_{\mathrm{exp,ZX}} = \begin{pmatrix} 24.6 \\ 0.00 \\ 5.24 \end{pmatrix} \mathrm{cm/s}$$

$$\mathbf{v}_{\mathrm{exp,ZY}} = \begin{pmatrix} 0.00 \\ 24.8 \\ 4.82 \end{pmatrix} \mathrm{cm/s},$$

yielding a bias of

$$\mathbf{B}_{\mathbf{v_{ZX}}} = \begin{pmatrix} -0.30 \\ -0.21 \\ -0.023 \end{pmatrix} \mathrm{cm/s}$$

$$\mathbf{B}_{\mathbf{v_{ZY}}} = \begin{pmatrix} 0.25 \\ -1.28 \\ 0.10 \end{pmatrix} \mathrm{cm/s}.$$

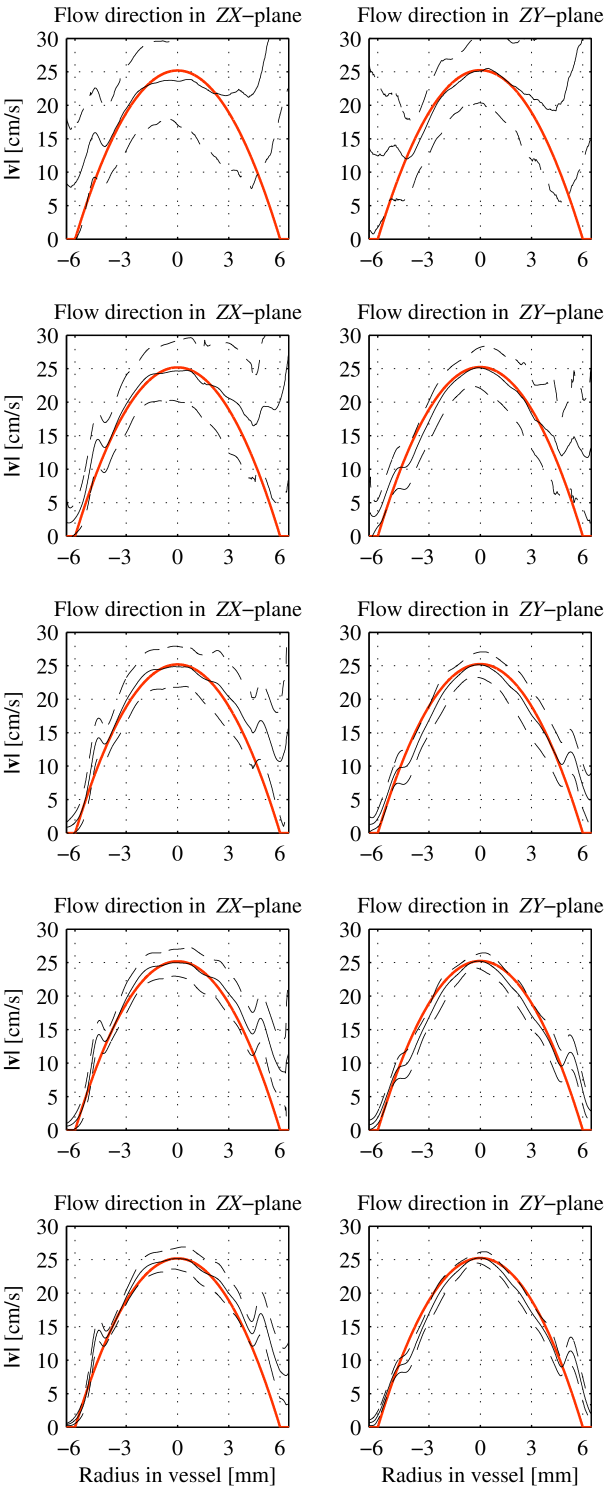

Figure 8. (Color online) Mean and the range of one standard deviation of the measured velocity magnitude profiles as a function of ensemble length in the velocity estimation. From top to bottom: 8, 16, 32, 64, 128 emissions per velocity estimate. Thick lines indicate the expected velocity profile, thin lines indicates the mean of the profiles, and dashed lines the range of one standard deviation.

With the three independent velocity components estimated, it is possible to calculate the true velocity magnitude. The velocity magnitude profiles are calculated

Table II. Estimated velocity magnitude at the center of the vessel in terms of mean ± one standard deviation and bias compared to the expected values. Results based on measurements. "Flow direction" refers to the two cases with the flow direction being either in the ZX- or the ZY-plane.

Metric / Flow direction	ZX	ZY	Unit
Expected $\lvert\mathbf{v}\rvert$	25.2	25.2	[cm/s]
Mean of $\lvert\mathbf{v}\rvert$	24.8	25.1	[cm/s]
Std. of $\lvert\mathbf{v}\rvert$	3.1	1.9	[cm/s]
Bias	−0.36	−0.12	[cm/s]

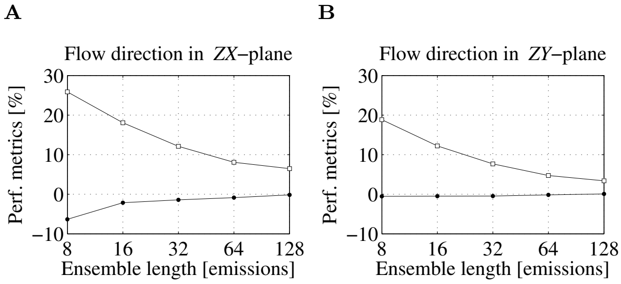

Figure 9. Performance metrics for the estimated velocity magnitude at the center of the vessel for the flow direction confined to **A** the ZX-plane and **B** the ZY-plane. (□) denotes the relative standard deviation and (·) the relative bias.

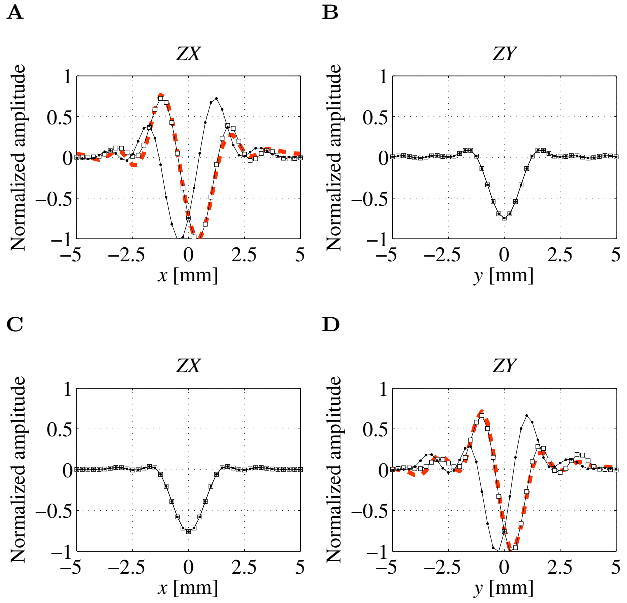

Figure 10. (Color online) Simulations of the TO fields at a depth of 30 mm for a specific time instance across either the transverse x-direction (**A** and **B**) or the elevation y-direction (**C** and **D**). Dots (·) denotes samples for the left beam, and squares (□) denotes samples for the right beam. **A** and **C** is for the two beams in the ZX-plane. **B** and **D** is for the beams in the ZY-plane. The thick dashed line is the Hilbert transform of the left beam (in **A** and **D**).

for each set of the three velocity component profiles. For the results presented in Fig. 6, the mean ± one standard deviation of the velocity magnitude profile is shown in Fig. 8 in the third row. For the peak velocity magnitude at the center of the vessel, the mean of the velocity magnitude, $|\mathbf{v}|$, the expected velocity magnitude, and the resulting bias are listed in Table II. As it can be calculated, the relative standard deviation and the relative bias compared to the expected value are 12 % and -1 % for the flow direction in the ZX-plane, respectively. For the flow direction in the ZY-plan, the values are 8 % and 0.5 %.

The performance of the velocity estimator depends on the SNR. The SNR inside the vessel was calculated based on 100 emissions where the flow had been turned off. On average, the SNR inside the vessel was 10 dB for the lines in the ZY-plane, and 7.5 dB for the lines in the ZX-plane. But these averages covers values range from 12 dB close to the first vessel wall down to 3 dB close to the second vessel wall. The drop in SNR is particularly present for the two TO lines in the ZX-plane.

Another parameter that affects the performance of the 3D TO estimator is the ensemble length, i.e. the number of pulses used in the calculation of the autocorrelation values. The velocity estimation was repeated for ensemble lengths of 8, 16, 32, 64, and 128 emissions per estimate. The resulting velocity magnitude profiles can be found in Fig. 8. For an ensemble length of 8, the standard deviations are large, especially at the far end of the lumen. As the ensemble length increases, the standard deviations decrease, yielding a better performance. The drawback of increasing the ensemble length, is of course the drop in frame-rate, and often, a compromise between frame-rate and precision has to be made. The performance increase is visualized in Fig. 9, which shows the relative standard deviation and relative bias at the center of the vessel lumen. As the ensemble size increases, the relative standard deviation decreases, whereas the relative bias only changes slightly.

V. SIMULATION RESULTS

Simulations with the same parameter settings as the measurements were carried out. Both the TO fields and velocities in a flow phantom were simulated.

A. Simulations of the TO fields

The TO fields were investigated at a depth of 30 mm in points along the x- and y-axis. The positions were the same as the measurements. The results are shown in Fig. 10. Fig. 10A and D illustrate that the left and right beams are 90° phase-shifted, whereas the left and right beam in Fig. 10B and C are not. The corresponding TO spectra are shown in Fig. 11. As it can be observed, the spectra in Fig. 11A and D are almost one-sided, while the spectra in in Fig. 11B and C are symmetrical around $0\,\mathrm{mm}^{-1}$.

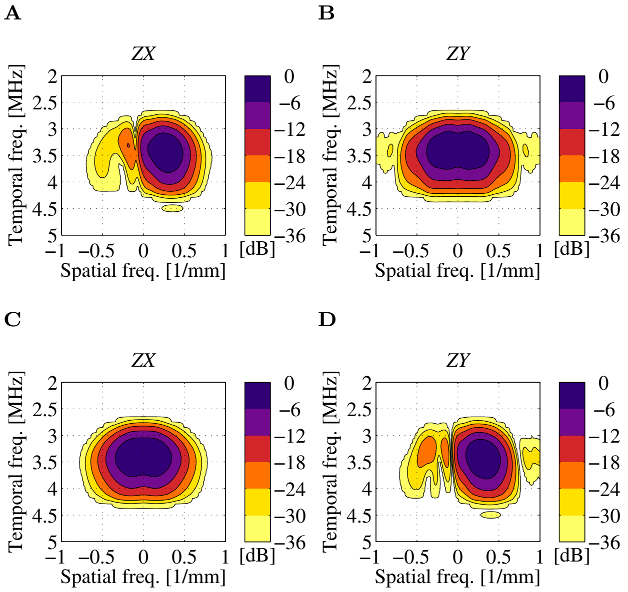

Figure 11. (Color online) The TO spectra corresponding to the TO fields in Fig. 10.

For the given parameter settings, the theoretical λ_x and λ_y are 3.4 mm and 3.0 mm, respectively. The mean transverse wavelength, $\bar{\lambda}_x$, and mean elevation wavelength, $\bar{\lambda}_y$, calculated based on the TO spectra (Fig. 11A and D) are 3.7 mm and 3.3 mm, respectively. In terms of frequency, this corresponds to $0.270\,\mathrm{mm}^{-1}$ and $0.302\,\mathrm{mm}^{-1}$. For Fig. 11B and C the mean frequencies are both $0\,\mathrm{mm}^{-1}$. The energy ratio, E_r, is -16 dB for Fig. 11A, -0.021 dB for Fig. 11B, -0.027 dB for Fig. 11C, and -18 dB for Fig. 11D.

The comparison of the simulated results to the measured results is found in Section VI.

B. Flow phantom simulation

The result of simulating velocities in the flow phantom is shown Fig. 12 for both cases. The simulated velocities follow the expected velocity profiles. The standard deviation for v_x and v_y are comparable, although slightly smaller for v_y than for v_x. The standard deviation is considerably smaller for v_z than for v_x and v_y. For all six velocity profiles, almost no bias is present except close the vessel boundaries. At the center, the mean of the estimated velocities for the two cases is

$$\bar{\mathbf{v}} = \begin{pmatrix} \bar{v}_x \\ \bar{v}_y \\ \bar{v}_z \end{pmatrix} = \begin{pmatrix} 24.6 \\ 0.97 \\ 4.18 \end{pmatrix} \pm \begin{pmatrix} 1.5 \\ 2.5 \\ 0.14 \end{pmatrix} \mathrm{cm/s}$$

$$\bar{\mathbf{v}} = \begin{pmatrix} \bar{v}_x \\ \bar{v}_y \\ \bar{v}_z \end{pmatrix} = \begin{pmatrix} 0.384 \\ 24.8 \\ 4.21 \end{pmatrix} \pm \begin{pmatrix} 3.3 \\ 1.6 \\ 0.14 \end{pmatrix} \mathrm{cm/s}.$$

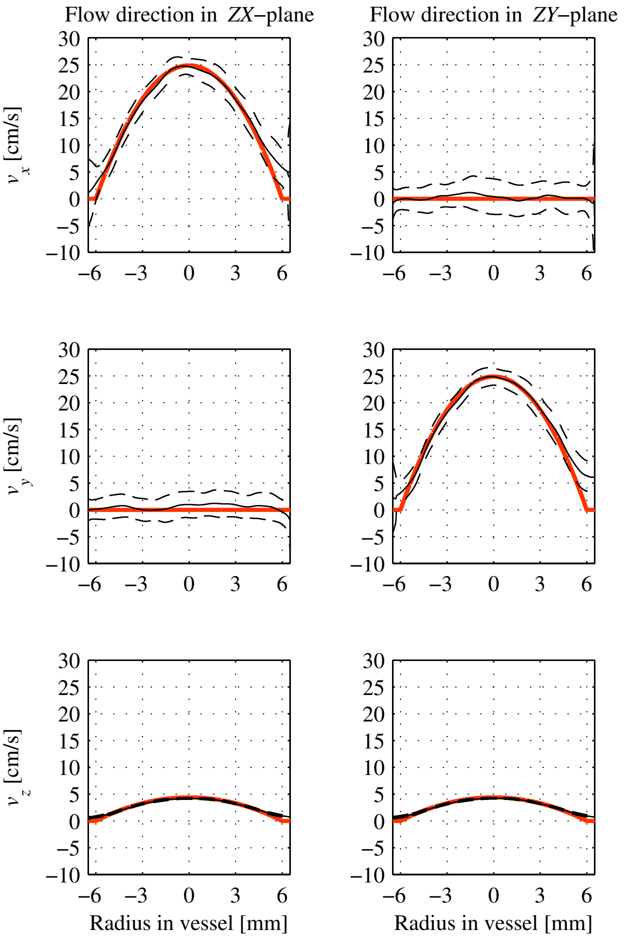

Figure 12. (Color online) Mean and the range of one standard deviation of the 50 simulated velocity profiles for the three estimated velocity components. Thick lines indicate the expected velocity profile, thin lines indicates the mean of the profiles, and dashed lines one standard deviation. Compare to the measured results in Fig. 7.

The expected velocities in the two cases were

$$\mathbf{v}_{\mathrm{exp}} = \begin{pmatrix} 24.9 \\ 0.00 \\ 4.38 \end{pmatrix} \mathrm{cm/s}$$

$$\mathbf{v}_{\mathrm{exp}} = \begin{pmatrix} 0.00 \\ 24.9 \\ 4.38 \end{pmatrix} \mathrm{cm/s},$$

yielding a bias of

$$\mathbf{B}_{\mathbf{v}} = \begin{pmatrix} -0.24 \\ 0.97 \\ -0.21 \end{pmatrix} \mathrm{cm/s}$$

$$\mathbf{B}_{\mathbf{v}} = \begin{pmatrix} 0.38 \\ -0.024 \\ -0.17 \end{pmatrix} \mathrm{cm/s}.$$

Table III. Estimated velocity magnitude at the center of the vessel in terms of mean ± one standard deviation and bias compared to the expected values. Results based on simulations. "Flow direction" refers to the two cases with the flow direction being either in the ZX- or the ZY-plane.

Metric / Flow direction	ZX	ZY	Unit
Expected $\lvert\mathbf{v}\rvert$	25.2	25.2	[cm/s]
Mean of $\lvert\mathbf{v}\rvert$	25.1	25.4	[cm/s]
Std. of $\lvert\mathbf{v}\rvert$	1.5	1.6	[cm/s]
Bias	−0.13	0.17	[cm/s]

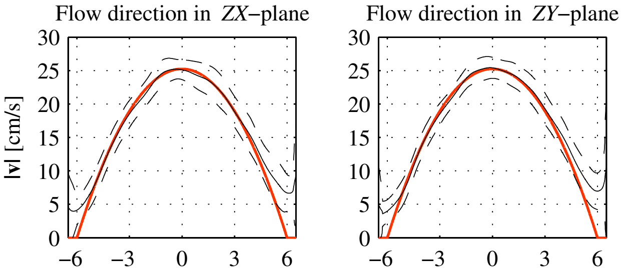

Figure 13. Mean and the range of one standard deviation of the simulated velocity magnitude profiles with an ensemble length in the velocity estimation of 32. Thick lines indicate the expected velocity profile, thin lines indicates the mean of the profiles, and dashed lines the range of one standard deviation.

The mean of the velocity magnitudes calculated for each set of velocity profiles is displayed in Fig. 13. The results at the center is listed in Table III. The relative standard deviation and the relative bias compared to the expected peak velocity magnitude is 6 % and -0.5 % for the first case and 6 % and 0.7 % for the second case, respectively. The described results were obtained with an average SNR inside the vessel of approximately 6.0 dB for the flow direction in the ZX-plane and 9.4 dB for the flow direction in the ZY-plane .

VI. DISCUSSION

This section discusses the results presented in this paper. First, the TO fields are discussed, and second, the obtained velocity estimates from measurements and simulations are discussed.

A. TO fields

The measurements of the double-oscillating pulse-echo fields presented in Fig. 4 as well as the simulated results shown in Fig. 10 demonstrate, that the TO fields, besides oscillating in the axial dimension, oscillate in the transverse and not in the elevation direction or vice versa. Additionally, the results demonstrate that in the oscillating direction, the left and the right beams are approximately 90° phase-shifted.

The signals in Fig. 4A and B are slightly off axis, which means, that the signals in Fig. 4C and D where not obtained at the center. This explains why E_r is lower for Fig. 4D (-8.5 dB) than for Fig. 4A (-14 dB). For comparison, the values for the simulated TO spectra are -16 dB and -18 dB for the oscillations in the transverse and in the elevation direction, respectively.

The measurements yielded mean spatial wavelengths of 8.0 mm and 5.4 mm for $\bar{\lambda}_x$ and $\bar{\lambda}_y$, respectively. This is somewhat higher than the simulated mean spatial wavelengths of 3.7 mm and 3.3 mm, respectively. The theoretical values are 3.4 mm and 3.0 mm for λ_x and λ_y, respectively. The differences in λ_x and λ_y are a result of the geometrical differences in the x- and the y-direction. The spatial mean wavelengths obtained through simulations were used in the beamforming and the velocity estimation of the experimentally measured as well as the simulated flow.

One of the differences between the measurements and the simulations comes from the phase errors and the noise in the measurement system, which are not present in the simulations. Additionally, the energy for the higher spatial frequencies are present both at negative and positive frequencies in the otherwise one-sided spectra. That effectively lowers the mean frequency, and thereby increases the mean wavelength. Furthermore, in the measurements, the scan plane may not be completely aligned with transmitted beam.

Nonetheless, the measured TO fields confirm the presence of the two double-oscillating fields, where the left and the right beam in the oscillation direction are approximately 90° phase-shifted.

B. Velocity estimation

Three-dimensional velocity estimates are obtained through experimental measurements and simulations of steady flow. Fig. 6 shows the individual estimated velocity profiles for the three velocity components v_x, v_y, and v_z measured in the experimental flow-rig. Fig. 7 shows the mean and the range of one standard deviation. As it can be observed, the bias is almost 0 for both of the flow directions, whereas the standard deviation for v_x is higher than for v_y.

One of the reasons for the higher variation and variance of the profiles for v_x compared to v_y is due to differences in the electronics. For estimation of v_x, other transducer elements and system channels are used compared to the ones used for estimating v_y. The elements used for estimating v_x have more errors (in phase and cross-talk) than the ones used for v_y. Additionally, there is more electronic noise present on the channels used to estimated v_x. The noise amplitude fluctuates, and hence, affects the different estimated velocity profiles differently. This explains that only some of the estimated velocity profiles exhibits higher variation than others. Additionally, some of the sampling boards are unstable, yielding increases in noise over time. This affect v_x, where the large fluctuations for v_x especially for the flow direction in the ZY-plane arose at the end of the measurements, and progressively got worse. Channels involved in estimating v_y were not affected by this. These issues where addressed and to some extend alleviated by removing channels with large fluctuations from the beamforming. Hence, for the measurements, it is expected that the standard deviations are larger for v_x compared to v_y. This is also reflected in the SNR, which was about 3 dB lower for v_x compared to v_y. Additionally, the SNR dropped considerably inside the vessel down to approximately 3 dB at the distal vessel wall. As the SNR begins to drop below 6 dB and then 3 dB, the performance of the estimator begins to degrade markedly. This is the reason for the poor performance at the distal vessel for v_x in the measurements. The simulations where not affected by this as there was no structure to the noise added and no phase error or short-circuits or temporal fluctuations.

Comparing the mean of the three estimated velocity components from measurements and simulations at the center of the vessel shows that the standard deviations are comparable. For the measurements they range from 2.1 cm/s to 2.6 cm/s, and for the simulations from 1.5 cm/s to 3.3 cm/s. In the measurements, the relative standard deviation normalized to the peak velocity magnitude ranges from 8 % to 12 %. In the simulations, it ranges from 6 to 13 %. To obtain these simulation results, noise was added to the channel data to obtain SNRs comparable to the measurements.

Similarly, the biases from measurements and simulations are of the same size and fluctuates around 0. For the measurements, the range is from -1.28 cm/s to 0.25 cm/s, and for the measurements it is -0.24 cm/s to 0.97 cm/s. The largest bias is less than 5 %. This demonstrates that using the mean spatial wavelengths obtained from simulations in the beamforming and the velocity estimation instead of the theoretically derived wavelengths eliminates the bias otherwise present.

Besides the SNR, the ensemble size in the velocity estimator affects the performance as illustrated in Figs. 8 and 9. As expected, the standard deviations (Fig. 9) are halved when the ensemble length is increased by a factor of four. This is due to the noise being uncorrelated from emission to emission, and therefore, the standard deviation drops with $1/\sqrt{N_i}$.

The results demonstrate, that under the same conditions, measurements and simulations provide comparable results. Thereby the validity of the simulation results presented here and previously reported has been verified.

With the 3D TO method, it is possible to obtain the true velocity magnitude in a given point as listed in Table II and III. The performance was comparable for simulations and measurements, and the relative standard deviation was less than 13 %, whereas almost no bias was present. The performance in the simulations is slightly better due to the reason discussed above.

VII. CONCLUSION

This paper has demonstrated that the 3D TO method synthesizes two double-oscillating fields that oscillate in the axial direction and either the transverse or the elevation direction. This is demonstrated through experimental measurements and through simulations. The double oscillating fields combined with spatial quadrature sampling is the foundation for the 3D TO method. To improve the performance of the method, the simulated mean wavelengths are used in the beamforming stage and in the velocity estimation.

Subsequently, the first 3D vector velocities obtained from an experimental setup using the 3D TO method are presented. Velocity measurements are conducted in an experimental flow-rig system with steady flow. The obtained velocity profiles are practically without bias and with relative standard deviations below 13 %. The experimental results and the simulated results—obtained under similar conditions—showed comparable performance. Thereby, the validity of the simulation results have been verified.

Estimation of the full 3D velocity vectors allows for calculations of the true velocity magnitude. The velocity magnitude is measured practically without bias and with relative standard deviations less than 13 % for flow directions almost parallel to the transducer surface.

The results verify that the 3D TO methods estimates the full three-dimensional velocity vectors. It is therefore possible to measure the correct velocity magnitude as well as the flow direction independent of transducer orientation. Because the three velocity components are estimated simultaneously, it will be possible to measure and visualize complex flow and the full 3D vortices and rotational flow as found for instance in the carotid artery—particularly at the bifurcation or at stenoses.

Acknowledgments

This work was supported by grant 024-2008-3 from the Danish Advanced Technology Foundation and BK Medical ApS, Denmark.

[1] S. Satomura, "Ultrasonic Doppler method for the inspection of cardiac functions", J. Acoust. Soc. Am. **29**, 1181–1185 (1957).

[2] P. J. Kilner, G. Z. Yang, R. H. Mohiaddin, D. N. Firmin, and D. B. Longmore, "Helical and retrograde secondary flow patterns in the aortic arch studied by three-directional magnetic resonance velocity mapping", Circulation **88**, 2235 – 2247 (1993).

[3] C. A. Taylor, T. J. R. Hughes, and C. K. Zarins, "Finite element modeling of blood flow in arteries", Comput. Methods Appl. Mech. Engrg. **158**, 155–196 (1998).

[4] K. L. Hansen, J. Udesen, F. Gran, J. A. Jensen, and M. B. Nielsen, "In-vivo examples of complex flow patterns with a fast vector velocity method", Ultraschall in Med **30**, 471–476 (2009).

[5] R. E. Daigle, C. W. Miller, M. B. Histand, F. D. McLeod, and D. E. Hokanson, "Nontraumatic aortic blood flow sensing by use of an ultrasonic esophageal probe", J. Applied Phys. **38**, 1153–1160 (1975).

[6] M. D. Fox and W. M. Gardiner, "Three-dimensional Doppler velocimetry of flow jets", IEEE Trans. Biomed. Eng. **35**, 834–841 (1988).

[7] B. Dunmire, K. W. Beach, K.-H. Labs., M. Plett, and D. E. Strandness, “Cross-beam vector Doppler ultrasound for angle independent velocity measurements”, Ultrasound Med. Biol. **26**, 1213–1235 (2000).

[8] G. E. Trahey, J. W. Allison, and O. T. von Ramm, “Angle independent ultrasonic detection of blood flow”, IEEE Trans. Biomed. Eng. **BME-34**, 965–967 (1987).

[9] A. A. Morsy and O. T. von Ramm, “FLASH correlation: A new method for 3-D ultrasound tissue motion tracking and blood velocity estimation”, IEEE Trans. Ultrason., Ferroelec., Freq. Contr. **46**, 728–736 (1999).

[10] L. N. Bohs, B. J. Geiman, M. E. Anderson, S. C. Gebhart, and G. E. Trahey, “Speckle tracking for multi-dimensional flow estimation”, Ultrasonics **38**, 369–375 (2000).

[11] V. L. Newhouse, K. S. Dickerson, D. Cathignol, and J.-Y. Chapelon, “Three-dimensional vector flow estimation using two transducers and spectral width”, IEEE Trans. Ultrason., Ferroelec., Freq. Contr. **41**, 90–95 (1994).

[12] A. McArdle, V. Newhouse, and K. Beach, “Demonstration of three-dimensional vector flow estimation using bandwidth and two transducers on a flow phantom”, Ultrasound Med. Biol. **21**, 679–692 (1995).

[13] W. Li, C. Lance, E. Ignacio Cspedes, A. Van Der Steen, and N. Bom, “Decorrelation of intravascular echo signals: Potentials for blood velocity estimation”, J. Acoust. Soc. Am. **102**, 3785–3794 (1997).

[14] J. Rubin, T. Tuthill, and J. Fowlkes, “Volume flow measurement using doppler and grey-scale decorrelation”, Ultrasound in Med. Biol. **27**, 101–109 (2001).

[15] T. Tuthill, J. Rubin, and J. Fowlkes, “Three-dimensional flow vectors from rf ultrasound signals”, in *Proc. SPIE - Medical Imaging - Ultrasonic Imaging and Signal Processing*, volume 4687, 210–217 (2002).

[16] O. Bonnefous, “Measurement of the complete (3D) velocity vector of blood flows”, in *Proc. IEEE Ultrason. Symp.*, 795–799 (1988).

[17] I. Hein, “3-D flow velocity vector estimation with a triple-beam lens transducer — experimental results”, IEEE Trans. Ultrason., Ferroelec., Freq. Contr. **44**, 85–95 (1997).

[18] J. A. Jensen and S. I. Nikolov, “A method for real-time three-dimensional vector velocity imaging”, in *Proc. IEEE Ultrason. Symp.*, 1582–1585 (2003).

[19] H. B. Kim, J. R. Hertzberg, and R. Shandas, “Development and validation of echo PIV”, Exp. in Fluids **36**, 455–462 (2004).

[20] L. Liu, H. Zheng, L. Williams, F. Zhang, R. Wang, J. Hertzberg, and R. Shandas, “Development of a custom-designed echo particle image velocimetry system for multi-component hemodynamic measurements: System characterization and initial experimental results”, Phys. Med. Biol. **53**, 1397–1412 (2008).

[21] C. Poelma, J. M. Mari, N. Foin, M. Tang, R. Krams, C. G. Caro, P. D. Weinberg, and J. Westerweel, “3D flow reconstruction using ultrasound PIV”, Exp. in Fluids **50**, 777–785 (2011).

[22] M. J. Pihl and J. A. Jensen, “3D velocity estimation using a 2D phased array”, in *Proc. IEEE Ultrason. Symp.*, 430–433 (2011).

[23] J. A. Jensen and P. Munk, “A New Method for Estimation of Velocity Vectors”, IEEE Trans. Ultrason., Ferroelec., Freq. Contr. **45**, 837–851 (1998).

[24] M. E. Anderson, “Multi-dimensional velocity estimation with ultrasound using spatial quadrature”, IEEE Trans. Ultrason., Ferroelec., Freq. Contr. **45**, 852–861 (1998).

[25] M. J. Pihl, J. Marcher, and J. A. Jensen, “Phased array vector velocity estimation using tranverse oscillations”, IEEE Trans. Ultrason., Ferroelec., Freq. Contr. **In press** (2012).

[26] J. A. Jensen, “A New Estimator for Vector Velocity Estimation”, IEEE Trans. Ultrason., Ferroelec., Freq. Contr. **48**, 886–894 (2001).

[27] C. Kasai, K. Namekawa, A. Koyano, and R. Omoto, “Real-Time Two-Dimensional Blood Flow Imaging using an Autocorrelation Technique”, IEEE Trans. Son. Ultrason. **32**, 458–463 (1985).

[28] T. Loupas, J. T. Powers, and R. W. Gill, “An axial velocity estimator for ultrasound blood flow imaging, based on a full evaluation of the Doppler equation by means of a two-dimensional autocorrelation approach”, IEEE Trans. Ultrason., Ferroelec., Freq. Contr. **42**, 672–688 (1995).

[29] J. Udesen, M. B. Nielsen, K. R. Nielsen, and J. A. Jensen, “Examples of in-vivo blood vector velocity estimation”, Ultrasound Med. Biol. **33**, 541–548 (2007).

[30] P. M. Hansen, M. M. Pedersen, K. L. Hansen, M. B. Nielsen, and J. A. Jensen, “Examples of vector velocity imaging”, in *15. Nordic-Baltic Conf. Biomed. Eng. and Med. Phys.* (2011).

[31] J. A. Jensen, H. Holten-Lund, R. T. Nielson, B. G. Tomov, M. B. Stuart, S. I. Nikolov, M. Hansen, and U. D. Larsen, “Performance of SARUS: A Synthetic Aperture Real-time Ultrasound System”, in *Proc. IEEE Ultrason. Symp.*, 305–309 (2010).

[32] M. J. Pihl and J. A. Jensen, “3D velocity estimation using a 2D phased array”, in *Proc. IEEE Ultrason. Symp.*, Accepted (2011).

[33] J. A. Jensen, “Field: A Program for Simulating Ultrasound Systems”, Med. Biol. Eng. Comp. **10th Nordic-Baltic Conference on Biomedical Imaging, Vol. 4, Supplement 1, Part 1**, 351–353 (1996).

[34] J. A. Jensen and N. B. Svendsen, “Calculation of Pressure Fields from Arbitrarily Shaped, Apodized, and Excited Ultrasound Transducers”, IEEE Trans. Ultrason., Ferroelec., Freq. Contr. **39**, 262–267 (1992).

[35] J. M. Hansen, M. C. Hemmsen, and J. A. Jensen, “An object-oriented multi-threaded software beam formation toolbox”, in *Proc. SPIE - Medical Imaging - Ultrasonic Imaging and Signal Processing*, volume 7968, 79680Y (2011).

Abstract A

Measuring 3D Velocity Vectors using the Transverse Oscillation Method

Michael Johannes Pihl and Jørgen Arendt Jensen

Proceedings of the IEEE International Ultrasonics Symposium

Accepted for conference in Dresden, Germany, 2012

Measuring 3D Velocity Vectors using the Transverse Oscillation Method

Michael Johannes Pihl and Jørgen Arendt Jensen

Center for Fast Ultrasound Imaging, Department of Electrical Engineering, Building 349
Technical University of Denmark
DK-2800 Kgs. Lyngby, Denmark
May 4, 2012

Background, Motivation and Objectives

Studies have shown that blood flow follows complex omnidirectional patterns. That illustrates the need for a 3D velocity estimator. Simulations have demonstrated that with a 2D transducer the Transverse Oscillation (TO) method can estimate 3D velocity vectors. This work verifies the method experimentally by presenting the first 3D TO velocity vector measurements obtained using the research ultrasound scanner SARUS and a 2D transducer.

Statement of Contribution/Methods

The 3D TO method estimates the two transverse velocity components based on two double-oscillating fields and spatial quadrature sampling. The axial velocity component is calculated using a conventional approach. Using a 3.5 MHz 32x32 element 2D transducer (Vermon S.A., Tours, France) with a pitch of 0.3 mm, data are acquired from all 1024 elements simultaneously with SARUS. Pulse-echo measurements are performed in a hydrophone scanning system (Onda, Sunnyvale, CA, USA) to evaluate the TO fields and the corresponding spectrum by means of the energy ratio between the left and the right side of the spectrum. Field II simulations are made for comparison. Flow measurements are carried out in a flow-rig system with a vessel radius of 6 mm. Based on the volume flow measured with a calibrated magnetic flow meter (Danfoss, Nordborg, Denmark), the peak velocity is 25 cm/s. The center of the vessel is located at a depth of 30 mm with a beam-to-flow angle of 78&[deg] in either the ZX- or ZY-plane. Data from 544 emissions at 500 Hz are sampled, and eight 3D velocity profiles are constructed using 64 emissions per estimate. Mean velocities and standard deviations are calculated to evaluate the performance.

Results, Discussion, and Conclusions

The pulse-echo measurements resulted in an average TO wavelength of 6.8 and 5.3 mm in the x- and y-directions. The Field II simulation values are 3.7 and 3.3 mm. The energy ratios are -7.3 and -10 dB compared to -32 and -36 dB in the simulations. The average of the measured velocity profiles are shown in the figure. At the center, <I>v_x</I> & <I>v_y</I> are 27&[plusmn]4.0 cm/s & 4.5&[plusmn]3.6 cm/s and 0.29&[plusmn]2.3 cm/s & 23&[plusmn]3.2 cm/s for flow in the ZX- and ZY-plane, respectively. The measurements demonstrate that the TO method can estimate the 3D velocity vector using a 2D array. This allows measurements of vortices and rotational flow as found for instance in the carotid artery.

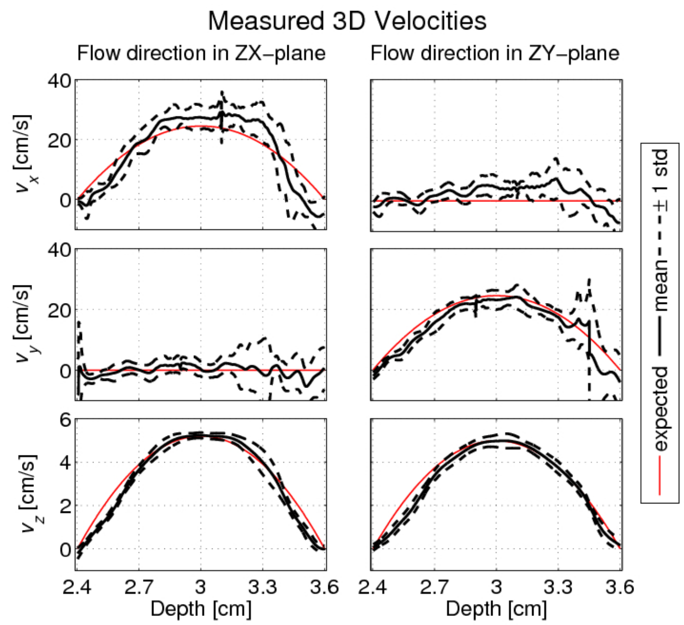

Abstract B

Preliminary example of 3D vector flow imaging

Michael Johannes Pihl, Matthias Bo Stuart,
Borislav Gueorguiev Tomov, Jens Munk Hansen,
Morten Fischer Rasmussen, and Jørgen Arendt Jensen

Proceedings of SPIE – Medical Imaging – Ultrasonic Imaging and Signal Processing

Submitted for conference in Orlando, Florida, United States, 2013

Preliminary example of 3D vector flow imaging

Michael Johannes Pihl[a], Matthias Bo Stuart[a], Borislav Gueorguiev Tomov[a],
Jens Munk Hansen[a,b], Morten Fischer Rasmussen[a], and Jørgen Arendt Jensen[a]

[a] Center for Fast Ultrasound Imaging, Dept. of Elec. Eng.,
Technical University of Denmark, 2800 Lyngby, Denmark.
[b] BK Medical ApS, 2730 Herlev, Denmark

ABSTRACT

This paper presents 3D vector flow images obtained using the recently proposed 3D Transverse Oscillation (TO) method. The method employs a 2D transducer and estimates the three velocity components simultaneously, which is important for estimating complex flow patterns. Data are acquired using an experimental ultrasound scanner on a flow-rig system with steady flow. The vessel of the flow-rig is centered at a depth of 30 mm, and the flow has an expected 2D circular-symmetric parabolic profile with a peak velocity of 1 m/s. Ten frames of 3D vector flow images are acquired in a cross-sectional plane of the vessel orthogonal to the length axis, which coincides with the y-axis and the flow direction. Hence, only out of plane motion is expected, which is unmeasurable by current commercial scanners. Each frame consists of 31 flow lines steered from -15 to 15 degrees in steps of 1 degree in the ZX-plane. For the center line, 3200 emissions are obtained yielding 100 M-mode lines. At the center of the vessel, the mean and standard deviation of the estimated velocity vectors are (v_x,v_y,v_z)=(-0.03,95,1.0)±(9,6,1) cm/s compared to the expected (0,96,0) cm/s. One of the 3D vector flow image frames is illustrated by the three velocity components and the true velocity magnitude. Practically no in plane motion (vx and vz) is measured, whereas the out of plane motion (vy) and the velocity magnitude exhibits the expected 2D circular-symmetric parabolic shape. The results demonstrate the capability of the 3D TO method for performing 3D vector flow imaging.

Keywords: Medical ultrasound, velocity estimation, three-dimensional vector flow imaging, 3D velocities, transverse oscillation method, spatial quadrature

1. INTRODUCTION

Ultrasonic velocity estimation of the blood is an important diagnostic tool in the clinic. As an example, the peak velocity in the carotid artery is a main diagnostic criteria in assessing the degree of stenosis.[1] Furthermore, hemodynamic studies have shown that the velocity of the blood is three-dimensional (3D) and exhibits complex flow patterns.[2,3] This underlines the need for a method that is able to estimate the full 3D velocities, and the authors[4] have recently suggested a 3D Transverse Oscillation (TO) method, which is capable of this. The purpose of this paper is to demonstrate the feasibility of employing the 3D TO method for 3D vector flow imaging (VFI). This is illustrated through preliminary examples of vector flow images in a cross section of an artificial vessel.

2. THE 3D TRANSVERSE OSCILLATION METHOD

A method employing transverse oscillations for 3D velocity vector estimation has recently been suggested by the authors.[4] The 3D TO method employs an approach that synthesises transverse oscillations as suggested by Jensen and Munk,[6] where Anderson[7] proposed a similar method. The 3D TO method estimates the transverse and elevation velocity components based on two double-oscillating fields and spatial quadrature sampling by employing a 2D matrix transducer. Five lines are beamformed in parallel in receive using the same sampled data. The center line is beamformed in the axial direction of the steered beam. Two TO lines are beamformed in the transverse direction of the beam confined in the ZX-plane (see right part of Fig. 1). Also, two TO lines are beamformed in the elevation direction of the beam (in the ZY-plane). Thereby, the velocity estimation is decoupled into three orthogonal velocity components. The inter beam spacing of the two pairs of TO beams is determined by the mean transverse wavelength, $\bar{\lambda}_x$, and the mean elevation wavelength, $\bar{\lambda}_y$, calculated based on the simulated TO spectra.[6,8] The beams are steered radially, hence, the estimated axial velocity, v_a, the

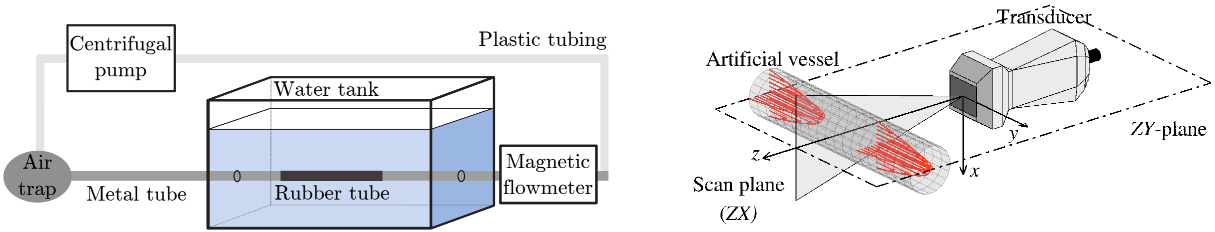

Figure 1: Illustration of the flow-rig system (left) and the measurement setup (right). The transducer is placed above the vessel. Data are obtained along the z-axis (vertically) and in the ZX-plane.

transverse velocity, v_t, and the elevation v_e must be rotated and scan converted to obtain v_x, v_y and v_z. The velocity estimation of v_t and v_e utilizes the estimator suggested by Jensen,[9] whereas v_a is calculated using a conventional autocorrelation estimator[10] with RF averaging.[11] The three velocity components are estimated simultaneously from the same data.

3. MATERIALS AND METHODS

A 3.5 MHz 32x32 element 2D matrix array transducer (Vermont S.A., Tours, France) with a pitch of 0.3 mm is employed. At a sampling frequency of 70 MHz, data from all the 1024 active elements are acquired simultaneously through the 1024 channels on the synthetic aperture real-time ultrasound system, SARUS,[12] and are stored for offline processing. Velocities are measured in a flow-rig system as illustrated in Fig. 1. A Cole-Parmer centrifugal pump (Vernon Hills, IL, USA) circulates a blood-mimicking fluid (Danish Phantom Design, Frederikssund, Denmark) in the closed loop circuit. The vessel radius is 6 mm and the length is long enough to ensure fully developed laminar flow, which has a parabolic flow profile. The volume flow-rate is measured by a calibrated MAG1100 flowmeter (Danfoss, Nordborg, Denmark) and used for calculating the peak velocity and the expected parabolic profiles. The velocity was set to be approximately 1.0 m/s to mimic the velocities of the blood in the carotid artery. The pulse repetition frequency was 2.4 kHz.

Ten frames of 3D vector flow images are acquired in a cross-sectional plane of the vessel orthogonal to the length axis, which coincides with the y-axis and the flow direction. Each frame consists of 31 flow lines steered from -15° to 15° in steps of 1° in the ZX-plane. For the center line, 3200 emissions are obtained yielding 100 M-mode lines The scan plane is the ZX-plane, and thereby, the expected flow direction is $\mathbf{v}/|\mathbf{v}| = (0, 1, 0)$ in (x, y, z). Hence, only out of plane motion is expected, which is unmeasurable by current commercial scanners. After matched filtration, the data are beamformed offline using the Beamformation Toolbox 3.[13] Mean stationary echo cancelling (clutter filtering) is performed by subtracting the mean ensemble value from the 32 M-mode lines prior to the velocity estimation. The estimated transverse and axial velocities have to be rotated as they are obtained orthogonal to or along, respectively, thee steered beams. The rotation of the axial, v_a, and the transverse, v_t, velocity components to obtain v_z and v_x is

$$\begin{pmatrix} v_z \\ v_x \end{pmatrix} = \begin{pmatrix} \cos\theta_{zx} & -\sin\theta_{zx} \\ \sin\theta_{zx} & \cos\theta_{zx} \end{pmatrix} \begin{pmatrix} v_a \\ v_t \end{pmatrix}$$

where θ_{zx} is the steering angle in the ZX-plane. Due to the position of the scan plane, the elevation velocities, v_e, are equal to v_y. Before displaying the 3D vector flow images, the velocities and the B-mode image are scan converted according to the steering angle of the lines from radial coordinates to Cartesian coordinates.

4. MEASUREMENT RESULTS AND DISCUSSION

Fig. 2 shows the velocity profiles for the three velocity components v_x, v_y, and v_z and the velocity magnitude obtained for M-mode lines along the diameter of the vessel. The mean of 100 velocity profiles along with the range of one standard deviation is displayed. The mean of the velocities follow the expected profiles. At the center of the vessel, the mean of the measured velocity vector along with the expected velocity and the resulting bias is

$$\bar{\mathbf{v}} = \begin{pmatrix} \bar{v}_x \\ \bar{v}_y \\ \bar{v}_z \end{pmatrix} = \begin{pmatrix} -0.03 \\ 95. \\ 1.0 \end{pmatrix} \pm \begin{pmatrix} 9. \\ 6. \\ 0.8 \end{pmatrix} \text{cm/s}, \quad \mathbf{v}_{\text{exp}} = \begin{pmatrix} 0. \\ 96. \\ 0. \end{pmatrix} \text{cm/s}, \quad \text{and} \quad \mathbf{B_v} = \begin{pmatrix} -0.03 \\ -0.8 \\ -1. \end{pmatrix} \text{cm/s}.$$

The results demonstrate the performance of the estimator and that the method is capable of estimating 3D velocities.

Frames of 3D vector flow images in the 2D scan plane forming a cross section of the vessel are acquired. Due to the flow direction, no in plane velocity is expected. Hence, conventional 1D or even 2D velocity estimators would not measure any velocity. One of the ten 3D vector flow image frames is visualized in Fig. 3. The figure displays the color flow images for the three velocity components and the absolute velocity magnitude. The velocity components v_x and v_z are almost zero in the scan plane as expected due to the flow direction. For v_y, the velocity is highest at the center of the vessel and lower at the vessel boundaries. Same appearance is found for the velocity magnitude $|\mathbf{v}|$. The shape is similar to the expected circular-symmetric 2D parabolic velocity profile.

5. CONCLUSION AND PERSPECTIVES

Three-dimensional vector flow images using the 3D TO method has been presented, and they demonstrate the feasibility of using the method for 3D VFI. With the 3D TO method, the full 3D velocity vector—including the out of plane motion—and the correct velocity magnitude can be measured in e.g. cross sections of blood vessel. Conventional and even 2D methods would fail to estimate any velocity in the presented 3D vector flow images. The correct velocity magnitude can be obtained regardless of the orientation of the transducer, and therefore, operator independently. Additionally, the simultaneous calculation of the three velocity components is important for visualizing complex flow patterns. Hence, it will be possible to measure and visualize the full 3D vortices and rotational flow as found for instance in the carotid artery—particularly at the bifurcation or at stenoses.

ACKNOWLEDGMENTS

The presented work was financially supported by grant 024-2008-3 from the Danish Advanced Technology Foundation and from BK Medical ApS, Denmark.

REFERENCES

[1] Arning, C., Widder, B., von Reutern, G. M., Stiegler, H., and Görtler, M., "Revison of DEGUM Ultrasound Criteria for Grading Internal Carotid Artery Stenoses and Transfer to NASCET Measurement," *Ultraschall in Med* **31**(3), 251–257 (2010).

[2] Hansen, K. L., Udesen, J., Gran, F., Jensen, J. A., and Nielsen, M. B., "In-vivo examples of complex flow patterns with a fast vector velocity method," *Ultraschall in Med* **30**, 471–476 (2009).

[3] Harloff, A., Albrecht, F., Spreer, J., Stalder, A. F., Bock, J., Frydrychowicz, A., Schollhorn, J., Hetzel, A., Schumacher, M., Hennig, J., and Markl, M., "3D blood flow characteristics in the carotid artery bifurcation assessed by flow-sensitive 4D MRI at 3T," *Magn Reson Med* **61**(1), 65–74 (2009).

[4] Pihl, M. J. and Jensen, J. A., "3D velocity estimation using a 2D phased array," in [*Proc. IEEE Ultrason. Symp.*], 430–433 (2011).

[5] Hansen, P. M., Pedersen, M. M., Hansen, K. L., Nielsen, M. B., and Jensen, J. A., "Examples of vector velocity imaging," in [*15. Nordic-Baltic Conf. Biomed. Eng. and Med. Phys.*], (2011).

[6] Jensen, J. A. and Munk, P., "A New Method for Estimation of Velocity Vectors," *IEEE Trans. Ultrason., Ferroelec., Freq. Contr.* **45**, 837–851 (1998).

[7] Anderson, M. E., "Multi-dimensional velocity estimation with ultrasound using spatial quadrature," *IEEE Trans. Ultrason., Ferroelec., Freq. Contr.* **45**, 852–861 (1998).

[8] Pihl, M. J., Marcher, J., and Jensen, J. A., "Phased array vector velocity estimation using tranverse oscillations," *IEEE Trans. Ultrason., Ferroelec., Freq. Contr.* **In press** (2012).

[9] Jensen, J. A., "A New Estimator for Vector Velocity Estimation," *IEEE Trans. Ultrason., Ferroelec., Freq. Contr.* **48**(4), 886–894 (2001).

[10] Kasai, C., Namekawa, K., Koyano, A., and Omoto, R., "Real-Time Two-Dimensional Blood Flow Imaging using an Autocorrelation Technique," *IEEE Trans. Son. Ultrason.* **32**, 458–463 (1985).

[11] Loupas, T., Powers, J. T., and Gill, R. W., "An axial velocity estimator for ultrasound blood flow imaging, based on a full evaluation of the Doppler equation by means of a two-dimensional autocorrelation approach," *IEEE Trans. Ultrason., Ferroelec., Freq. Contr.* **42**, 672–688 (1995).

[12] Jensen, J. A., Holten-Lund, H., Nielson, R. T., Tomov, B. G., Stuart, M. B., Nikolov, S. I., Hansen, M., and Larsen, U. D., "Performance of SARUS: A Synthetic Aperture Real-time Ultrasound System," in [*Proc. IEEE Ultrason. Symp.*], 305–309 (Oct. 2010).

[13] Hansen, J. M., Hemmsen, M. C., and Jensen, J. A., "An object-oriented multi-threaded software beam formation toolbox," in [*Proc. SPIE - Medical Imaging - Ultrasonic Imaging and Signal Processing*], **7968**, 79680Y (2011).

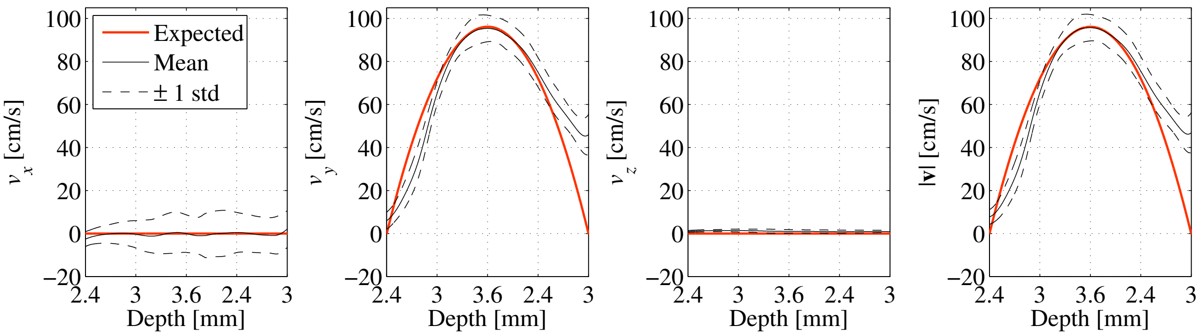

Figure 2: The mean and the range of one standard deviation as well as the expected profiles are plotted for the three velocity components and the resulting velocity magnitude through the center of the vessel.

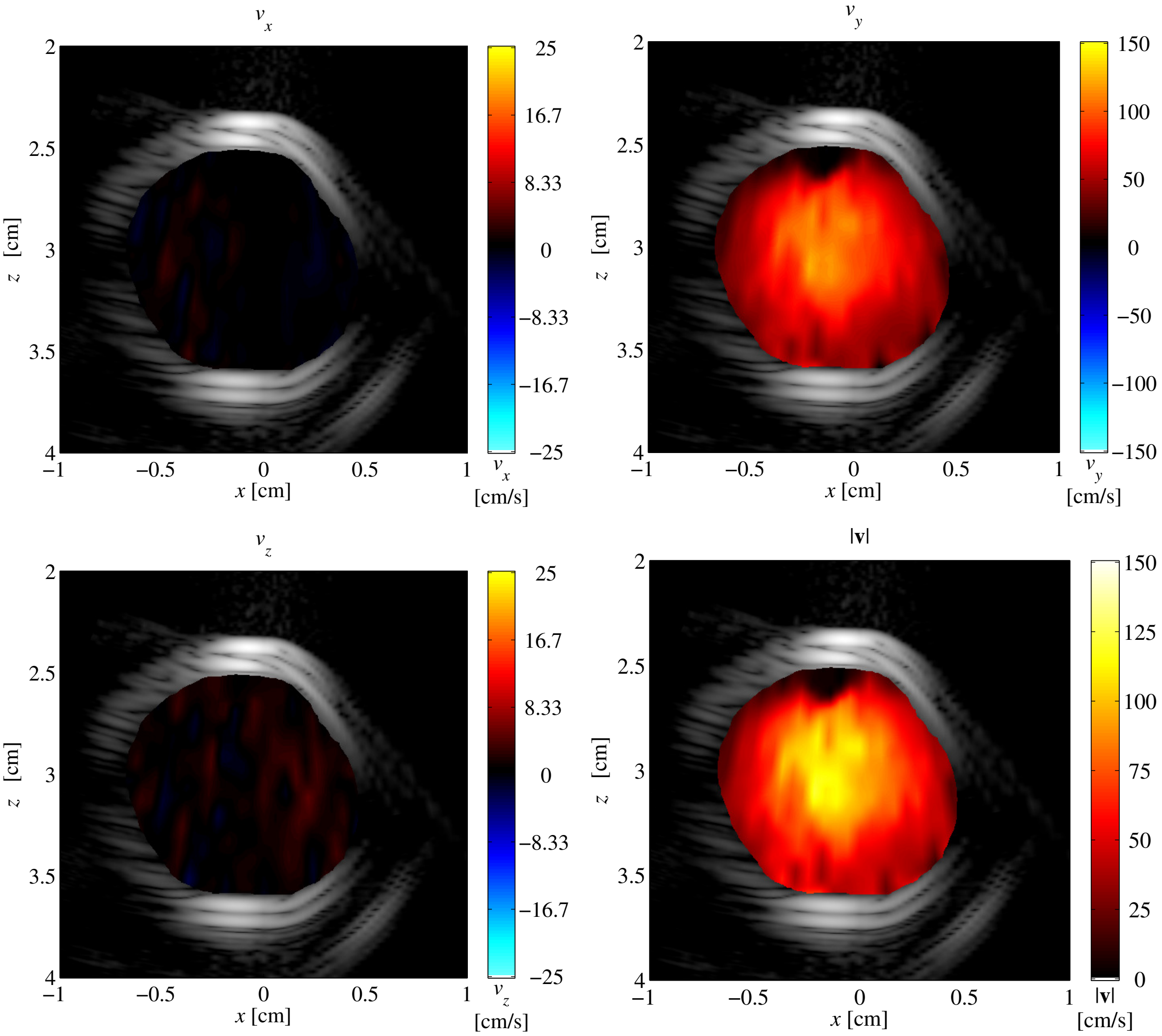

Figure 3: Measured 3D vector flow images in a 2D scan plan for the three scan converted velocity components v_x, v_y, and v_y and the absolute velocity. The scan plan is orthogonal to the flow direction. Please note the different scaling of the colorbars. The mask for mapping the flow data was created by manually selecting the outline of the inner lumen based on the B-mode image (70 dB dynamic range). The black area in the top of the vessel lumen is due to clipping in the sampled channel data because of the strong reflections at the top of the vessel.

Hovedformålet med ph.d.-projektet har været at udvikle en metode til at måle blodets hastighed i tre dimensioner (3D) med ultralyd. At kunne måle blodets hastighed og strømningsforhold er vigtige redskaber for lægerne, når de skal diagnosticere en lang række kredsløbssygdomme. Det kan for eksempel være åreforkalkning i halspulsåren, hvor man ved at måle blodets gennemstrømningshastighed kan sige noget om hvor forsnævret pulsåren er.

Når lægerne i dag måler blodets hastighed, kan de kun måle i én retning- det vil sige i én dimension – og det et problem fordi blodstrømningerne i blodkarrene kan pege i alle mulige retninger. For at kunne undersøge de faktiske strømningsforhold og hastigheden, er det derfor afgørende at kunne måle i alle retninger, det vil sige i alle tre rummelige dimensioner.

I afhandlingen præsenteres en metode, der er udviklet til netop at måle blodets hastighed i alle tre rummelige dimensioner samtidigt. Det er vigtigt, at målingerne er foretaget samtidigt, når man måler komplicerede strømningsforhold, som for eksempel hvirvelstrømme.

Computer-simuleringer og eksperimentelle målinger på et flow-fantom har vist, at metoden virker, og der er efterfølgende optaget todimensionelle billeder af væsken, der strømmer ud af billed-planet – noget man hidtil ikke har kunnet. Målingerne viser, at det er muligt at måle hastigheden ud af planet, og at metoden dermed kan bruges til at lave 3D-billeder af blodgennemstrømningen.

Den metode der er udviklet gør det muligt for lægerne at måle den sande hastighed – uden at kompensere for, at der kun er målt i én retning – det betyder hurtigere og mere præcise skanninger.

På sigt kan det tænkes, at 3D metoder vil kunne benyttes til at screene patienter, som er i risiko for at udvikle åreforkalkning. Målingerne vil også gøre lægerne i stand til at måle de komplicerede strømningsmønstre, der opstår omkring forkalkninger i blodbanen og omkring for eksempel hjerteklapper.

www.elektro.dtu.dk

Department of Electrical Engineering
Center for Fast Ultrasound Imaging
Biomedical Engineering
Technical University of Denmark
Ørsteds Plads
Building 348
DK-2800 Kgs. Lyngby
Denmark
Tel: (+45) 45 25 38 00
Fax: (+45) 45 93 16 34
Email: info@elektro.dtu.dk

ISBN 978-87-92465-70-2